H2020 5G-Crosshaul project
Grant No. 671598

INTEGRATION OF PHYSICAL AND LINK LAYER TECHNOLOGIES IN XHAUL NETWORK NODES

Abstract

This document presents the physical and link layer integration of the different technologies considered in the 5G-Crosshaul network, as presented in D2.1. Based upon the requirements defined within the project, detailed experimentation and simulation results of each considered technology under its corresponding network scenario are presented. These results focus on the innovation introduced by the 5G-Crosshaul project with respect to the state of the art and their alignment with the KPI's and objectives defined in the project.

This deliverable is organized into four main parts. The first one is dedicated to deriving the data transport requirements for the relevant use cases defined in WP1. The second part assesses, by means of experimentation, the analysis of each technology started in D2.1. The third part combines each technology in node and related network scenarios to analyze them according to the transport requirements derived from WP1. Finally, the fourth part reports a summary of the results, the novelty with respect the state of the art, as well as the match with respect to the KPIs and objectives of the project.

Document Properties

Document Number:	D2.2
Document Title:	Integration of physical and link layer technologies in Xhaul network nodes
Document Responsible:	UC3M
Document Editor:	José Alberto Hernández (UC3M)
Authors:	
Target Dissemination Level:	Public
Status of the Document:	Final
Version:	3.3

Production Properties:

Reviewers:	Nuria Sánchez (VISIONA), Andrea di Giglio (TI)

Document History:

Revision	Date	Issued by	Description
1.0	17/07/2017	José Alberto Hernández	First integration of IR2.3, IR2.4
2.0	04/09/2017	José Alberto Hernández	Rearrengement of document contents and final sectioning and table of contents
3.0	18/09/2017	José Alberto Hernández	New material and contributions added after new experiments. First integrated version.
3.1	25/09/2017	José Alberto Hernández	Second integrated version with changes made by section editors and responsibles
3.2	25/10/2017	Nuria Sánchez, Andrea di Giglio	Document review
3.3	30/10/2017	José Alberto Hernández	Final version

Disclaimer:

This document has been produced in the context of the 5G-Crosshaul Project. The research leading to these results has received funding from the European Community's H2020 Programme under grant agreement Nº H2020-671598.

Table of Contents

List of Contributors

Partner no.	Partner short name	Contributor's name
P01	UC3M	José Alberto Hernández, David Larrabeiti
P03	EAB	Miguel Berg, Chenguang Lu, Daniel Cederholm
P04	TEI	Paola Iovanna
P06	NOK-N	Thomas Deiss, Bertold Dickhaus
P07	IDCC	Ping-Heng Kuo, Alain Mourad
P08	TID	Luis M. Contreras, Nicolás A. Serrano
P09	TI	Andrea di Giglio, Antonia Paolicelly, Laura Serra, Roberto Morro
P10	ORANGE	Luiz Anetneto, Phillipe Chanclou
P11	VISIONA	Nuria Sánchez, Carlos Navarro
P15	TELNET	Enrique Masgrau, José V. Galán
P16	FhG-HHI	Peter Farkas, Volker Jungnickel Dominic Schulz, Anagnostis Paraskevopoulos
P17	CTTC	Jorge Baranda, Josep Mangues, José Núñez, Marco Miozzo, Paolo Dini, Josep M. Fábrega, Michela Svaluto, Iñaki Pascual, Laia Nadal
P20	ULUND	Per Ödling, Kaan Bür
P21	ITRI	Sean Chang, Kun-Yi Lin, Rabin Chen

List of Figures

List of Acronyms

Acronym	Description
µWave	Microwave
3GPP	3rd Generation Partnership Project
ADC	Analogue to Digital Converter
AMCC	Auxiliary Management and Control Channel
API	Application Programming Interface
B2B	Back to Back
BBU	Baseband Units
BER	Bit Error Rate
BGA	Ball Grid Array
BH	BackHaul
BS	Base Station
C&M	Control & Management
CapEx	Capital Expenditures
CAPS	Combined Amplitude Phase Shift
CLI	Command Line Interface
CPRI	Common Public Radio Interface
C-RAN	Cloud Radio Access Network
CWDM	Coarse Wavelength Division Multiplexing
DAC	Digital to Analogue Converter
DMT	Discrete Multi-Tone
DD	Direct Detection
DSL	Digital Subscriber Line
DSON	Decentralized Self Organized Network
DWDM	Dense Wavelength Division Multiplexing
EDFA	Erbium Doped Fiber Amplifier
EE	Energy Efficiency
EH	Energy Harvesting
EIRP	Equivalent isotropic radiated power
EMMA	Energy Management and Monitoring Applications
EN	Exchange Node
E/O	Electrical-to-optical
EVM	Error Vector Magnitude
FA	Forwarding Agent
FDD	Frequency Division Duplex
FDM	Frequency-Division Multiplexing
FEC	Forward error correction
FH	FrontHaul
FOV	Field of View
FSO	Free Space Optics
FWHM	Full Width Half Maximum
GC2D	Dual Polarization Grating Coupler
GHG	Greenhouse Gases
GPON	Gigabit-capable Passive Optical Network
GUI	Graphical User Interface
HEU	Head-end unit
ICT	Information and Communication Technology
I/Q	In-phase/Quadrature
IFFT	Inverse Fourier Transform

IM/DD	Intensity Modulation Direct Detection
LDPC	Low-density Parity Check
LED	Light Emitting Diode
LoS	Line-of-Sight
MCS	Modulation and coding scheme
MIMO	Multiple-Input Multiple-Output
MMI	Multi-mode Interferometer
mmWave	Millimeter wave
MZI	Mach-Zhender Interferometer
MZM	Mach-Zhender modulator
NBI	NorthBound Interface
NFV	Network Function Virtualisation
NGPON	Next-Generation Passive Optical Network
OAM	Operation, Administration and Maintenance
OADM	Optical Add and Drop Multiplexer
OBPF	Optical Band Pass Filter
ODL	OpenDayLight
ODN	Optical Distribution Networks
O/E	Optical-to-electrical
OFDM	Orthogonal Frequency Division Multiplexing
OLT	Optical Line Terminal
ONF	Open Networking Foundation
ONOS	Open Network Operating System
ONU	Optical Network Unit
OOK	On-Off Keying
OpEx	Operational Expenditures
OSC	Oscilloscope
OWC	Optical Wireless Communications
PD	Photodiode
PLL	Phase-Locked Loop
PAM	Pulse-Amplitude Modulation
PoC	Proof of Concept
PON	Passive Optical Network
PT	Pilot Tone
RoF	Radio over Fiber
QL	Q-learning
QPSK	Quadrature Phase Shift Keying
RAN	Radio Access Network
RAU	Radio Access Unit
RES	Renewable Energy Source
RF	Radio Frequency
RL	Reinforcement Learning
ROADM	Reconfigurable Add and Drop Multiplexer
RRM	Radio Resource Management
RRU/H	Radio Remote Units/Heads
RTT	Round Trip Time
SBI	SouthBound Interface
S-BVT	Sliceable Bandwidth Variable Transceivers
SC	Small Cell
SDN	Software Defined Networking
SFP	Small-Factor Pluggable
SNMP	Simple Network Management Protocol

SOC	State Of Charge
SOP	State of Polarization
SSB	Single Sideband
SSMF	Standard Single Mode Fibre
SSS	Spectrum Selective Switches
TBD	Testbed Device
TCP	Transmission Control Protocol
TC	Transmission Convergence
TDD	Time-Division Duplexing
UDP	User Datagram Protocol
URI	Uniform Resource Identifier
VOA	Variable Optical Attenuator
WIA	Wireless Interface Agent
WSS	Wavelength Selective Switches
XCI	5G-Crosshaul Control Interface
XFE	5G-Crosshaul Forwarding Element
XG-PON	10-Gigabit-capable Passive Optical Network

Executive Summary

This deliverable aims at integrating both physical and link layer technology in 5G-Crosshaul network nodes, further validated by means of analysis and experimentation.

The deliverable is organized in four main parts. The first one is dedicated to deriving the requirements for transport for the relevant use cases defined in WP1. The second part assesses by means of experimentation the analysis of each technology already started in D2.1. The third part, that includes chapter 4 and 5, combines each technology in node and related network scenarios to analyze them according the transport requirements presented in WP1. Finally, the fourth part (corresponding from chapter 6) reports the summary of the results, the novelty with respect the state of the art and the match with respect to the KPIs and objectives of the project. Chapter 2 and chapter 6 can be considered to facilitate the readability of this deliverable to provide an exhaustive overview of the work, while chapters 3, 4, and 5 report very detailed analysis and results.

5G-Crosshaul refers to an innovative transport that evolves by traditional wire connectivity among the radio equipment towards a network able to support both fronthaul, backhaul and different client traffic. The design of a transport network at the worst case is not reasonable in terms of cost and availability of technology, and is further not necessary because it could be not required to meet all the use cases concurrently. For example, there are some use cases with tight requirements about bandwidth needs, some others about the latency, and just a subset could ask tight requirements for both bandwidth and latency concurrently. Moreover, some use case can be delivered in very limited geographical area (e.g. stadium, etc..) while other use cases are served in a distributed area, hence the geographical location where the service is provided is relevant as well. Hence the approach is to define the scenarios, the corresponding services and analyze which technology can be used in the several scenarios for the specific use case.

Four key 5G reference network scenarios have been considered, namely i) very dense deployment of indoor and outdoor small cells, ii) WDMPON-based network, iii) multi-layer packet-optical networks, and iv) virtualized RAN based network.

Each scenario has been analyzed considering four relevant use cases of WP1 described in D1.1, namely i) high-speed train and vehicle safety, ii) media distribution, iii) dense urban society, and iv) mobile edge computing which require up to 10 Gbit/s peak rates.

In addition to the end user service type or use case, the requirements on transport also depend on the radio split options utilized. Several alternatives for the radio split options are under discussion in the standardization bodies. So, chapter 2 of this deliverable report the analysis performed to derive the corresponding transport requirements suitable for each use cases and for each radio split option. Table summarizes such requirements in detail.

The transport requirements for each use case in terms of bandwidth and latency have been derived considering the radio functional split options, ranging from option 8 (i.e. CPRI) to option 1 (i.e. backhaul). For simplification, the functional split options have been organized in three main groups: 1) CPRI (i.e. option 8), 2) NR with centralized HARQ procedure (option 5-7) and 3) NR with distributed HARQ procedure (option 1-4). The higher the option number is, the more transport bandwidth is required. Basically, the transport requirements are derived such that the required bandwidths for NR option 1-4 are considered the same as the required service rate and the required CPRI option 8 bandwidths are given as reference values for comparison. For more details, the derived transport requirements are listed in Table in Chapter 2.

Examples of remarkable achievements obtained and reported in this deliverable are listed in the following:

- Prototype of silicon photonic integrated reconfigurable optical add drop multiplexer, providing optical 5G-Crosshaul networks with enhanced flexibility, at dramatically reduced cost compared to current solutions;
- Advanced compression schemes for fronthaul, allowing the reuse of the copper access infrastructure, as enabler for massive deployment of indoor small cell;
- SDN enabled mesh mmWave networks, as an enabler for indoor small cells and frequency reuse with wireless transport technologies;
- Prototype of time-deterministic multi-layer switch based on a protocol agnostic framing protocol, capable to arbitrarily multiplex backhaul and fronthaul client signals on the same optical channel;
- Highly spectrally efficient fronthaul schemes, based on Hybrid Analogue-Digital Radio over Fibre over WDM optical networks.

1 Introduction

This report complements D2.1 [5] with the analysis, simulation, experimentation and validation of physical and link layer technologies overviewed in D2.1 for the design of 5G-Crosshaul network nodes.

In this light, this document starts with an overview of relevant 5G use cases along with their service-level requirements in terms of bandwidth and latency (Chapter 2). Then the corresponding fronthaul (FH) transport requirements for some selected functional splits like option 8 and option 1-4 [4]have been derived in terms of the required FH transport bandwidth and latency to fulfill the service-level requirements. Such FH transport requirements are used to analyze and evaluate different data-plane technologies for the reference network scenarios. Finally, a reference note to the new evolved CPRI standard (eCPRI) recently released is considered for the sake of completeness.

Chapter 3 reports the analysis by experimentation of the technologies described in [5] with the objective to assess the several technologies. Wireless solutions are experimentally analysed based on existing solutions for commercial spectra bands, millimetre wave (mmWave) or new wireless optics technologies. Field trials results are reported with microwaves and mmWaves to guarantee the network coverage in different deployment scenarios, from long distance backhauling in rural and suburban area, including over sea transmission for islands connections, to street level small cells backhauling and fronthauling. SDN controlled meshed transport networks based on mmWave are experimentally investigated as well to enable high rate wireless links, increase spatial frequency reuse, and cost-effective transport and capillary transport for ubiquitous connectivity. Finally, wireless optics measurements report latency and data rates in varying visibility conditions.

Next, as mentioned, technologies to enable 5G-Crosshaul on fixed access networks are also discussed in Chapter 3. Coexistence of residential users and radio terminals on XG-PON and NG-PON2 standards is numerically investigated, focusing on delay values for fronthaul and backhaul traffic with dynamic bandwidth allocation algorithms. The impact on radio performance in a WDM PON of an Auxiliary Management and Control Channel (AMCC) is also experimentally investigated showing significant but acceptable impact on the jitter. Finally, novel elastic networking solutions based on sliceable bandwidth variable transponders are also proposed as future evolution of flexible PONs. The results show successful transparent connections from BBU to RRH at capacities beyond 50 Gbit/s over 60 km distance.

Chapter 3 ends with the assessment of optical technologies for 5G-Crosshaul, including cost and energy studies of 100 Gbit/s transmission solutions based on direct detection using 3rd order Combined Amplitude and Phase (CAPS-3) as a new promising modulation format; and a mini-ROADM prototype that introduces flexibility in the 5G-Crosshaul network segment at two order of magnitude reduced cost compared to current optical switching solutions. Experiments to evaluate the radio performance with Analogue Radio over Fibre and spectrally-efficient Hybrid Analogue/Digital Radio over Fibre solutions back compatible with CPRI are also reported in this chapter. Finally, a successful field trial experiment has been performed with the goal of testing two different vendor solutions in a realistic DWDM system configuration with 200 Gbit/s coherent technology.

Technologies to enable 5G-Crosshaul circuit and packet switching and multiplexing are discussed in Chapter 4. First, a set of numerical and simulation-based experiments of a set of XPFEs with Ethernet backhaul and packetized fronthaul client signals competing for a single service unit at the output port is carried out. The analysis was performed with different client signals, load ratios and proportions of FH/BH showing that the Strict Priority queueing discipline guarantees that not only average delays are compliance with the service requirements, but also worse case delays and Packet Delay Variation. Next, the XCSEs are studied using the new deterministic-delay framing, showing the possibility to aggregate fronthaul and backhaul on the same wavelength with no degradation on the demanding performance of CPRI signals. Both approaches can complement themselves with the help of a multi-layer algorithm that favors packet switching over circuit when possible, taking advantage of the statistical multiplexing benefits of the former approach. Finally, high efficiency fronthaul compression schemes based on the elimination of redundancy sources (oversampling and over-quantization) and entropy coding in digital fronthaul are also numerically investigated within Chapter 4, showing that compression factors between 4x and 5x are achievable. Much higher compression factors (e.g. 30) are possible with more complex but still practical linear prediction and Huffman coding techniques, also investigated by simulations.

Chapter 5 focuses on three reference network scenarios for the purpose of demonstration the suitability of the investigated technologies in a variety of situations, namely: i) very dense deployment of indoor and outdoor small cells; ii) WDMPON-based network; and iii) virtualized RAN based network. For each scenario, the performance metrics in terms of bandwidth and/or latency are evaluated by analysis, lab tests and simulations in order to assess on their feasibility to fulfill the transport requirements. The evaluation results show that option 8 functional split is too demanding for all 5G use cases in all scenarios. Other splits are indeed needed to relax the transport requirements and provide the required 5G service rate. In addition, FH compression of option 8 is shown feasible as an alternative for the indoor small cell scenario.

Basically, the evaluation results for different scenarios show that the optical solutions with high speed WDMPON or direct point-to-point fibre connections can fulfill the requirements of all use cases, due to the high capacity transmission capacity by optical technologies. More particularly, WDMPON only supports NR option 1-4 functional split (possibly up to option 6) while multi- layer packet-optical networks can support option 7 and up. For the indoor and outdoor small cell scenario, the cost-effective solutions based on copper Ethernet (up to 10Gbit/s) and mmWave technologies can support the use case of dense urban society. The indoor solution can also be used for the high speed train use case. In the vRAN scenario, option 2, i.e. PDCP/RLC functional split is evaluated experimentally, showing how bandwidth and latency requirements can be relaxed down to the backhaul level and even good tolerance to packet losses.

A summary of these key achievements and results, along with their relationship with WP1’s use cases and scenarios are overviewed in Chapter 6. This chapter also shows the relationship of D2.2. with the overall project’s objectives and KPIs, highlighting the main contributions of WP2 to the overall 5G-PPP KPIs and objectives, including the CAPEX/OPEX savings and the energy efficiency introduced by technological (e.g. Silicon Photonic based ROADM) and architectural (multi-tenancy, Fronthaul/Backhaul coexistence) choices.

Finally, Chapter 7 concludes this document reporting a summary of its main contributions and the most important achievements of WP2 during the entire Project lifetime.

2 Overview of WP1 use cases and requirements

WP1 of 5G-Crosshaul project has defined two types of use cases: service-oriented use cases and functional-oriented use cases, where the former mostly focus on the service layer, whilst the latter mostly focus on the infrastructure layer, as reported in D1.1 [1]. In more details, among a total of five use-cases, three of them are service-oriented, which means that they are related to specific applications or set of applications, while other two are functional-oriented. They have been selected in order to represent transversal scenarios considering a particular use of the 5G-Crosshaul network. The five use cases are described in the following.

- Vehicle mobility

This use case is focused on both passengers' connectivity needs for mobile Internet when they are inside vehicles and setting up communications among vehicles, e.g., for traffic safety. The most challenging situations are passengers using 5G services, e.g. video in particular, on a very high speed train (up to 500 km/hour) and real time messaging among vehicles for emergency and safety.

- Dense urban society

In the "dense urban information society" use case, connectivity is required at any place and at any time by humans in dense urban environments, considering both the traffic between humans and the cloud, and direct information exchange between humans or with their environment. Furthermore, a particular aspect arising in urban environments is that users tend to gather and move in "dynamic crowds", leading to sudden high peaks of local mobile broadband demand.

- Media distribution: Content Delivery Networks (CDN) and TV broadcasting & multicasting content distribution

Video traffic is expected to be the dominant contributor to the mobile data traffic demand, being increasingly present in everyday life communications, anywhere, any time and in end-user multi-device environments. Especially relevant scenarios for content delivery are massive events such as international music festivals or big sport events in which high volumes of traffic are needed, maintaining an acceptable quality for the end users. Video consumption is then becoming the most demanding component of the traffic growth observed in current networks. This trend will even increase in the future 5G networks. Thus, providing efficient ways of delivering content to end users is a must.

- Mobile Edge Computing

Mobile-Edge Computing proposes the deployment of IT and cloud-computing capabilities within the Radio Access Network (RAN), in close proximity to mobile subscribers. Content, service and application providers can leverage on such distributed computing capabilities to serve the high-volume, latency-sensitive traffic on dense areas concentrating high number of users. Three categories of services are benefited by MEC:

- Consumer-oriented services: these are innovative services that generally benefit directly the end-user, i.e. the user using the user equipment (UE). This allows end-users to offload applications or data to the edge network nodes for battery-saving purposes or for accessing computing capacity beyond their resource-limited handset.

- Operator and third-party services: these are innovative services that take advantage of computing and storage facilities close to the edge of the operator's network.
- Network performance and QoE improvements: these services are generally aimed at improving the performance of the network, either via application-specific or generic improvements. To this purpose, in-network analytics can be an example of efficient exploitation of these capabilities from the operator's point of view, by performing the computation at the network edge and only transmitting the significant set of results to more advanced computation platforms.

Table reports the list of the relevant use cases defined for 5G Crosshaul in the framework of WP1 activity documented in D1.1 [1], where for each use cases the requirements defined in joint work with WP1 are reported the required bandwidth and latency.

Table 1: 5G-Crosshaul use cases characterization

Use case	**Bandwidth**		**Latency User**	**Latency Transport**
	User	Transport		
High-speed train	Peak rate: 110.1 Mbit/s per cell (BW=15MHz/20MHz MIMO 2*2)	CPRI option 8: 7.5 Gbit/s (3* 2.5 Gbit/s)	21 ms (minimum RTT)	100 us
Vehicle safety	< 1Mbit/s per user 150 Mbit/s per cell (for "high and full vehicle automation" 100 Mbit/s per vehicle is required)	CPRI option 8: 7.5 Gbit/s (3* 2.5 Gbit/s)	<10ms (application) <1 ms (PoA – mobile core)	100 us
Media distribution: Content Delivery Networks (CDN) and TV broadcasting & multicasting	High throughput. Peak data rate 10 Gbit/s or more Guaranteed user data rate 50 Mbit/s	Per sector about 160-200 Gbit/s CPRI option 8 [1] NR (option1-4): 3*10 Gbit/s [2]	Low latency. As low as 5 ms (end-to-end) 1 ms on the radio link	100 us (relaxed value for NR)
Dense urban society	50 Mbit/s per user 2 Gbit/s per cell	CPRI option 8: 3*25 Gbit/s NR option (1-4): 3* 2 Gbit/s	<100 ms (voice) <50 ms (PoA – mobile core)	100 us (relaxed value for NR)
Mobile edge computing	10 Gbit/s per cell	CPRI option 8: 3*5*25= 375 Gbit/s NR (option 1-4): 10 Gbit/s *3	<1ms	100 us (relaxed value for NR)

---

[1] This estimation is done considering MIMO 4*4, air BW 800 MHz (3200 MHz to manage with CPRI), proportional to LTE 20 MHz MIMO 2*2 (200 Mbit/s peak rate, about 2.5 Gbit/s CPRI[4]

[2] This estimation is done assuming that the transport BW is close to the radio peak rate. This value could increase for higher radio split options (6 and 7) [2].

Such use case requirements and transport requirements of several functional split options for the radio have been analyzed. At the moment, the definition of the radio split options is still ongoing. It is important to note that the CPRI options represent extreme cases in terms of bandwidth, often too high to fulfill transport requirements; for this reason, New Radio (NR) options have been considered as well, even if the standardization process is still ongoing. Recently[3], the CPRI consortium (Ericsson, Huawei Technologies, NEC and Nokia) has released the new evolved CPRI specification (eCPRI v1.0), whereby the interface specification allows Ethernet or Ethernet/IP transport layers for the transport of air interface data. eCPRI considers the possible splits of PHY to allow bandwidth efficient transport of the data, the achievement of multiplexing gains and an easy support especially of massive MIMO and beamforming, which is seen as one of the key technologies in 5G for its deployment in higher frequency bands (> 6GHz).

The eCPRI standard focuses on defining a flexible message framework for eCPRI services, like user data mapping and real-time-control, and makes no assumptions for control- and management-plane, synchronization-plane and other functionality, other than that standard protocols from well-known packet based protocol suites are used. eCPRI is backward compatible with conventional CPRI. A summary of eCPRI is further available as an annex in this document.

The estimation of the amount of required bandwidth is calculated considering I/Q resolutions, and sample frequency. Taking into account that, for backward compatibility with 3G, CPRI sampling frequency is multiple of 3.84 MHz. For example, the sample frequency of 15 MHz LTE signal is approximated to 19.2 MHz (5 x 3.84 MHz) and 20 MHz to 30.72 MHz. For 15 MHz (15 bits resolution) 2x2 MIMO, the net CPRI rate is 1152 Mbit/s (3.4 Gbit/s for 3 sectors), while the net CPRI is 1843 Mbit/s per sector (5.5 Gbit/s for 3 sectors) for 20 MHz.

Concerning latency, two main cases have been considered: technologies where HARQ (Hybrid Automatic Repeat reQuest) is centralized and where it is distributed. In the first case, namely CPRI, the latency is bounded at 100us, while in the second case, namely some CPRI options and New Radio the latency requirement is to be considered similar to the service tolerated latency, as described in [3].

These requirements are inherited from LTE and they represent a preliminary list of options not fully agreed in the standard discussion. Hence, on the basis of the assumptions for LTE reported in the TR, and according to 3GPP TSG RAN Meeting #75 RP-170843, three main categories have been considered:

- Split options with fully distributed functions at the Remote Radio unit (option 1-4)
- Split options with centralized HARQ [2] procedure (option 5-7)
- CPRI option, that is based on centralized HARQ as well (option 8)

According to the **latency value** reported in [3] the latency value in the case of centralized HARQ is 100 us (options 5-8). This value represents the worst-case value for assessing the several scenarios.

Evolved CPRI specification (eCPRI) v1.0 released [3] on 31 August of 2017, available at http://www.cpri.info/spec.html

Regarding the **bandwidth value,** reported in the column "bandwidth for transport", instead, the following assumptions have been considered:

Option 1-4: According to the value reported in [2] the bandwidth value is assumed similar to the cell peak.

Option 5-7: For these options the range value reported in the TR are considered, where simulation results are provided for relevant values (e.g. minimum, maximum, and average) used as references in this document.

Option 8: I/Q resolution is 15 bits, sample frequency is 19,2 MHz in case of 15MHz as bandwidth on air. For compatibility with 3G, the sample frequency is a multiple of 3.84 MHz. The net CPRI rate is 1152 Mbit/s (3.4 Gbit/s for 3 sectors). In case of MIMO 4*4, with bandwidth on air of 800 MHz, the bandwidth to manage with CPRI is 3200 MHz that is proportional to LTE 20 MHz MIMO 2*2 (150 Mbit/s peak rate, about 2,5 Gbit/s CPRI).

3 Analysis of transport technologies and physical media for 5G-Crosshaul

The technology map defined in 5G-Crosshaul D2.1 document [5] presents various transport technologies, which are suitable to exploitation from a data-plane perspective in 5G-Crosshaul networks. In this section, we will focus on wireless, fixed access, and optical alternatives. Among these technologies, wireless solutions are identified as a suitable technology to cover the scenarios where wireline technologies cannot be deployed or are too costly to deploy. As the requirements for 5G emerge, the wireless backhaul and fronthaul technologies face new challenges for provisioning the huge increase (1000x) of access capacity, which implies a high level of network densification, or to achieve a significant drop in latency, among others.

Re-use of existing fixed access infrastructure and systems will be important in 5G deployments. 5G-Crosshaul access network segment may in turn provide an efficient use of available infrastructure for backhaul/fronthaul integration purposes. Whereas residential mass-market can benefit from shared copper and fibre infrastructure thanks to Digital Subscriber Line (xDSL) and Passive Optical Network (PON) technologies, mobile backhaul networks mostly rely on dedicated infrastructure, each base station being backhauled by several fibres or by copper technologies. Using dedicated copper cables or fibres to backhaul each base station is currently not an issue because the number of base station sites remains moderate. However, with the deployment of small cells and heterogeneous networks, RANs will become denser and denser. The integration of backhaul/fronthaul networks with fixed broadband access networks will then be required to limit the deployment of new copper and fibre infrastructure and streamline the use of existing copper and fibre infrastructure in the perspective of 5G-Crosshaul.

The analysis of different technologies carried out in [5] concluded that optical technologies have an important gap in terms of carried bandwidth in comparison with wireless ones. Coarse Wavelength Division Multiplexing (CWDM) was identified as the most cost and energy efficient technology, especially suitable for outdoor installations when moderately high capacities are needed. The Dense Wavelength Division Multiplexing (DWDM) merits were recognized instead in both capacity and link budget, compatibility with any kind of topology (bus, tree, ring, mesh), supported operation administration and maintenance (OAM) features, and possibility to adapt the optical channels allocation in the transport network to the RAN traffic distribution, using reconfigurable add drop multiplexers (ROADMs).

3.1 Technologies for 5G-Crosshaul wireless networks

3.1.1 Introduction

In wireless communications, traditional frequencies below 50 GHz are already very crowded and fragmented, hence the trend in the industry today and the main efforts of 5G-Crosshaul project is to focus on higher frequency bands, such as millimetre wave (mmWave), both in E-Band (71-76 GHz, 81-86 GHz) or V-Band (57 to 64 GHz). Here, the interest of mmWave technology mainly resides in mesh deployments formed by small cells to increase network capillarity and help addressing the high capacity challenge previously mentioned. Furthermore, mmWave is considered also in pure fronthaul scenarios, where the high capacity links will enable the C-RAN concept to support the upcoming capacity needs. Nevertheless, it is worth highlighting that wireless solutions in the µWave band are still in development and used by mobile operators. Another wireless alternative is optical wireless communications (OWC), whose interest resides in the completely license-free spectrum of light and its immunity to electromagnetic interference.

The following sections present experimentation work performed by 5G-Crosshaul partners towards the link characterization of the different wireless approaches under investigation and development in 5G-Crosshaul project [5].

3.1.2 Wireless technologies transmission on currently used (uWave) and new (mmWave) spectrum

An increasing capacity demand and a faster request of coverage in mobile communications are the main drivers for the current deep transformation/development of the usage of wireless solutions in the microwave (µWave) band. This technology seems to satisfy the high volume of mobile connections and the spectrum efficiency, yet keeping limited power consumption. Furthermore, µWave systems have a reduced environmental impact making investment on this technology very profitable.

Thus, within 5G-Crosshaul, some work has been devoted on testing different solutions available on the market for a complete analysis of this technology from operator point of view as an enabler to the transition between current network deployments and future 5G-Crosshaul networks. Figure 1 depicts one of the several tested µWave deployments, where one device of radio link is placed on a TIMLab tower in Italy and the second one is on the roof of the building that is designated at the right distance for the trial.

Figure 1: Example trial scenario

The measurements on both fronthaul and backhaul links are highlighted and summarized in Table 1. This table also includes a performance comparison with a tested mmWave deployment, showing the relevance of this technology for future 5G network deployments.

Table 1: Characteristics of main parameters for backhaul and fronthaul links

	Fronthaul	**Backhaul**
Capacity	7.5 Gbit/s with carrier @5.8GHz and channel width of 70MHz 10 Gbit/s adopting carrier @80GHz with channel width 500MHz and 256 QAM modulation format	Different solution available from carrier @5.8 GHz to @80 GHz. Typical values are ≥ 1Gbit/s for carrier @60 GHz or 80GHz with channel width 50MHz and 4096 QAM modulation format
Link distance	100 m @5.8 GHz with flat antennas 2 km @ 80 GHz with antennas diameter < 1 m	-- 2 km @5.8 GHz with flat antennas -- 5 km for 6 GHz ≤ carrier ≤ 42 GHz with 2.4 m ≤antennas diameter ≤ 0.3 m -- up to 0.7 km @60 GHz (O_2 absorption peak) with antennas diameter < 0.2 m -- up to 3 km @80 GHz (with bit rate 3Gbit/s) with antennas diameter ≤ 0.6 m
Energy efficiency	Up to 35W per edge site	Up to 50W per edge site
Latency	<200 us (for FDD based systems)	From hundreds of microseconds to tens of milliseconds It depends on the electronic L2 elaboration (latency may be higher for TDD based systems)
Synchronization	Compatible with both synch Eth. and 1588 Transport Clock	Compatible with both synch Eth. and 1588 Transport Clock

3.1.3 Packetized fronthaul and backhaul mmWave mesh wireless solutions for small cells

As stated at the beginning of this section and as it will be further developed in next sections, the interest of 5G-Crosshaul in wireless technologies resides in the mmWave technology. In particular, it is of relevant interest mmWave mesh deployments formed by small cells to increase network capillarity and help addressing the high capacity challenge previously mentioned. Furthermore, mmWave is also considered in pure fronthaul scenarios, where the high capacity links will enable the C-RAN concept to support the upcoming capacity needs.

Next paragraphs show the performance characterization of different mmWave links used within the 5G-Crosshaul project to study the use of this technology in packetized mesh deployments of small cells. These mmWave links are based on the IEEE 802.11ad [35] (with standardized data rates up to 6.7 Gbit/s), which can, in principle, reduce costs in front of fibre and traditional microwave solutions, where the lower cost can be achieved by leveraging high-volume production chipsets and the use of free spectrum (as in the case of V-Band). However, IEEE 802.11ad devices are still under development and there are few of them commercially available.

The first device under characterization is the Tensorcom TC60G-USB3.0 mmWave card depicted in Figure 2. The link characterization has been done taken into account the technology parameters defined in [1] with the setup represented in Figure 3. In this setup, two mmWave transport nodes, each one mounting a Tensorcom TC60G-USB3.0 device, are placed over movable tables to perform measurements of parameters when distance and alignment between communication end points are varied.

Figure 2: Detail of Tensorcom TC60G-USB3.0 mmWave link. The right part shows the GUI measurement tool provided by the vendor

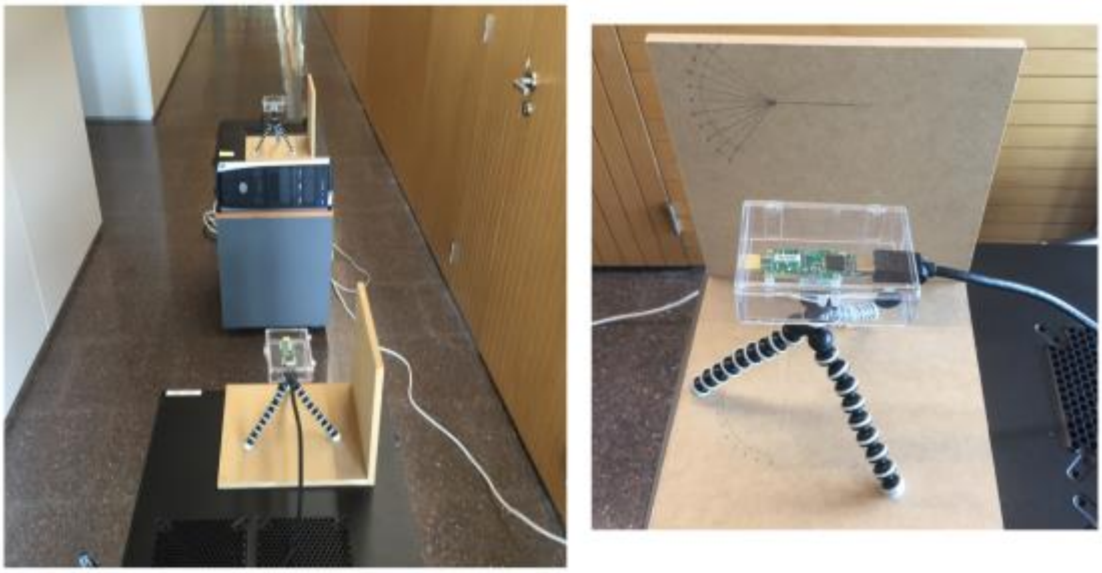

Figure 3: Setup detail to perform throughput vs. distance/misalignment measurement of Tensorcom TC60G-USB3.0 mmWave link

Table 2 presents throughput versus distance performance of this mmWave link of the seven available modulation and coding schemes (MCS). The maximum achievable data rate is of about 1Gbit/s, when using the maximum available modulation and coding scheme (MCS7). The maximum link range has been obtained when both the transmitter and the receiver are totally aligned and the link starts experiencing degradation (reported by the MAC counters of the GUI measurement tool provided by the vendor shown in Figure 2). The maximum reported data rate is in line with the values reported for mmWave devices in [5]. However, the Tensorcom device is still under development and these measurements will have to be revisited in the future when the vendor releases new firmware and device drivers.

Table 2: Throughput vs distance performance of Tensorcom TC60G-USB3.0 device

Modulation and Coding Scheme	PHY Rate (Mbps)	Effective Throughput Rate (Mbps)[4]	Receiver sensitivity (dBm)[5]	Range (meters)
MCS_1	385.00	325	-74	16,9
MCS_2	770.00	565	-70	15,7
MCS_3	962.50	665	-67	10,3
MCS_4	1 155.00	760	-67	8,2
MCS_5	1 251.25	790	-67	4,8
MCS_6	1 540.00	900	-65	3,6
MCS_7	1 925.00	1 020	-62	2,6

The achieved distance reported in Table 2 is not in line with the values reported in [5]. The fact that the device is connected to a USB port, limits the amount of power and the kind of antennas this device can receive/mount. In particular, current antennas present 10 dBi of gain and a transmitted equivalent isotropic radiated power (EIRP) of 14 dBm. However, these distances are suitable to perform the required networking experimentation from a control plane perspective, while validating the mmWave physical technology.

Figure 4 presents the achieved effective data rate when the alignment between transmitter and receiver varies at a distance of 1.2 meters and using MCS_7, the maximum available modulation and coding scheme, hence, the most sensitive to misalignment effects.

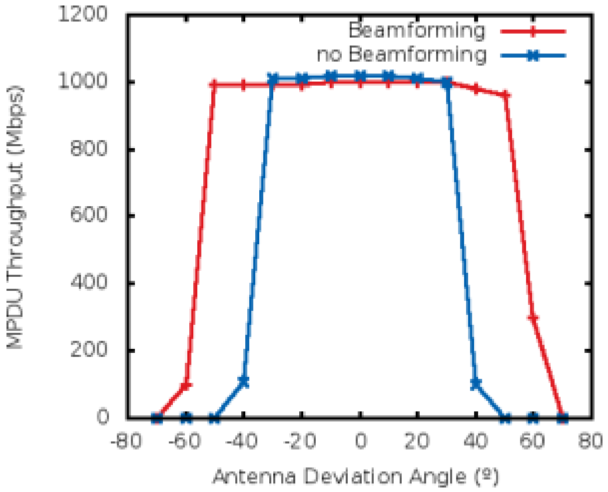

Figure 4: Throughput vs misalignment performance

When no beamforming mode is used, TC60G-USB3.0 device achieves higher peak transmission rates with respect to the beamforming node due to the lack of beamforming training procedures. However, with a fixed configured antenna sector, the device throughput performance is more sensitive to misalignments between transmitter and receiver. On the other hand, when the

---

[4] This is the effective measured data rate reported by the measurement tool providing MPDU values.
[5] This is the effective measured RSSI reported by the measurement tool.

beamforming mode is configured, the antenna array at the receiver (acting as station) is able to follow the movement of the transmitter so the throughput performance is kept under a wider misalignment, in comparison to the previous case.

Link latency measurements reveal a round trip time (RTT) value (min/avg/max) of 1.0/3.3/5.6 ms. This value has been obtained using transmission control protocol (TCP) data packets of 4000 bytes, transmitted using MCS_4 at a distance of 1.2 meters. From this result, it can be inferred that the latency component due to propagation and transmission is not as relevant as the one due to chip processing. With respect to energy considerations, the transmitted power consumption is lower than 270 mW and the received power consumption during receive packet decoding is lower than 520 mW according to the provided datasheet. These values are rather reduced in comparison with those reported in [3] but are in line with the kind of device under test.

The second device under characterization is the EdgeLink node, which is being evolved within the context of 5G-Crosshaul project. EdgeLink node is based on Freescale 1043A boards that host a 64-bit ARM-based quad-core processor for embedded networking with a fanless design. Such boards provide two 10 Gbit/s Ethernet ports supporting PoE (Power-over-Ethernet) and three USB3.0 ports used to connect the mmWave IEEE 802.11ad wireless card and antennas.

EdgeLink node adopted the Peraso W110 chipset, which employs the PRS1125 and PRS4001 integrated circuits to implement the necessary IEEE 802.11ad functionality. The W110 chipset a USB3.0 interface used to interconnect the wireless card to the motherboard. The PRS4001 incorporates the Analog Front End, BB PHY/MAC, and two RISC CPU cores supporting supports the IEEE 802.11ad single carrier modulations MCS0 to MCS12 (16-QAM), variable rate low-density parity-check (LDPC) forward error correction (FEC), beamforming, and 128-bit AES security (GCMP). The PRS1125 is a single chip direct conversion RF transceiver providing 60 GHz single-ended IEEE 802.11ad standard compliant receiver and transmitter antenna interfaces. Such component provide phase noise and linearity characteristics aimed at maximising the robustness of point-to-point wireless links at up to 64-QAM modulation, and facilitating energy efficiency better than 300pJ/bit. The PRS1125 is a 0.6mm thick, 6mm x 6mm Ball Grid Array (BGA) package with accessible 50 Ω single-ended RF signal ports to interface with external Tx and Rx antennas, providing a transmit ouput power of up to +14dBm, a receiver noise figure of 5 dB, and a phase-locked loop (PLL) control system for all IEEE 802.11ad channels. Figure 5 shows the internal architecture of Peraso chipset.

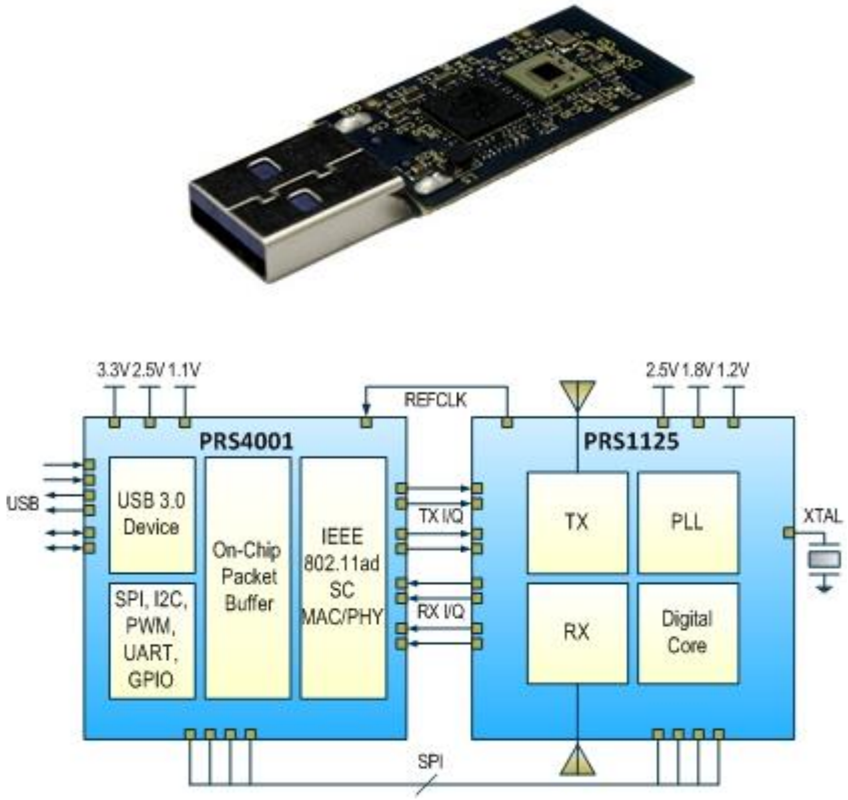

Figure 5: Peraso W110 IEEE 280.11ad wireless chipset

The SencityMatrix V-band antenna *1360.99.0003* from HUBER+SUHNER (as shown in Figure 6) is equipped in the EdgeLink nodes to emit radio signals at 60GHz. This adopted antenna has almost identical electrical characteristics when operating in three prominent 60GHz bands namely 57000 – 60800MHz (band 1), 60800 – 62500MHz (band 2), and 62500 – 66000MHz (band 3). The antenna features a high gain of 38dBi and a narrow 3dB beamwidth[6] of 1.8 degree, with side lobe suppression that meet the requirements of Class 2 antenna specifications in ETSI EN 302 217-4-2 V1.5.1. Such characteristics allow signals to be radiated with very high directivity and a good transmission range up to 500m, under favourable propagation environments with line-of-sight (LoS) path that is presumed in each hop of an mmWave mesh networks. In addition, signals between different polarisations are well isolated due to a high cross-polar ratio (21dB), and this leads to a small form factor (135 × 130 mm^2) that can be easily mounted on EdgeLink nodes.

---

[6] The beamwidth indicates the angle between the point with peak-radiated power of the main lobe and the point where the power drops below half of the peak.

Figure 6: HUBER+SUHNER's SencityMatrix V-band antenna 1360.99.0003

Measurements of EdgeLink nodes were conducted in an outdoor environment in Berlin over a 185 meters link between two buildings of HHI premises. The average measured latency of the link is 700µs. Measurements take into account the packet loss rate for both DL/UL user datagram protocol (UDP) and TCP traffic, under different MCS specified in IEEE 802.11ad, as covered in Table 3.

Table 3: EdgeLink node link performance

MCS	DL UDP/TCP Mbps (pkt loss %)	UL UDP/TCP Mbps (pkt loss %)	Jitter DL/UL (µs)
9	1700/910 (0.87/0)	1340, 1100 (1.1/0)	24/11
8	1220/972 (0.23/0)	1300, 1070 (0.69/0)	20/12
7	1080/894 (0.76/0)	1160, 966 (1.1/0)	29/7
6	910/781 (1.1/0)	986, 856 (0.65/0)	25/11
5	866/760 (0.28/0)	869, 760 (1.1/0)	29/14
4	814/719 (0.34/0)	812, 718 (0.96/0)	13/29
3	705/633 (0.26/0)	709, 633 (0.39/0)	20/20

In general, TCP traffic exhibits better reliability (in terms of packet loss rate) than UDP at the expense of a lower data rate. This is due to the retransmission and congestion avoidance mechanisms of TCP. Jitter is generally low (around 10µs to 30µs) in all cases. EdgeLink node results show that mmWave links are able to support Gigabit per second transmissions over hundreds of meters. The narrow beam of the transmission (1.8º) enables the effective spatial reuse of unlicensed bands thanks to the high directionality of the transmission. This is a critical aspect in the dense urban reference scenario where multiple links (sectors) and many Gbps links need to be provisioned in the same area to cope with the ever-increasing traffic demands.

3.1.4 Optical wireless technologies

Finally, optical wireless communication (OWC) has recently attracted high interest due the completely license-free spectrum of light and its immunity to electromagnetic interference. Since the distances to small cells are shorter than those to macro cells, the probability of LoS increases, OWC links (based on free space optics (FSO) links with light emitting diodes (LED) instead of laser diodes) are capable to operate at those distances and could represent a backhaul/fronthaul wireless infrastructure today. An example of such a deployment is depicted in Figure 7, where an LED-Based optical Backhaul link between HHI premises and Technical

University of Berlin has been installed, with a distance of 100 m, which could be a typical macro- to small cell or inter-small cell distance for backhauling. In parallel, an FSO link was operated in order to have a comparison between OW links with different beam characteristics under the same weather conditions. The visibility was measured with the Vaisala PWD12 weather station. The resulting availability graph in Figure 8 (top) demonstrates that when the visibility decreases, e.g. due to fog, the data rate of the LED-link decreases as well. Nevertheless, the connection still remains active because of the rate adaptive function of the OWC chipset. In the same time window measured data of the FSO-System (see Figure 8(bottom)) show that under the low visibility conditions a link outage occurred, as the received optical power was too low. This demonstrated the advantage of a rate adaption scheme.

Figure 7: Measurement site between HHI and TUB building with a transmission distance of 100 m and a height difference of 25 m for the OW experiments

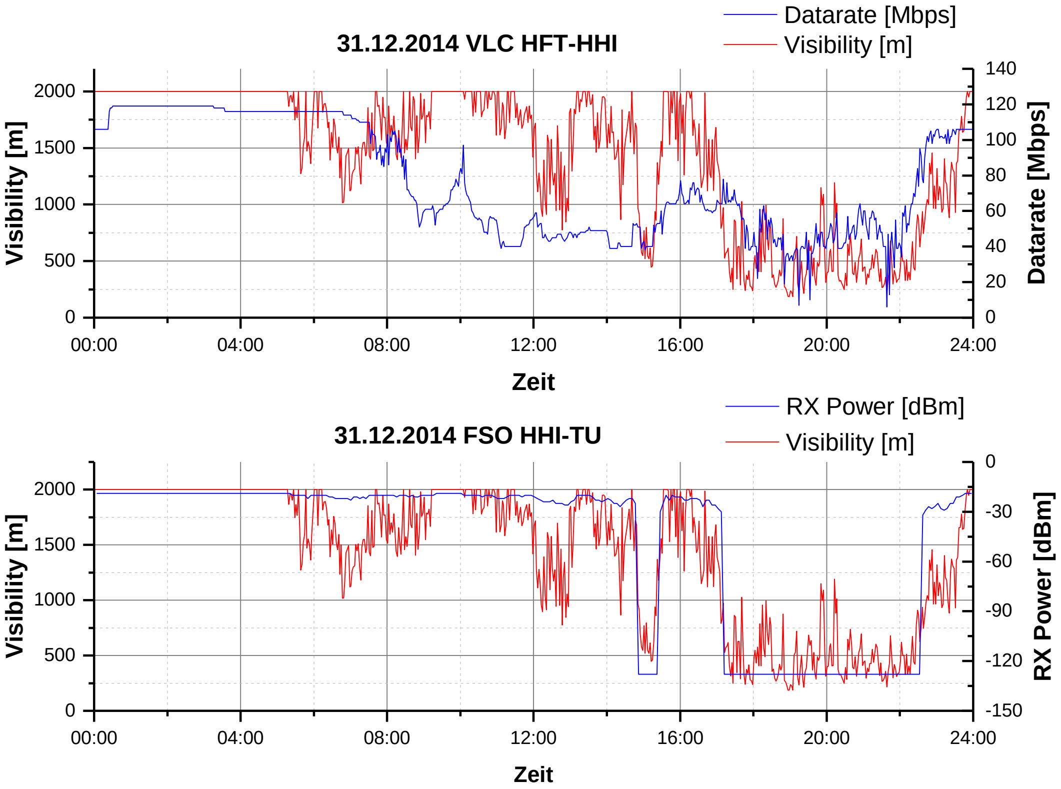

Figure 8: Comparison of visibility and OWC data rate (top), as well as visibility and received signal power of an FSO (laser) link (bottom) for the same time period. While the FSO link is down in the case of low visibility, the OWC link remains active due to the data rate adaptation

3.2 Technologies to enable 5G-Crosshaul on fixed access networks

3.2.1 Introduction

Technologies to enable 5G-Crosshaul on fixed access networks may so allow for sharing the existing fixed access infrastructure with mobile base station backhauling and fronthauling, e.g., the copper and/or fibre access infrastructure that already exists in many residential and/or commercial buildings, fixed distribution nodes, macro and small cell sites with their backhaul links. This sharing or convergence of legacy infrastructure will allow reducing costs and time for cost sensitive deployments of small cells in 5G. In this light, 5G-Crosshaul access network segment will be a mix of legacy copper and fibre access networks. A thorough analysis of optical and copper access networks to enable 5G-Crosshaul has already been carried out in [5].

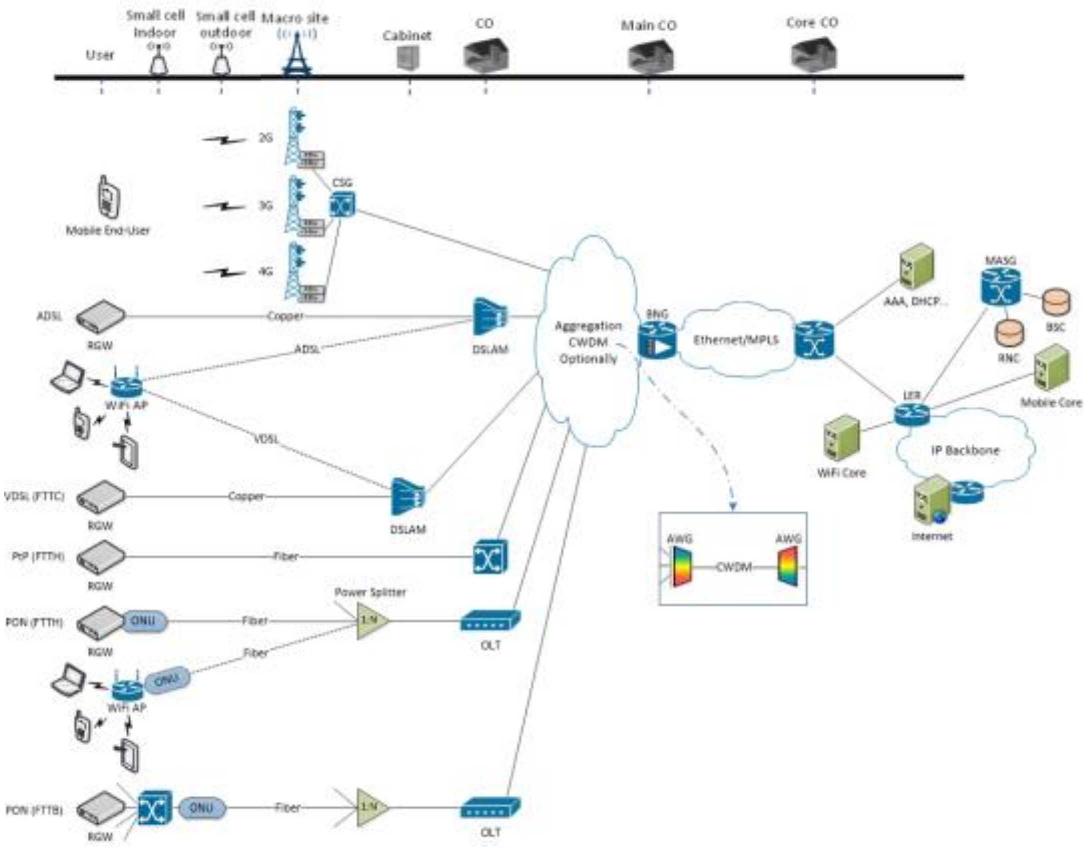

Figure 9: Current whole network scheme

Concerning copper access technologies, the main conclusion is to focus on using Ethernet xBASE-T technologies for the combination of fronthaul and backhaul in 5G-Crosshaul due to its wide use in enterprises, homes and even in data centers, dominating by far among the copper infrastructures and technologies. Other copper technologies like DOCSIS3.1, DSL, G.fast and G.hn were also analysed in [5]. However, latency in copper technologies can be a big issue to fulfil the strict latency requirements of fronthaul traffic.

As far as optical access technologies is concerned, current PON standards were analysed in [5]. The conclusion is that XGS-PON and NG-PON2 are the most suited current PON technologies to fulfil the bit-rates capacity requirements of the 5G-Crosshaul with similar maximum traffic capabilities per single optical link or wavelength (up to 10 Gb/s per optical channel). However, as they respectively use TDM and TWDM access to a shared media, novel emerging PON technologies like tunable WDM-PON would be the best choice in terms of delay and jitter compared to TDM- and TWDM-based PON technologies, since individual optical network units (ONUs) do not have to compete for channel access. Moreover, longer-term disruptive technologies like OFDM Flex-PONs have also be identified in [5], as a future candidate technology for 5G-Crosshaul in the longer term evolution of optical access networks.

Using new tech enablers such as PtP WDM-PON and TWDM-PON (NG-PON2) telecom operators can allocate head-end equipment as optical line terminals (OLTs) at Main COs instead of at COs, in this way, access network extends its reach, the level of sharing resources between the different services increases and the centralization approach for coordinating radio access networks is achieved placing the Radio Controller (RCC) at Main CO with NG-PON2 OLTs. In addition, these novel optical technologies allow operators to improve the capacity of their current legacy PONs, i.e., both XGS-PON and TWDM-PON consider 10 Gbit/s per network deployment, whilst PtP-WDM solutions introduce 10 Gbit/s per fiber connection, then, accumulating N OLTs at the Central Node is possible to guarantee service to multitude of fixed and mobile subscribers per CO coverage area with many less PONs than before.

Note that TWDM-PON gives services to fiber subscribers replacing GPON as the chosen access, whilst PtP WDM alternatives (WS-WDM-PON or WR-WDM-PON) are used to supply final applications with high network requirements (4G Small-Cells, mobile cell sites etc.), i.e., fronthaul mobile communications. Finally, if we introduce the 5G-Crosshaul design for the network topology, the access segment would result as similar as the scheme of Figure 10.

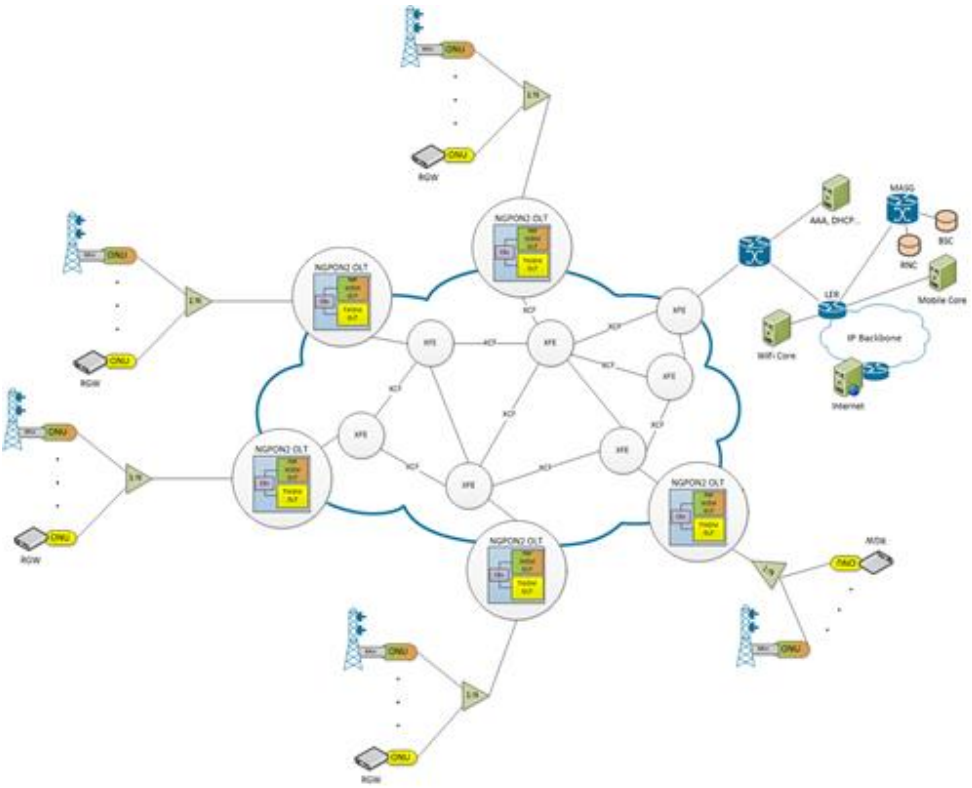

Figure 10: 5G-Crosshaul services support over new PON schemes

3.2.2 NG-PON2 and its coexistence with legacy PON technologies

NG-PON2 is the new standard approved by the ITU which has been defined as ITU-T G.989 with the objective to upgrade the current FTTH networks up to high-capacity systems for facing the growing demand of bandwidth capacity in our society. Recommendation ITU-T G.989 series describes 40-Gigabit-capable passive optical network (NG-PON2) systems in an optical access network for residential, business, mobile backhaul and other applications. This Recommendation includes principal deployment configurations, migration scenarios from legacy PON systems, and system, service and operational requirements. The physical layer specifications for the NG-PON2 physical media dependent (PMD) layer are described in Recommendation ITU-T G.989.2. Table 4 presents the wavelength plans covered in the ITU-T G.989.2 standard. The transmission convergence (TC) layer is described in Recommendation ITU-T G.987.3, with unique modifications for NG-PON2 systems captured in Recommendation

ITU-T G.989.3. The ONU management and control interface (OMCI) specifications are described in Recommendation ITU-T G.988 for NG-PON2 extensions.

In the case of NG-PON2 evolution for brownfield scenarios, a smooth PON migration is preferable to avoid possible problems related to client connections and to assure the corresponding quality of service, to achieve it a coexistence approach is a good choice allowing a gradual increase of the total capacity of the whole access PON. In fact, to promote backward compatibility with existing optical distribution networks (ODNs), this standard maintains characteristics from legacy PON systems: ITU-T G.982, ITU-T G.983, ITU-T G.984, and ITU-T G.987 series of Recommendations.

Table 4: NG-PON2 compatible systems and options (ITU-T G989.2)

NG-PON2			
Wavelength compatible systems	TWDM		PtP WDM
	DS	US	US/DS
GPON, RF video overlay, XG-PON, XGS-PON	1596-1603 nm	Wideband option 1524-1540 nm Reduced band option 1528-1540 nm Narrow band option 1532-1540 nm	Expanded spectrum 1524-1625 nm (PtP WDM PON) Shared Spectrum 1603-1625 nm (PtP WDM Overlay)

Assuming current fiber access infrastructures, to carry out the migration from legacy GPON deployments towards future NG-PON2 networks is necessary to plan in detail some constraints. Firstly, current GPON subscribers must not be affected by the new tech implementation where in principle, the current optical power budget will remain intact (non-desired changes in passive network elements as power splitters). Normally, fiber operators design access PONs stablishing power margins between 3-8 dB what requires the usage of coexistence filters with very low insertion losses as a starting point for PON migration purposes. Second, new PON technologies are not added to the current access infrastructure at the same time, they should be deployed step-by-step according to the state-of-the-art (mainly CAPEX) and the bandwidth demand in each area. Currently, main GPON operators are considering XGS-PON as first upgrade for fixed subscribers and PtP WDM overlay to satisfy new mobile requirements. Finally, to achieve a PON coexistence scenario, a correct wavelength plan needs to be defined for allocating the different legacy and novel PON technologies, see Figure 11.

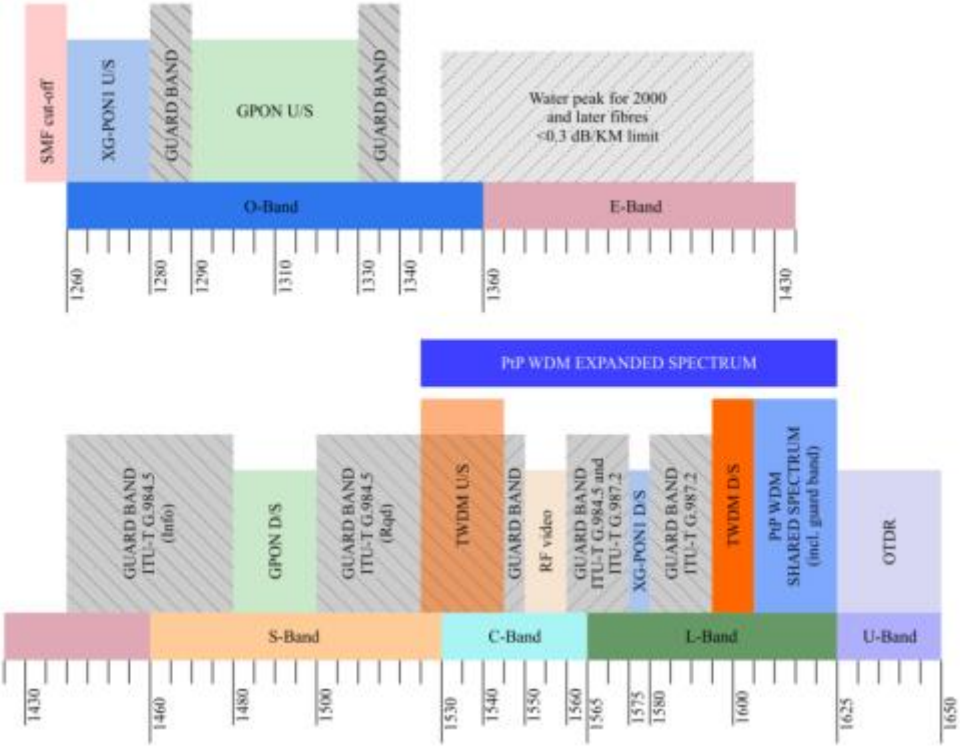

Figure 11: Wavelength plan approved by ITU-T

Hence, the NG-PON2 logical architecture can be extended to the PON coexistence scenario of Figure 12.

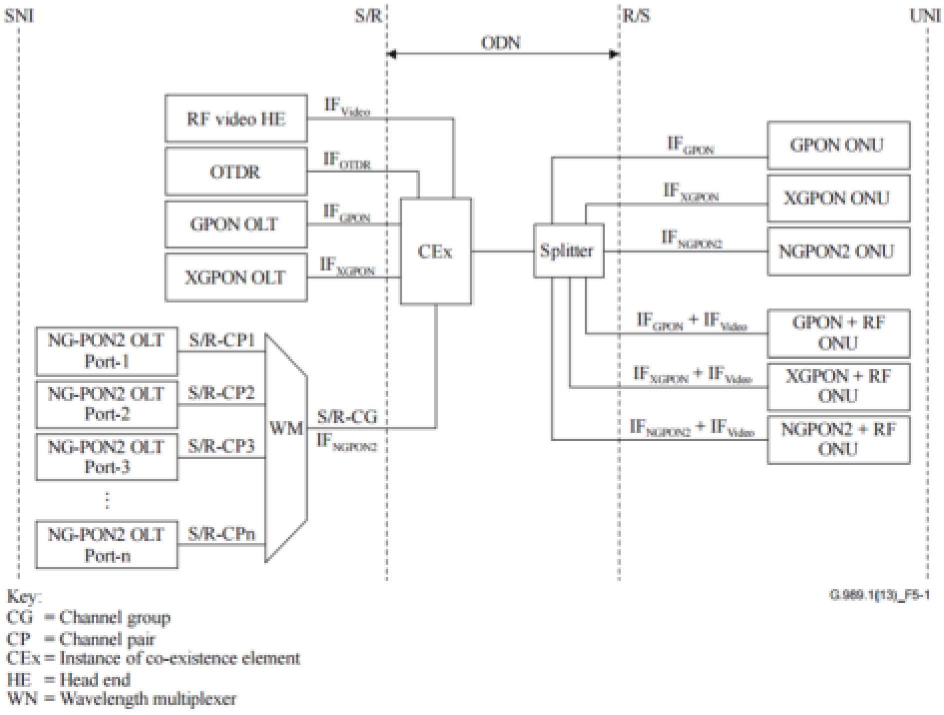

Figure 12: NG-PON2 coexistence logical architecture

Concerning technical details, NG-PON2 offers 4-8 channel pairs (with each channel pair comprising one DS and one US wavelength channel) which make use of combined Time and Wavelength Division Multiplexing (TWDM). Per-channel-pair TWDM bit rates are 10 Gbit/s DS and 10 Gbit/s US, 10 Gbit/s DS and 2.5 Gbit/s US, or 2.5 Gbit/s DS and 2.5 Gbit/s US, respectively. In addition to the 4-8 TWDM channel pairs, so-called point-to-point (PtP) WDM channel pairs are required as an option (1G, 2.5G and 10G classes). These PtP WDM channels must be based on tunable lasers. Each NG-PON2 OLT channel termination refers to a TWDM or PtP WDM channel pair (DS/US) combined via optical multiplexing.

Following the G.989 recommendations, TWDM-PON can be defined as a multiple wavelength PON solution in which each wavelength is shared between multiple optical network units (ONUs) by employing time division multiplexing and multiple access mechanisms. In a TWDM-PON system, each TWDM available channel is associated to XGEM frames multiplexing that belong to different downstream logical connections, each of the ONUs filters and processes its corresponding XGEM Port-IDs. The ONU's traffic entities that are recipients of the upstream bandwidth allocations are identified by their allocation IDs (Alloc-IDs). Within each bandwidth allocation, the ONU uses the XGEM Port-ID as a multiplexing key to identify the XGEM frames that belong to different upstream logical connections (see Figure 13).

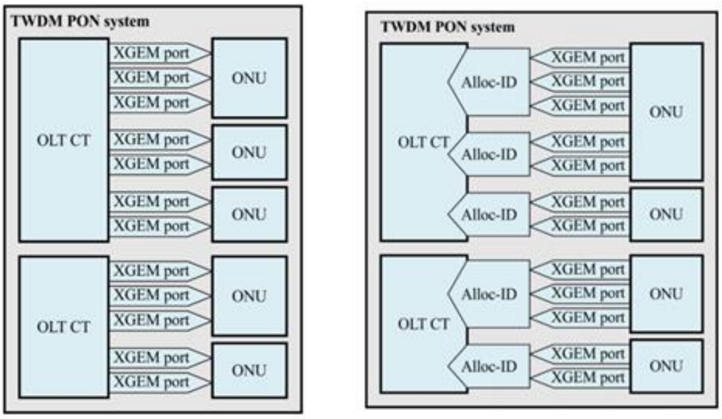

Figure 13: Downstream and upstream multiplexing in TWDM-PON

Table 5 shows the possible data rate interfaces that are supported by TWDM-PON optical transceivers (channel termination).

Table 5: TWDM-PON data rate interfaces

OLT channel line data rates		**ONU line data rates**	
DS line rate (Gbps)	US line rates (Gbps)	DS line rate (Gbps)	US line rate (Gbps)
2.48832	2.48832	2.48832	2.48832
9.95328	2.48832	9.95328	2.48832
9.95328	9.95328	9.95328	9.95328

Regarding network topologies, there are mainly two different alternatives for access WDM deployments: Wavelength Routed-WDM-PON (WR-WDM-PON) and Wavelength Selected-WDM-PON (WS-WDM-PON). Basically, the corresponding ODN differs in the usage of AWGs (WDM filters) for WR-WDMPON architecture or power splitters as a broadcast system in case of WS-WDM-PON. The DWDM OLTs include L2 switches for metro-access traffic coordination in addition to the optical components (both passive and active), as depicted Figure 14.

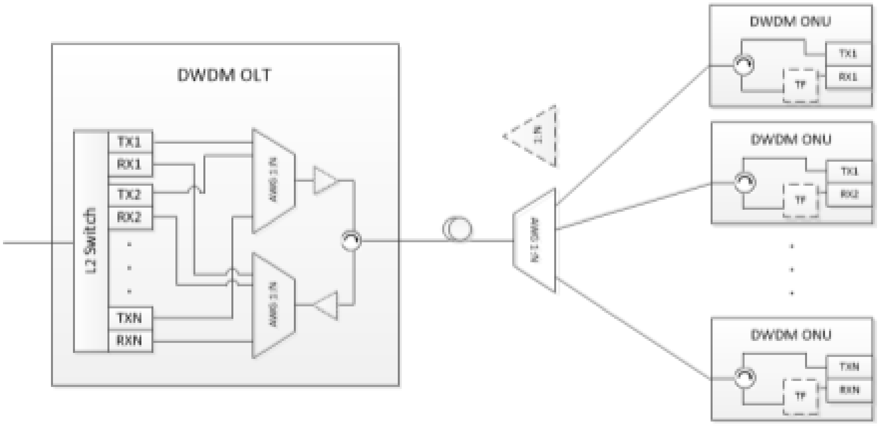

Figure 14: Access DWDM-PON schemes

The choice of a certain solution implies several physical consequences: Power splitters present high attenuation levels, equals to LOG$_2$N [dB], whilst AWGs show attenuation values close to 5 dB (for a typical DWDM MUX 1:40). This mean that WS-WDM alternative present greater path losses than WR-WDM for splitting ratios from 1:4. Note that the attenuation for an AWG of 80 DWDM channels (twice the aggregated capacity) increases about 2 dB, whilst a splitting ratio between 1:64 – 1:128 (18-21 dB) would be required to achieve a similar aggregated capacity in case of WS-WDM-PON, in other words, a difference of about 12 dB between both WDM-PON alternatives. Then, optical amplification in both stream directions will be needed to assure the optical power budget for high splitting ratios, which increases CAPEX considerably. WS-WDM-PON is a broadcast system, i.e. all optical signals arrive to each optical termination (ONUs), hence, additional filtering is required in DS RX for removing unwanted optical signals. In fact, to achieve colorless ONUs, tunable filters must be considered, whose prices are high, anyway, additional tunable filters are also required in WR-WDM ONUs to achieve a colorless solution. Most of legacy and novel PON technologies are power-splitter based networks, in this way; WS-WDM alternative allows operators greater levels of flexibility and coexistence between PON technologies.

3.2.3 Physical layer analysis and results of WS WDM-PON systems

The following Figure 15 depicts the data plane architecture of the WS WDM-PON system. The OLT is based on DWDM SFP/SFP+ C-band transceivers supporting bit rates of up to 10 Gb/s, which are plugged into the OLT SDN switch based on the LS2085A platform from NXP manufacturer. At the ONU side, tunable SFP+ (T-SFP+) components are used which are also capable for bit rates of up to 10 Gb/s.

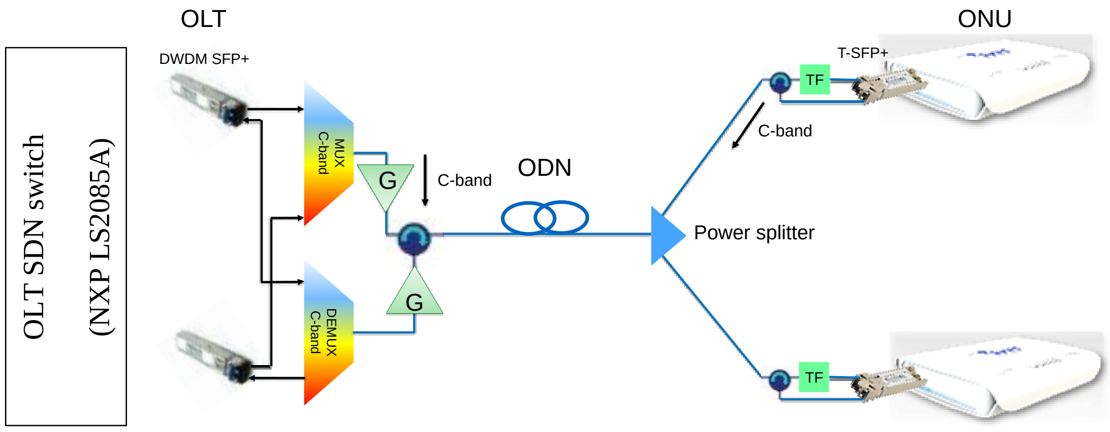

Figure 15: WS-WDM-PON system with SDN capabilities

The tunability in the downstream on each ONU is achieved by the use of a low cost tunable filter (TF). The tunability of both laser and tunable filter ONU is managed and controlled from the ONU. Target fibre reach of the solution is that of the typical reach of GPON systems, i.e. 20 km. In order to achieve that reach with relatively good power budget and splitting ratios of at least 1:32, variable optical amplifiers of gain G=15-20 dB are used at the OLT side.

Physical and link layers of the system have already been analyzed. OLT and ONU min Tx power and sensitivity are shown in Table 6 to estimate the power budget required:

Table 6: WS-WDM-PON OLT and ONU modules specifications

OLT	Optical module sensitivity (dBm)

10G SFP+ module Tx power (min)	0 dBm
10G SFP+ module sensitivity	-24
ONU	
10G SFP+ module Tx power (min)	0 dBm
10G SFP+ module sensitivity	-24

According to the above measurement, both the downstream and upstream optical budgets were about 24 dB. Measured insertion loss for the optical components in the system are:

1. WS-WDM--PON OLT: 5.5 dB
2. CEx filter: 0.5 dB
3. Splitter 1:32: 16 dB
4. 20 km fibre: 10 dB
5. WS-WDM-PON ONU: 3 dB
6. TOTAL: 35 dB

This way, the system requires minimum G = 11 dB gain amplification at the OLT side in both cases. Figure 16 represents the upstream and downstream performance of the system as a function of the OLT amplification (G).

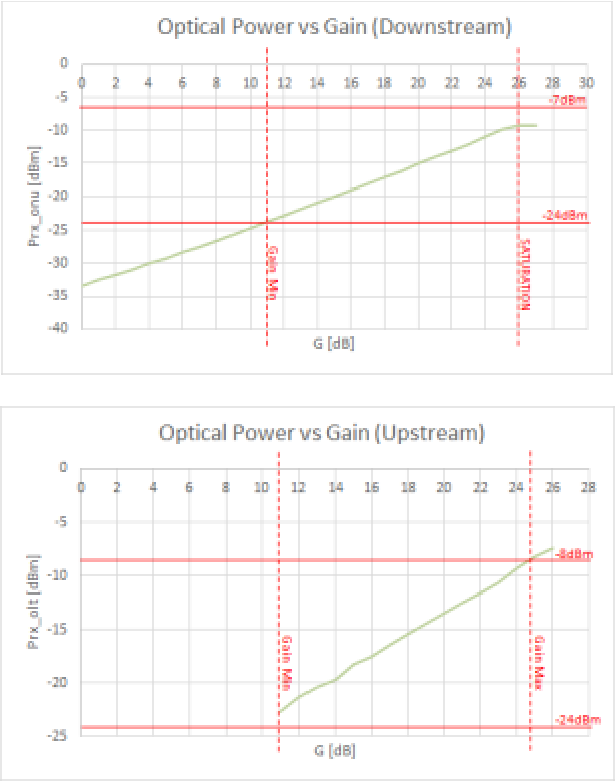

Figure 16: Optical Power vs Gain for upstream and downstream of the WS-WDM-PON system

For the downstream, a booster amplifier with maximum gain of 26 dB is employed, whilst for the upstream, a pre-amplifier mode amplifier is used with a maximum gain of 25 dB. In both cases, the minimum gain is set to 11 dB, which is needed to meet the power budget requirements in both cases. In the figures, the ONU SFP+ (downstream) overload input optical power is shown (-7 dBm), as well as OLT SFP+ (upstream) overload input optical power (-8 dBm), values that delimitate the horizontal boundaries of the above graphs. It can be seen, that in both cases the system can accommodate an amplification range between 11-25 dB. Larger splitting ratios, e.g. 1:64, could be then supported by the system, as it will just imply 3 dB extra loss.

Figure 17 shows the SNR of the system as a function of G, and Figure 18 shows the SNR for G = 18 dB in one of the ONUs, which is about 23 dB:

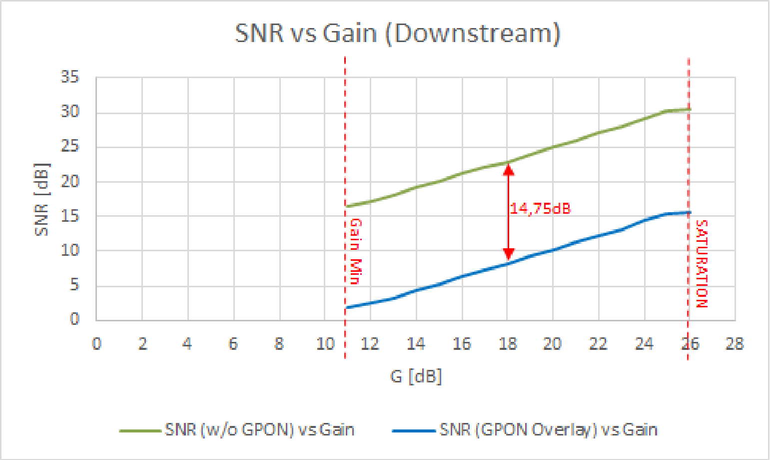

Figure 17: SNR vs Gain of the WS-WDM-PON system.

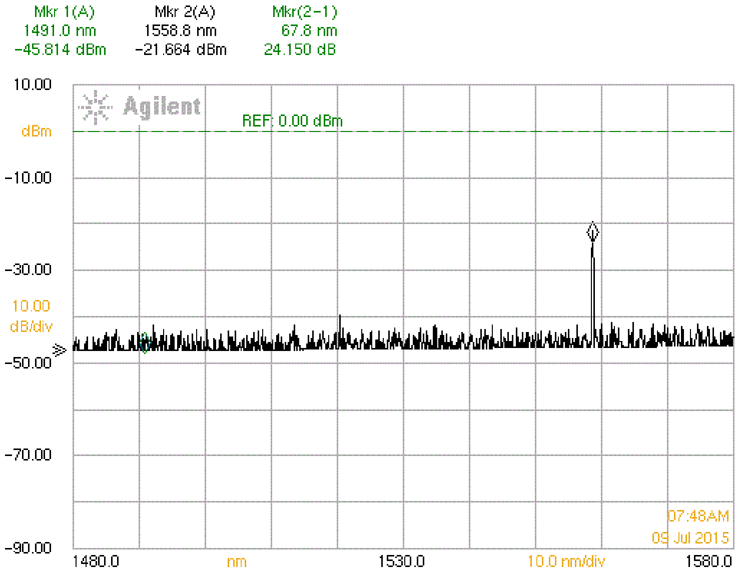

Figure 18: SNR for G=18dB of the WS-WDM-PON system

The next figure illustrates the four optical channels in the downstream before and after G = 18 dB amplification respectively at OLT and ONU sides:

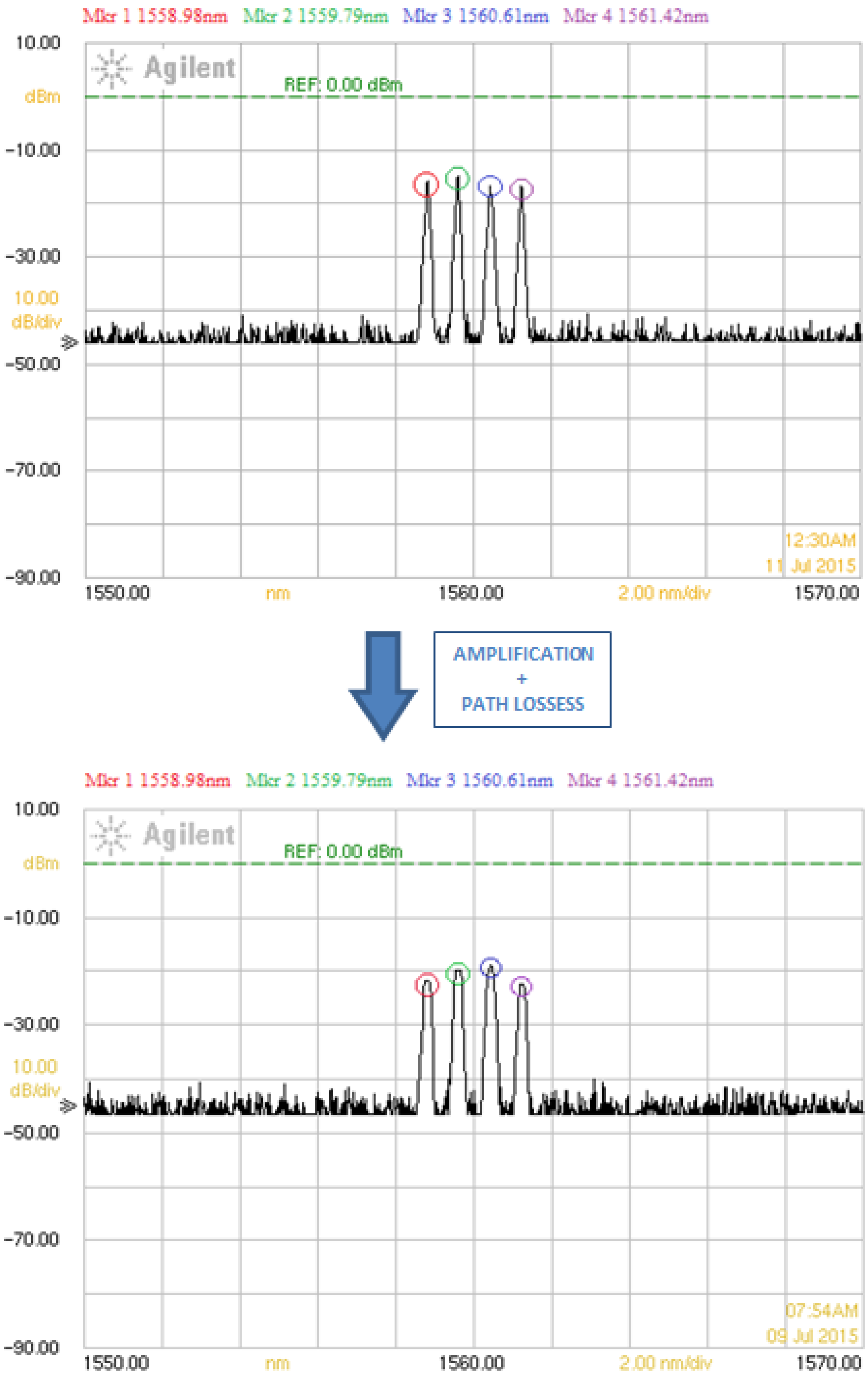

Figure 19: The downstream optical channels (a) before, and (b) after amplification

The centre value deviation of the optical wavelength for each channel with respect to the theoretical ITU-T values is lower than ±1 pm. Link Performance of the system is analyzed at 10 Gb/s symmetric data rates for different amplification values using a 10G Ethernet traffic generator and analyser. Table 7 illustrates the Frame Loss Rate (FLR) performance for different amplification values in the downstream:

Table 7: Downstream and upstream FLR performance for different values of G

G	FLR	FLR

11	**DS**	1.1×10^{-4}	**US**	6.3×10^{-9}
12		1.3×10^{-6}		2.9×10^{-9}
14		1.8×10^{-7}		0
16		3.4×10^{-8}		0
18		10^{-9}		0
20		0		0

Almost negligible FLR was obtained for $G > 18$ dB for both upstream and upstream. The differences between upstream and downstream in terms of FLR are due to the tunable filter performance, which is far from the ideal case because of calibration deviations.

Preliminary tests have also been performed in order to evaluate end-to-end latency of 10 Gbit Ethernet traffic transmission over the entire system. Figure 20 depicts the end-to-end latency of the system as a function of the 10 Gbit Ethernet frame size. As we can see, end-to-end latency spans from about 8 microseconds for a packet size of 64bytes, to about 37 microseconds for a packet size of 9100 bytes. Current efforts are in the direction towards achieving lower latency values below 2-5 microseconds for packet sizes of 64-128 bytes.

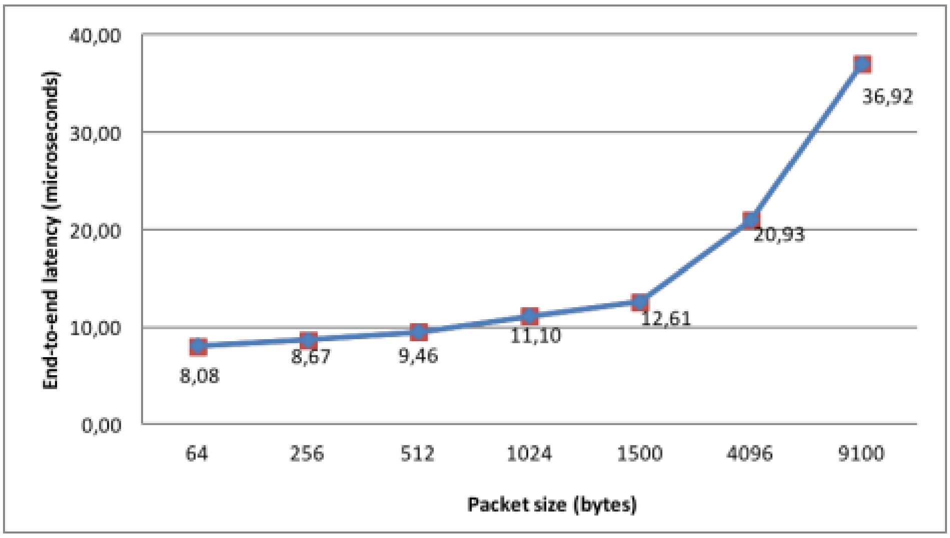

Figure 20: End-to-end latency as a function of the Ethernet frame size

3.2.4 Delay analysis of converged FH/BH traffic in PONs

This section studies the suitability of PONs for having both residential users and RRHs coexisting in the same wavelength. In particular, this study starts from an XGS-PON technology (Recommendation ITU-T G.9807.1 "10-Gigabit-capable symmetric passive optical network") whose physical layer follows the XG-PON standard (ITU-T G.987.2). Its main features include: a maximum reach of 40 km (even 60 km with reach extenders) and up to 128 ONUs sharing a pair of wavelengths with capacity 10G/10G symmetrical bandwidth in the upstream and downstream. Such 10G symmetric bandwidth availability has been demanded by operators as an intermediate solution between GPON and NG-PON2 for business solutions and mobile backhaul.

Essentially, we are interested in evaluating whether or not classical Dynamic Bandwidth Allocation (DBA) algorithms defined for the upstream channel of a TDM-PON meets the requirements for both fronthaul (i.e. CPRI or NGFI traffic generated by the RRHs) and backhaul traffic (data traffic sourced at the residential ONUs). The results obtained for the analysis in a single 10G/10G wavelength can be further generalized to the NG-PON2 standard with static wavelength association, which comprises a stacking of 4 x XG-PON or 8 x XG-PON [89].

Assumptions

We assume an XGS-PON with N residential ONUs and one or many RRHs as depicted in Figure 21.

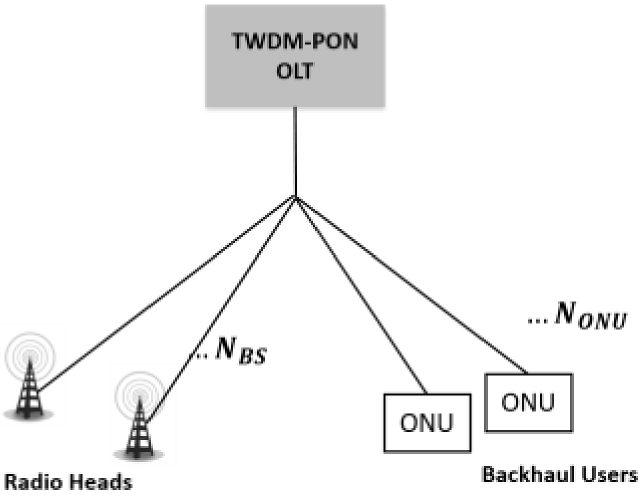

Figure 21: XG-PON serving users and Remote Radio Heads (RRHs)

Following the XG-PON standard, when the OLT assigns transmission windows to the different ONUs, it can differentiate between four classes of service, namely Fixed bandwidth, Assured bandwidth, Non-Assured bandwidth and Best-Effort. In what follows, we assume that fronthaul ONUs will be granted Fixed bandwidth using periodic reservations (T_{FH} transmission windows of Figure 22), while residential ONUs shall share the remaining transmission windows (Vi, i=1,2,… within the T_{BH} of Figure 22) in dynamic fashion, using classical DBA algorithms.

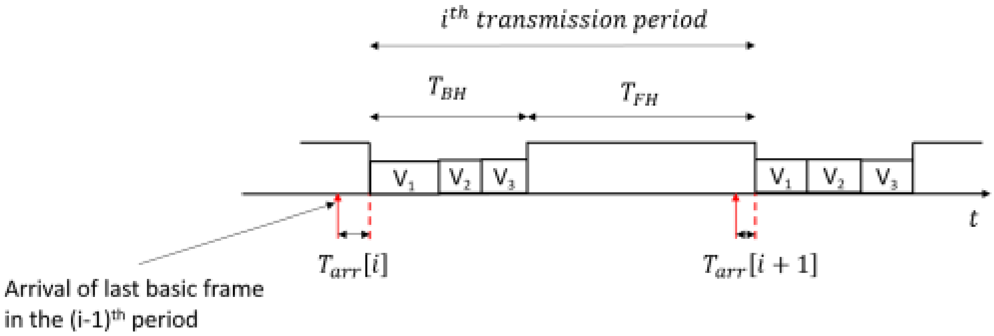

Figure 22: Upstream transmission period using fixed bandwidth alloc. for fronthaul

As per Figure 22, let η (with η<1), be the duty cycle of the assigned fronthaul period i.e.

$$T_{FH} = \eta T_p; T_{BH} = (1-\eta)T_p$$

where T_p is the transmission period.

In this scenario, the following questions need to be answered:

- What percentage of time needs to be reserved for a certain CPRI option, in other words, an RRH serving K sectors with MxM MIMO and B LTE bandwidth? How much time is left for residential ONUs?
- What should be the period between reserved grants and how does this affect delay and jitter to fronthaul traffic?
- What is the average delay perceived by backhaul (i.e. residential) traffic?

Fronthaul analysis

To answer the above questions, we will briefly overview the CPRI specification. For all CPRI options, a 'Basic Frame' (BF) is generated every $T_c = \frac{1}{f_c}$ seconds where f_c is the nominal chip rate set based on the OFDM sampling rate for 2.5 MHz LTE signal (remark that $f_c=3.84$ *MHz*, and $T_c=260.41667$ *ns*) [90]. One BF contains 15 words of IQ data and 1 word of Control & Management. The length of BF depends on the CPRI option which defines the line rate and, accordingly, the word length. Table 8 shows the number of bits per BF for all CPRI options.

Table 8: Length of BF for all CPRI options

CPRI Option	CPRI data rate (Mb/s)	Length S of BF (bits)
1	614.40	160
2	1 228.80	320
3	2 457.60	640
4	30 720.00	800
5	4 915.20	1 280
6	6144.00	1 600
7	9 830.40	2 560
7A	8 110.08	2 112
8	10 137.60	2 640
9	12 165.12	3 168

Backhaul load and delay

The transmission cycle time, $T_{SS} = T_{FH} + \sum_{i=1}^{N_{ONU}} V_i$ where V_i is the transmission window allocated to each ONU. (N_{ONU} is the total number of users). For Poisson arrival, it can be shown that on average, the transmission cycle is

$$T_{SS} = \frac{\left(T_{FH} + N_{ONU}T_g\right)}{1-\rho}$$

where T_{FH} refers to the amount of time reserved for the transmission of fronthaul traffic (see Figure 22), N_{ONU} is the number of residential ONUs in the PON, T_g is the guard time between two ONUs and ρ is the total load.

The last condition is obtained by substituting the minimum η that must be allotted to the fronthaul for stability. To be able to allot all users a slot within a transmission period,

$$\eta < \left(1 - \frac{N_{ONU} T_g}{T_{FH} + T_{BH}}\right).$$

Thus, the CPRI latency and the guard time limits the number of ONUs that can be allotted within a transmission period. If we consider the CPRI example from above with 30 ONUs and one RRH and a guard time of $0.01\mu s$ each, the total guard time takes up ~6.3% of the maximum allowable OFF period. If we consider CPRI option 5 with $\eta = 0.5$ and $T_{OFF} = 4.5\mu s$ ($T_{SS} = 9\mu s$), the backhaul load per transmission period, $\rho^* \leq 0.4667$. In terms of bytes, this is a total of 5250 bytes that can be backhaul data per transmission period. (The bytes can be allotted equally to each ONU or proportionally to their load but the assumption is that all the ONUs are allotted at least 1 byte to transmit).

In practice, ONUs generate large packets infrequently [91]. In the following discussion, L refers to the number of ONUs allocated transmission time per OFF period and M is the number of transmission periods that correspond to a transmission cycle.

Simulation results

Next, we compute design parameters for a few CPRI options and then calculate the backhaul delay for different backhaul loads. As mentioned in the previous section, we assume XG-PON with 10 Gbit/s in the upstream and a guard time of $0.01\mu s$. We also assume $N_{ONU} = 30$ and $N_{BS} = 1$.

Example 1: CPRI Option 1: CPRI option 1 can support 8 1.25MHz LTE signals or a LTE 10MHz signals. For this option, the word length is 8. Thus, $S = 160\ bits\ per\ BF$. CPRI line rate = $S \times f_c = 160 \times 3.84MHz = 614.4Mbps$ => $\eta \geq 0.06144$.

Example 2: CPRI Option 3: CPRI option 3 can support 32 1.25MHz LTE signals up to 4 LTE 10MHz signals. For this option, the word length is 32. Thus, $S = 640\ bits\ per\ BF$. CPRI line rate = $S \times f_c = 640 \times 3.84MHz = 2457.6Mbps$ => $\eta \geq 0.24576$.

Example 3: CPRI Option 5: CPRI option 5 can support 64 1.25MHz LTE signals up to 8 LTE 10MHz signals. For this option, the word length is 64. Thus, $S = 1280\ bits\ per\ BF$. Let CPRI line rate = $S \times f_c = 1280 \times 3.84MHz = 4915.2Mbps$ => $\eta \geq 0.49152$.

Figure 23, Figure 24 and Figure 25 show the mean and maximum waiting times for the fronthaul and the mean delay to the backhaul for distance 5km, 10km and 20km respectively. Each curve is shown until the corresponding ρ_{max}.

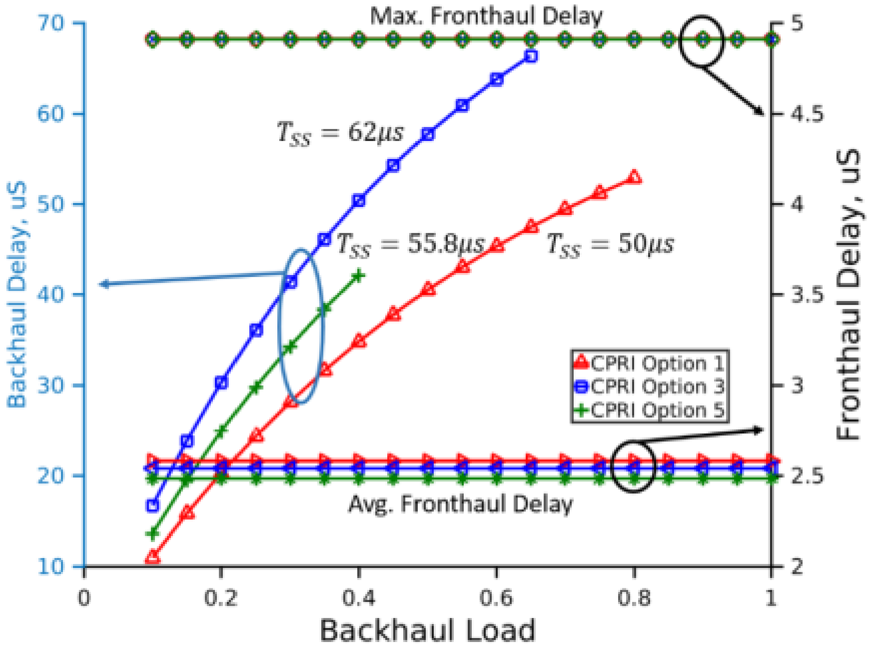

Figure 23: Backhaul and fronthaul delay for maximum distance of 5km ($T_{SS,min} = 50\mu s$)

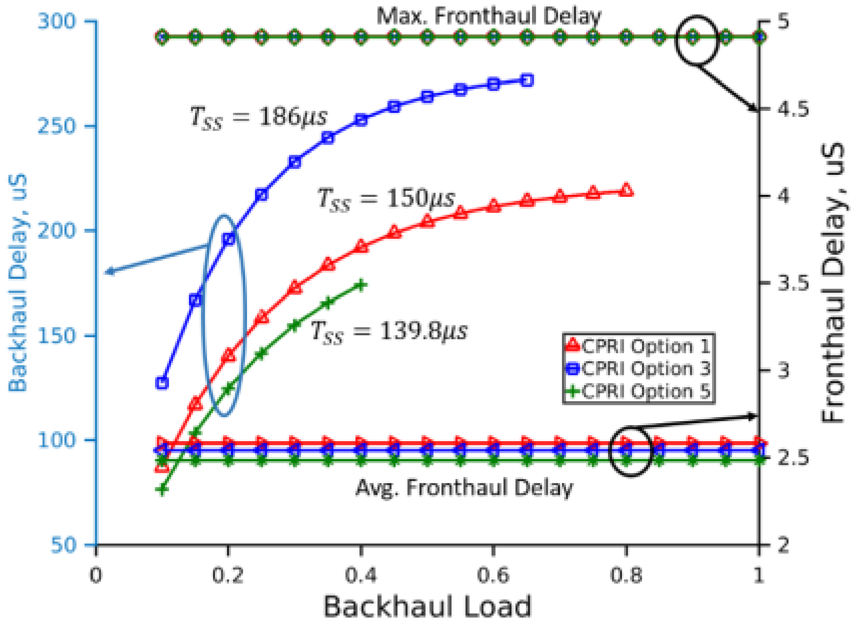

Figure 24: Backhaul and fronthaul delay for maximum distance of 10km ($T_{SS,min} = 100\mu s$)

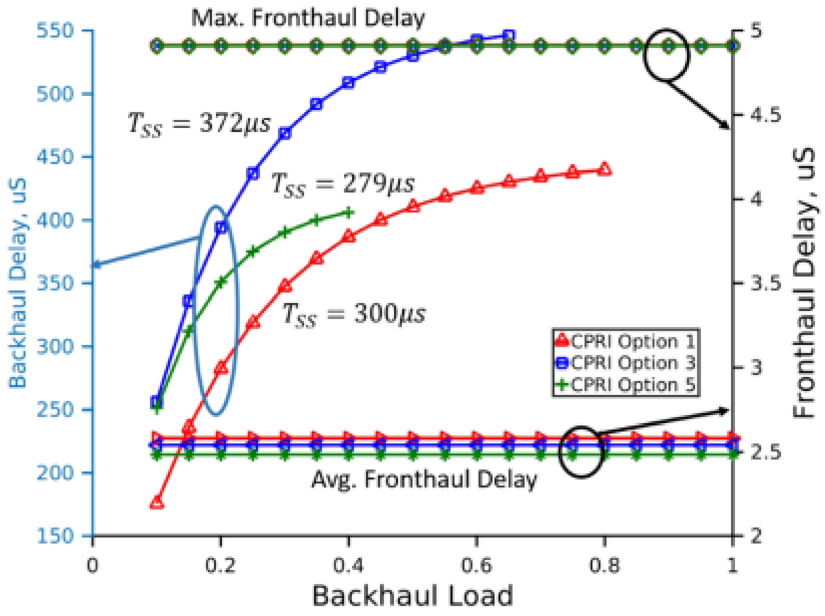

Figure 25: Backhaul and fronthaul delay for maximum distance of 20km ($T_{SS,min} = 200\mu s$)

3.2.5 Control and management for structural fixed-mobile convergence with WDM-PON

Wavelength tunability and transport of monitoring data are carried in the WDM-PON by an out-of-band control channel, as indicated by the ITU-T G.989.2 standard. This channel, as known as Auxiliary Management and Control Channel (AMCC), transmits wavelength assignment and allocation information as well as Operation Administration and Management (OAM) data. It will be inserted in each upstream and downstream wavelength. AMCC can be implemented either by baseband over-modulation or by a radio frequency pilot tone (PT). In the standard, a 500 kHz RF carrier is modulated by a 128 kbit/s Non Return to Zero (NRZ) signal with a modulation index of 10%.

Our interest in this subsection is focused on control and management solutions for a WDM-PON optical infrastructure and their impact on the performance of both fronthaul interfaces (based on CPRI in our experiments) and Ethernet signals, emulating backhaul and business services. We start with an experimental assessment of the impact of AMCC on a fronthaul link. Then, we assess an industrial prototype with embedded wavelength tunability function based on a similar principle.

Impact of AMCC on the fronthaul link

Essentially, AMCC transmission over a 20 km fronthaul link is carried out using a Directly Modulated Laser of a commercial Small Form factor Pluggable (SFP). Different measurements are carried out to verify the performance of the AMCC and to evaluate its impact on CPRI and radio signal integrity. The experimental setup is shown in Figure 26.

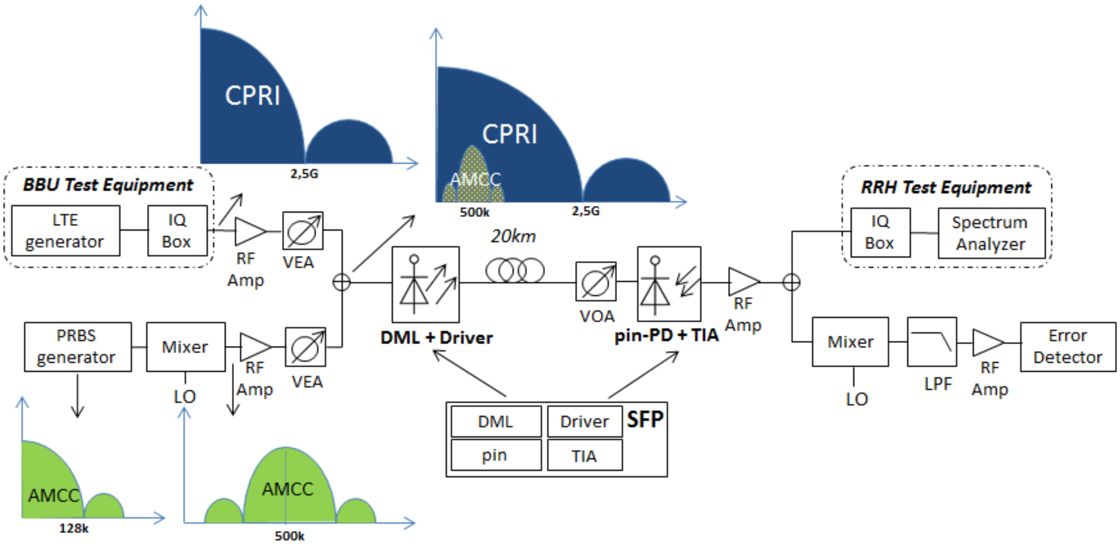

Figure 26: Experimental setup and principle of AMCC implementation and evaluation of its impact on fronthaul transmissions.

At the transmission side, a signal generator is used to generate a 20 MHz LTE carrier using standardized test model E-TM3.1 [75]. This signal is converted to CPRI (performing sampling, quantization, and coding) using an IQ box. A Pseudo Random Binary Sequence (PRBS) generator is used to emulate the AMCC transmission using a 2^7-1 bits sequence. This low frequency signal (128 kbit/s) is up-converted using a mixer and a Local Oscillator (LO) at 500 kHz. Both AMCC and CPRI signals are separately amplified and attenuated by a Variable Electric Attenuator (VEA) so that their voltage ratio can be changed. The signals are then summed up with a power combiner. The obtained signal is fed to a driver then to a Directly Modulated Laser (DML) diode operating at 1590 nm and transmitting 0 dBm into 20 km of standard single mode optical fibre. The received optical signal is detected by a pin-photodiode then amplified with a Trans Impedance Amplifier (TIA). Laser, photodiode, driver and TIA are embedded in a commercial SFP module as shown in Figure 26. The received RF signal is amplified and sent to a power splitter. The first output of the splitter is connected to an RRH test equipment composed of a IQ box for CPRI-to-LTE conversion and a Spectrum Analyser for LTE analysis. The signal at the second output is down converted and low-pass filtered by a 250 kHz filter to remove CPRI high frequency components and potential harmonics and intermodulation products generated by the mixers. After filtering, the signal is amplified before performance evaluation.

We focus our analysis on three main performance indicators: Bit Error Rate (BER), Error Vector Magnitude (EVM) and jitter. We started by investigating the BER variation of both CPRI and AMCC signals as a function of the relative modulation index, defined as ratio of the peak-to-peak voltage values of AMCC with respect to CPRI. The results for CPRI 3 (2.45 Gb/s) and a 128 kbit/s AMCC are depicted in Figure 27, which shows that error free AMCC and CPRI transmissions (BER $\leq 10^{-8}$ and 10^{-12} respectively) can be obtained for modulation indexes between 18% and 20%.

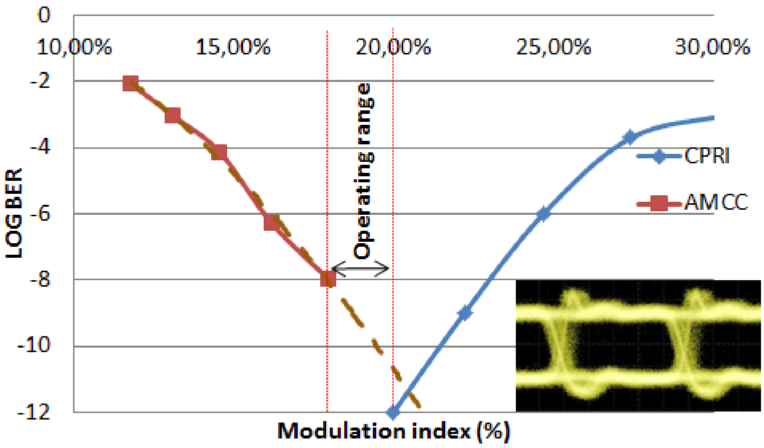

Figure 27: CPRI and Pilot Tone BER performance for different modulation index and optical eye diagram at 20% modulation index.

In order to evaluate the impact of introducing the AMCC in a fronthaul link, we fixed the relative modulation index to an optimal value of 20%. Figure 28 displays the eye diagrams at the input of the RRH test equipment at 2.45 Gbit/s with and without the AMCC signal. Some noise can be noticed as well as some jitter due to the introduction of the control signal.

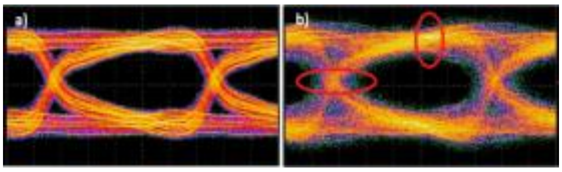

Figure 28: Eye diagrams of received CPRI 3 with (a) and without (b) pilot tone transmission.

Figure 29 shows the impact of the AMCC on the LTE EVM while varying the Received Optical Power (ROP) at the input of the PIN photodiode. Measurements are carried out for CPRI 3 and 6 (2.45 Gb/s and 6.14 Gb/s respectively) without the AMCC, with a 128 kbit/s AMCC up-converted to 500 kHz and with a 128 kbit/s AMCC up-converted to 1 MHz. 64 QAM modulation is used for LTE transmission since it has the most stringent EVM requirement (9%) according to the 3GPP standard. We notice a penalty of 0.85 dB in the optical budget when inserting the AMCC on CPRI 3 and 1.35 dB for CPRI 6 for a fixed EVM of 0.06%. We also observe very similar performances when the AMCC is up-converted at 500 kHz and 1 MHz. Figure 29 also shows that an optical budget of up to 22 dB can be obtained before achieving 3% EVM which allows for a 6% extra margin with respect to the 3GPP standard.

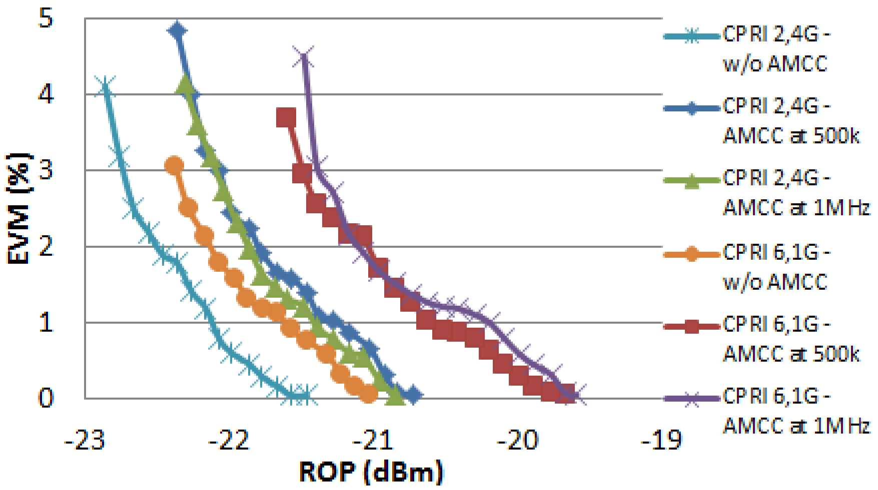

Figure 29: EVM performance as a function of the Received Optical Power (ROP)

We also evaluated the AMCC BER performance at 128 kbit/s and 64 kbit/s and with an up-conversion of 500 kHz and 1 MHz as depicted in Figure 30. We notice a better performance at 128 kbit/s which we believe is due to the filter characteristics at the receiver side. On one side, by transmitting at 64 kbit /s and using a 250 kHz low-pass filter at the receiver, we keep more lobes of the AMCC signal spectrum, which allows having a more squared time-domain signal, thus a better transmission. On the other side, more energy of the CPRI signal is contained inside the filtered AMCC, which degrades the performances. The shape of the obtained BER curves can be explained by the presence of a limiting TIA in the SFP, which causes a sudden BER deterioration.

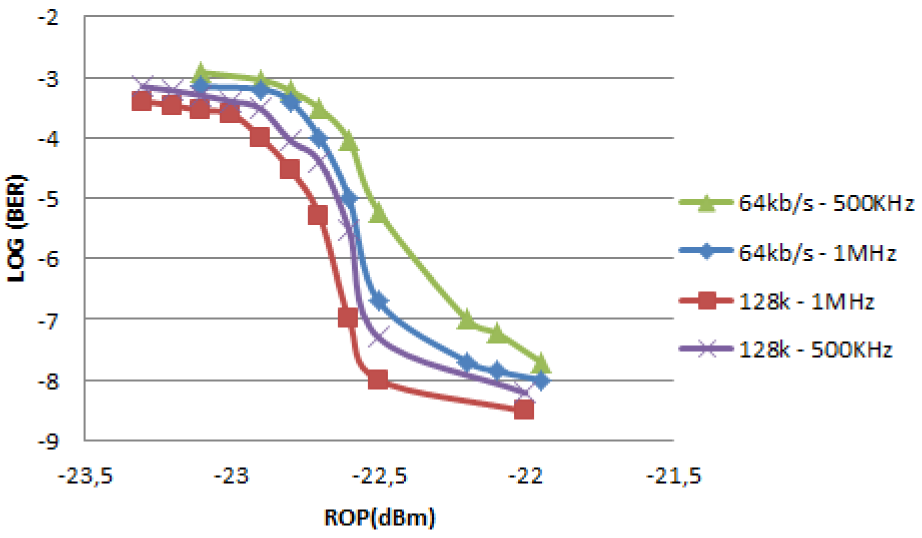

Figure 30: BER performance as a function of the received optical power.

Finally, we evaluated the jitter introduced on the 2.45 Gbit/s CPRI channel upon the insertion of the AMCC. The presence of a low frequency signal prevented us from using the accurate dual-Dirac jitter estimation approach [76]. An alternative method was then carried out by means of an analysis of the CPRI eye diagram. In order to verify the reliability of the eye diagram approach, we first performed a reference measurement without the AMCC and compared it to the dual-Dirac approach. We measured 132 mUI with the dual-Dirac model and 148 mUI with the eye diagram one, which validated our method. The jitter with the AMCC signal was 406 mUI. A significant amount of jitter is introduced upon AMCC insertion but it still respects the maximum value defined by 3GPP (650 mUI). We notice that lower jitter values could be obtained filtering out the AMCC from the CPRI signal by means of a band-stop filter. However, the impacts of such filtering on the CPRI performances have to be evaluated.

Evaluation of an industrial prototype

The WDM-PON system under test is a prototype having three upstream channels in the C-band and three downstream channels in the L-band. These channels are multiplexed by a cyclic arrayed waveguide grating (AWG) offering 40 channels with a channel spacing of 100 GHz in L-band and ~97 GHz in C-band as standardized by ITU-T G.698.3. AWGs are located at the Central Office (CO) and the Remote Node (RN) as shown in Figure 31. One downstream channel operates up to 10 Gbit/s and the two other ones at 1 Gbit/s. The ONUs are colorless, meaning that they can be tuned to the wavelength corresponding to the AWG port they are attached to, e.g. by means of a feedback-based wavelength-locking process.

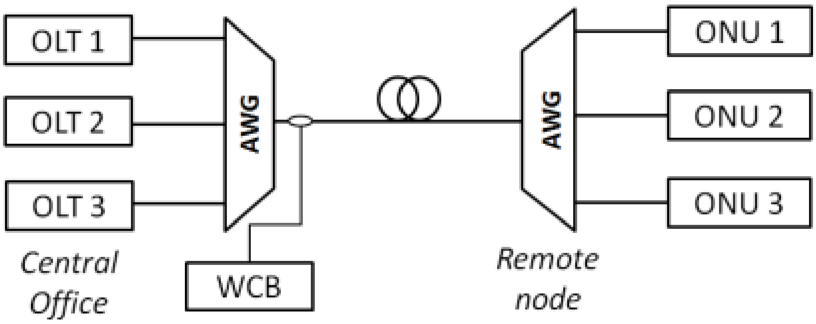

Figure 31: WDM-PON system architecture

In order to distinguish the upstream signals and their deviation with respect to the ITU grid, a unique pilot tone in the frequency range [100 kHz – 1 MHz] is added to each upstream signal. A Wavelength Control Board (WCB) measures the power received from different users thanks to a Fast Fourier Transform (FFT) before and after a common centralized wave-locker. This wave-locker uses an etalon filter as a centralized wavelength discriminator which has a sinusoidal response over the C-Band spectrum with a 100 GHz free spectral range. It is set so that the ITU frequencies are located halfway up on the rising edge of its response curve. The ONU wavelength deviation can be calculated from the ratio of the signals, estimated by FFT, before and after passing through the etalon. Such a way, the system can determine frequency deviations in the +/-25 GHz frequency range. In the downstream, the feedback on wavelength deviation and power levels is implemented by using pilot tones with an additional Embedded Communication Channel (ECC) at the rate of 1 kbit/s. This pilot tone is added to the downstream WDM spectrum via an over-modulation performed by a fast variable optical attenuator.

Figure 32 shows the experimental setup used to measure the performance of a business service and a fronthaul link using the proposed system. An Ethernet tester is used to emulate the transmission of a 1 GB/s Ethernet business service. The performance is evaluated in terms of frame loss. In the adjacent channel, a mobile fronthauling service is transmitted using a signal generator for LTE generation and an IQ box for LTE to CPRI conversion. The standardized E-

TM3.3 LTE test model is used with 20 MHz carrier bandwidth. CPRI performance measurements are carried out in the downlink direction at three CPRI line rates: 2.45 Gbit/s, 4.91 Gbit/s and 9.83 Gbit/s.

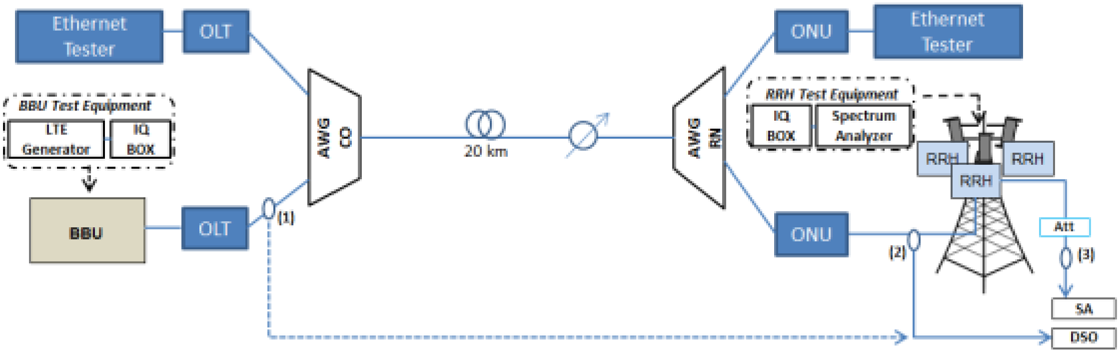

Figure 32: Experimental setup for proprietary WDM-PON C&M evaluation

After 20 km transmission over single mode optical fibre, an IQ box is used to convert the CPRI signal to LTE before the analysis with a Spectrum Analyser (SA). The optical link budget (OB) is 22 dB for a BER of 10^{-12}. At the RRH side, colorless ONUs (OB = 24 dB) with a pilot tone based tuning process are used. In order to evaluate the performance impact of the wavelength locking process and the transmission of an adjacent channel, EVM measurements are done at the output of the RRH using the SA. Jitter on the electric signal is measured at the transmitter (1) and the receiver (2) with a Digital Storage Oscilloscope (DSO) as shown in Figure 33 and a frequency accuracy evaluation of the LTE signal is carried out with an SA, this time at the output of a commercial RRH operating at 2.645 GHz. A latency measurement is done as well using CPRI measurement equipment to assess the delay introduced by the WDM-PON system.

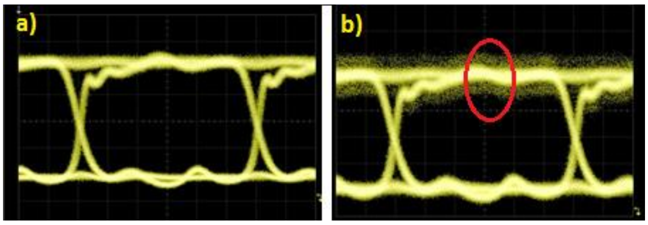

Figure 33: Eye Diagram before (a) and after (b) adding a pilot tone

Adjacent channels could affect the transmission due to crosstalk. Also, using pilot tones for the wavelength tuning could generate noise as it is shown on the eye diagrams depicted in Figure 33. To address these points, we investigated the transmission performance in terms of Ethernet frame loss, EVM and frequency accuracy of the LTE signal, and jitter on CPRI signal.

First, we start by investigating EVM values and Ethernet frame loss while attenuating the Received Optical Power (ROP) in the ONUs with a variable optical attenuator (VOA). For QPSK, we measured 0.07% of EVM for received optical powers (ROP) greater than -25.5 dBm when using the test instrumentation. Ethernet transmission in the adjacent channel was frame loss free at this point but starts degrading at -28 dBm. A degradation of the EVM value (1%) is noticed when we use a commercial RRH due to the amplifier’s noise. The same EVM value is obtained when using a dark fibre fronthaul, therefore no EVM degradation is introduced by pilot tone use.

The same test was conducted for a 64QAM transmission using the test model E-TM3.1 at the three tested line rates (2.45 Gb/s, 4.91 Gb/s and 9.83 Gb/s), leading to the same EVM value (0.07%). No EVM variation is observed when we remove the Ethernet signal whatsoever. Thus, there is no inter-channel crosstalk impact on EVM. These results are compliant with 3GPP maximum EVM value of 17.5% for QPSK and 9% for 64QAM.

Secondly, we evaluated the jitter introduced by the system on the CPRI signal. We notice that there is much jitter at the receiver compared to the measured values at the transmitter. This is certainly introduced by the active components in the ONU used for the wavelength locking operation. We also observe that the measured values respect, however, the CPRI specification for line rates of 2.45 Gb/s and 4.91 Gb/s. The maximum value is instead slightly exceeded at 9.83 Gb/s. Resynchronization with an appropriate Clock Data Recovery (CDR) would be necessary in that case for jitter cleaning.

In order to verify the potential jitter impacts, we started by measuring the BER with the CPRI test equipment. We obtained a BER < 10^{-12} for the three CPRI line rates as required in the CPRI specification. Then, we measured the LTE frequency deviation with respect to 2.645 GHz at the output of a commercial RRH during 24 hours using 2.45 Gb/s CPRI line rate. We obtain ±1.4 ppb when using fronthaul over dark fibre and ±2 ppb using the WDM-PON system (for 99.99% of the measured points). These results are largely below the ±50 ppb maximum frequency deviation imposed by 3GPP. Finally, the latency introduced by the system, excluding the fibre, was only 26 m (130 ns).

In summary, we can conclude that NG-PON2 based on PtP WDM PON offers an appealing solution for fixed-mobile converge in 5G. OAM information can be carried by using standardized or standardizable in-band low bit rate channels. The only warning aspect is the additional jitter introduced by these channels, which was however compatible with the 3GPP specification in almost all the performed experiments.

3.2.6 Future evolution: OFDM Flex-PONs for 5G-Crosshaul

The advent of elastic optical networking, enabled by the adoption of the flexible channel grid and programmable transceivers, opens the door to a truly dynamic management of optical networks [30][31]. This is especially interesting for achieving the pursued integration between optical metro/access and RAN. In fact, approaching this paradigm, specific channels can be set up according to the requirements of the services to deliver. Furthermore, elastic networking also enables to, transparently, set a RAN network over the optical metro/access. For example, a pool of BBUs would be located at a selected node of the metro network segment, while the RRUs could be scattered along one or multiple access trees, both interconnected by a mesh of exchange nodes (ENs). In this scheme, a highly centric traffic pattern is expected, posing different requirements in terms of cost and data rate compared to typical transmission technologies for the transport/core networking.

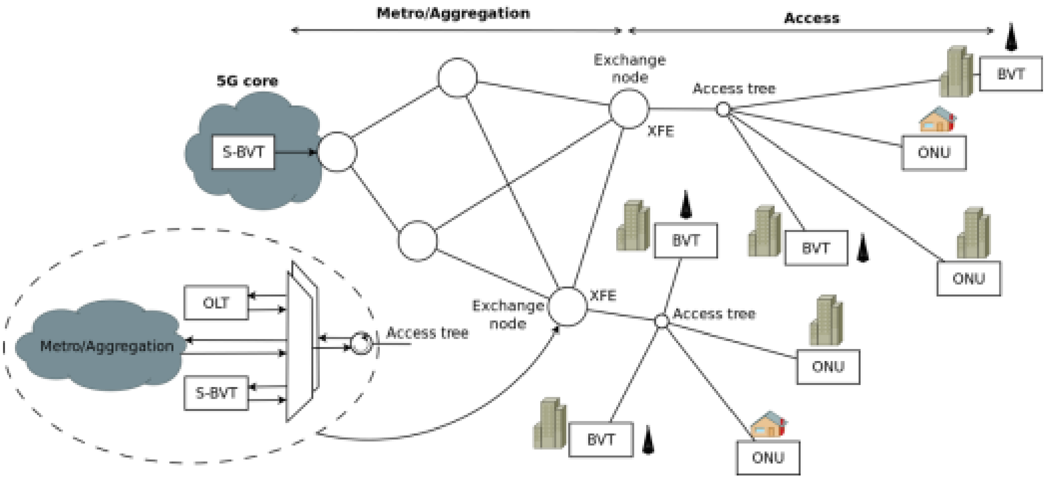

Figure 34: New 5G-Crosshaul network scenario and architecture

Within 5G-Crosshaul project, we propose to transparently and dynamically deliver mobile front-/back-haul in a converged metro/access environment, following the elastic networking paradigm in order to take advantage of the already deployed fiber infrastructure. In order to cope with that in a cost-effective way, we propose to use sliceable bandwidth variable transceivers (S-BVTs) based on OFDM employing direct detection (DD). Please, note that this technology is still foreseen as long-term, being under strong assessment and with almost no interaction with control/application layers.

The network and signal delivery scheme is depicted in Figure 34. There, programmable S-BVTs are present at the 5G core and exchange nodes in order to concurrently serve different cell sites. At the other end of the network, each cell site has a programmable BVT. The (S-)BVTs can be remotely configured by the control plane, for an optimal management of the network resources [31][32]. The parameters to be configured at each (S-)BVT include wavelength, spectral occupancy and modulation format/power per flow. So, the proposed (S-)BVTs scheme may deliver data flows with variable spectral occupancy and rate, according to the network and path conditions. Among all the options for implementing the (S-)BVTs, those based on DD orthogonal frequency Division multiplexing (DD-OFDM) are the most attractive for cost-effectively coping with the flexibility requirements of elastic optical networks [32]. In fact, OFDM provides advanced spectrum manipulation capabilities, including arbitrary sub-carrier suppression and bit/power loading. Thanks to these features, DD-OFDM transceivers can be ad hoc configured for achieving a certain reach and/or coping with a targeted data rate adopting low complex optoelectronic subsystems [32][28].

In order to ensure full compatibility with the deployed optical metro and access networks, a specific wavelength plan is envisioned. In fact, legacy access standards (e.g. GEPON, GPON) use 1490 nm for downstream; while late standards (10G-EPON and XGPON) recommend the range of 1575-1580 nm also for downstream. Thus, the entire C-band is available for performing a wavelength overlay of channels in order to provide different additional services over the same access infrastructure. Also, in such infrastructure, the feeder cables cover the majority of the distance (from the EN to the splitter distribution hub) and typically have a loose-tube design containing several fibers. Thus, in case the RRUs can be attached to the splitter distribution hub, a dual-fiber duplex across the transmission link is ensured with no need for deploying new cables.

At the ENs of the metro network, the mobile front-/back-haul signals are eventually filtered out and transparently routed/dropped to their destination access tree. This fact does not pose any strict constraint, since commercial standard flexi-grid spectrum selective switches (SSS) and optical amplifiers typically operate at C-band. Additionally, each EN includes the corresponding optical line terminals and aggregation switches/units for delivering fixed access services to the network users across the corresponding access trees. Please note that these ENs can be considered as XFEs according to the 5G-Crosshaul general architecture/terminology.

Regarding the size of traffic to support, it should be noted that the most bandwidth demanding service is the mobile front-haul based on CPRI, which in the other hand does not allow any dynamic management of the capacity in the transport network. In order to relax these requirements, more functions can be decentralized and adopted by the RRUs, trading latency and data rate against flexibility. In fact, for transmitting up to 100 km, 1 ms minimum round trip delay should be expected. This requires a functional split at PHY2 or MAC-PHY level, relaxing the bitrate requirement [33]. With these other functional splits it is desirable to have mechanisms for dynamic management of the bandwidth in the transport network, being (S-)BVT one of the suitable technologies for that.

3.2.7 Technologies working on copper fixed access infrastructure

Today's time-domain fronthaul protocols like CPRI are often carried over fibre since the bit-rate requirement is very demanding and 5G will lead to even higher fronthaul bit-rate demands.

For short distances, e.g. inside buildings, it would in many cases be advantageous to be able to use the copper LAN infrastructure to transport the fronthaul, e.g. using mature 10GBASE-T and the emerging 2.5GBASE-T and 5GBASE-T technologies. However, with classical CPRI bit rate option 7 (9.8 Gbit/s) only 160 MHz of radio bandwidth in SISO mode can be supported, which may not be enough for 5G applications with multiple antennas and high bandwidths. The newer bit rate option 8 (10.1 Gbit/s) is slightly more efficient, supporting 200 MHz radio bandwidth due to the use of 64b/66b line coding instead of the older 8b/10b line code, but this does not solve the bit rate problem.

One way of reducing the fronthaul requirement is to make a new functional interface higher in the protocol stack for LTE and 5G, e.g. by locating part or all of the radio physical layer processing from the baseband processing unit to the remote radio unit. While this will substantially decrease fronthaul bit rate, it will also increase computational complexity in the remote radio head (RRH) or remote radio unit (RRU), where baseband resource pooling is limited and where cooling may be an issue.

Another option is to improve the time-domain fronthaul, since the redundancies in today's CPRI standard shows great potential for compression. As an example, by utilizing resampling and entropy coding, the fronthaul rate for LTE downlink can be compressed five times if 3% EVM is acceptable. This means that a 10GBASE-T copper link could carry up to ~1000 MHz of radio bandwidth (e.g. 250 MHz 4x4 MIMO) over 100 meter CAT6a cable.

3.3 Technologies for 5G-Crosshaul optical networks

3.3.1 Introduction

This section overviews optical transport technologies that allow fulfilling the 5G-Crosshaul requirements, both in terms of performance and cost. The focus of optical technologies is concentrated on Coarse Wavelength-Division Multiplexing (CWDM) and Dense WDM (DWDM). The key differences between these two variants result from their unique channel-spectrum allocations, what encourage the rise of specialized component technologies, price-points, and applications. Generally, CWDM offers lower price-points as compared with DWDM and hence is extremely amenable to many cost-sensitive access and enterprise applications.

CWDM has been widely used for backhaul mobile areas and business access services since the beginning of twenty-first century. It approaches up to 18 channel systems with a large wavelength plan from 1270 nm to 1610 nm and a channel spacing of 20 nm according to ITU-T Recommendation G.694.2. Common CWDM deployments are often based on ring topologies, mainly using add-drop multiplexers (OADMs), with per-channel bit rates of 10 Gbit/s typically. However, the typical CWDM scheme considers WDM filters for signal combining and demultiplexing.

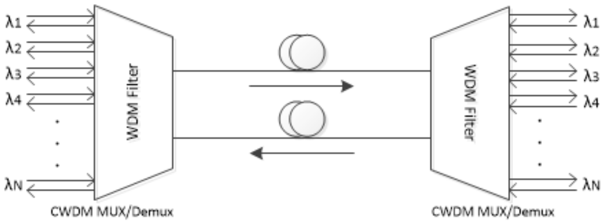

Figure 35: CWDM scheme

When the number of wavelength channels is above 20 in a WDM system, it is referred to as DWDM. DWDM's tighter wavelength spacing (0.2 nm or 25 GHz, 0.4 nm or 50 GHz, 0.8 mn or 100 GHz) allows fitting more channels onto a single fiber, but cost more to implement and to operate in comparison to legacy CWDM deployments. A key advantage to DWDM environment is that it offers versatility and flexibility (bit-rate protocol independent), in this way, traditionally DWDM technology has been used for backbone networks. In order to extensively use DWDM in regional network (this is possible only reducing cost of DWDM solutions), 5G-Crosshaul project proposes new solutions based on Silicon Photonics to cut down the cost of the optical switches by two orders of magnitude.

The suitability of direct detection modulation formats to realize cost effective 100 Gbit/s transceivers as well as their issues in achieving sufficient distance and link budget figures are addressed in Section 3.3.2, where simulations and preliminary experiments are presented to show how these limitations can be overcome with negligible cost impact.

3.3.2 Direct Detection 100 Gbit/s transceivers

The introduction of the 5G RAN and in particular the network centralization and cloudification require the capability to convey traffic from several distant RRH sites to a single hub node, adding a distance requirement to the capacity requirement, pushing the introduction of higher capacities (100+ Gbit/s). Typical distances to be supported in CPRI-based fronthaul are up to 20 km, according to the maximum propagation delay that widely used fronthaul protocols (CPRI) can tolerate. DWDM networks can satisfy both capacity and distance requirements. Figure 36 reports the aggregate capacity per fibre with 100 Gbit/s short reach grey optical interfaces, i.e. single channel transceivers with non-stabilized wavelength; with 100 GHz spaced DWDM, is the most suitable option for 5G-Crosshaul for cost reasons; while 50 GHz coherent DWDM, which widely used in regional and backbone networks but is too costly for 5G-Crosshaul purposes.

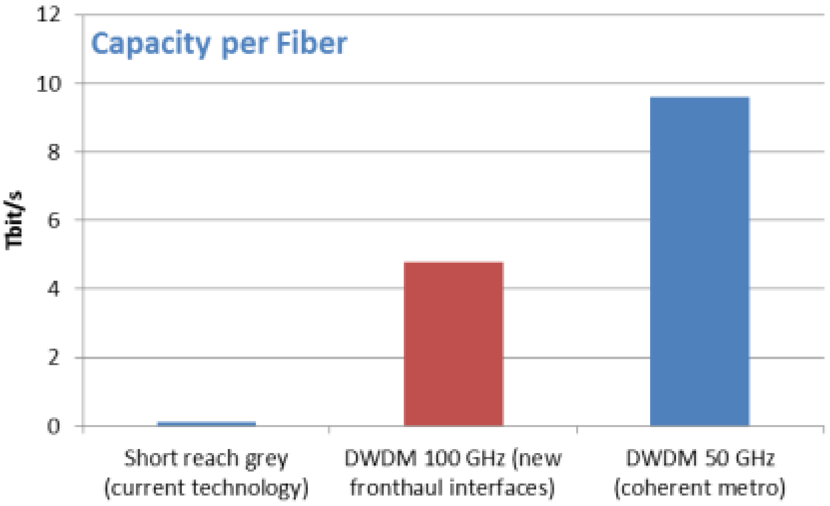

Figure 36: Capacity per fibre with different optical interface technologies

Regarding distance, coherent interfaces can achieve thousands of kilometres, through electrical equalization at the receiver to compensate for the channel distortion introduced by the fibre chromatic dispersion. However, considering that the link distance is much shorter in 5G-Crosshaul, direct detection interfaces may be useful to lower cost and power consumption.

Today, there are two types of 100 Gbit/s transceivers, very different as regards achievable distance and cost:

- Transceivers for Datacom interconnections, based on 1310 nm grey optical interfaces with direct detection and having a reach of 2 km. PAM-4 and DMT are examples of direct detection modulation formats.
- Metro (500+ km) and long-haul (1000+km) DWDM coherent interfaces based on DP-QPSK.

Figure 37 reports the cost of these optical interfaces (blue dots) normalized to the cost of a 10 Gbit/s Small-Factor Pluggable (SFP+). The red dot in the figure indicates the cost that would be suitable for the 5G-Crosshaul application space, which is currently not covered by commercial optical transceivers.

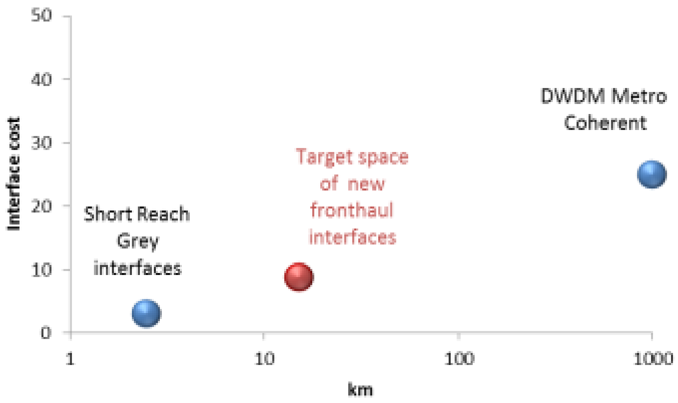

Figure 37: Normalized cost vs. distance for different 100 Gbit/s technologies

A study to understand what kind of modulation format could fill this gap has been performed within 5G-Crosshaul project. An outcome of the study was that, in order to achieve sufficient link budget and distance, it is necessary to split one 100 Gbit/s optical channel in two 50 Gbit/s wavelengths. Then, different direct detection modulation formats were compared by simulations, as shown in Figure 38, which reports the optical sensitivity penalty at BER=10^{-3} versus the fibre link distance. Penalty values are referred to the performance of a 50 Gbit/s OOK channel at 0 Km.

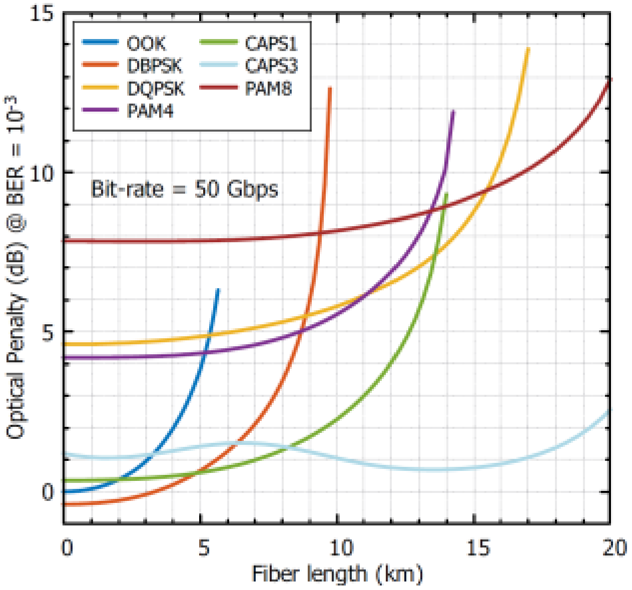

Figure 38: Optical penalty vs. distance for different direct detection modulation formats

In Figure 38, the chromatic dispersion is the main penalty source when the link distance increases. PAM4 and PAM8 are well known multi-level amplitude modulated signals, with four and eight amplitude levels, respectively. DBPSK and DQPSK are differentially encoded phase modulated signals differentially encoded so that they can be detected by means of interferometers and balanced photodiodes with no need of a local oscillator at the receiver.

The CAPS (Combined Amplitude Phase Shift) modulation formats family see a transmitter including a digital encoder and an I/Q modulator. The receiver always requires a simple photodiode, as OOK. For CAPS-N, the number of encoder states is 2^N so that only low order modulation formats of the family have practical interest.

The simulations show that CAPS3 can meet the 5G-Crosshaul link distance requirements and, using direct detection, it avoids the cost of the local oscillator at the receiver. Moreover, it does not need external dispersion compensating devices, leading to further cost saving. Receiver sensitivity (and link budget) is about 3dB better than PAM4, which is the main solution proposed today by optical modules manufacturers.

Due to lack of instrumentation able to perform 50 Gbit/s modulation, preliminary lab experiments at 25 Gbit/s were performed within 5G-Crosshaul activities (dots in Figure 39), comparing them with simulations (curves): the agreement is excellent.

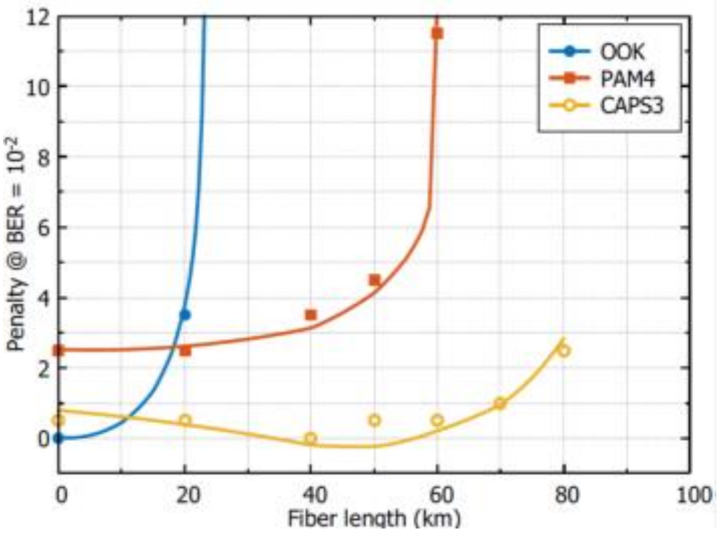

Figure 39: Simulations (lines) vs experiments (dots)

Compared to the curves in Figure 38, which consider ideal modulators and receivers, those in Figure 39 consider actual transfer function and the bandwidth of the transmitter and receiver and transmitter used in the experiments.

3.3.3 Cost-effective ROADMs based on Silicon Photonics

Current DWDM optical switches are based on Wavelength Selective Switches (WSS) devices that are costly and bulky devices, being based on complex free-space optics. These aspects have prevented, up to now, the introduction of photonic switching in fronthaul and backhaul network segments, where cost and footprint are critical but the low number of intermediate nodes and short path lengths might demand lower performances compared to WSS based solutions, designed for long haul networks.

Photonic Integration, and in particular Silicon Photonics, has the highest potential in the implementation of devices presenting low power consumption, high miniaturization, high level of integration (number of integrated functions) and large capacity. For high volume applications, like the ones in 5G-Crosshaul, Silicon Photonics can also guarantee high yield and low cost due to use of well-developed CMOS infrastructure. Hence, a new type of Silicon Photonics ROADM was realized as a building block for the 5G-Crosshaul needs. The device depicted in Figure 40 is simpler with respect to conventional ROADMs having only one line input port and one line output port and a number of wavelength (local) ports equal to 12 (but up to 24 ports are feasible with the same technology).

The fundamental functions performed by the ROADM are: add and drop of selected local channels, automatic switch of the propagation direction in a ring, for failure recovery without duplicating the number of optical interfaces connected to the add/drop ports. In optical power regulation, these are especially useful in centralized RAN scenarios to compensate for unequal distances of different RRHs from the baseband hotel. The prototype of the silicon photonic ROADM is able to perform add and drop 12x10 Gbit/s wavelengths with a channel spacing of 200 GHz on the C-Band ITU grid (see Figure 40).

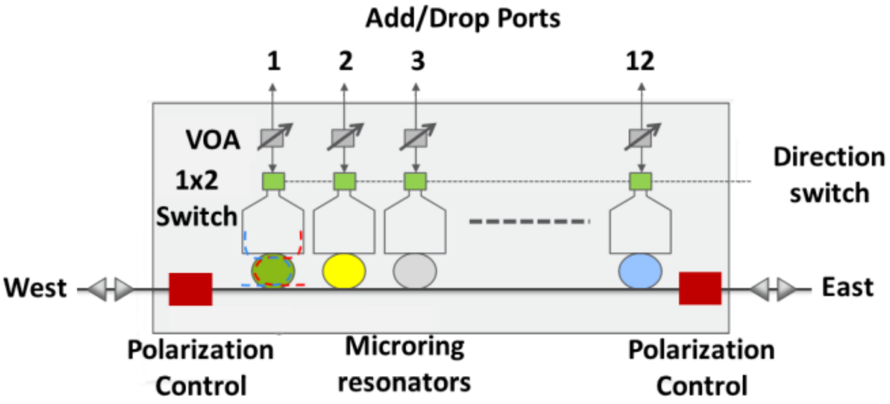

Figure 40: Silicon photonic ROADM scheme

The prototype comprises more than 50 integrated optical devices and is based on an optical bus with twelve micro-ring resonators coupled as add/drop elements. The micro-ring resonance is tuned and controlled through integrated silicon (Si) heaters and monitored by means of germanium (Ge) on Si photodetectors. To reconfigure the network for protection against fibre breaks, each micro-ring is provided with a 1x2 optical switch allowing the selection of the Eastbound or Westbound propagation direction on the bus. Integrated variable optical attenuators (VOAs) are present at each add port to regulate the optical power of the added channel. Furthermore, optical bus input and output are provided with an integrated polarization controller, based on a dual polarization grating coupler, to transform the random input state of polarization in a linear polarization state aligned with the main propagation mode of the device. Figure 41 shows the layout of the polarization controller.

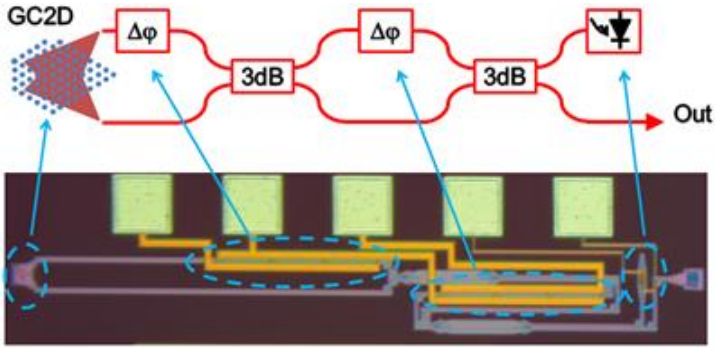

Figure 41: Polarization controller layout

A dual polarization grating coupler (GC2D) receives arbitrary polarized light at the input, and splits and rotates the light into two separate transversal electric (TE) waveguides. A first thermal phase shifter is placed on one of the waveguides to adjust the phase difference between the two arms. Then a balanced Mach Zehnder Interferometer (MZI), composed of two 50:50 multi-mode interferometer (MMI) couplers and a single thermal phase shifter, is used to send the power to the output waveguide of the circuit. One output of the MZI is terminated by a power monitor photodetector. The second MZI output, i.e. the circuit output, ends into a single polarization TE grating coupler. An active control loop is provided by using the power monitor photodetector and the two thermal phase shifters. For any given state of polarization (SOP) the photocurrent of the photodetector is minimized by adjusting the two phase shifters.

The polarization controller was first experimentally characterized at a single wavelength (1550 nm) for 50 random polarization states: all the arbitrary polarization states were compensated within 1dB accuracy.

The chip size of the integrated silicon photonic ROADM is 5 mm x 5 mm. The chip is fully packaged on a QFP160 package and equipped with an array of fourteen standard single mode fibres, and a TEC for the temperature control. Figure 42 shows the packaged ROADM Si photonic integrated circuit.

Figure 42: Packaged Si Photonics ROADM

Figure 43 shows the output spectrum, measured by means of an external cavity laser. The spectrum is normalized to the total insertion loss, which for the current device is high, about 18 dB, due to the non-optimal libraries utilized for the design of input and output dual polarization grating couplers. With the right libraries, already available in silicon foundries, 2dB per port are achievable. The maximum drop loss difference from the first to the last channel is about 1.5dB.

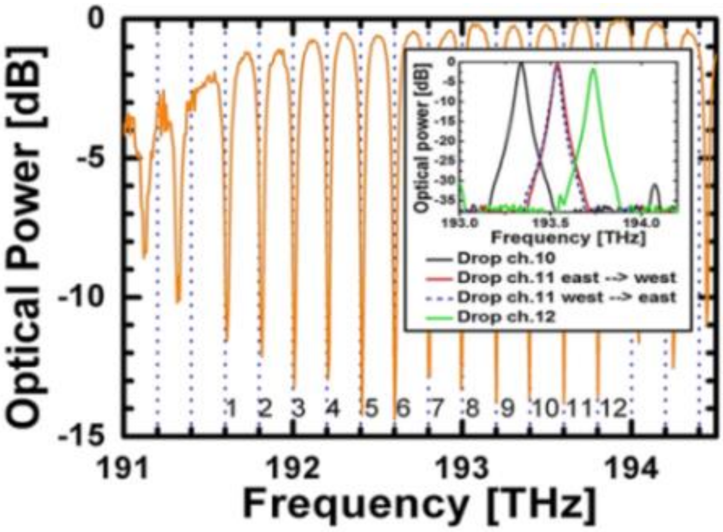

Figure 43: Measured output spectrum of the SI Photonics ROADM

The bi-directionality of the device was tested by BER measurements on an OOK 10Gbit/s signals. Figure 44 shows that in both directions the ROADM introduces an overall penalty lower than 0.7dB compared to the back-to-back curve.

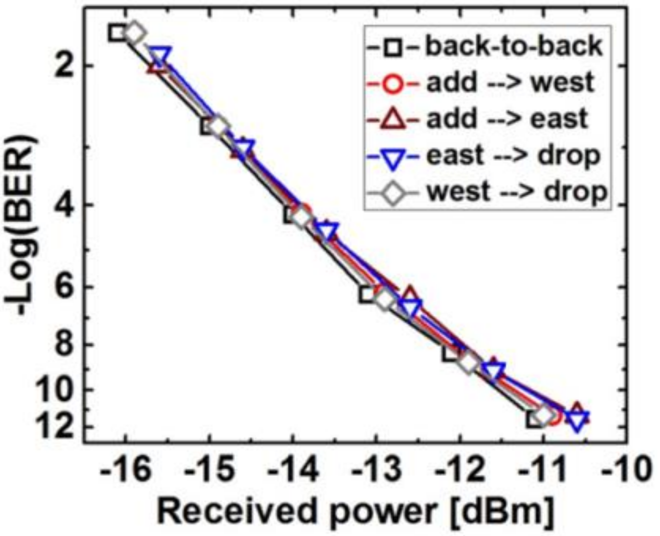

Figure 44: BER measurements of the SI Photonics ROADM

To test the device in a more realistic network environment, we used an Ericsson MHL3000 DWDM system, equipped with four 10 Gbit/s Small Form Factor Pluggable DWDM optical transceivers to generate and receive the optical channels.

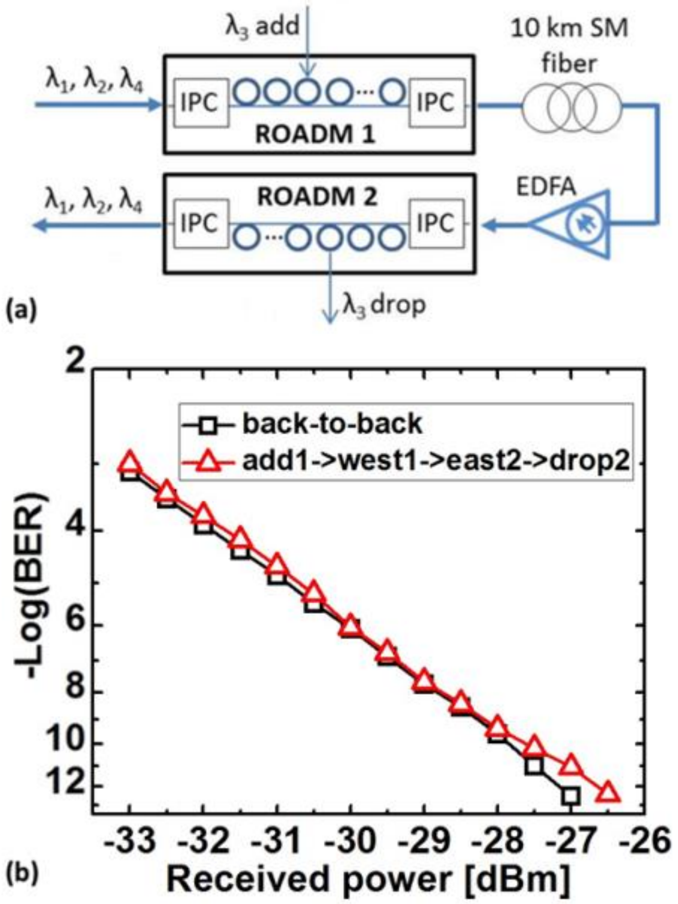

Figure 45: (a) characterization set-up. (b) BER results of the SI Photonics ROADM in a realistic network environment

The setup is shown in Figure 45(a). We used two packaged ROADMs: ROADM-1 output bus was connected to ROADM-2 input bus through a 10km fibre spool. An EDFA was used as a pre-amplifier to compensate for devices and fibre loss. Channels at wavelengths λ_1, λ_2, λ_4[7] were generated by the MHL3000 and sent to ROADM-1, where the polarization controller at the input was configured to maximize the power on the bus. Another channel, λ_3, was sent from the MHL3000 to an add port of ROADM-1 and multiplexed with the other channels on the bus. We used the integrated VOA to equalize the power of λ_3 with the other channels power. The four multiplexed signals were coupled out of ROADM-1 and reached ROADM-2 after propagating through 10km of fibre. Here λ_3 was dropped and sent back to the MHL3000. BER measurements versus received power were performed by using an external VOA connected before the receiver. We first characterized the back-to-back performance sending the channel signal through the fibre and the EDFA into the receiver. Figure 45 (b) shows the measured BER. We obtained a power penalty lower than 0.7 dB at BER=10^{-12}. **These results are encouraging towards the use of Si photonics as an affordable technology in 5G-Crosshaul networks.**

---

[7] Consecutive wavelength numbers indicate consecutive optical channels on the 200 GHz grid

3.3.4 DWDM trials in a real network settings

Within 5G-Crosshaul project, a field trial has been performed with the goal of testing a realistic DWDM system configuration with 200 Gbit/s coherent. The field trial focused on two different solutions provided by two vendors (Vendor 1 and Vendor 2), based on integrated photonic technology. Currently, coherent transmission is not a cost effective option for 5G-Crosshaul but it could become in future for large deployments based on standardized modules and multi-source agreements, making coherent multi-vendor solutions worthwhile to be investigated.

Fibre pairs starting in Torino (TILAB Optical Transmission Lab, near Torino Stampalia node exchange) and ending around 40 km far, in Chivasso (Figure 46) were dedicated to the experiment. Four Network exchange nodes are placed in between and they are based on optical interconnections performed by means of optical patch-cords and patch panels. The overall link is composed by five sections: the distance of the segments are reported in Table 9. To obtain a fibre span starting and terminating at TILAB, a fibre loop was done in Chivasso. Some 80 km spans were also used in the trial, each of them starting and terminating in TILAB.

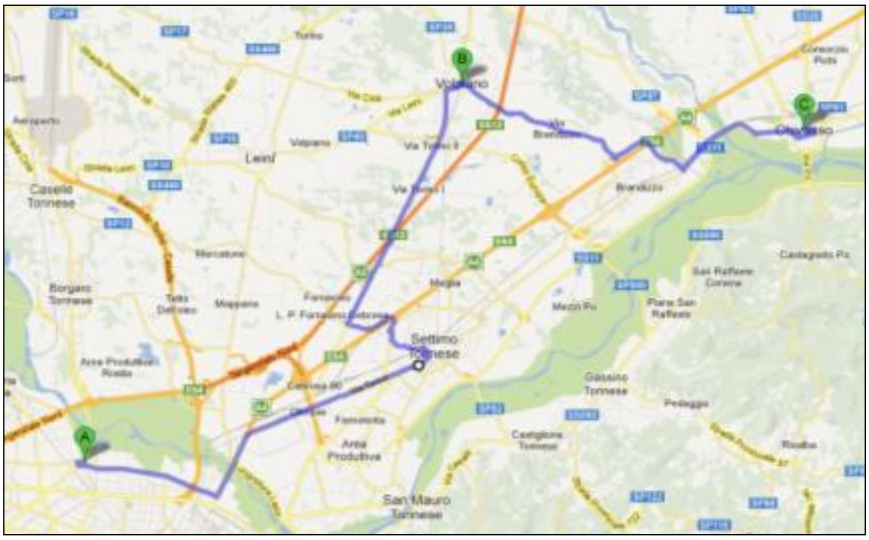

Figure 46: Geographical map with network exchange sites (Torino-Chivasso)

To concatenate the spans and realize a transmission link, dual stage line amplifiers with a configured gain ranging from 25 to 30 dB have been utilized (Figure 47). Up to seven spans have been concatenated to obtain a 560 km link. The amplifiers operate in constant output power regime and the power is configurable by software.

Table 9: Span length [km] of the different segments composing the real network trial

TORINO STAMPALIA	**TORINO STURA**	**3.996**
TORINO STURA	SETTIMO	6.75
SETTIMO	VOLPIANO	11.435
VOLPIANO	CHIVASSO	14.944
		37.125

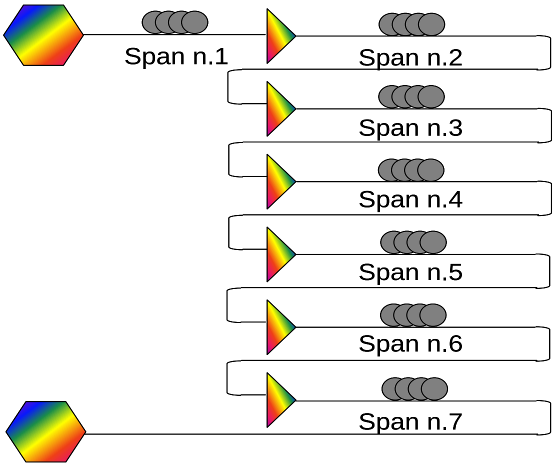

Figure 47: Transmission link set-up.

Figure 48 reports the trial results in terms of Q factor, calculated as a function of the measured pre-FEC error rate, versus OSNR (0.1 nm resolution bandwidth), for different optical frequencies, in THz. Extrapolating the curves, it is possible to estimate the minimum value of OSNR that can guarantee a Q factor of 6 dB, which corresponds to a BER equal to 2x10^{-2}, the minimum value acceptable for current soft-decision FECs.

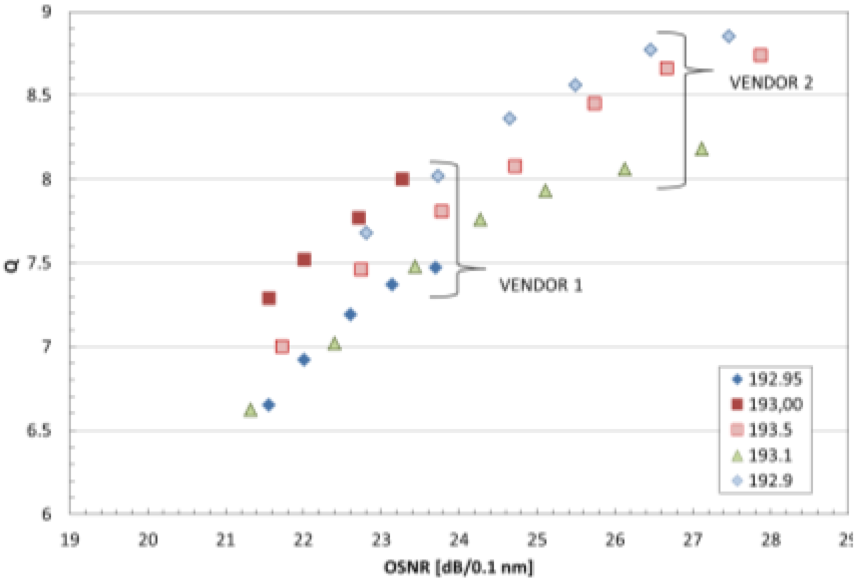

Figure 48: Q values w.r.t measured OSNR.

Figure 49 shows Q factor versus channel power with 21 dB OSNR. The optimal channel power is around 6 dBm.

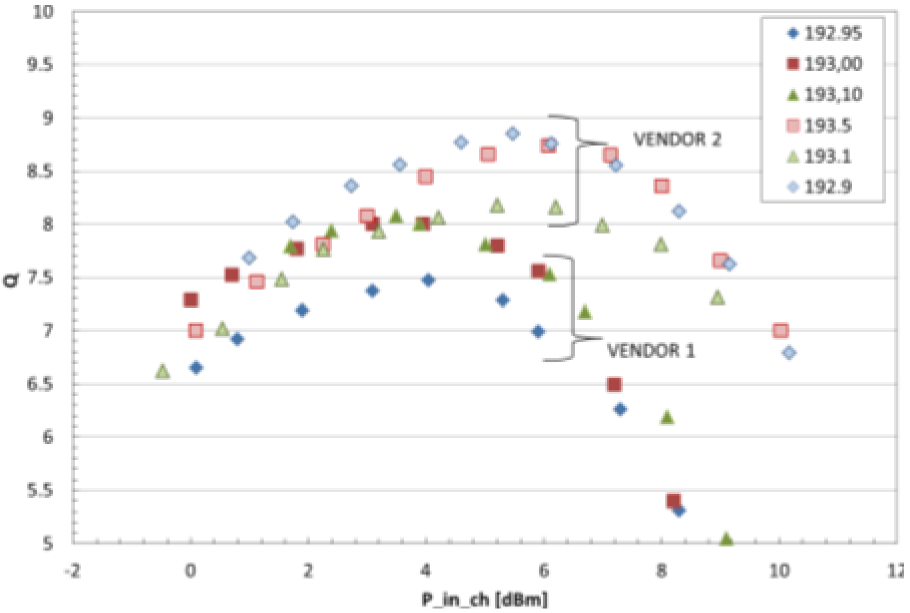

Figure 49: Q values w.r.t. launch power.

The reported results show that a common performance specification for coherent transmission solutions provided by different vendors is possible, allowing the adoption of standardized solutions suitable to be deployed in large volumes.

3.3.5 Analogue radio over fibre technologies for 5G-Crosshaul

The research community refers to Analogue RoF (A-RoF) as any type of non-NRZ modulation solution transporting mobile data over optical links. The major advantage of such solution is that it provides increased spectral efficiency, especially for multicarrier approaches such as OFDM (used for downstream LTE transmissions) and transparent transport of different radio access technologies. However, A-RoF has two potential drawbacks compared to D-RoF: it is much more susceptible to noise and it can suffer pronounced degradations due to nonlinear conversions in the link, giving rise to harmonics and intermodulation products that could affect different frequency ranges. Next subsections presents a pure A-RoF system and a hybrid A/D-RoF system developed within this project to evaluate its suitability as alternatives to deploy in 5G-Crosshaul networks.

A-RoF system

The developed analogue radio-over-fibre (A-RoF) system is composed of a head-end unit (HEU) and a remote antenna unit (RAU). The system is based on three main modules: electrical-to-optical (E/O) and optical-to-electrical (O/E) modules; multiplexer/de-multiplexer module; and radio frequency (RF) module. The system architecture of a time-division duplexing (TDD) A-RoF system for 2x2 MIMO transmission is shown in Figure 50. In downlink, the HEU converts RF signals from the two antenna ports of a base station into optical signals through the E/O module and transmits them to the RAU over a single fibre by an optical multiplexer. In the RAU, the received optical signals are converted into electrical signals and radiated through antennas after amplification in the RF module. The process is reversed for the uplink.

The A-RoF system uses a CWDM optical multiplexer module to reduce the number of fibres for transmitting multiple data streams. According to Figure 51, four wavelengths are used for uplink and downlink when the base station uses 2x2 MIMO.

Figure 52 shows a practical deployment scenario for A-RoF. A base station connects multiple RAUs to extend its coverage area and reduce the number of handovers. This is especially useful to prevent user equipment (UE) on high-speed trains from frequent handover which may degrade the throughput performance.

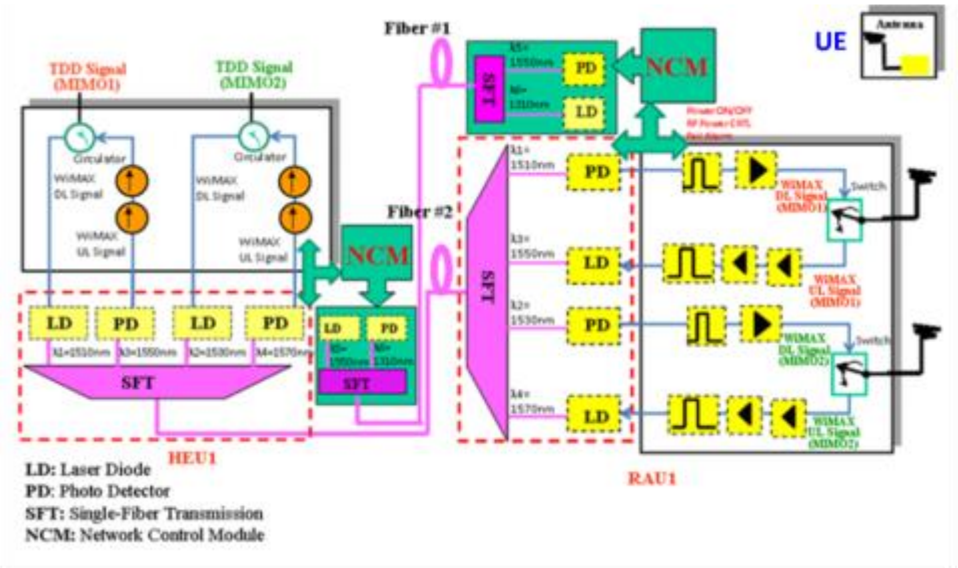

Figure 50: The system architecture of TDD A-RoF

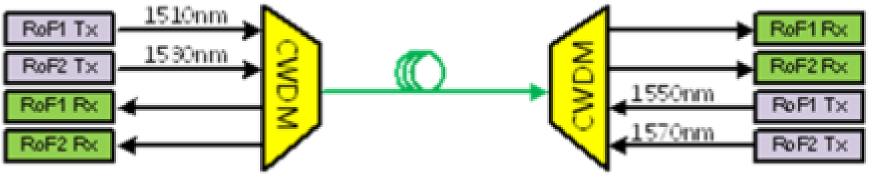

Figure 51: The architecture of CWDM modules in A-RoF for 2x2 MIMO

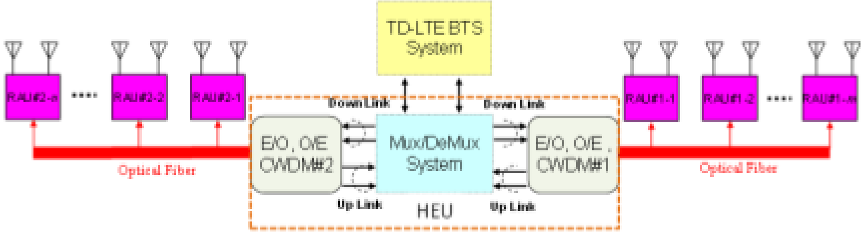

Figure 52: The practical application environment of TDD A-RoF

E/O-O/E conversion efficiency and working range

To determine efficiency and best working range of the E/O-O/E conversion circuits, a test environment was setup (see Figure 53). Different configurations of the testbed device (TBD) are defined in Table 10. The output Error Vector Magnitude (EVM) corresponding to various TBDs is shown in Figure 54 versus TBD output power.

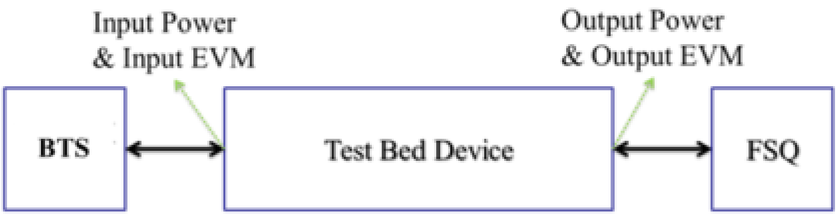

Figure 53: The test environment for O/E-E/O conversion circuits

Table 10: Definition of testbed device (TBD)

Symbol	Content	Gain (dB)
TBD-0	E/O+O/E	-18
TBD-1	TBD-0+LNA	+3
TBD-2	TBD-1 + 1x4 CWDM x2	-1.5
TBD-3	TBD-1 + 1x4 PLC Optical Splitter	-13.5
TBD-4	TBD-1 + 1x4 CWDM x2 + 1x4 Optical Splitter	-15.5

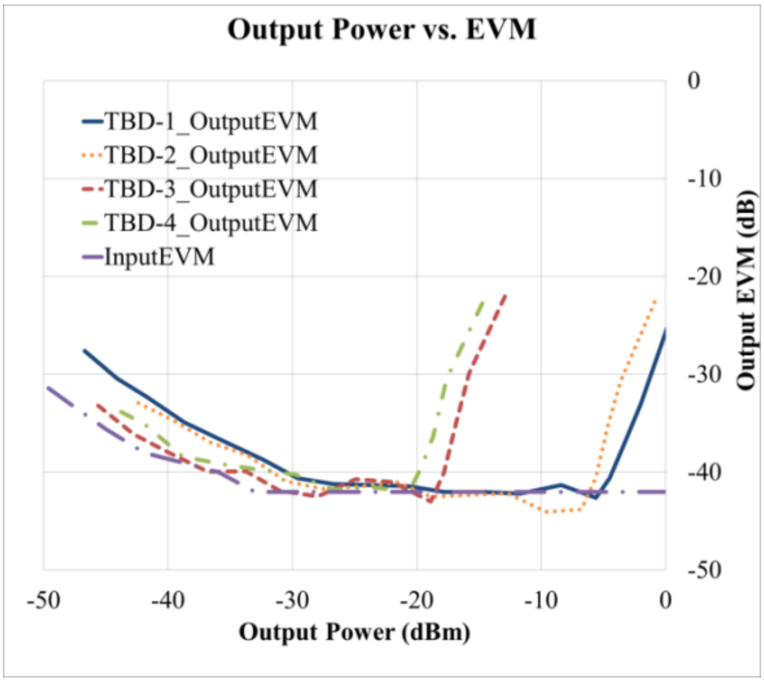

Figure 54: EVM test results

A-RoF system throughput

To measure the system throughput, TD-LTE eNB and UE are connected to the A-RoF system as shown in Figure 55. The two transceiver ports of the eNB are connected to HEU and RAU through fibre. Two PCs are connected to eNB and UE for uplink and downlink throughput measurement. The results are shown in

Table 11.

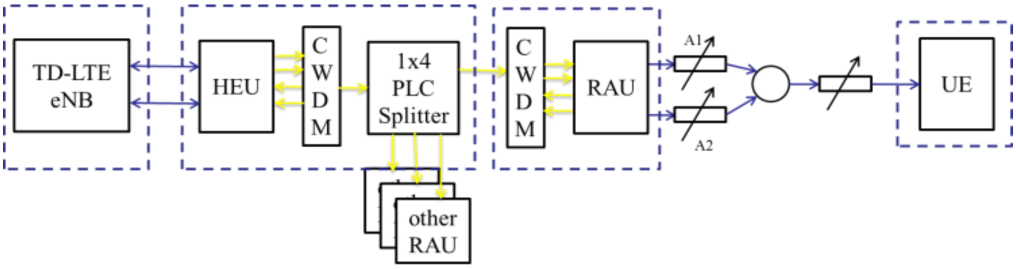

Figure 55: System configuration for throughput measurement

Table 11: Experiment results of system throughput

Downlink TCP (Mbps)	Uplink TCP (Mbps)
53.9	9.6

Hybrid A/D-RoF fronthaul

It is well known that current digital fronthaul interfaces are bandwidth inefficient, hence the need to study a hybrid analog/digital RoF solution to achieve bandwidth-efficient fronthaul transmission via frequency-division multiplexing (FDM). In this section, we evaluate a RoF solution where six 10 MHz LTE signals are transposed to low frequencies (below 125 MHz) and transmitted through a fibre link. The main advantage of this solution is that it can be seamlessly adapted to already deployed CPRI-based RRHs and BBUs. Indeed, CPRI-to-A-RoF and A-RoF-to-CPRI conversions are implemented natively in the equipment. In other words, it provides the transportation of up to 3 MIMO 2x2 CPRI signals at 2.5 Gbit/s each using less than 65 MHz bandwidth in the most spectrally efficient configuration.

Figure 56 shows the experimental setup. We use an LTE signal generator followed by a I/Q box to create a 2.5 Gbit/s CPRI signal corresponding to a 10 MHz downstream link in a 2x2 MIMO configuration. We split this signal with an optical power splitter to emulate 3 different CPRI links, which are sent to different SFPs. Each SFP is preceded by a different length of standard single mode fibre (SSMF). The transmitter converts each CPRI signal into six A-RoF bands which are later transposed to low frequencies between 100 and 240 MHz. In our 2x2 MIMO configuration, each SFP generates two 10 MHz bands, each corresponding to an antenna. This operation is only performed on the part of the CPRI frame corresponding to actual IQ samples. CPRI operation and control data are transmitted separately, at 240 MHz. The insets A and B of Figure 56 show the spectra of the signals in the D-RoF and A-RoF sections of the link. In the A-RoF section, we notice a proprietary A-RoF C&M channel at 100 MHz.

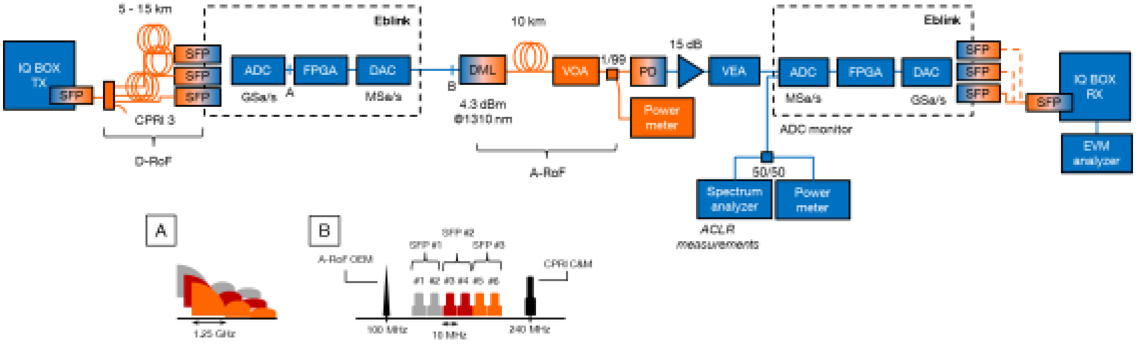

Figure 56: A-RoF experimental setup

The A-RoF signal modulates a DML, propagates through 10 km SSMF and is detected by a PIN photodiode. A variable optical attenuator (VOA) is used to set the optical budget of the link. The photodiode is followed by an electrical amplifier and a variable electrical attenuator (VEA) to optimize the power level of the signal that is the input of the receiver, where A-RoF to CPRI conversion is performed. Finally, the received CPRI signal of the three SFPs on the receiver are alternately connected to an I/Q box which converts it back to OFDM modulation and performs EVM analysis according to the LTE test model 3.1. Figure 57 shows a picture of the experimental test bench.

Figure 57: A-RoF test bench

Figure 58 shows the A-RoF spectrum after propagation. A separation of only 500 kHz can be used to separate adjacent bands, meaning that the useful data occupies a bandwidth of only 63 MHz. Despite such a small frequency gap, up to 20 dB optical budget was achieved while still respecting 3GPP EVM specifications (EVM below 8% for 64QAM) for all bands, as shown in Figure 59. The insets show average, minimum and maximum EVM per subcarrier of band #2 (centred at 140.5 MHz) as well as the received constellation with 10 dB optical budget. Measurements were done over one LTE frame (10 ms).

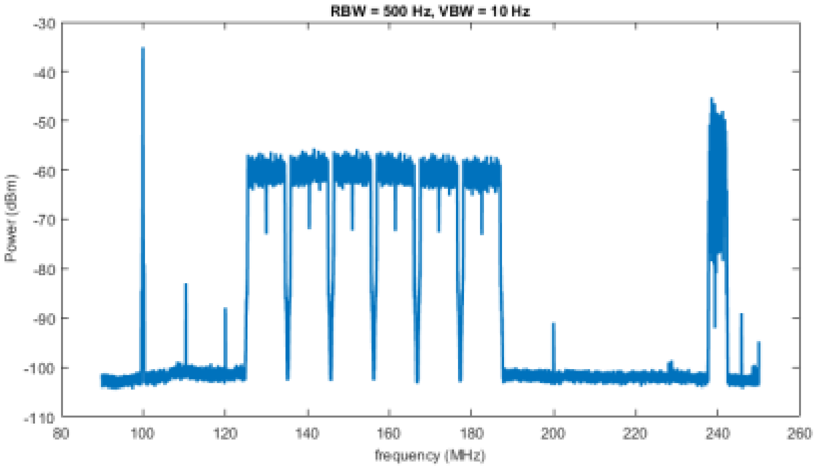

Figure 58: A-RoF spectrum

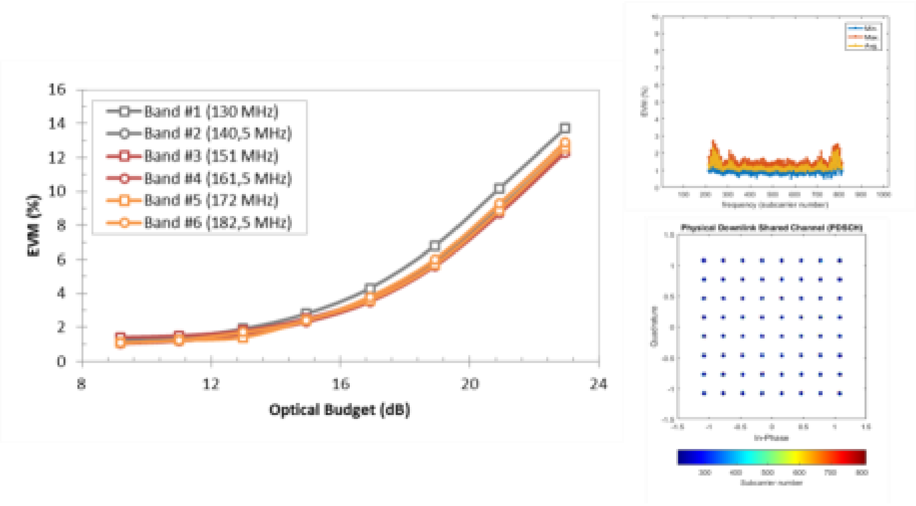

Figure 59: A-RoF EVM variation with optical budget

To increase the fronthaul bandwidth efficiency compared to CPRI, we proposed a method which separates sampled I/Q digital data from other kind of information, aggregating signals from multiple antennas (AxC) in the frequency domain. A hybrid signal composed of spectrally efficient analogue signals combined with non-I/Q M-QAM modulated data, multiplexed with the I/Q analogue signal via FDM is transmitted. This working principle was first implemented in the EBLINK FL58 Wireless Fronthaul (WFL) product which transmits up to three CPRI LR3 (3 x 2.5 Gbit/s) signals via a FDD wireless link operating in the 5.8 GHz unlicensed band.

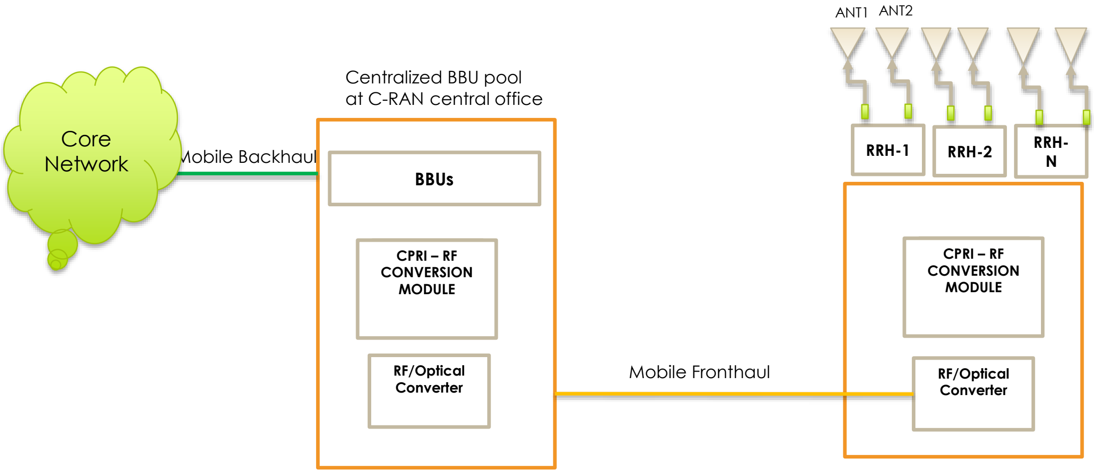

Figure 60: C-Ran architecture with A/D RoF technology

To extend the concept to optical fibre transmission, the EBLINK FL58 WFL modules have been modified. Apart from power supply and interface daughter board, FL58 CENtral and REMote modules are composed of two boards, a Digital Board and an RF board interfacing each other at IF. The new modules used for the hybrid A/D RoF tests are now mainly composed of CPRI-RF conversion modules (Digital Board) interfacing at IF frequencies (typically between 100 and 250 MHz) as illustrated in

Figure 61 and Figure 62.

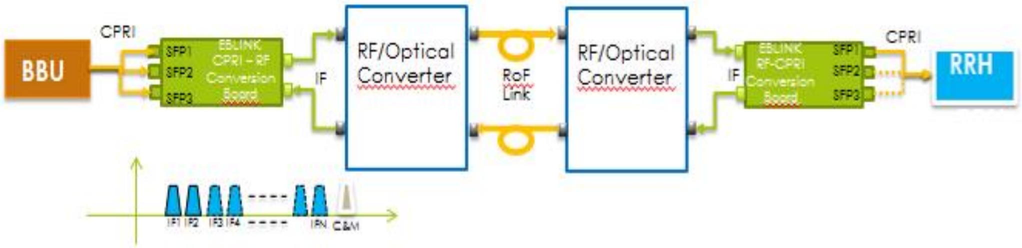

Figure 61: Hybrid Analog /Digital RoF Fronthaul Block Diagram

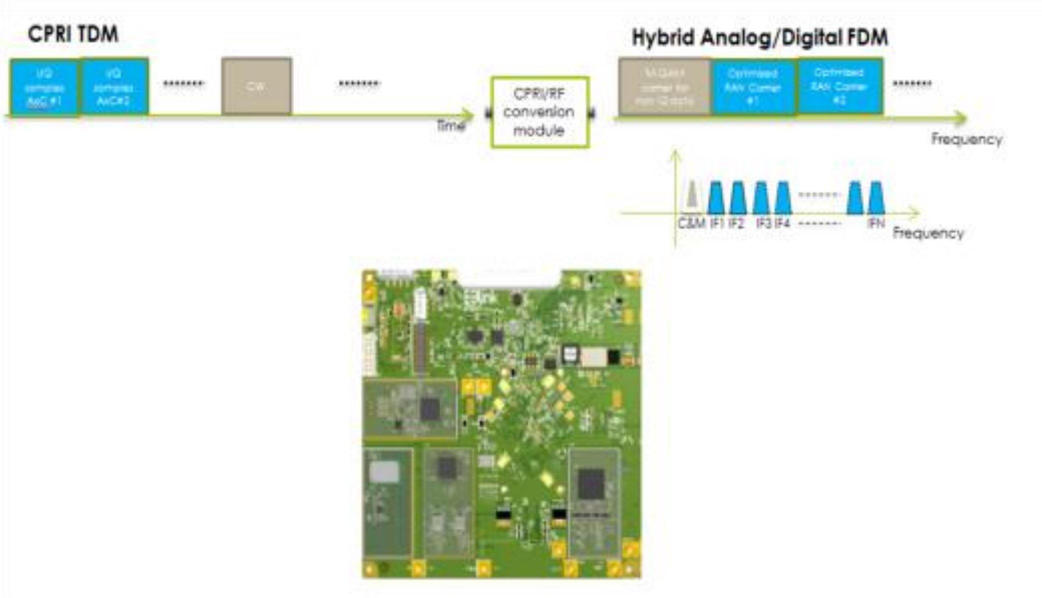

Figure 62: CPRI/RF Conversion Module

The setup to assess the downlink EVM performance from BBU to RRH is shown in Figure 63. A numerical simulation tool (Link Budget Tool) was also developed.

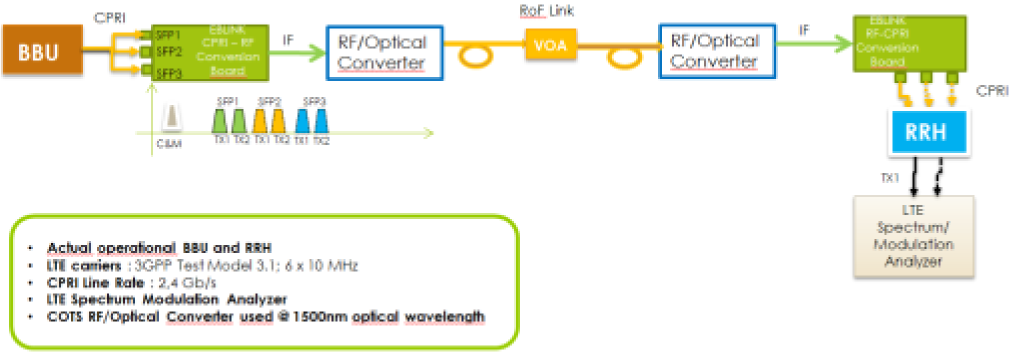

Figure 63: Experimental setup for performance evaluation

The wavelength of the RF/optical converter is 1500 nm. The BBU provides 6x10MHz LTE carriers with 3GPP TM3.1. Optical link budget and RF/Optical converter received power have been adjusted by means of a VOA in the fibre link.

The graph in Figure 64 reports downlink the EVM measured at the RRH output versus the RF/optical converter input power per I/Q carrier. As benchmark, the EVM is 1.1% with the RRH standalone.

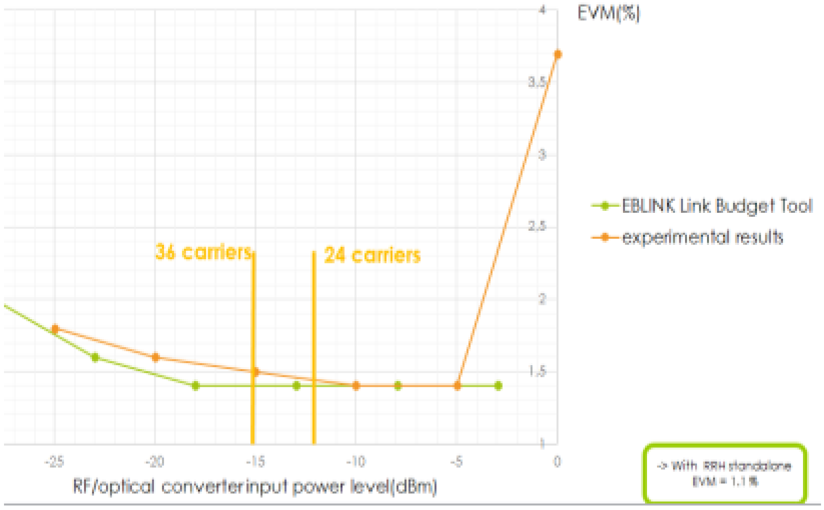

Figure 64: DL EVM at RRH output versus RF/Optical input power

The experimental results show an EVM degradation at power levels higher than - 3dBm, due to the RF/optical converter saturation. Figure 64 also reports the back-off level normalized to 6 carriers, defined as 20·Log(number of carriers/6) for 24 and 36 carriers, EVM at RRH output versus the optical link attenuation is shown in Figure 65 at -3 dBm per carrier.

With an EVM value of 3% and 6 carriers at -3dBm/carrier at the RF/Optical converter input, the achievable optical link budget is 18 dB (corresponding to 90 km of fibre with 0.2 dB/Km attenuation coefficient).

Increasing the number of carriers requires to reduce their power, not to saturate the RF/optical converter. With a maximum EVM value of 3 %, and 36 carriers at -18 dBm per carrier at RF/Optical converter input, the achieved link budget was 10.5 dB (52.5 km with 0.2 dB/km fibre attenuation coefficient). The use of an optical amplifier could increase this figure.

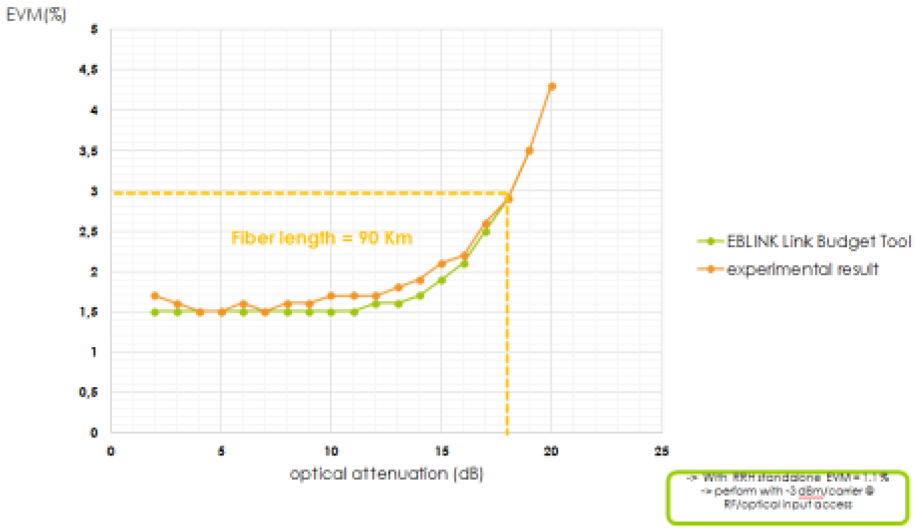

Figure 65: EVM at RRH output versus optical fibre link attenuation

The hybrid Analogue/Digital RoF fronthaul solution demonstrated here is backward-compatible with installed CPRI solutions. The experiments performed in the downlink direction show that up to 90 km and 52.5 km are achievable with 6 and 36 carriers, respectively. The next steps will be to address the uplink performances and to assess the impact of DACs and ADCs depending on the number of carriers.

4 5G Crosshaul multiplexing and switching

4.1 Introduction

As described in D2.1, the multi-layer Crosshaul node (XFE) is a multi-layer node composed by a packet and circuit layers. XFEs may include all layers or only one of them according the different requirements of the services to be supported. In D2.1 a description of each layer has been reported highlighting that the innovation part with respect the status of the art is the packet framing of the XPFE, the agnostic framing of the XCSE, and the novel optical switch based on silicon photonics that allows to reduce cost and energy consumption. In this deliverable, instead, such layers are analyzed in a network context to assess how to combine them to support all WP1 the use cases.

As shown in Figure 66 (top), most of the existing networks are based on monolithic Radio Base Station (RBS) that are P2P connected to the first aggregation node. The first level of evolution towards fronthaul is shown in Figure 66 (middle), where some radio functions have been split and centralized in the Baseband Units that are geographically separated and aggregated in pool. That radio functions will be evolved in cloud functions that will be implemented using generic processors as hardware instead of dedicated hardware. Actually, this scenario defined the creation of a network in a new segment that is moved from the traditional aggregation/metro to the antenna site.

5G Crosshaul further innovates the scenarios reported in Figure 66 (bottom) by providing the same infrastructure for backhaul and fronthaul where the end users can be devices realizing the IoT conditions. Actually, the 5G Crosshaul approach enables an agnostic transport for support any type of traffic (fronthaul, backhaul) with very tight requirements of latency and bandwidth that are specific for 5G use cases.

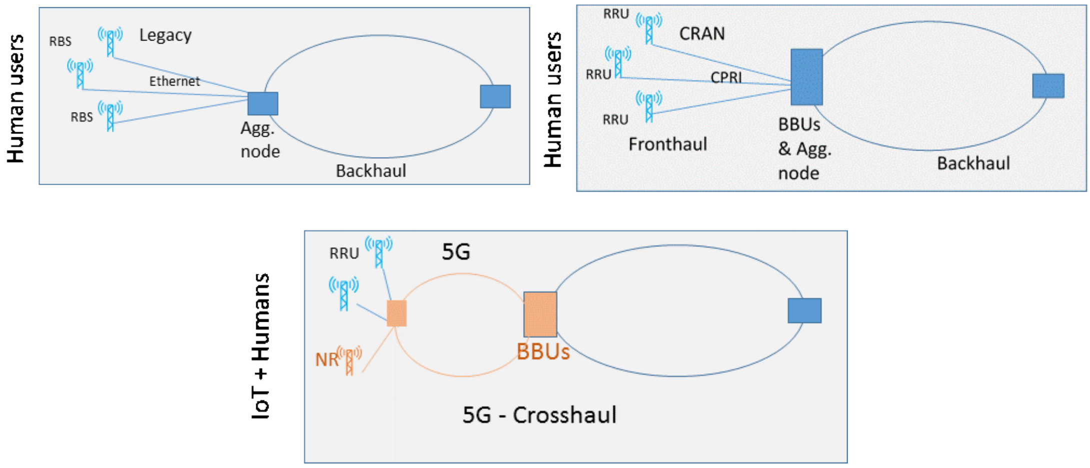

Figure 66: Evolution towards a Crosshaul scenario

In order to meet such challenging requirements, both node and network analysis is performed. In the next sections, the analysis of the packet and circuit layer is performed by means of simulations, allowing to define also how these layers can be used in a network infrastructure and how to map the several services on them.

4.2 Packet-based multiplexing and switching

Packet-based multiplexing makes sense especially when the data rate is load dependent since this enables statistical multiplexing gain. Such load dependency is inherent for backhaul. However, this is not the case for fronthaul traffic. Even with constant bit rate fronthaul, there may be benefits from multiplexing it together with backhaul on a packet-based technology since it can allow cost-sharing, unified management and better utilization of link capacity.

This section presents a study whose goal is to analyse the queueing delay at an XFE fed with both packetised fronthaul and backhaul traffic in different 5G-Crosshaul scenarios, namely where both BH and FH traffic are mixed together at the packet level. Essentially, this analysis is interested in: (1) studying different traffic prioritisation policies and queue management; (2) provide delay bounds for fronthaul and backhaul traffic; (3) provide a simple model that helps in dimensioning the links conforming the Crosshaul network, where both fronthaul and backhaul traffic is mixed.

4.2.1 Assumptions and theoretical background

Let us assume a packet switch with multiple input ports competing for a single service unit at the output port. Fronthaul traffic is assumed to be packetised and marked as high-priority traffic. We further assume two separate queues: one for fronthaul (FH) and another one for backhaul (BH) traffic, as shown in Figure 67. We further assume a non-pre-emptive policy and strict priority to the FH queue. In other words, when the server completes the service time of a packet, the FH queue is checked first no matter how long the BH queue has been waiting for service.

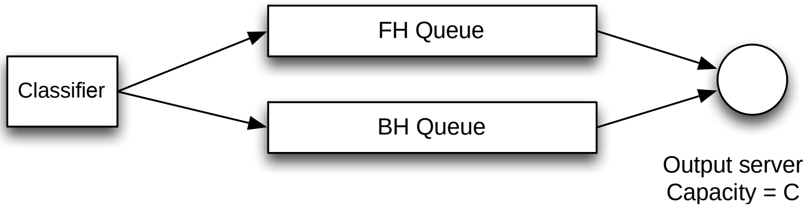

Figure 67: Packet switch model under analysis

Following the classical analysis of M/G/1 queues with priorities [87][88], the average waiting time in queue for packets with two different priorities follow:

$$E\left(W_q^{FH}\right) = \frac{E(R)}{1-\rho_{FH}} \qquad \text{and} \qquad E\left(W_q^{BH}\right) = \frac{E(R)}{(1-\rho_{FH})(1-\rho_{FH}-\rho_{BH})}$$

where E(R) is the average residual life of a packet at the server at the arrival time of a packet of either fronthaul or backhaul type:

$$E(R) = \frac{1}{2}\left(\lambda_{FH}E(X_{FH}^2) + \lambda_{BH}E(X_{BH}^2)\right)$$

where λ_{FH} and $E(X_{FH}^2)$ refer to the fronthaul packet arrival rate and second moment of the packet service time respectively; and λ_{BH} and $E(X_{BH}^2)$ have the same meaning for the backhaul traffic. Similarly:

$$\rho_{FH} = \lambda_{FH}E(X_{FH}) \qquad \text{and} \qquad \rho_{BH} = \lambda_{BH}E(X_{BH})$$

refer to the fronthaul and backhaul load values respectively, where $\rho_{FH}+\rho_{BH}<1$ for the stability of the queue.

A numerical example of the analysis is presented next to provide a context for the experimentation section. Consider a packet switch with multiple input ports and a single output port operating at 100 Gb/s. Both fronthaul and backhaul traffic is offered at the output port which has two separate queues: a high-priority one for fronthaul traffic and a low-priority one for backhaul traffic. We assume that the total offered traffic is 0.4 (i.e. 40%) and that one quarter of it belongs to FH while the rest belongs to BH traffic. We further assume that BH packets follow the Internet's empirically observed trimodal MIX distribution, i.e. a 40-Byte packets in a proportion of 7 out of 12, 576-Byte packet in a proportion of 4 out of 12 and 1500-Byte packets in a proportion of 1 out of 12[8]. Fronthaul packets are assumed to be fixed of 40-Byte packets (i.e. 320-bit packets), each one containing the IQ samples and control word of one CPRI option 2 traffic flow.

First of all, the first and second moments of FH and BH traffic are:

$$E(X_{FH}) = 5.12\,ns \qquad \text{and} \qquad E(X_{FH}^2) = 26.21\,ns^2$$

$$E(X_{BH}) = 27.23\,ns \qquad \text{and} \qquad E(X_{BH}^2) = 1913.762\,ns^2$$

With these values, we compute the packet arrival rate for each type of traffic:

$$\lambda_{FH} = \frac{0.4\,x\,0.25}{5.12\,ns} = 0.195\,Mpacket/s \quad \text{and} \qquad \lambda_{BH} = \frac{0.4\,x\,0.75}{27.23\,ns} = 11.02\,Mpacket/s$$

and the average residual life of a packet in the server at the arrival time is:

$$E(R) = 10.8\,ns$$

Finally, the average waiting time in queue for fronthaul and backhaul packets are:

$$E\left(W_q^{FH}\right) = 12\,ns \qquad \text{and} \qquad E\left(W_q^{BH}\right) = 20\,ns$$

4.2.2 XPFE analysis and simulations for queueing delays

Following the methodology above, the experiments show average waiting time in queue of both FH and BH packets in different scenarios.

Experiment 1 - Different bit rates: This experiment considers a fixed portion of BH and FH traffic (50% each) and shows the average waiting time in queue for FH and BH traffic assuming a packet switch whose output port operates at 10, 40 and 100 Gb/s respectively. As shown, FH delays are always kept below BH, especially as the total load increases.

---

[8] Internet MIX, https://en.wikipedia.org/wiki/Internet_Mix

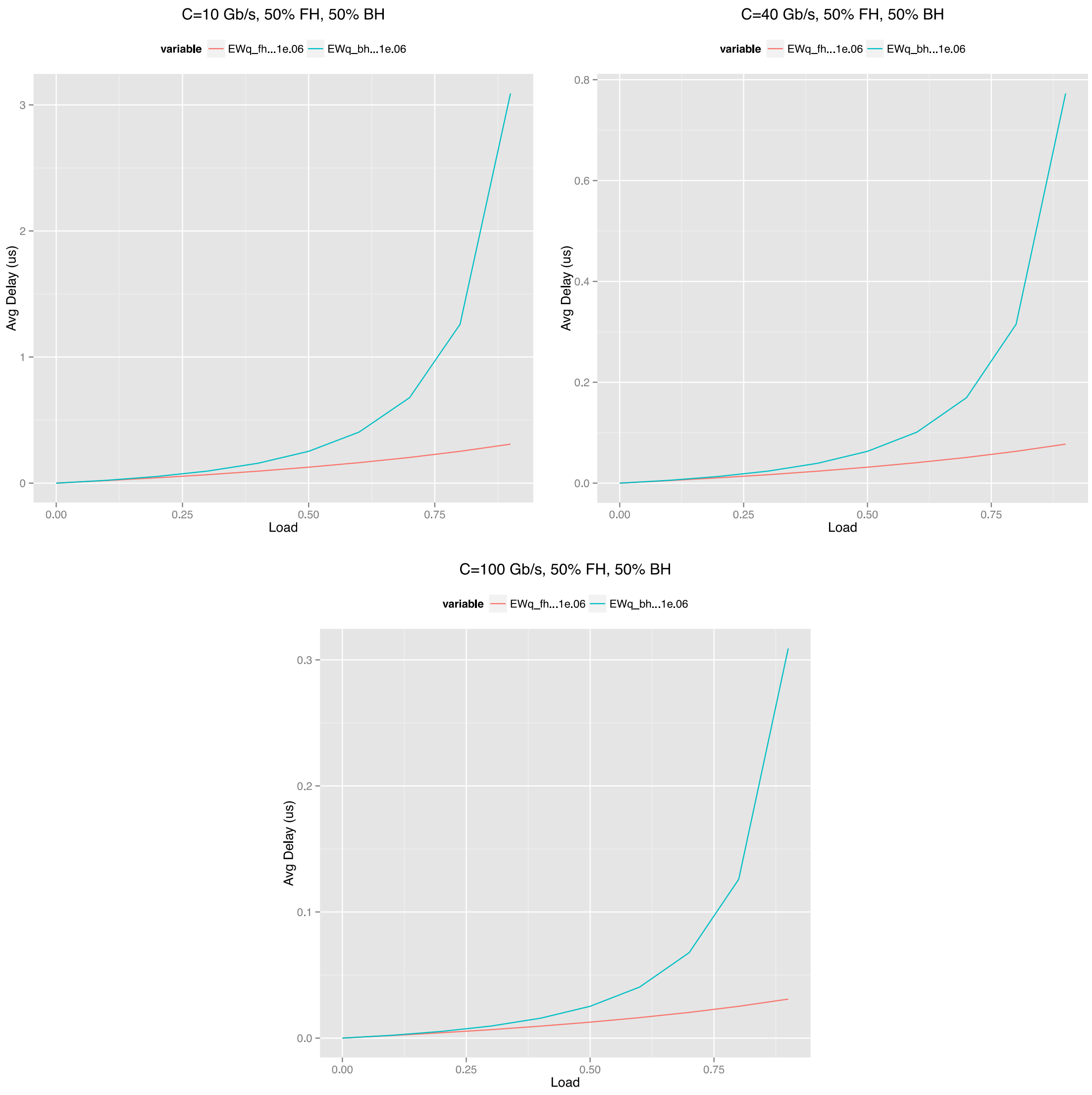

Figure 68: Average delay on different transmission speeds (10, 40 and 100 Gb/s): Same behaviour with different absolute values

Experiment 2 - Different FH/BH ratios: In this experiment, the output port operates at 100 Gb/s fixed, but three combinations of percentages (%) of FH-BH traffic ratio are considered: 25%-75%, 50%-50% and 75%-25% respectively. The purpose of this selection is to represent 3 cases with (i) mainly BH traffic, (ii) equal share, and (iii) mainly FH traffic. As observed, there is not a big impact regarding this issue.

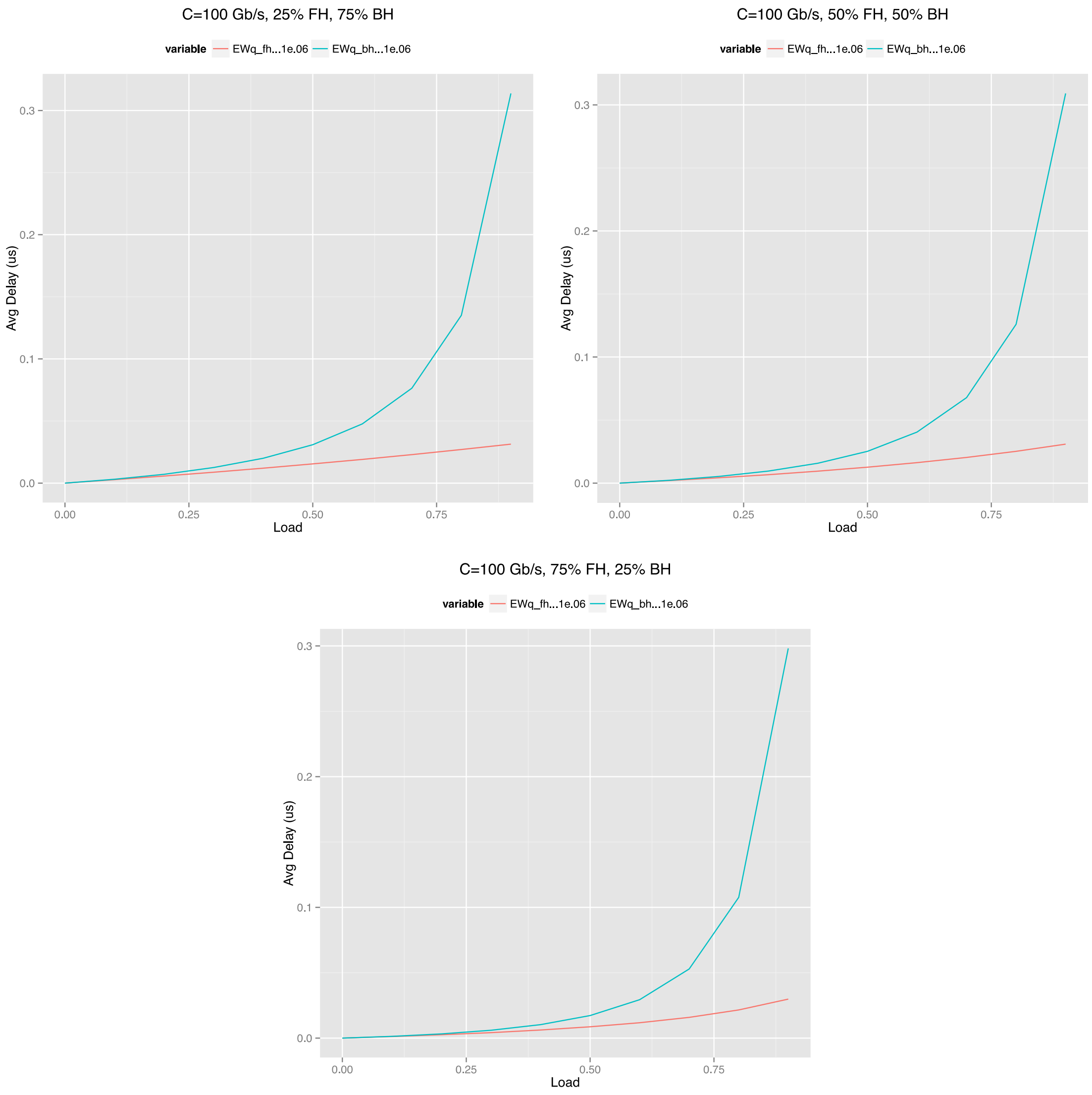

Figure 69: Average delay under different percentages of FH-BH traffic ratio

Experiment 3 - Different CPRI options: This experiment considers a variable portion of FH and BH traffic modulated by w_FH (percentage of FH traffic over the total) and a fixed output capacity of 40 Gb/s. Two different CPRI options are used (i.e. different FH packet sizes), namely: option 1 (20 Bytes per Basic Frame) and option 7 (320 Bytes per Basic Frame). As shown, the difference in average delay is larger when the percentage of FH traffic is small. However, when the average BF size approaches the average size of BH traffic (i.e. 340.3 Bytes), such difference in delay maintains for different percentages of FH-BH traffic.

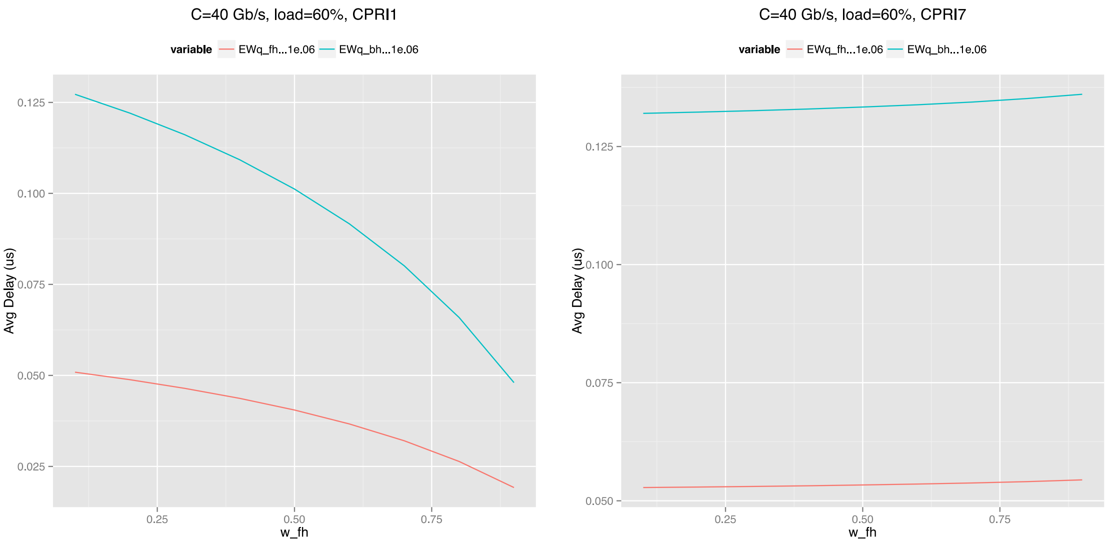

Figure 70: Average delay in different CPRI options, i.e. different Basic Frame size

Experiment 4 - Different BF aggregation schemes: In this experiment, we aggregate several BF in one single Ethernet packet, making it more efficient as the number of BF per packet increases (overhead is 46 bytes, namely 21 of Provider Backbone Bridges (PBB, or MAC-in-MAC) plus 16 of Customer MAC plus 4 bytes of RoE header plus 4 bytes of Checksum). As shown below, the more BFs in the same packet, the more efficiency per packet because the overhead is reduced.

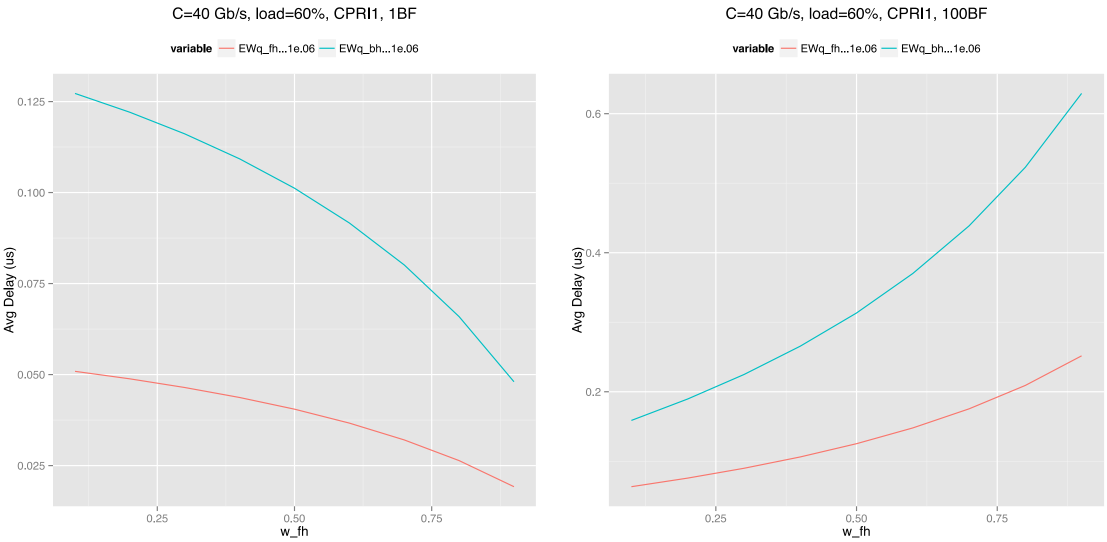

Figure 71: Average delay assuming different BF aggregation schemes

According to the previous experiments, we observe that the average queueing delays for both fronthaul and backhaul traffic is in the range of tens of nanoseconds when operating at 100 Gbit/s, and several hundreds of nanoseconds when operating at 40 Gbit/s and 10 Gbit/s. The following table below summarizes these numbers for an M/G/1 queue fed with 50% fronthaul and 50% backhaul traffic, using strict priority (without preemption) to favor fronthaul traffic:

Table 12: Average delays for the M/G/1 with Strict Priority at 100 Gb/s

	Load = 25%	Load = 50%	Load = 75%
25% FH / 75% BH	18 / 25 ns	40 / 79 ns	64 / 255 ns
50% FH / 50% BH	14 / 19 ns	33 / 66 ns	60 / 241 ns
75% FH / 25% BH	9 / 4 ns	25 / 50 ns	53 / 215 ns
100% FH / 0% BH	4 / - ns	12 / - ns	37 / -

The values of the table above assume that FH packets are of 126 Bytes fixed size (i.e. 80B for basic frames of CPRI option 3 plus 46B of header), while BH traffic follows the IMIX trimodal distribution. As shown, even at high-loads, queueing delays for FH and BH packets never reach 100 ns and 300 ns respectively, showing that, in theory, average queueing delays are always below 1 us. Regarding worst-case delays (i.e. 90-th, 95-th and 99-th percentiles), we observe the following queueing delay values for the 75%-load 50/50 FH/BH case:

Table 13: Worst-case delays: 90th, 95th and 99th percentiles at 100 Gb/s

	FH	BH
90th-percentile	172 ns	690 ns
95th percentile	239 ns	938 ns
99th percentile	294 ns	1515 ns

In this scenario, we show the five-number summary (minimum, first, second and third quartiles, maximum) along with the mean delay:

Table 14: Five-number summary of delays

FH traffic (delay in ns)	**Min.**	**Q1**	**Median**	**Mean**	**Q3**	**Max**
	0	1.5	33	61	92	363
BH traffic (delay in ns)	Min.	1st Qu.	Median	Mean	3rd Qu.	Max
	0	2.6	108	252	355	2181

According to the ITU-T Rec. Y.1540, Packet Delay Variation (PDV) is the difference in the end-to-end one-way delay between packets. In this light, the latency of the i-th packet is computed as:

$$\text{Latency}[i] = \text{ArrivalTime\_atDestination}[i] - \text{DepartureTime\_atSource}[i]$$

and gives the absolute one-way delay, including all serialization, queueing, processing and propagation components of the delay. The PDV is obtained from the individual Latency values as:

$$\text{PDV} = \max(\text{Latency}[i+1] - \text{Latency}[i]), \quad i=1,2,\ldots$$

To get a notion on the jitter for both traffic classes, we proceed by substracting maximum delay minus minimum delay. We also compare with the interquartile range (IQR), i.e. Q3-Q1:

Table 15: Inter-Quartile Ranges (IQR) and Packet Delay Variation (PDV) for FH and BH traffic

FH traffic (delay in ns)	**IQR**	**PDV**
	90	300
BH traffic	IQR	PDV

(delay in ns)	352	920

Finally, the Empirical CDFs obtained from simulation for both BH and FH traffic are depicted in Figure 72 below.

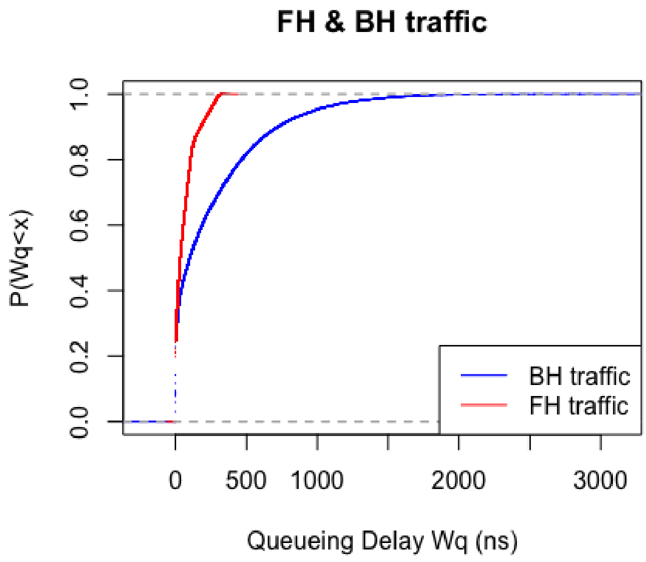

Figure 72: Empirical CDF for waiting time in queue delays

Finally, we repeat the above experiments for the case of FH flows traversing multiple XPFEs in a feedforward queueing network, as shown in Figure 73. At each XPFE, FH packets compete with BH packets for the output port, again following a Strict Priority queueing discipline.

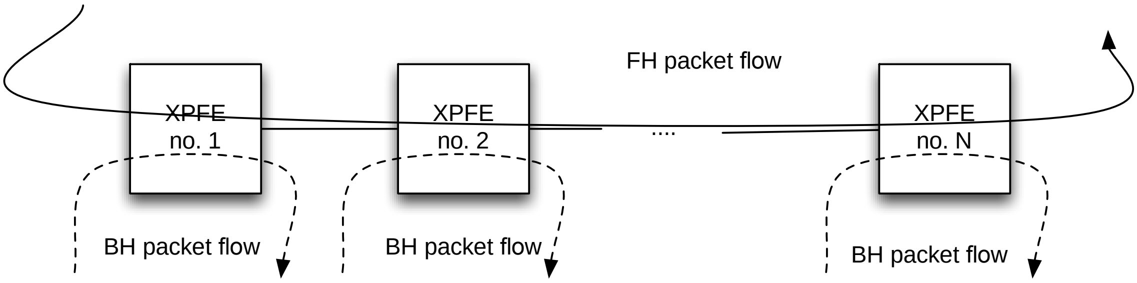

Figure 73: Experiment traversing N nodes. Scenario configuration: 75%-load 50/50 FH/BH, switches operating at 40 Gbit/s

Table 16 shows the delay summaries for a sequence of two XPFEs, and five XPFEs.

Table 16: Delay summaries for 2 and 5 consecutive XPFEs

FH traffic 2 XPFEs	Min.	1st Qu.	Median	Mean	3rd Qu.	Max	IQR	PDV
(delay in ns)	0	31	91	116	175	593	144	518
FH traffic 5 XPFEs (delay in ns)	Min.	1st Qu.	Median	Mean	3rd Qu.	Max	IQR	PDV
	0	161	268	285	386	1178	225	878

In conclusion, although the average queueing delay for FH traffic at 40 Gb/s may be of only a few hundred nanosecs, delay variability as measured by the PDV and IQR, may reach about 10x this quantity, especially after traversing multiple hops, even in a scenario where FH/BH traffic differentiation is implemented with full strict priority for FH traffic.

4.3 Circuit based multiplexing and switching

4.3.1 XCSE theoretical analysis and simulations

In this chapter the analysis of circuit layer is performed. As shown in Figure 74, the XCSE is composed by an agnostic framing, a TDM based switching and an optical switch, then a DWDM transmission allows to provide logical point-to-point connectivity between RRU and corresponding BBU.

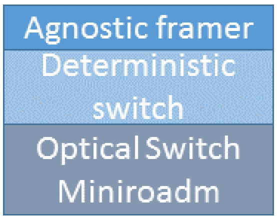

Figure 74: XCSE building blocks

In Figure 75, a network architecture is proposed where a XCSE is located towards the RRUs clusters and another XCSE is located at geographical distance with respect the RRUs cluster to host the pooling of Baseband Unit equipment.

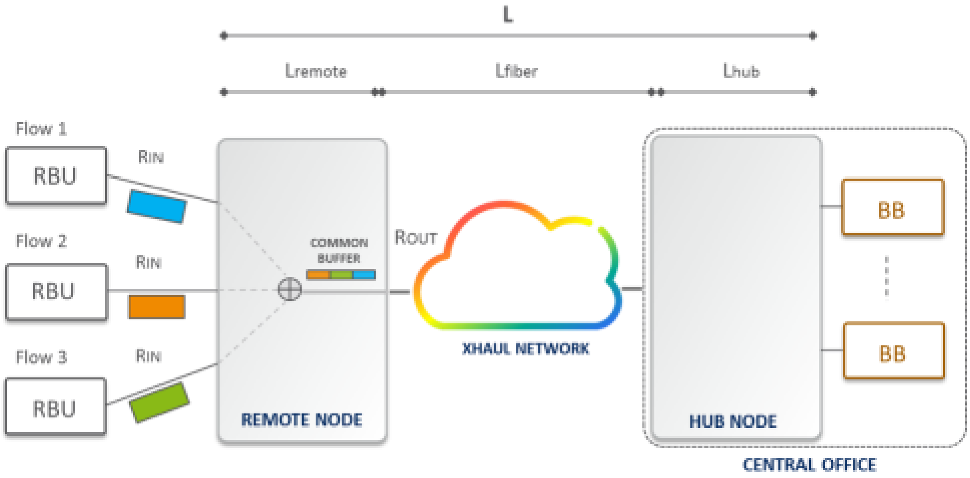

Figure 75: XCSE-based network architecture

Radio interfaces (such as CPRI and its evolution) consume high transport bandwidth and they also require a strict latency control. In the uplink direction RBUs (Radio Baseband Units) latency-critical traffic is collected on a common buffer at the remote node and after fast processing, transmitted through the optical network to the Hub Node. Baseband processing units

(BBs) in pool are used to process the radio traffic. In the downlink direction radio traffic processed by the BBs is buffered and processed at the Hub Node and then sent to the RBUs to be distributed among the different antennas.

Overall latency budget is split in three parts: L_{remote}, L_{hub}, due to the buffering and fast processing in the remote node and in the hub, respectively, and L_{fiber}, for fiber transmission. L_{fiber} is directly related to the distance between remote node and hub node.

A "circuit like" radio interface, such as CPRI, has a constant bit-rate which does not depend on the radio traffic. In a packet-based interface, some radio functions previously carried out by baseband processing units, are now carried out by RBUs (e.g. the FFT/IFFT functions to generate I/Q symbols to be transmitted over the air). Performing some radio functions at the RRUs dramatically reduces the transport bandwidth at the price of making more complex the correlation between radio signals from different antennas.

The increase in the complexity is managed by processing algorithms more advanced and efficient, but a small and controlled latency with which the radio flows are transmitted remains paramount in order to ensure a satisfactory use of radio spectrum and to provide adequate capacity to the radio access network. The bit rate of the new packet-based radio interfaces changes depending on the radio traffic. A detailed radio traffic modeling is not available, but the system has been developed according to the following practical hypothesis:

1. Assuming a time slotted system to collect and delivery traffic, the traffic flows from different radio interfaces afferent to a common remote node cannot overcome remote node output traffic (R_{OUT}) for more than one transmission slot. If concurrent traffic peaks from different NR flows, they are "absorbed" by following slots
2. A peak always occurs when the buffer is empty: former peaks have been "absorbed". If the buffer is not empty when a peak occurs, then its content is discarded (load condition) and data loss is managed by upper radio layers
3. New radio interfaces (NR) are not organized in different QoS: XHaul transport manages all the NR flows from different antennas in the same way.
4. Radio QoS are managed by upper layers
5. Very small label (Tag) for each NR flow is used according to the ingress port on the framer in ingress RN. (Layer 1.5).
6. Tag processing can be assumed negligible compared with other source of latency (e.g. buffering and distance)
7. Ethernet (or any other traffic sources) flows can be combined with NR flows, but NR flows are managed with higher priority over Ethernet flows
8. Ethernet starving is avoided by remote node output traffic (R_{OUT}) over-provisioning.

Model description

In the following we will refer to the uplink direction (from the RRUs to the BBUs) but the extension to the downlink direction is straight-forward. The here-presented model is based on a time slotted system with a common buffer for all the flows afferent to the remote node. The buffer is not filled entirely but in relation to the latency budget that it is possible to spend at the remote node.

Remark the three latency contributions to the overall latency budget dedicated to the transport (L): L_{remote}, L_{hub} and L_{fiber}. Maximum buffer (B_{MAX}) compatible with acceptable latency in the remote node (Lremote) is shown in eq.1

$$B_{MAX} = L_{remote} * N * R_{IN} \tag{1}$$

where Lremote is the latency budget available at the remote node for buffering, N and R_{IN} are the number of flows afferent to the remote node and their rate respectively.

Due to the radio nature of the latency sensitive flows to the remote node, it is convenient to define a time slot equal to one TTI (Transmission Time Interval). The TTI is related to the size of the data blocks passed from the higher network layers to the radio link layer. Having a transport network which is tuned to the TTI is useful also for the following needed assumptions about the radio traffic:

- Aggregated traffic from radio flows cannot overcome R_{OUT} for more than one transmission slot
- A peak always occurs when the buffer is empty: if not, buffer content is discarded and the data loss is managed by upper radio layers

The former assumption states that the radio traffic peaks are sporadic enough to avoid that consecutives peaks overload the transmission buffer. This condition is consistent with the common practice that three sectors of a single radio site can be backhauled with a bandwidth equal to the peak of one sector. The latter assumption states that in the very rare condition a peak occurs when the buffer is not empty and it is acceptable to have a data loss. Data loss condition is rare enough to be well managed by the upper radio layers.

In the time of one TTI, the instantaneous buffer size (B) follows:

$$B = (N * R_{IN} - R_{OUT}) * TTI$$

where R_{OUT} is the rate of the aggregated flow to be sent on the Crosshaul network. Assuming an identical latency contribution for buffering at the remote node and at the hub node, the overall transport latency L is described by:

$$L = 2L_{remote} + DF_D$$

where DF_D is the latency contribution due to fiber transmission, in which D is the fiber distance between remote node and hub and F_D is the fiber delay due to the speed of light in fiber (approx. $2*10^8$ m/s): F_D has a fixed value of 5 us/km.

To stay within the latency budget allocated to the remote node, B is always less or equal than BMAX and then it is possible to obtain the following equation:

$$R_{OUT} \geq R_{OUT}^{MIN} = NR_{IN} * \frac{(2\,TTI - L) + DF_D}{2\,TTI},$$
$$with\ D \leq \frac{L}{F_D}\ and\ L - DF_D < 2TTI$$

It is useful to define a bandwidth compression factor (BCF) defined as:

$$BCF = \frac{(2\,TTI - L) + DF_D}{2\,TTI}, \quad 0 < BCF \leq 1$$

BCF gives a measure of how it is possible reduce the aggregated bandwidth (R_{OUT}) to carry the NR_{IN} flows. R_{OUT} can be reduced with deeper buffers, which means higher latency budget to be spent at the remote node and then, if the overall transport latency L is fixed, a shorter distance between remote node and hub.

BCF is bounded by two boundary conditions:

- **No Buffer (NB) Condition**: this happens when fiber distance consumes all the latency budget available for transport and buffering at the remote node (or at the hub node) is not possible.
- **Huge Buffer (HB) Condition**: this happens when latency budget at the remote node reaches one TTI and the buffer is enough deeper to absorbs all the peaks, regardless of the aggregated output bandwidth (R_{OUT}), which can be arbitrarily small.

No Buffer (NB) condition

If the physical distance consumes all the latency budget allocated for transport, it is not possible to buffer any traffic: latency budget for the remote node (L_{remote}) is zero.

The distance between the remote node and the hub reaches a maximum value:

$$D = D_{MAX}, \qquad where\ D_{MAX} \triangleq L/F_D.$$

As the distance reaches D_{MAX}, bandwidth compression factor (BCF) goes to 1 because to avoid data loss R_{OUT} must be chosen as N*RIN. In this condition there is no benefit, in terms of bandwidth, in aggregating the radio flows

Huge Buffer (HB) Condition

In the huge buffer condition, for any chosen distance D, latency at the remote node (L_{remote}) reaches 1 TTI and the buffer is enough large to absorb peaks even if output rate (R_{OUT}) is almost zero.

$$L_{remote} = \frac{L - DF_D}{2} = TTI$$

Huge Buffer condition is a boundary condition, as it supports arbitrarily small values for R_{OUT}.

Under normal conditions, the aggregated output rate R_{OUT} can be arbitrarily small only if the radio traffic is very low or frequent data losses, due to the forced emptying of the buffer, are acceptable.

To avoid arbitrarily small value for the aggregated rate, a lower bound for R_{OUT} needs to be introduced: ρ_{OUT}

ρ_{OUT} can be decided in advance and it corresponds to the minimum aggregated output rate. It depends on the load of the radio cells served by the remote node and on the acceptable data loss imposed by the Crosshaul transport. Aggregated output rate definition is extended by the next equation, which now includes the ρ_{OUT} parameter.

$$R_{OUT} = MAX\left\{NR_{IN} * \frac{(2*TTI-L)+D*F_D}{2*TTI};\ \rho_{OUT}\right\}$$

$$with\ DF_D \le L < DF_D + 2\left(1-\frac{\rho_{OUT}}{NR_{IN}}\right)TTI$$

If the system is working close to the NB condition, most of the latency budget is consumed by the fiber transmission (R_{OUT} greater than ρ_{OUT}). As soon as the latency buffer available at the remote node approaches one TTI, and the bandwidth compression factor (BCF) comes down, the aggregated output rate reaches ρ_{OUT}.

The equation for R_{OUT} above also includes the boundary conditions for the transport latency, which depend on the physical distance, on the number and rate of the afferent flows, on the minimum aggregated rate ρ_{OUT} and on the radio TTI.

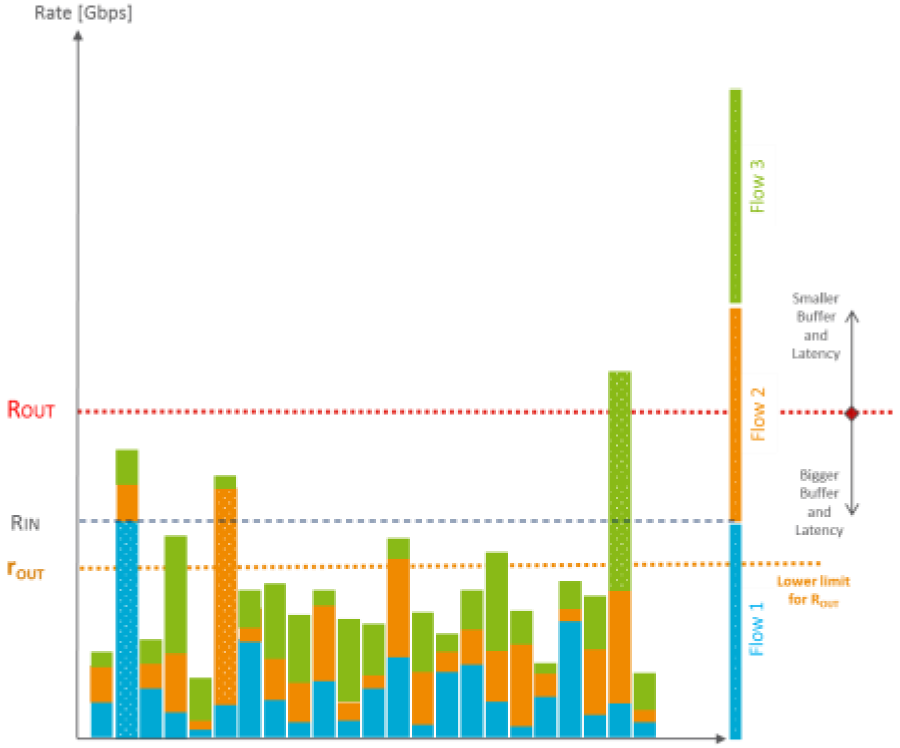

Figure 76: Illustration of R_{IN} and R_{OUT} for three flows

In Figure 76, the case of 3 afferent flows to the remote node is shown. The value of R_{OUT} increases if the distance consumes most of the latency budget available for the transport, up to the boundary NB condition. R_{OUT} can be reduced up to ρ_{OUT}, if there is enough latency budget at the remote node to use a deeper buffer.

Simulation Results

The system presented can be applied to radio flows transport over a geographical network, leveraging the benefits from radio processing centralization and from network convergence. Network convergence is guaranteed by the possibility to combine different kind of traffic (e.g. radio flows with Ethernet).

The case of three radio flows afferent to a common remote node has been considered: one radio flow per sector. Chosen radio access rates are compatible with 5G rates, with 10 Gbit/s peaks rates per sector. Two TTI values have been taken into account: 125us and 250us. A transport overhead of 13% has been applied to any radio flow, independently on the radio split option. It is compatible with light FEC and tagging used to send the traffic to the right destination ports.

Three different “packet oriented” radio split options have been considered for the radio flows, following 3GPP guidelines [2]:

- Option 1, with RRC/PDCP radio functional split
- Option 7A with intra-phy radio functional split
- Low rates flows
- High rates flows

Option 1 is similar to a traditional backhauling, as all the L1 functions are implemented near the antennas (RBU). In this option the rate from each sector is roughly the same of the radio peak (10Gbit/s/sector).

Option 7A is characterized by some physical layer functions still managed by the BBs, but with I/Q symbols generation entirely managed by the RBUs. The differences between the “low rates” and “high rates” is due to the control signals needed to manage the correlation between all the radio flows.

Once again the reference peak rate offered over the air is 10Gbit/s/sector, but the flow rates are significantly higher: 25.2/55.3Gbit/s per sector and 55.5/75.9Gbit/s per sector for DL and UL.

A value of 100us for latency budget assigned to the transport, and which include the transmission delay due to the distance between hub and remote node, has been considered. It is compatible with current ITU-T recommendations for the transport of radio flows.

A transport latency of 100us sets a maximum distance between remote node and hub of 20km. If the distance approaches 20km, there is no more latency budget for buffering: NB condition with R_{OUT} which is exactly 3x the single radio flow rate.

Single optical rates used to carry the radio flows have been chosen as 50 or 100Gbit/s. Multiple of single rate values has been considered in case of very high bandwidth flows.

Figure 77 shows the aggregated output bandwidth versus distance for the option 1 case. It is characterized by almost symmetrical 10Gbit/s flows. A single 50Gbit/s optical interface has been used to carry all the 3 flows. The lower the distance, the higher is the available bandwidth to transport other kind of traffic, e.g. Ethernet from wireline traffic. In addition, fixed the overall latency budget, lower value of TTI guarantees a better reduction of the aggregated output rate.

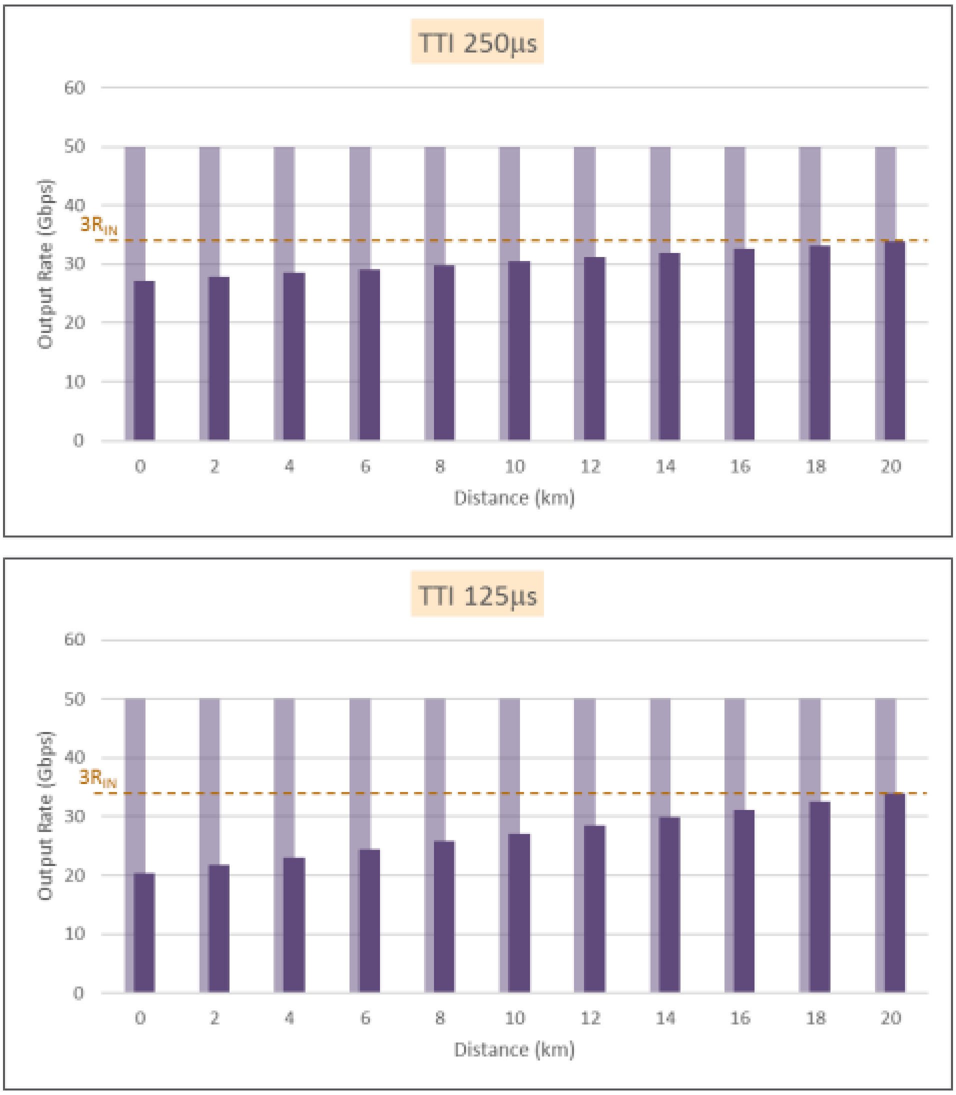

Figure 77: Option1 RRC/PDCP - 3x11.3Gbit/s, L=100us, Optical 50Gbit/s

In Figure 78 and Figure 79, Option 7A Low Rate has been reported for the downlink and uplink case. A 100Gbit/s optical rate is enough for the downlink case, but 200Gbit/s (2x100Gbit/s) have been chosen to carry uplink radio flows. Any distance up to 20km (maximum distance) is supported, but with better performance in the case of TTI=125us.

Figure 78: Option7A Intra-PHY Low Rate - Downlink - 3x28.53Gbit/s, L=100us, Optical 100Gbit/s

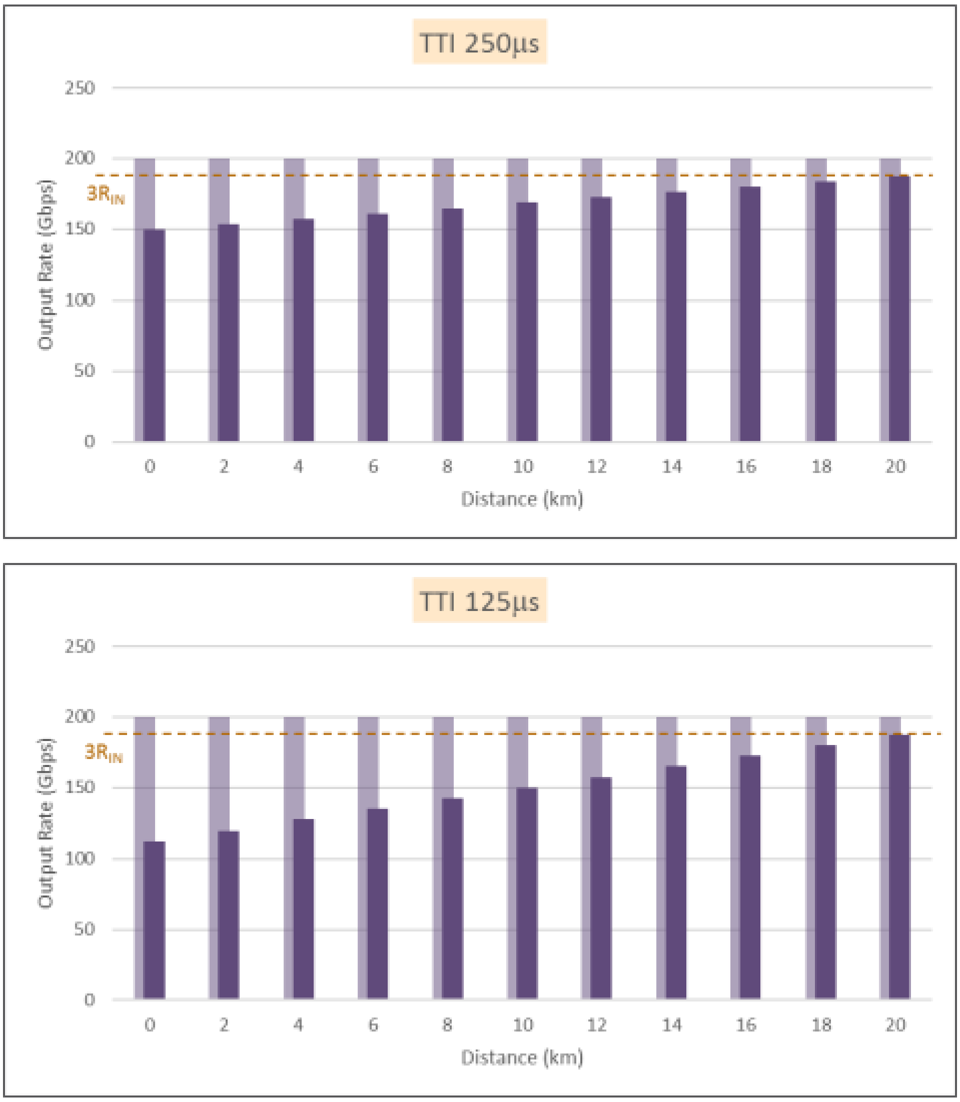

Figure 79: Option7A Intra-PHY Low Rate - Uplink - 3x62.49Gbit/s, L=100us, Optical 2x100Gbit/s

Option 7A high rate is characterized by higher rates and a total 200 Gbit/s has been allocated for the both directions downlink and uplink. This case has been reported in Figure 80 and Figure 81.

The main difference, compared with the previous cases, is that while in the downlink 200Gbit/s are sufficient to cover any distance, for the uplink direction a portion of the latency budget must be reserved for the buffer. So in the Option 7A high rate uplink case (Figure 81) if the distance is below 2km and 10km with TTI equal to 250us or 125us, it is not necessary to allocate an extra wavelength (e.g. 3x100Gbit/s) but a node buffer is able to absorb the radio flows peaks and at the same time to maintain the overall latency always below 100us.

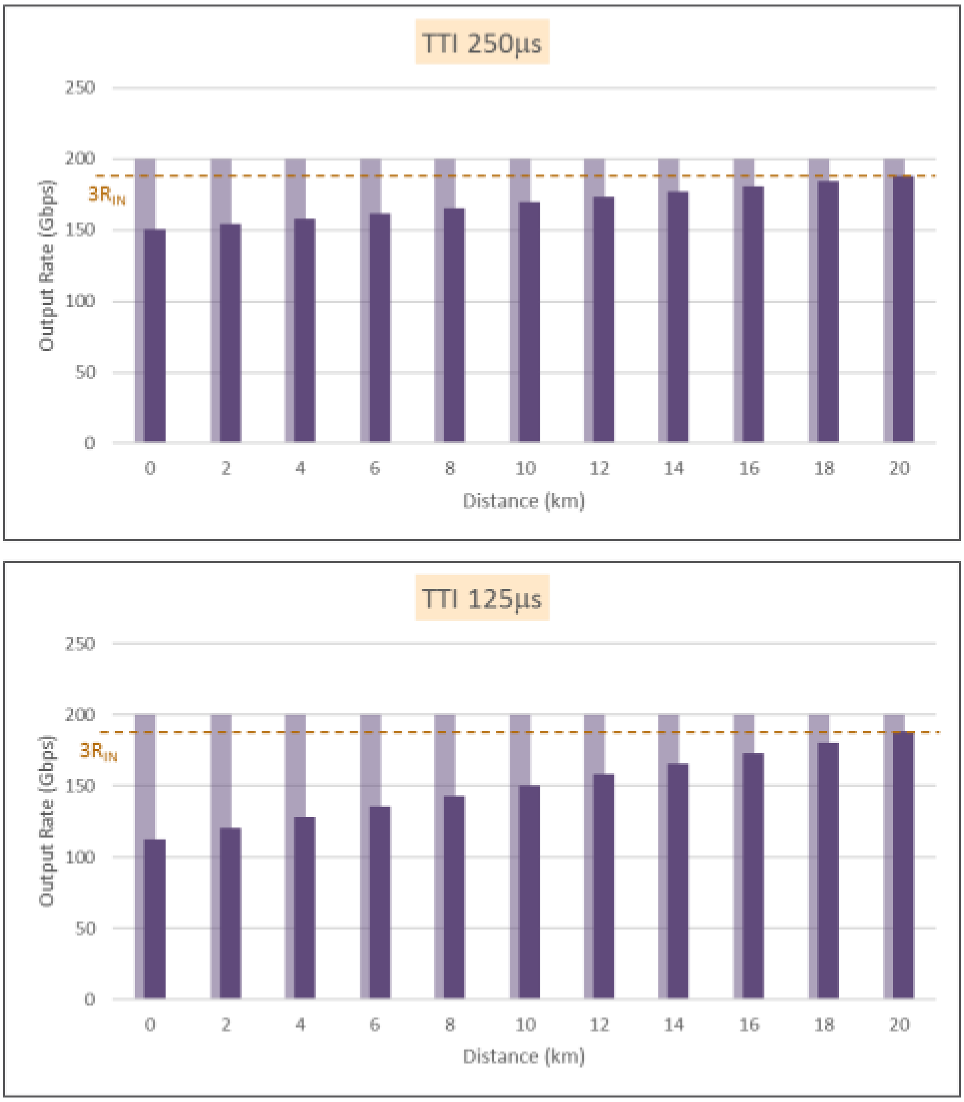

Figure 80: Option7A Intra-PHY High Rate - Downlink - 3x62.72Gbit/s, L=100us, Optical 2x100Gbit/s

Figure 81: Option7A Intra-PHY High Rate - Uplink - 3x81.25Gbit/s, L=100us, Optical 2x100Gbit/s

4.3.2 Optical Circuit multiplexing and switching experiments

The new deterministic delay multiplexing protocol proposed in D2.1 [5] and the related XCSE architecture described in the same document were implemented by TEI in a demonstrator at Ericsson facilities (Figure 82). The purpose of the demonstrator is to test the concurrent and reconfigurable transport of Ethernet-packet-based and CPRI traffic over both dedicated and shared optical channels.

Figure 82: Demonstrator

The test bed, schematically illustrated in Figure 83, is constituted by two remote nodes, located at the antenna side, and a hub node. Remote nodes include RRHs for radio signal processing, a XCSE, and a passive optical add-drop multiplexer box. The hub node includes: digital units (DUs) for radio baseband processing, a similar but larger XCSE, and DWDM multiplexer and de-multiplexer boxes. The ring is realized with double fibre, one for each direction. The length of fibre spanning from Hub to Remote 1 node is 14 km, from Remote 1 to Remote 2 is 4 km, and from Remote 2 to Hub is 6 km. Two DWDM multiplexer/de-multiplexer, based on arrayed waveguide grating (AWG), are located near the Hub to allow mixing two different optical channels into the same fibre on each direction in the Hub-to-Remote direction, while at the same time separating two received wavelengths for the Remote-to-Hub connections.

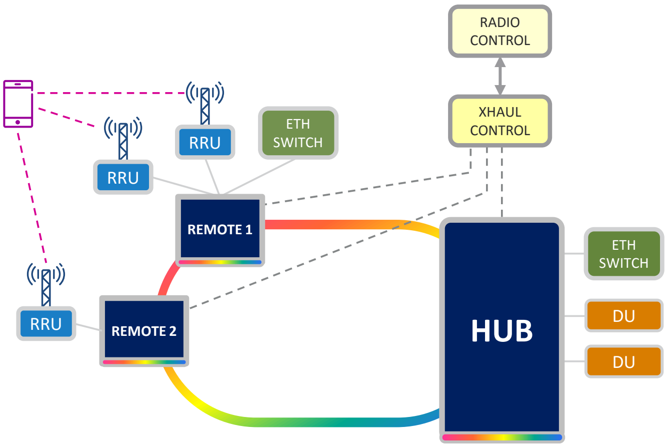

Figure 83: Block diagram of the demonstrator setup

Therefore, the Hub has 4 DWDM bi-directional links:

- Hub-to-Remote 1 connection on clockwise direction
- Hub-to-Remote 1 connection on counter-clockwise direction
- Hub-to-Remote 2 connection on clockwise direction
- Hub-to-Remote 2 connection on counter-clockwise direction

Each of the four connections operates at a rate of 9.8304 Gbit/s using the deterministic delay framing protocol described in D2.1 [5] to mix CPRI and Ethernet traffic on the same link. The protocol includes also FEC capabilities to improve link budget allowing Bit Error Monitoring, as well as a dedicated in-band OAM channel to manage Remote nodes from the Hub.

The client links for the Hub are 2 x CPRI Option 3 (2.4576 Gbit/s) connected to DU, and 2 x Gigabit Ethernet (GbE) connected to an Ethernet Switch. At the Remote 1, there are connected 2 RRU and an Ethernet Switch. At the Remote 2, there is connected 1 RRU. The Hub is connected to a rack-mounted PC running Linux OS hosting the 5G-Crosshaul control functions. The DUs have their S1 interfaces connected to Core Network functions, not appearing in Figure 83 for simplicity.

The experiments show no significant channels performance degradation transporting the new frame compared to OTN channels put on the same optical path, even increasing the link attenuation by means of VOAs. The round trip latency introduced by the FEC was lower than 8 μs, a value compatible with most fronthaul links.

Using the experimental configuration shown in Figure 84, we have also tested protection and delay compensation mechanisms. In this experiment, 4 CPRI option 3 channels have been generated by a Field Programmable Gate Array (FPGA) and multiplexed into a single 10 Gbit/s DWDM optical channel, using the deterministic delay framing protocol described in D2.1 [5].

The optical channel is TDM-demultiplexed at the remote radio unit (RRU) transponder node and client CPRI signals extracted. Ring 1:1 protection is introduced against fibre cuts. In order to minimize any asymmetry between upstream (US) and downstream (DS) wavelength paths, WDM channels propagation is bidirectional over a single fibre and US and DS signals always travel, into opposite direction, along the same portion of the ring. This holds for both working and protected wavelengths.

In the experimental setup, FPGA evaluation boards are used as CPRI client signals generator/analyzer, CPRI aggregator and RRH transceiver. At the BBU, 4 parallel frequency-synchronous 2.4576 Gbit/s CPRI signals are generated and multiplexed in a 9.8304 Gbit/s link, i.e. exactly four times the client bit rate. The 8B10B coding of the tributaries links is removed to allow the insertion of additional information to the payload without increasing the aggregate line rate.

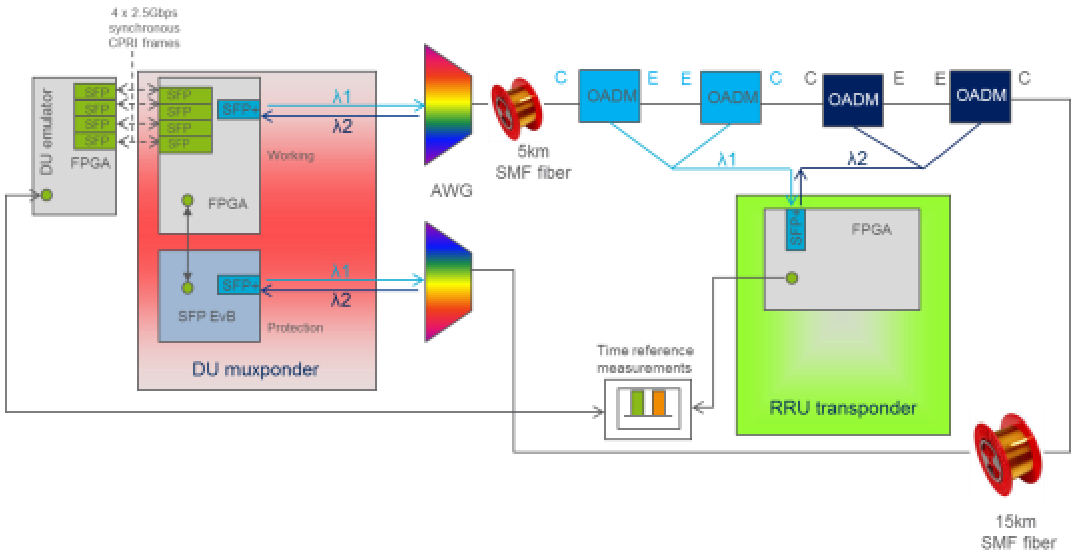

Figure 84: Experimental for the deterministic delay multiplexing protocol

The adopted framing structure is conceived with the objective to allow synchronous multiplexing, OAM, link supervision, DC-balancing and clock recovery, while keeping latency low and reducing by design potential asymmetries sources. The implementation is done inside a single FPGA using a very limited amount of resources compared to OTN. Clock reference is extracted from one of the four tributaries and used to generate the downlink stream. A few Hz bandwidth PLL is used to fulfil CPRI jitter requirements. The 10 Gbit/s signal is sent to working and protection transceivers, emitting at different wavelengths λ_1 and λ_2. The protection transceiver is normally switched off, and it is automatically activated in case of a fibre cut (e.g. following a loss of signal alarm).

The OADM node is able to add or drop the 10 Gbit/s channel, regardless it comes from the working or the protection path. Different RRHs can be connected to the same OADM, each corresponding to separate 2.5 Gbit/s clients.

As shown in Figure 85, the timing reference delay between DU and RRH is monitored in order to fulfil the tight CPRI specification on US/DS delay asymmetries. According to D2.1 [5], the delay estimation accuracy on one CPRI interface link must be within ±8.138ns in order to support radio interface standards where time alignment among different RRUs is required. However, this is not guaranteed by standard OTN. On the other hand, the CPRI delay calibration procedure is based on the assumption that DS and US delays are equal, so that the one-way delay can trivially be estimated by halving the round-trip delay. This does not generally hold for optical links, due to several causes: use of different wavelengths, delay asymmetries introduced by optical filters, unequal patchcords, and digital processing (e.g. Serialization/Deserialization, buffering, etc.). In the proposed solution, all these factors are considered and compensated for at the Hub node.

To validate the compensation mechanism, different fibre lengths, 5km and 15km, have been used in the setup for the working and protection path, respectively. In order to check the accuracy of the timing control, a two tracks oscilloscope has been used. The oscilloscope screenshot reported in Figure 85 shows a pulse generated by the DU emulator at the instant where the DU expects the CPRI frame reference to be received at the RRU site (blue line); the above track shows the actual pulse generated at the RRU transceiver when the frame reference is detected in the downlink stream (yellow line). The pulse width equals the required timing accuracy, i.e. 16 ns.

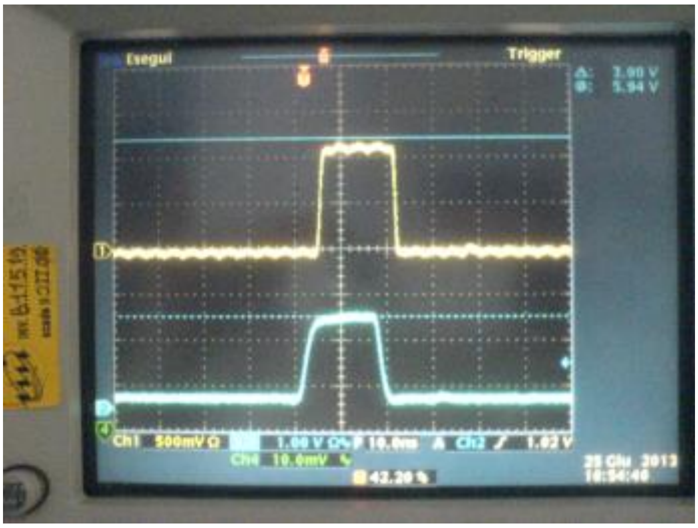

Figure 85: Oscilloscope tracks for timing accuracy check

4.3.3 Supervision functions and OAM at the XCSE

A TDM scheme has been defined on top of the optical layer to provide a common infrastructure that allows to carry on the same wavelength a mix of CPRI based fronthaul traffic, with its very tight latency and synchronization requirements, and backhaul traffic, based on Ethernet interface. For this reason, there are not standards already available. So we defined specific supervision functions for the WDM layer.

For what concerns from the CPRI clients, the reference document is CPRI Specification v7.0 (www.cpri.info), while for Ethernet clients, the relevant specification is IEEE 802.3 (2012).

The supervision functions that can be implemented in XCSE can be summarized as follows:

Monitoring of WDM links

1) Loss Of Signal (LOS): The optical signal is under the RX sensitivity threshold.
2) Loss Of Frame (LOF): The receiver cannot lock to the TDM frame.
3) Received Bit Error Rate (BER): Measured by FEC decoder.
4) Excessive BER: The received BER is above the acceptable (programmable) threshold.
5) Received Optical power on WDM links: Measured by optical transceiver module.

Monitoring of CPRI clients

1) Loss Of Signal (LOS): The optical signal is under the RX sensitivity threshold.
2) Parity and out-of-table error rate: Rate of received symbol that violate 8B/10B or 64B/66B line coding rules.

Monitoring of Ethernet clients

1) Loss Of Signal (LOS): The optical signal is under the RX sensitivity threshold. Not applicable for copper clients where electrical SFP module is plugged.
2) Link Status: According to IEEE 802.3 specification for 1000BASE-X.
3) Parity and out-of-table error rate: Rate of received symbol that violate 8B/10B line coding rules.

Monitoring of Synchronization

1) Loss of Synchronization reference on Hub node: The source of synchronization on Hub node (chosen among one of the CPRI clients) is faulty.
2) Loss of Synchronization reference on Remote node: The Remote node has lost its synchronization reference (chosen among one of the WDM links).

Finally, it is worth noticing that D3.2 covers the main challenges and solutions to implement packet-based Operations, Administration & Maintenance (OAM) mechanisms in SDN. Essentially OAM defines *stateful* mechanisms that must be executed on the switch, while OpenFlow defines a *stateless* forwarding model for the switch and delegates stateful logic to the controller. Thus, the implementation of common packet-based OAM mechanisms such as Connectivity Check Messages (CCMs), Loopback (LBM) and Link Traces Messages (LTM), as defined in the IEEE 802.1ag and ITU-T Y.1731 requires either to: (a) be triggered by the controller or (b) use SDN-compliant tools to define OAM procedures locally at the switches.

4.4 Integration of packet and optical layers

According the analysis about packet and circuit layer, a method about deciding when to use the packet-based or circuit-based resources is provided. On one hand, circuits provide guaranteed resources with deterministic delay, but wavelengths are scarce resources. On the other hand, packet-based forwarding offers statistical multiplexing gains, however at the expense of random queueing delays. Thus, an optimal trade-off would be to follow the algorithm of Figure 86, which essentially proposes that:

1. Upon setup of FH flow (with requirements for BW_needed and Max_delay)
2. (By Default) use XPFE when possible:
   - Because wavelengths are scarce resources
   - Because of statistical multiplexing gains
3. Unless (XCSE):
   - (average/worst-case) delays exceed some threshold (100us - propagation)
     OR
   - The entire FH flow requires a wavelength

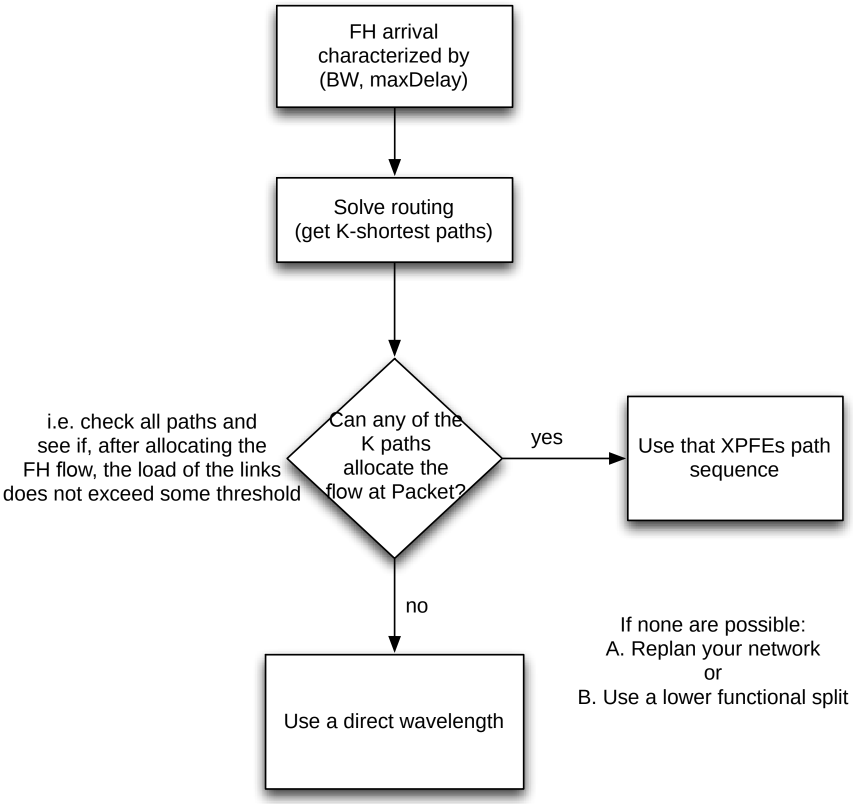

Figure 86: XCSE vs XPFE decision algorithm

4.5 Enabling technologies for packet: Fronthaul compression

Fronthaul (FH) is one of the key enablers for C-RAN to further increase radio network capacity, and to reduce the cost and energy consumption. One of the main obstacles for deploying fronthaul is the high-speed transport requirement, which may require deploying high-speed links (e.g. based on fibre or on multiple high-quality copper cables) per site. For example, with a commonly used assumption of today's CPRI [58] configuration for a 20 MHz LTE carrier over a single antenna, the sampling rate is 30.72 Msps and the quantization is 15 bits, both for the in-phase (I) and quadrature (Q) branches. The data rate required for transporting IQ samples thus becomes ~922 Mbps (excluding CPRI control & management and not taking the overhead introduced by the 8b/10b or 64b/66b line codes into account), although the traffic peak rate is only 100 Mbps with 256-QAM modulation. Here, FH requires an order of magnitude higher bit rate than backhaul (BH). The transport cost is expected to increase dramatically, which may jeopardize even the feasibility of the C-RAN concept, especially for 5G supporting multi-antenna transmission with very wide bandwidth.

To reduce the FH bit rate, there have been mainly two kinds of solutions under discussions in academia and industry. One is to compress the IQ data in the current time-domain FH protocols like CPRI. This approach is compatible with the current FH interface. The other is to create a new interface using a new split on the radio protocol stack [2]. For example, a new FH interface between MAC and PHY would reduce the bit rate to the traffic rate level.

In this section, FH compression is focused as it requires minimum changes in the existing BBU and RRU design. There are currently a variety of FH compression schemes exploiting different techniques such as resampling and re-quantization [60], vector quantization [96] etc. These studies show the possibility to achieve high compression ratio. In this section, we present first in Section 4.5.1 a theoretical bit rate bound showing the compression limit is in the range of 4-5 times, to achieve the high performance required for 256-QAM and 64-QAM. In Section 4.5.2, the re-sampling and re-quantization based compression schemes are experimentally evaluated, which verifies that the high compression is achieved in the lab tests. However, the complexity of performing aggressive resampling to achieve high compression is quite high. To reduce the compression complexity, Section 4.5.3 presents a low-complexity linear predictive coding based scheme and shows high performance close to the bound by simulations and lab tests with a developed prototype.

4.5.1 Theoretical bounds for FH compression

As described previously, it is desirable to derive a compression bound to understand how much the FH signal, i.e. IQ data, can be compressed theoretically. Here, data compression is achieved by squeezing out the redundancy without compromising the required signal quality. In this work, we first analyse and identify the sources of redundancy. Then we derive a compression bound by removing the identified redundancy, which shows the maximum achievable compression for a given signal quality requirement, e.g. a certain error vector magnitude (EVM) value. We also show via simulation results that resampling plus entropy coding is one way to approach the bound.

Redundancy analysis

In this work, we focus on an OFDM signal and take CPRI-based LTE fronthaul as a reference. All identified redundancy sources are listed and analysed below.

Cyclic prefix: In OFDM, a cyclic prefix (CP) is used to keep the orthogonality between subcarriers and reduce the complexity of channel equalization. Basically, each OFDM symbol is preceded by a copy of the end part of the same symbol. At the receiver side, the CP is removed. Therefore, it is redundant information for FH. For example, in DL, the CP can be added in the remote radio unit (RRU) or remote radio head (RRH) when CP is not transported from the BBU. In LTE with normal CP configuration, there is 6.67% CP redundancy.

Oversampling: For digital communication, oversampling above the Nyquist sampling rate is usually applied to ease the anti-aliasing filter complexity. In LTE, the oversampling is included in the IFFT operation. For example in a 20 MHz LTE system, 1200 data subcarriers are mapped to the centre of 2048 subcarriers specified by 2048-point IFFT. With the subcarrier spacing of 15 kHz specified in 3GPP, the sampling rate per IQ branch is 30.72 Msps. However, each IQ branch has only 9 MHz low-pass bandwidth, meaning that the Nyquist frequency is 18 MHz (for LTE DL it is actually 18.015 MHz since there is an unmodulated DC subcarrier in the centre). Therefore, the oversampling factor is (30.72-18)/18 = 70.67% and the redundancy becomes (30.72-18)/30.72 = 41.41%.

Over-quantization: In the current CPRI, the quantization bit width is usually set to 15 bits per IQ component. Following the derivation in [63] for a standard normal distributed signal, Signal-to-Quantization-Noise Ratio (SQNR) is ~80 dB with 15 bits. However, the 3GPP requirements related to SNR for LTE are much less than 80 dB, e.g. specified in [64] and [65]. For example, the EVM requirement for LTE DL using 256-QAM is 3.5% [65], which is interpreted as SNR > 29.1 dB. In this case, it is unnecessary to quantize the signal with 15 bits. If 7 bits can provide sufficient SNR, the redundancy in quantization is (15−7)/15 = 53%.

Entropy coding: Entropy coding like Huffman coding can further compress out the redundancy in the quantized samples in a lossless manner to reach the entropy of the data samples. Basically, it represents the frequently occurring bit sequences with few bits and rarely occurring ones with many bits. The more concentrated the data sample distribution is, the more redundancy is present in the data. OFDM IQ samples follow approximately a Gaussian distribution. Use of entropy coding can further reduce the number of bits per sample.

Derived bit-rate bound

To obtain a lower bound for compressed fronthaul bit rate, we assume to remove all the redundancy listed above, given a signal quality requirement, e.g. EVM or SNR etc. In this work, we derive a lower bound of the number of bits per sample as follows, where the sample rate equals the classical CPRI sampling rate.

1. Given a uniform quantizer defined by the bit-width = N and the quantizer range = $[-C_N,\ C_N]$, the SQNR can be represented as function of $N$and C_N as

   $$SQNR = f(N, C_N)$$

   Note that if EVM is used, the relation between EVM and SQNR is $EVM = 1/\sqrt{SQNR}$.

2. Given any N and C_N, the quantization step size is $q = 2C_N/2^N$ and there are totally $M = 2^N$ steps. Therefore, the probability P_m that a sample falls in the mth step can be calculated, following the Gaussian distribution. Then the entropy is calculated as

   $$N_{E=} \sum_{m=1}^{2^N} P_m log2(P_m)$$

3. Finally, the bound for the given quantizer is derived as

   $$N_B = \left(1 - OH_{cp}\right)(1 - OH_{ov})N_E$$

   where OH_{cp} is the overhead of cyclic prefix and OH_{ov} is the overhead of oversampling. As an example, $N_B = 15$ would correspond to no compression relative to classical CPRI while $N_B = 7.5$ would correspond to compression by a factor of 2.

This way, one can obtain the compressed number of bits per sample N_B versus SQNR or EVM by changing N above.

To get the true lower bound, one needs to apply an optimal quantizer. In this work, we use the uniform quantizer setting from [63], which is optimized for a Gaussian distributed signal to achieve the maximum SQNR, considering both clipping noise and quantization noise. The analytical SQNR formulation in [63] is also used for calculating N above.

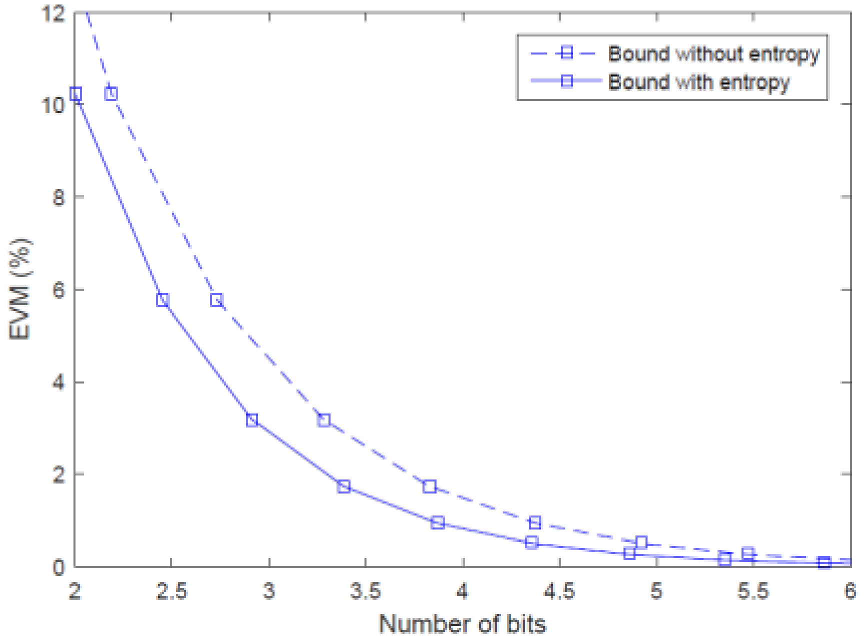

Figure 87: Bound for EVM vs number of bits with and without entropy coding for 20 MHz LTE downlink.

Figure 87 shows the derived lower bounds for a 20 MHz LTE signal with the normal CP setting for two cases: with and without entropy coding. The corresponding CP and oversampling overheads have been removed. It shows that applying entropy coding can further reduce the number of bits by ~10%. The bound also shows the big potential for time-domain fronthaul compression. It shows that 3.4 bits per IQ component can achieve less than 1.75% EVM, which is half of the 3GPP requirement for 256-QAM in DL and therefore still leaves a significant margin for other implementation losses to achieve 100 Mbps peak rate. Comparing with CPRI, 4.4 times compression is achieved. In this case, only 209 Mbps is needed to carry the IQ samples, which is only 2.1 times as high as the backhaul bit rate. Furthermore, greater than 5 times compression is achievable for EVM above 3%. It shows that the compression is able to dramatically reduce the FH demand for capacity and thereby save transport costs.

Simulation results

In this section, a resampling-based compression approach similar to [60] is evaluated via simulations and the results are compared with the derived bound.

Figure 88 shows the block diagram of the simulated system. In the simulation, IQ samples from a 20 MHz LTE signal with 256-QAM is generated at 30.72 Msps with 15 bits quantization. The CP is first removed to eliminate the CP redundancy. Then the IQ data stream is down-sampled to a lower rate to reduce the oversampling redundancy. After down-sampling, the samples are re-quantized to fewer bits to avoid over-quantization. The quantization applies the setting from [63]. Then entropy coding can be applied to compress it further, losslessly. In our simulation, no specific entropy coding scheme is implemented. Instead, the entropy is calculated. In practice, Huffman coding can be used to achieve the entropy. At the other side of the FH link, the process is reversed to uncompress and recover the IQ samples.

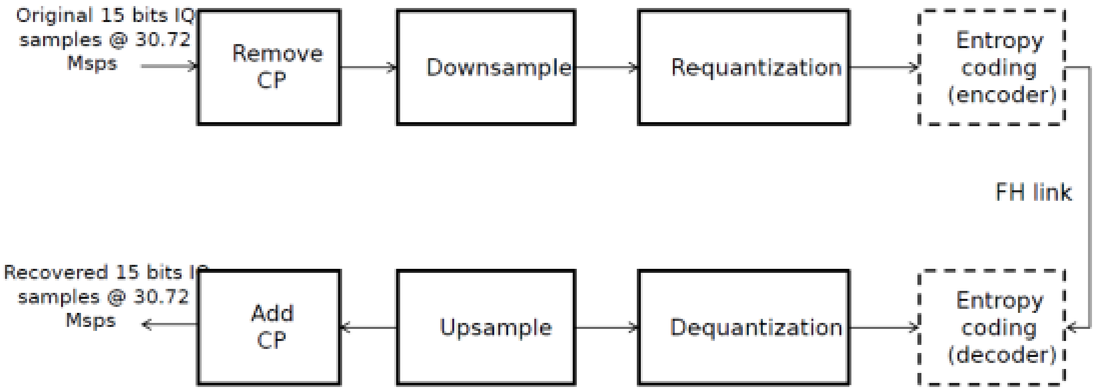

Figure 88: Block diagram of the simulated resampling-based compression scheme.

The simulation results are shown in Figure 89 in comparison with the derived bounds. First, it shows that the entropy coding improves the two resampling cases more significantly than the corresponding improvement in the bounds. For a given EVM value, entropy coding can reduce the number of bits by more than 20% for both the 19.2 Msps and 23.04 Msps resampling cases. Second, the entropy results show that using 19.2 Msps can get performance quite close to the bound. In both cases, it confirms practically the big potential for compression. One achieve more than 4.1 times compression (3.6 bits per sample) at less than 1.75% EVM. Even with 23.04 Msps resampling, it is possible to achieve 3.5 times compression (4.3 bits per sample) under the same EVM requirement. It should be remembered that computational complexity increases when resampling closer to the Nyquist limit since steeper filters are needed to prevent aliasing and to remove the images in reconstruction.

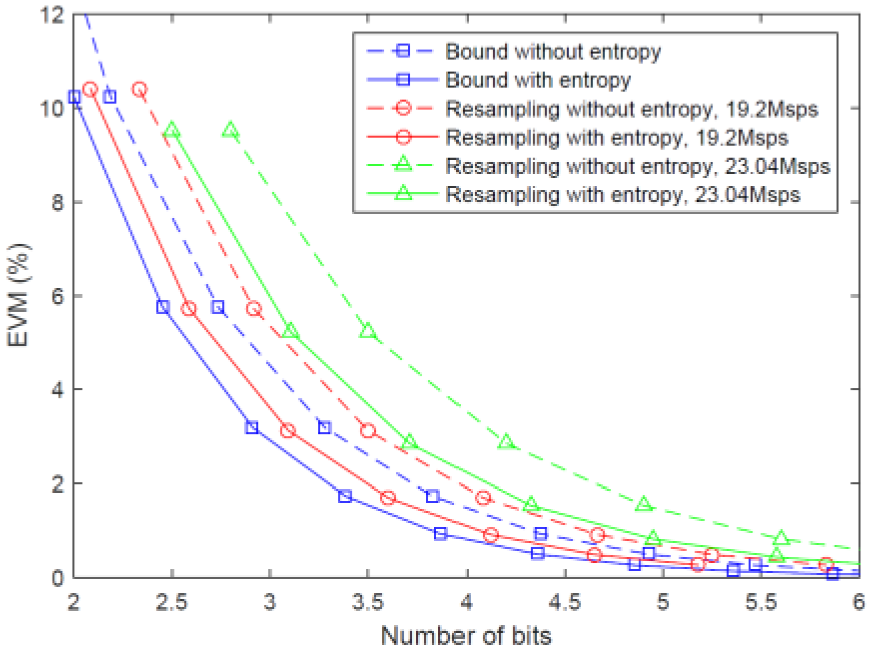

Figure 89: Simulation results comparing resampling-based systems with the derived bound.

4.5.2 Experimental evaluation of resampling and re-quantization based schemes

In this section, we experimentally evaluate two different compression approaches. The first approach concerns different nonlinear quantization algorithms on the time-domain mobile signal, which were assessed by means of offline processing. The second one consisted of a proprietary real-time compression solution which is transparent to CPRI and compresses the IQ samples by both resampling and re-quantization. In this section, we compare both solutions and assess their impacts on transmission performances.

Re-quantization-based compression

Here, we experimentally investigate the impact of the FH compression using different quantization techniques based on fixed-length coding. Figure 90 depicts our experimental setup. We generate a 20 MHz downlink (DL) LTE signal which is transformed using different quantization approaches. A digital-to-analog converter (DAC) generates the analogue NRZ signal used to modulate a directly modulated laser (DML) of a commercial SFP (small form factor pluggable) module. The optical signal propagates through 25 km SSMF before being directly detected by an avalanche photodiode (APD). Extra 14 dB attenuation is added to emulate 1:16 point-to-multi-point splitting-ratio in the link. The received NRZ signal is digitized by an analog-to-digital converter (ADC) and decision is taken on the received NRZ data to obtain the binary sequence used for conversion back to the original LTE orthogonal frequency division multiplexing (OFDM) modulation. Finally, root mean square (RMS) EVM measurements are realized over 20 LTE slots (1 frame = 10 ms).

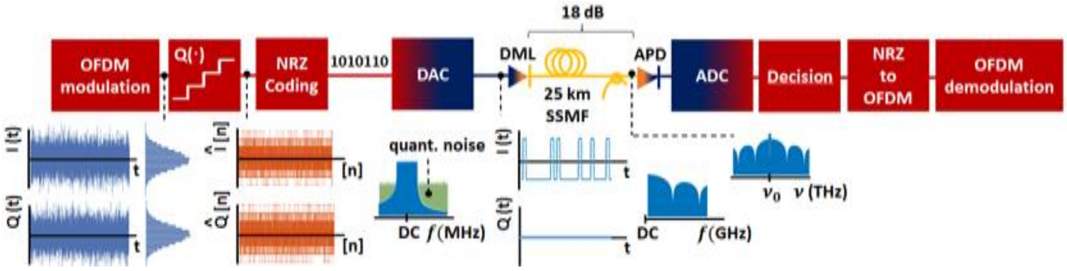

Figure 90: Experimental setup used in offline compression assessment.

Figure 91 shows the impact on the received EVM when we vary the number of bits used to quantify each sample of the time-domain radio signal and thus the fronthaul bit-rate. The compression rate is defined using 15 bits as a reference for quantization and we consider the same number of quantization bits for all signal samples. In Figure 91, we compare two scalar (1D) quantization solutions namely uniform quantization currently adopted in CPRI and OBSAI and non-uniform quantization defined in ORI, the latter implemented using Lloyd's algorithm [78]. We also assess two vector quantization solutions using the Linde-Buzo-Gray (LBG) algorithm [79]. For the first vector quantization, we take I and Q components as the dimensions of a two-dimensional (2D) solution. For the second one, we go further and separate I and Q into odd and even indices samples to implement a four-dimensional (4D) vector quantization.

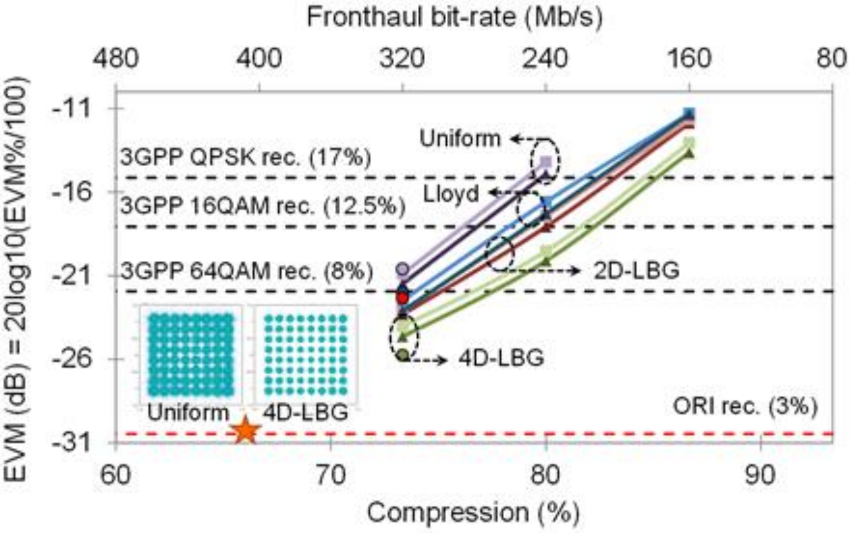

Figure 91: EVM for different compressions and quantization techniques. 64QAM

From the central-limit theorem, we know that the probability density function (PDF) of the OFDM signal amplitude takes the form of a Gaussian distribution (insets on the left side of Figure 90). Hence, uniform quantization cannot provide an optimal solution in our case. Indeed, from Figure 91 we see that reducing the number of quantization bits using the uniform approach would only hold regarding the 3GPP error vector magnitude (EVM) for compressions below approximately 70% for all modulation formats. Lloyd's algorithm consists precisely of adapting the quantization levels to the PDF of the signal. It provides higher precision (quantization levels closer together) for amplitudes that have a higher probability of being generated. Non-uniform quantization allows for an improvement of about 2 dB in the EVM compared to the uniform solution, as also shown in Figure 91.

Even if Lloyd's solution provides better results than uniform quantization, performances can be further improved. Figure 92 (left) shows all possible combinations of quantization levels (yellow circles) for independent non-uniform 1D quantization in the I and Q components of the signal (green dots). It is clear that the corresponding mesh-grid (decisions thresholds of the quantization levels) does not provide an optimal sphere-packing solution. We can notice that the individual distributions on the imaginary and real axes can be seen in fact as a tridimensional Gaussian distribution when plotting the I samples as a function of the Q samples. Indeed, the simple separated use of non-uniform quantization in each of these axes will not allow us to benefit from the correlation between I and Q samples of the OFDM signal that happens due to the Fourier transform at the LTE modulator.

The LBG algorithm consists of an n-dimensional generalization of Lloyd's algorithm that allows benefiting precisely from such statistical dependency and thus providing better EVM results, as shown in Figure 91. The 2D-LBG solution shown in Figure 92 (right) has an optimized arrangement of the quantization levels with the Voronoi cells representing the decision thresholds of the quantization levels.

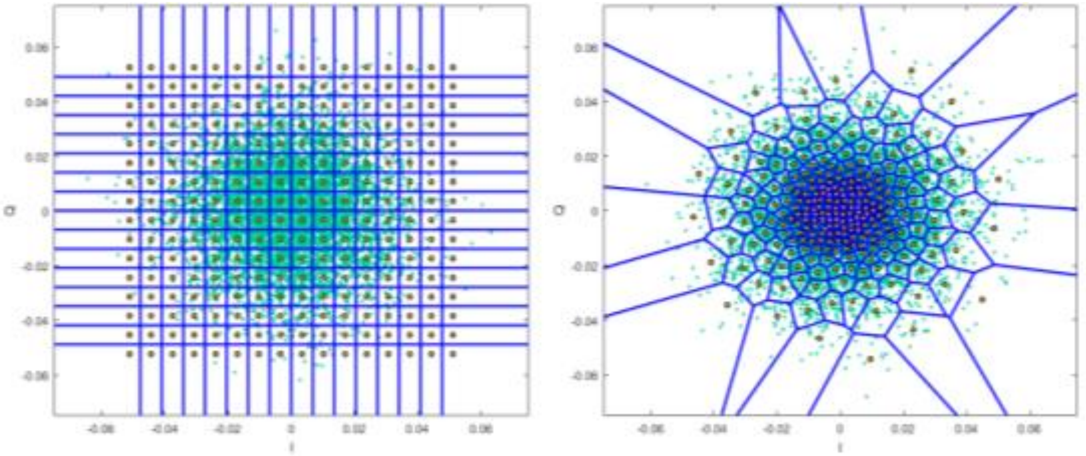

Figure 92: 4 bits/sample comparison between scalar (left) and 2D vector quantization used in 2D-LGB solution (right).

Finally, it is interesting to notice that I and Q samples of the time-domain OFDM signal also have some sort of inner degree of correlation, which is why we implemented a 4D-LBG solution by separating the odd and even samples of the real and imaginary components of the signal. 4D-LBG allows a 4 dB gain in EVM with respect to uniform quantization and enables compliance with 3GPP EVM recommendations with a compression rate of up to 73%. This corresponds to reducing the fronthaul bit-rate from 1.2 Gb/s to approximately 320 Mb/s in SISO mode. The received 64QAM constellations for uniform and 4D-LBG with 73% compression are compared in the insets of Figure 91. We estimate that a 4D-LBG solution would allow up to approximately 67% compression (red star) compliant with Open Radio Interface (ORI) specification.

We must note that the achieved compression ratios could be further increased by means of cyclic prefix subtraction (6.67% of the slot duration) and low-pass filtering (LPF) allowing removal of unused border subcarriers of the OFDM signal [80]. As a reference, 4D-LBG would enable in this case up to 83% compression while keeping a 10% margin for the roll-off of the LPF.

It is very important to highlight that digital signal processing (DSP) based compression techniques such as the ones presented could be used together with wavelength multiplexing approaches to increase fronthaul capacity even further. The inexpensive CWDM solution, for instance, can accommodate up to 18 channels. This would allow up to 9 bidirectional (upstream and downstream) channels in bi-fibre configuration working at up to about 12 Gbit/s each. Single-fibre SFP transponders already exist on the market allowing to double such numbers thanks to splicing of each of the CWDM channels into two sub-channels. Other solutions capable of providing up to 6 sub-channels have also been reported recently [81].

Table 17: Number of transported CPRI3 links with different solutions and 10 Gbit/s interfaces.

Solutions	Number of bi-directional CPRI3 links (10 Gbit/s interfaces)
Conventional CWDM	36
Enhanced CWDM (2 sub-channels)	72
Enhanced CWDM (6 sub-channels)	216
Enhanced CWDM (2 sub-channels) + 4D-LBG (64QAM 3GPP|ORI)	252 | 216
Enhanced CWDM (6 sub-channels) + 4D-LBG (64QAM 3GPP|ORI)	756 | 648

Table 17 shows the number of CPRI3 (2.45 Gbit/s) links that could be accommodated inside a 10 Gbit/s interface through time-multiplexing using different optical and DSP-based approaches. Up to 756 bidirectional CPRI3 links could be transported using enhanced transponders with six sub-channels per CWDM channel and 4D-LBG compression while still respecting 3GPP EVM specifications for 64QAM constellations. It is interesting to notice that the use of bidirectional transceivers with only two sub-channels per CWDM channel plus a 4D-LBG compression could allow the same performances as those obtained with and enhanced transceiver with 6 sub-channels per CWDM channel all alone while still respecting ORI recommendations for non-uniform quantization.

Resampling and re-quantization based compression

Contrary to the previously presented compression techniques, which have been performed offline, we have also evaluated a proprietary real-time technology based on the compression of a Layer 1 functional split type of signal [82]. The compression principle is as follows. After separating the Control and Management (C&M) data from the user data (I/Q), a proprietary compression algorithm is applied to the I/Q components of the signal. This process can be performed into up to eight CPRI3 links (2.45 Gbit/s) before encapsulating them into a single 10 Gbit/s frame. The compression consists mainly of three operations: i) a Layer 1 functional split equivalent operation consisting of moving some of the BBU's L1 functions to the decompression card; ii) low-pass filtering of the LTE spectrum to remove up to 1/3 of unused LTE spectrum attributed to border guard subcarriers (for a 20 MHz downlink LTE signal, the sampling frequency is thus reduced from 30.72 MSa/s to 20.48 MSa/s) and iii) reduction of the quantification resolution of a uniform quantizer. Delay compensation corresponding to the algorithm latency is performed in parallel on the C&M data and both compressed data and uncompressed C&M are finally mapped into a CPRI frame with reduced bit rate.

Figure 93 shows the experimental setup carried out to evaluate the performance of the proposed CPRI compression technique. At the transmitter side, a signal generator creates a 20 MHz LTE signal. Standardized test models E-TM3.3, E-TM3.2 and E-TM3.1 [74] are used to investigate the performance of QPSK, 16QAM and 64QAM mappings respectively. Then, an IQ box handles the LTE to CPRI conversion (sampling, quantization, and coding). The bit rate is fixed to 2.45 Gbit/s. These two components emulate the BBU. The generated CPRI signal is fed to the compression card. At the receiver side, a decompression card de-multiplexes different CPRI links and restores them to their original bit rate. An IQ box is then used for CPRI to LTE conversion and a spectrum analyzer with embedded demodulator handles the LTE performance assessment.

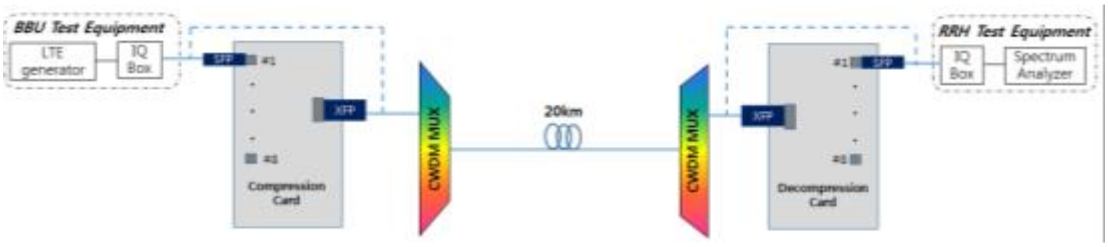

Figure 93: Experimental setup used in the assessment of proprietary compression solution.

The optical transmission between the RAN test equipment and the compression/decompression cards is done with uncolored Small Form-factor Pluggable (SFP). Colored 10G Small Form-factor pluggable (XFP) are used at the output of the compression card and the input of the decompression card. This potentially allows the use of CWDM to multiplex signals from other compression cards operating at different wavelengths. We compare the performances of the proposed solution to what could be obtained by simply reducing the number of quantization bits used in the standard digitalization of the baseband radio signals, i.e., uniform quantization of time-domain baseband I/Q samples.

According to 3GPP, the maximum EVM shall not exceed 17.5% for QPSK modulation, 12.5% for 16QAM and 8% for 64QAM [74]. To take into account the EVM degradation caused by the amplification in the RRH, we take an extra 5% margin on these values. This leads to an EVM threshold of 3% (-30.45dB) for 64QAM which is also compliant to Open Radio Interface (ORI) compression recommendation [83]. Figure 94 shows similar compression performances for all 3 LTE mappings, as expected. Also, a compression of up to approximately 60% can be obtained by simply reducing the number of bits of a standard uniform quantizer operating in the time-domain I/Q samples (solution 1) whereas 73% can be obtained with the evaluated compression card (solution 2) while still respecting the 3% EVM threshold. Therefore, CPRI compression allows reduction of the bit-rate from 2.5 Gbit/s to 1.25 Gbit/s with the first approach and to 0.64 Gb/s with the evaluated proprietary solution. Thus, 20% higher compression could be obtained with solution 2. Also, almost 18 dB EVM increase can be obtained with solution 2 at 60% compression compared to solution 1.

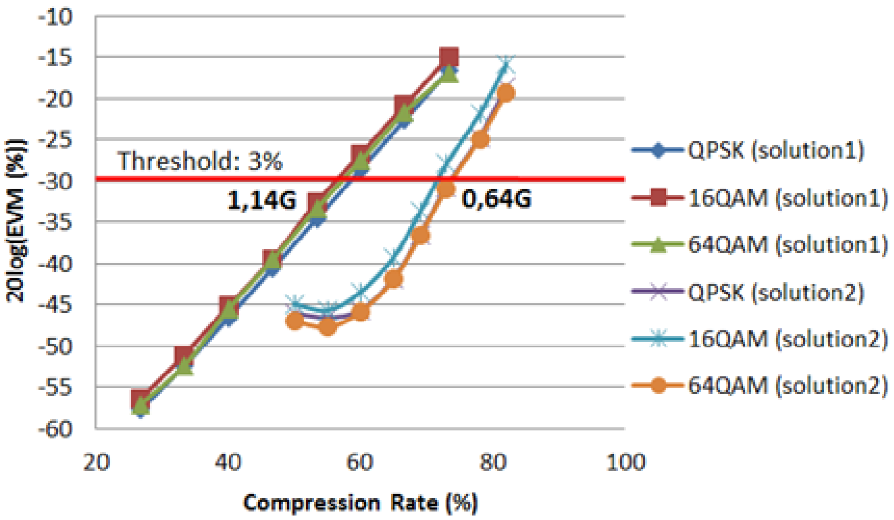

Figure 94: EVM performance as a function of compression rate

Table 18 compares performances of time-domain 4D-LBG compression with the ones obtained with the evaluated L1-functional split based solution. It is worth noting, however, that a considerable part of the compression factor of the proprietary solution is obtained thanks to the low-pass filtering operation, which has not been applied to the time-domain compression algorithms evaluated in the previous section.

Table 18: Comparison between tested compression solutions

Number of bi-directional CPRI3 links (10 Gbit/s interfaces)	Enhanced CWDM (2 sub-channels) + compression (ORI)	Enhanced CWDM (6 sub-channels) + compression (ORI)
Time-domain (4D-LBG)	216	648
L1 functional split + low-pass filtering	252	756

Finally, we evaluated the latency that could be introduced due to the electronic processing of the proposed Layer 1 compression solution. This was realized by means of Round Trip Delay (RTD) and uplink/downlink latency imbalance measurements. The latter could namely affect the User Equipment (UE) positioning accuracy. Ten measurements were carried out on the C&M CPRI channel using appropriated CPRI test equipment. The maximal, average and minimal RTD values for different compression rates are presented in Figure 95. We obtained practically the same RTD of approximately 8.5 µs for all tested compression rates. This value is largely below the ORI recommendation (40 µs) [83]. Also, Coordinated MultiPoint (CoMP) implementation for LTE-A tolerates a maximum RTD of 150 µs. If we assume a C-band optical carrier propagating through standard single mode fibre, this would correspond to approximately 15 km. Therefore, the latency introduced by the evaluated solution would reduce the maximum transmission distance by less than 1 km (i.e, 14.15 km). Moreover, the maximum end-to-end latency imbalance is limited to ±163 ns by 3GPP [75]. Only ±16 ns is specified by RAN providers for the fronthaul segment. The latter value is respected by the compression system according to the performed measurements.

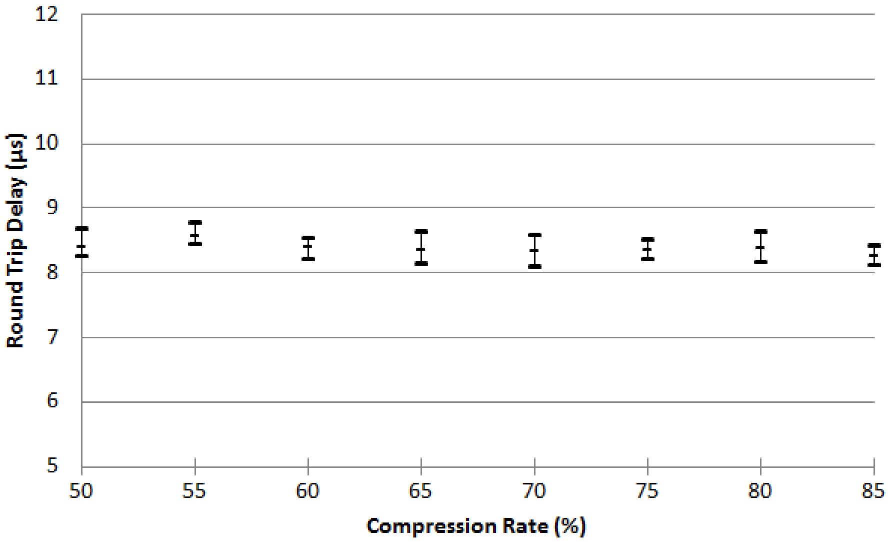

Figure 95: Round trip delay as a function of compression rate

4.5.3 Low-complexity LPC-based compression

As mentioned earlier, the transmission of IQ samples between BBU and RRU in C-RAN may require very high data rates and FH compression is an important enabling technology in C-RAN. Point-to-point [60], [62], [68], [69] and distributed [70] FH compression methods have been proposed. This work focuses on point-to-point methods for the downlink, in which the RRU receives a clean signal from the BBU.

Among the many possible splits of functionality that influence the compression method, the one adopted in [69] moved most of the modulation and demodulation processing from the BBU to the RRU. This allows the direct transmission over the fronthaul of the bits that would be converted to QAM symbols by the modulator. A huge compression factor F = 30 (or 30:1) is then achieved, at the expense of having a significant parcel of the baseband processing at the RRU. In contrast, the focus here is not on maximizing F, but minimizing the computational cost. Indeed, even the resampling procedure is avoided.

For 20 MHz LTE, a CPRI sample rate of 30.72 Msps is commonly used since it is the bit rate from the transmit IFFT after adding the cyclic prefix. Resampling is widely used in FH compression [60], [62], [68] because the LTE signal is oversampled. For example, when an inverse Fast Fourier transform (IFFT) of 2048 points is used to create a 20 MHz LTE signal, only the 1,200 central sub-carriers are filled with QAM symbols [65] while the others are zeroed. In fact, more than 1/3 of the LTE sub-carriers are not used and the oversampling factor is 2048/1200 ≈ 1.7.

Among the FH compression methods that rely on resampling, the one in [60] is representative due to the good performance and relatively low computational cost. In [60], the LTE signal is resampled by a factor of 2/3 and the output samples are quantized in blocks of N_s samples. For the k-th block, the maximum absolute value S[k] among the real and imaginary components is used as a scaling factor to limit the dynamic range of the I/Q component quantizers to $[-1, 1]$. The associated computational cost per input complex-valued sample, not taking the quantization in account, is $C_f \approx \left(\frac{N_f}{2} + \frac{2}{3}\right)$ where $2\frac{N_f}{2}$ multiply and accumulate operations are the parcel due to resampling when optimized polyphase filtering is adopted, with N_f being the order of a symmetric FIR filter, and the scaling by 1/S[k] requiring two multiplications per output sample. A similar method was adopted in [68] with distinct encoding strategies after resampling. In the next section the proposed method is presented and later compared to the baseline [60].

Proposed Method: linear predictive coding based compression

Instead of using resampling to benefit from the oversampling of LTE signals, the proposed method is based on the well-known linear predictive coding (LPC) [71], which takes advantage of the correlation among consecutive samples, illustrated in Figure 96. This correlation can be utilized to reduce the number of bits needed for quantization of the signal. As a starting point, for a given antenna and carrier, each baseband IQ sample of an LTE signal is represented by $2b$ bits, where $b = 15$ is commonly used for LTE.

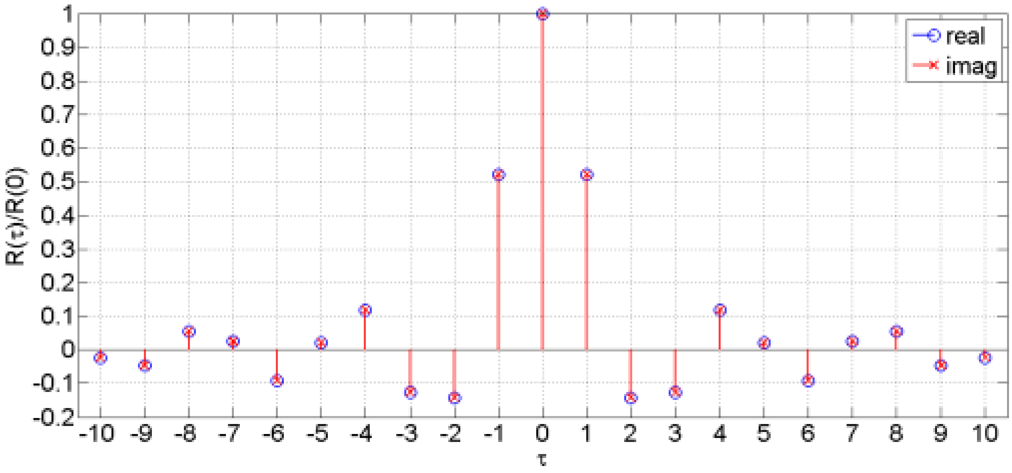

Figure 96: Estimated (normalized) autocorrelation function of a 20 MHz LTE signal

In LPC, a predictor $A(z) = \sum_{i=1}^{P} a_i z^{-i}$ uses the P previously quantized signal samples to create a prediction $\tilde{x}[n]$ of the current sample $x[n]$. The prediction error $e[n] = x[n] - \tilde{x}[n]$, which ideally has a white spectrum, is then quantized and transmitted. The decoder should be able to reconstruct the sample $\hat{x}[n] = \hat{e}[n] + \tilde{x}[n]$ using the quantized version $\hat{e}[n]$ of the prediction error. At both encoder and decoder, the prediction $\tilde{x}[n] = \sum_{i=1}^{P} a_i \hat{x}[n-i]$ uses previously quantized samples $\hat{x}[n]$ because the original signal $x[n]$ is not available at the decoder.

The prediction error $e[n]$ can be quantized with either a uniform (USQ) or non-uniform scalar quantizer (NUSQ). The latter requires a codebook. The quantizer creates an index $I[n]$ of b_e bits to represent $\hat{e}[n]$. Entropy (e.g. Huffman) coding can be used to reduce the average rate to a value L closer to the entropy of $I[n]$ [71]. These basic concepts of predictive and entropy coding were used to design the proposed predictive uniform scalar quantization with Huffman coding (PUSQH) method, which is described in the sequel.

It is assumed that the system knows where each OFDM symbol starts and ends (the two endpoint indexes). This is a sensible assumption: for example, the CPRI specification supports for the downlink the option of cyclic prefix insertion at the RRU [58]. Knowing the endpoints enables to circumvent the block effect among OFDM symbols, which is illustrated in Figure 97, where a large prediction error occurs between OFDM symbols. Circumventing this effect is a crucial feature of PUSQH to achieve improved performance, since this high prediction error could potentially degrade the prediction $\tilde{x}$ based on quantized samples $\hat{x}$. The block effect is eliminated by simply transmitting the original first P samples ($x[0]$ to $x[P-1]$) as side information using the original resolution (e. g., 30 bits per complex sample). This strategy is further detailed within the overall PUSQH method, described in the sequel.

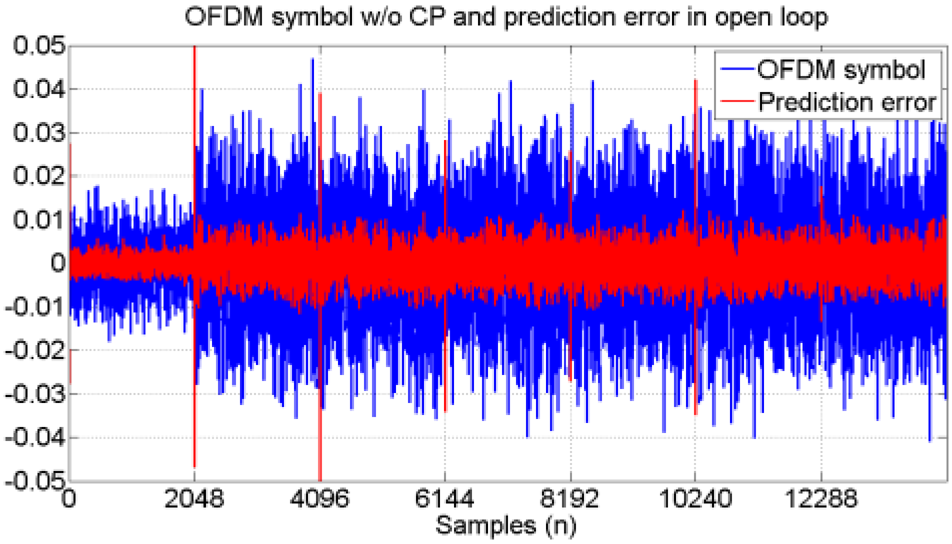

Figure 97: Real part of an LTE signal x[n] and its prediction error e[n] illustrating the block effect in the border of consecutive OFDM symbols.

PUSQH encodes each OFDM symbol individually and, due to their statistical independence, the real and imaginary (IQ) components are also individually processed. Hence, a given I or Q component of an OFDM symbol with N real-valued samples is denoted as $x[n]$, where N is the IFFT size, and encoded as depicted in Figure 98. The scalar quantizer represents $\tilde{e}[n], n = P, P+1, \dots, N-1$ with b_e bits, and is followed by a Huffman encoder. The N_{CP} samples of the CP are not transmitted by the encoder. At the decoder, all inverse operations are performed to obtain the reconstructed symbol $\hat{s} = \hat{s}_i + j\hat{s}_q$ with the CP included.

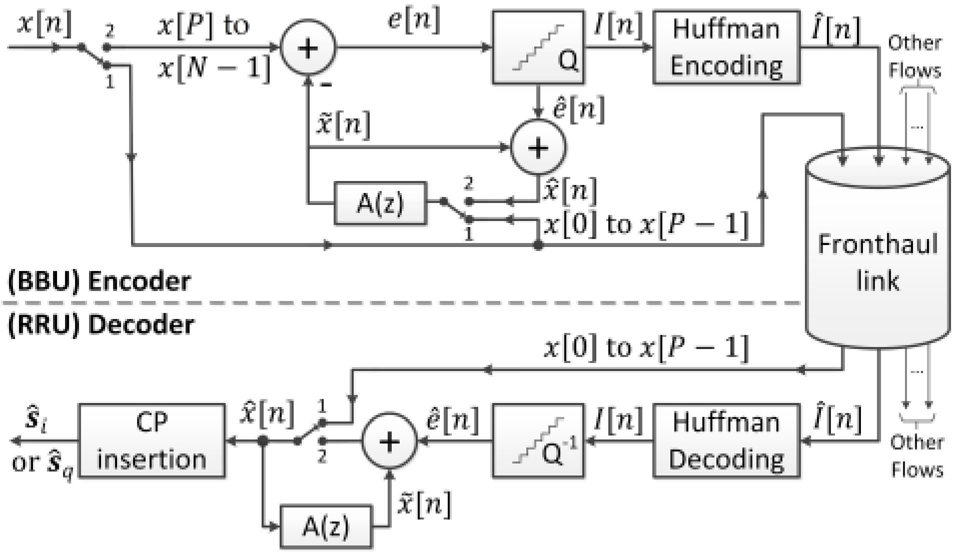

Figure 98: Proposed PUSQH method using predictive and entropy coding for each individual OFDM symbol. The first P samples are passed to the receiver while the remaining $N-P$ are quantized.

The mentioned lossless coding of the first P elements corresponds to having $\hat{x}[n]=x[n]$, where $n=0,1,\ldots,P-1$, for each OFDM symbol. The prediction error $e[n]$ is calculated for the remaining samples $x[n], n=P,P+1,\ldots,N-1$, quantized and transmitted as $\hat{I}[n]$. Besides, at the beginning of each OFDM symbol, the first P samples (for which $\hat{x}[n]=x[n]$) are used to initialize the predictor memory. This is indicated by the switches in position 1 in Figure 98. The switch at position 2 indicates that after the predictor memory is filled with the first P samples, the remaining iterations use predictions that rely on the lossy encoding of e[n], which means $\hat{x}[n]$instead of $x[n]$. For example, the prediction of sample $P+1$ is calculated as $\tilde{x}[P+1]=a_1\hat{x}[P]+\sum_{i=2}^{P}a_i\hat{x}[P+1-i]$.

There are many methods to calculate the coefficients of $A(z)$, such as the Levinson-Durbin algorithm [71] which requires only estimated values $\hat{R}(\tau)$ of the autocorrelation function. If $A(z)$ is calculated offline, as it is in this work, its design does not impact the computational cost of real-time operation and can focus on performance. The following strategy takes in account the mentioned blocking effect and leads to improved performance: $R(k,\tau)$ is obtained for each OFDM symbol k (i.e. for each $x[n]$) and the average $\hat{R}(\tau)=E\left[\hat{R}(k,\tau)\right]$ is used as input to the Levinson-Durbin algorithm.

The average output rate achieved by the proposed method is $R=\frac{L(N-P)+bP}{N+N_{CP}}$ bits/sample, where L is the average number of bits when entropy coding is applied to $I[n]$, and its compression factor is F = b/R.

Regarding computational cost, the CP insertion is a simple operation and Huffman encoding/decoding can be efficiently implemented by a lookup table and a search tree, respectively [72] [73]. The cost of the remaining linear prediction stage can be estimated as follows.

The predictor error $e[n]$ is obtained with P multiply and accumulate operations followed by one addition for $N - P$ samples of the total $N + N_{CP}$ samples that compose $\hat{s}_i$ or $\hat{s}_q$. Hence, in average, the proposed method requires $C_p = \frac{2(P+1)(N-P)}{N+N_{CP}}$ arithmetic operations per complex-valued sample in order to implement prediction. For example, adopting $P = 4$ for PUSQH and $N_f = 64$ as in [68] for the baseline [60], a 20-MHz LTE slot (15,360 complex samples with a duration of 0.5 ms) with $N_{CP} = 144$, leads to $C_p = 143{,}229$ and $C_b = 1{,}003{,}520$ and, consequently, $C_b \approx 7C_p$. This comparison assumed that addition, multiplication and multiply and accumulate operations have the same cost.

PUSQH is also very competitive with respect to latency. The lossless transmission of the first P samples allows the decoder to output these samples as soon as they are received and, for $n > P$, the process continues without further delay. In contrast, a method that relies on resampling using a FIR filter of order N_f has to cope with a minimum latency of $N_f = 2$ imposed by the filter's group delay. In the sequel, PUSQH is evaluated with respect to rate vs distortion.

Evaluation Methodology and Results

The proposed method was evaluated using the EVM versus the average number of bits per component sample R or compression factor F, which are common figures of merit associated to F compression methods. The average root mean square (RMS) EVM was calculated here as indicated in Annex E of [65]. As a guideline, the overall link should have a maximum EVM of 17.5, 12.5, 8 and 3.5% to support QPSK, 16- , 64- and 256-QAM [65], respectively. Obviously, the signal distortion introduced by FH compression algorithms should be kept as low as possible because the downlink signal quality will be further degraded by phase noise and non-linear distortion in the transmitter.

The adopted evaluation methodology took in account that an LTE frame uses several distinct signals. Care must be exercised when evaluating the compression methods that rely on training data such as entropy coding, predictors and non-uniform quantizers. Here, disjoint sets of training and test data with a variety of LTE signals were used, and it was avoided to design quantizers or predictors using a specific LTE signal and evaluate the compression using only the same kind of signal.

Table 19 lists results for distinct configurations for the LTE signals, with identifiers (ID) C1 to C8. The configurations C1 to C4 correspond to an LTE bandwidth of 20 MHz, while C5 to C8 have a bandwidth of 10 MHz. In LTE, there are 100 and 50 available resource blocks (RB) when bandwidth is 20 and 10 MHz, respectively. The simulations also take into account the number of active RBs (aRB), which indicates the cell load. For example, C4 and C8 correspond to a lightly loaded situation given that only 10 RBs are being used (out of 100 and 50, respectively). The other signals in Table 19 are fully loaded. The modulation order M adopted for the physical downlink shared channel (PDSCH) is 64, 16, or 4 (QPSK).

Table 19: Rate and distortion results of PUSQH for distinct combinations of training (C1 or C6) and test (C1–C8) configurations.

			***P* = 4**		***P* = 6**	
Test	LTE parameters	Train	Avg. EVM	R	Avg. EVM	R

ID	BW; M; aRB	ID	(%)	(bits)	(%)	(bits)
C1	20; 64; 100	C1	1.65	4.39	1.02	4.47
C2	20; 16; 100		1.65	4.39	1.02	4.47
C3	20; 4; 100		1.65	4.39	1.02	4.47
C4	20; 64; 10		1.65	3.85	1.01	3.90
C5	10; 64; 50	C6	1.62	4.45	1.05	4.48
C6	10; 16; 50		1.62	4.45	1.05	4.48
C7	10; 4; 50		1.62	4.45	1.04	4.48
C8	10; 16; 8		1.56	3.91	1.03	3.97

The predictor $A(z)$, quantizers and Huffman codes were designed from a training sequence with configuration C1 for tests with 20 MHz signals (C1C4) and configuration C6 for testing with 10 MHz signals (C5C8).

The predictor was found to be relatively robust to mismatched conditions, when the configuration of the test signal differs from the one used for training. The motivation to use predictor orders of $P = 4$ and $P = 6$ in Figure 99 came from the following strategy. When choosing the predictor order P, a convenient figure of merit is the open-loop prediction gain $G_{olp} = 10 \log_{10}\left(\frac{E[|x[n]|^2]}{E[|e[n]|^2]}\right)$ in dB [71], where $E[\cdot]$ is the expected value and the quantizer is not used ($b_e \rightarrow \infty$). As an example, for configuration C1, this gain increases linearly according to $G_{olp} \approx 18 + 1.7P$ from $P = 1$ to 6, and then starts to saturate, as depicted in Figure 99.

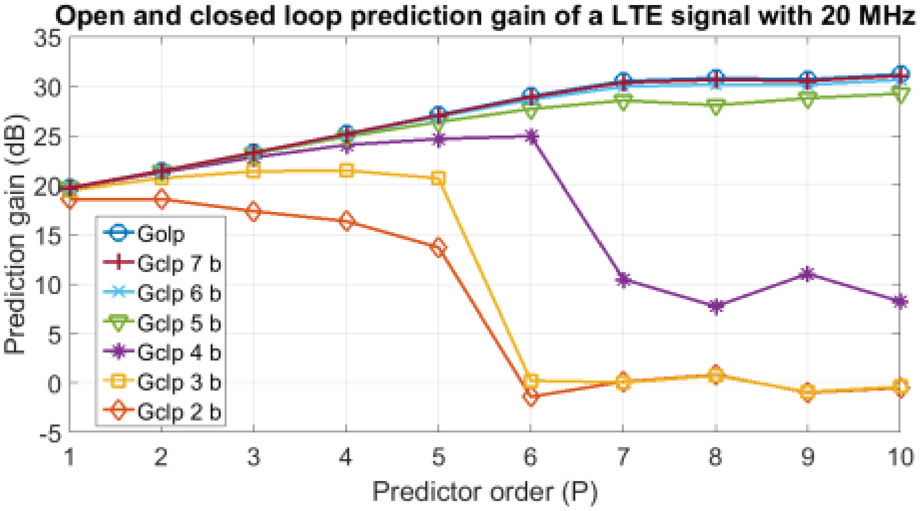

Figure 99: Prediction gains of a 20 MHz LTE signal, where e. g., “7 b” indicates b_e = 7 bits.

The value of G_{olp} is convenient because it does not depend on the adopted quantizer, but the actual performance is better inferred from the closed-loop gain G_{clp}, which has the same expression of G_{olp}, but the quantizer is used [71]. In other words, the prediction $\tilde{x}[n]$ uses x[n] or $\hat{x}[n]$ to obtain G_{olp} or G_{clp}, respectively. For $b_e \geq 6$, the two gains are essentially the same, i.e., $G_{clp} \approx G_{olp}$, as indicated in Figure 99. From G_{clp} curves, which were confirmed by complete simulations involving EVM estimation, choosing $P = 6$ gives the best rate vs distortion but $P = 4$ may be adopted if its lower computational cost is attractive. The results in Table 19 were obtained with $b_e = 6$ bits.

Slightly improved performance can be achieved if the encoder at the BBU informs that the OFDM symbol is of a specific configuration as a side information, and the encoding scheme can be chosen accordingly. For example, the first OFDM symbol of a subframe is restricted to carry QPSK-only and a specific predictor, quantizer and Huffman code could be adopted. Such adaptation was avoided in this work for the sake of having a very simple decoder at the RRU.

The proposed method is contrasted to [60] in Figure 100, which was generated with an LTE signal of configuration C1 (BW = 20 MHz) and corresponds to 10 LTE frames (1400 OFDM symbols). The parameters were changed as follows: the predictor order was varied from P = 4 to 7 and the number of quantization bits from $b_e = 2$ to 8 bits.

The proposed linear prediction was also evaluated without Huffman, identified by the acronym PUSQ (suffix H omitted), and corresponding to a lower computational cost than PUSQH. PUSQ achieves lower performance than PUSQH and, with P = 6 and P = 7, its results are close to the ones from the baseline [60], which is based on resampling. The results in Figure 100 indicate that PUSQH outperforms the baseline when F > 3, while achieving similar rate-distortion performance for smaller F. At 1% EVM, the proposed method (PUSQ, P=6 and 6 bit quant.) needs on average 4.47 bits per I or Q sample, which is about 15% above the theoretical bound shown in Section 4.5.1. This discrepancy could likely be decreased somewhat by choosing a longer predictor (e.g. P=7 or 8 taps instead of 6) as indicated by the prediction gain curves in Figure 99.

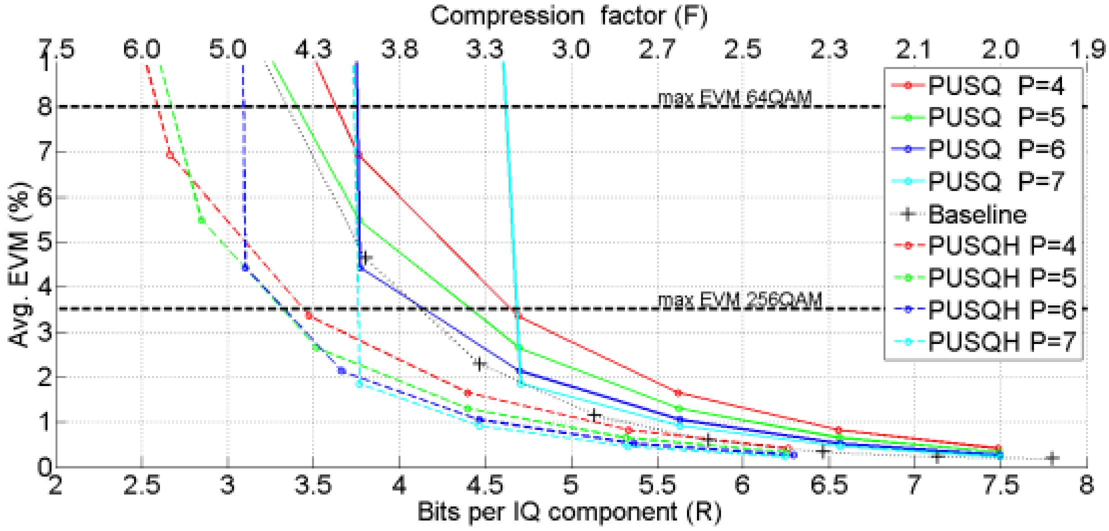

Figure 100: EVM versus both rate R and compression factor F for PUSQH (with Huffman), PUSQ and baseline [60]

To obtain further insight on the behavior of PUSQH, 100 frames (equivalent to 14000 OFDM symbols) of a LTE signal with configuration C1 were used to estimate histograms and power spectral densities (PSDs), assuming a predictor order P = 6 and quantizer with $b_e = 6$ bits.

Figure 101 shows the corresponding histogram, in a case which the average EVM is 1.12%, and its minimum and maximum values are 0.90% and 1.38%, respectively. The EVM values are approximately distributed as a Gaussian.

As indicated in Figure 102, the quantization noise inserted by the adopted PUSQH is white, with a PSD equally spread over the entire band $\left[-\frac{F_S}{2}, \frac{F_S}{2}\right[$ where the sampling frequency $F_S =$ 30.72 MHz. In this case, approximately 25% of the noise power is out of band.

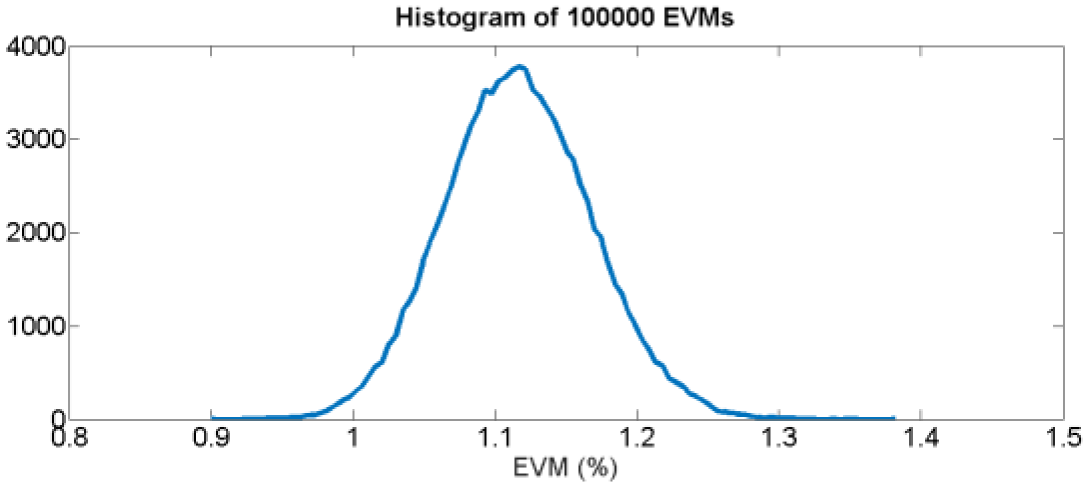

Figure 101: Histogram of EVMs for PUSQH with P = 6 and b_e = 6 bits.

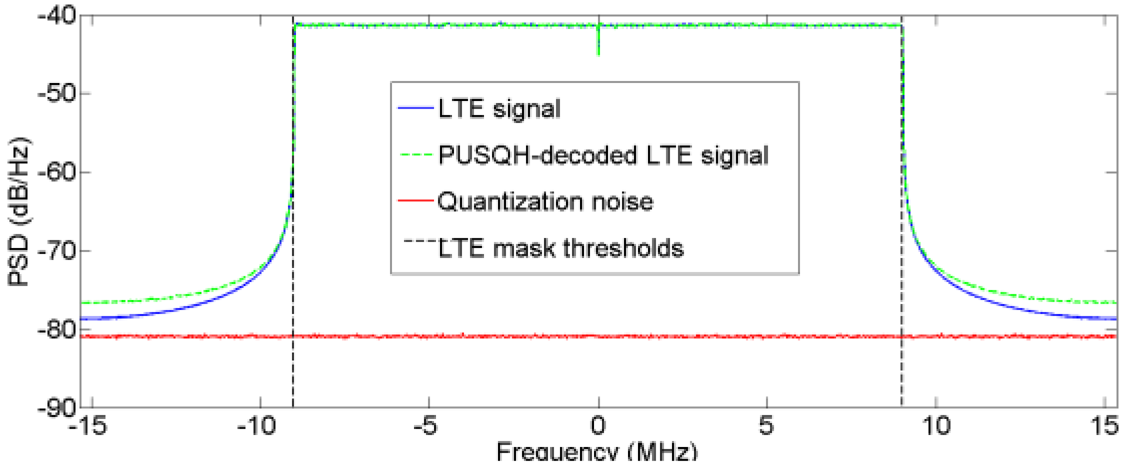

Figure 102: Power spectral densities of noise, original signal, and PUSQH-decoded signal

To summarize, **the results show that the proposed method achieves competitive latency and rate versus distortion results when compared with state-of-the-art alternatives**. When contrasted to the baseline resampling approach [60] it led to a decrease in computational cost by a factor of approximately seven. For an EVM target of 1%, the proposed method yields a bit rate approximately 15% above our derived bound. For higher EVM values, performance is even closer to the bound. Further, a slightly longer predictor could decrease the gap further, especially at low EVM levels.

5 Scenario experiments

5.1 Very-dense deployment of indoor and outdoor small cells

Heterogeneous networks integrating a small cell layer under the macro cell layer have been considered as a cost-effective alternative to macro cell densification for further increasing the network capacity, meeting the ever-increasing traffic demand. Therefore, the small cell becomes an essential part of the radio network and is critical to offload macro cells and improve user experience in the dense urban area where the population density and the traffic density are very high.

For small cells, the transport, i.e. backhaul (BH) and fronthaul (FH), represents a significant part of the total cost of the radio network. In this chapter, we focus on the innovations of 5G-Crosshaul systems integrating FH and BH for two scenarios of indoor small cell and outdoor small cells, leveraging Ethernet LAN technologies for indoor, as well as mmWave and OWC (optical wireless communication) for outdoor. For each scenario, the 5G-Crosshaul systems are described and compared to the state of the art. The performances in terms of transport bandwidth, latency and energy consumption are analyzed, simulated, or measured, showing the possibility of fulfilling the 5G requirements for different use cases specified in Section 2.

5.1.1 Indoor small cell system design and performance analysis

More than 80% of the total mobile traffic happens indoors, such as in-office buildings, hotels, airports, stadiums, homes. Providing high capacity to the indoor is thereby critical to improve user experience, while WiFi has shown its scalability issue with increased user density for dense deployment due to the channel contentions and interferences from neighboring WiFi cells and from other wireless systems (alien WiFi cells, BLE, Zigbee etc.) operating on the same unlicensed band.

To design a radio system for indoor coverage and capacity, the indoor challenges should be understood from the RF perspective, as listed below:

(1) High penetration loss into buildings from the outdoor macro base station: to reduce energy consumption for heating and cooling in the real estate segment, the modern buildings are built with thick concrete walls and highly isolated glass windows. The radio signals can easily get attenuated by more than 10 dB just behind a wall, which is often referred to as penetration loss. The penetration loss is even high for high frequencies like 28 GHz or above which will be used for 5G. Hence, it is inefficient to cover the indoor by the outside-in approach. Further, if dedicated indoor systems are deployed, it will be not only more power efficient but also the whole network benefits from traffic indoor offloading and the reduced interferences between indoor and outdoor systems.

(2) Hostile indoor RF propagation environment: the indoor propagation channel first characterizes high path loss, e.g. NLOS (none line of sight), due to penetrating the interior walls and blocking by other indoor objects etc. This limits the coverage. Secondly, the indoor channel also features with rich scattering with many multipath

components from the reflections. MIMO techniques can exploit the indoor multipath channel to increase the capacity.

(3) Indoor RF regulations: For outdoor, there is no limit in regulation for the transmit power of a macro base station, e.g. usually 46 – 50 dBm (or 40 - 100 Watts). The ERIP (Effective Isotropic Radiated Power) is even much higher with a sector antenna, e.g. with 13 dB antenna gain. However, the indoor regulation is very strict to keep the low EIRP, mainly due to the health concerns regarding radio exposures. For example, FCC regulates in [42] that the EIPR is up to 30 dBm, while normally the transmit power to the antenna port is up to 23-24 dB.

Given these challenges, it can be concluded that there is a need to have a dedicated indoor radio system which should deploy many low power antenna sites supporting MIMO to provide both coverage and high capacity. In today's terminology, each lower power antenna site can be referred to as an indoor small cell. Distributed Antennas Systems (DAS) have been a dominant indoor small cell solution since 1990s in the 2G era. However, DAS represents a legacy design which is mainly for voice coverage and have shown its difficulties to scale up for higher capacity in mobile broadband (i.e. 3G, 4G and the coming 5G) era. New types of indoor small cell solutions are needed to meet the ever-increasing demand for mobile traffic and applications.

In the following sections, we will describe today's indoor system designs such as distributed antenna system (DAS) and analyzes its pros and cons. Then we focus on a new FH-based indoor system designed in the framework of 5G-Crosshaul project with the desired features for 5G, e.g. baseband pooling, dynamic cell split, and enabling crosshaul (BH and FH) traffic through an Ethernet network, i.e. based on the copper-based Ethernet cabling infrastructure widely-used in the in-building IT systems. The dimensioning results are also given for different system configurations, showing the capability fulfilling the 5G requirements for use case 1.a and use case 3 described in Section 2. This section is then concluded with a summary of key contributions from this work to the state of the art for the indoor small cell scenario.

State of the art and the trend

As the first indoor radio solution, DAS have evolved from passive DAS to hybrid DAS. In passive DAS, the dense deployed distributed antennas are connected to the RF port of a base station via a tree-topology coax cabling infrastructure with passive RF components like attenuators, splitters, and filters. To have an acceptable level of insertion loss and achieve a desired distance, the coax cables used are thick, heavy, and hard to bend, which is difficult to deploy. Nevertheless, the high insertion loss from both the cabling and passive components results in low SNR and thereby low system capacity. For extending the voice coverage, it serves the purpose. To improve this, hybrid DAS reduce the coax cable length by replacing the first part of the coax cable to the base station with a fiber connection using radio over fiber (RoF) technologies. But the last part of connection to the antennas are still of the tree topology and passive with the coax cabling and passive RF components like splitters. In this way, the insertion loss is reduced. However, hybrid DAS have a complicated system architecture as they operate on the RF bands directly and rely on the RF components, as shown in Figure 103. The installation cost is not reduced as the fiber installation is also costly, while the component costs of both passive and active optical components are high. One of the main problems of DAS is that it is difficult to increase the system capacity by adding MIMO and performing cell split (i.e. supporting multi-cells). It needs to install a parallel cabling infrastructure well calibrated with the existing branch to support MIMO. To increase capacity by cell split, the cabling topology has to be manually changed by re-installation. Both are complicated and costly.

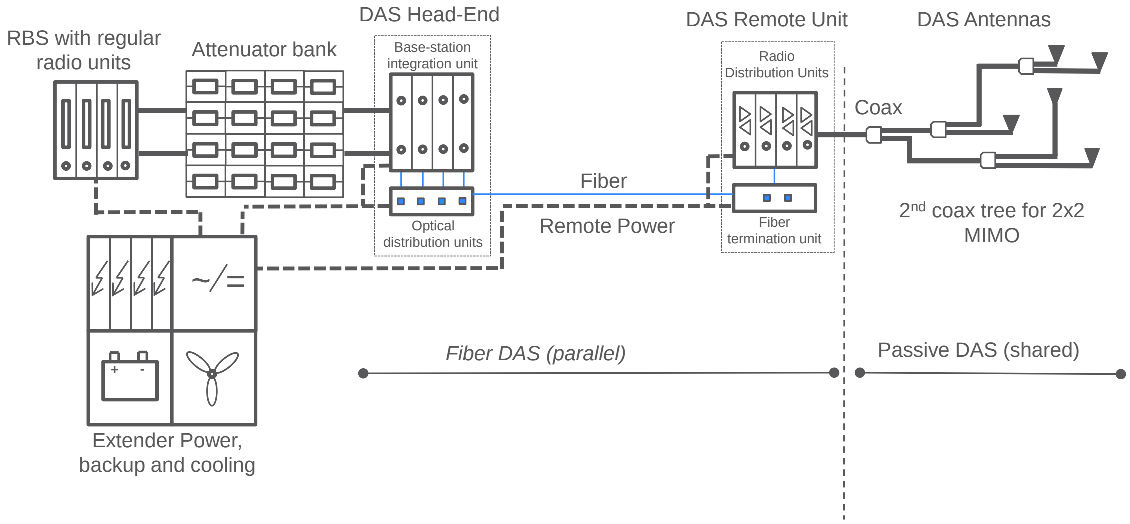

Figure 103: System diagram of hybrid DAS

Nowadays, new types of indoor small cell solutions target to provide high capacity with built-in scalability and flexibility, which DAS cannot do. One design is a Femto-like solution having small and less capable but fully equipped base stations deployed as indoor small cells, in a similar manner of WiFi access points. One problem is the frequent handover between cells such as ping-pong effects, which dramatically increases the handover signaling and thereby causes unstable mobile connectivity. Currently, some higher layer functional split like Femto-GW has been proposed to offload the handover signaling to mitigate the issue of frequent handovers. Nevertheless, the scalability of the solution is limited when so many small cells are deployed in large premises without the possibility of utilizing advanced coordination features coping with interferences between small cells. And it is not future-proof, since it is often difficult to support the evolved features standardized in 3GPP by software upgrades, which is similar to the situation of today’s WiFi access points. The operators need to replace the existing small cells to support new features every a few years. This implies repeated investments.

The other design is a FH-based design deploying small radio heads and utilizing the same baseband unit (BBU) design as used for macro cells. One advantage is that it can offer tightest coordination features such as combined cell, CoMP etc. by joint processing in a centralized BBU following the centralized RAN (C-RAN) architecture which provide the best possible performance scaling with the number of cells. It offers also the feature parity with the macro cells, which keeps a consistent user experiences across the whole network of indoor and outdoor. Furthermore, indoor small cells get simultaneous feature upgrades and roll-out as for macro cells. Therefore, we focus on further developing the FH-based indoor small cell solution to support multiplexing BH and FH in the same network.

<u>FH-based indoor small cell solution supporting crosshaul over Ethernet</u>

Based on the concept of 5G-Crosshaul, it is envisioned one network integrating BH and FH traffic. Figure 104 sketches an indoor crosshaul scenario with an FH-based indoor small cell solution and a WiFi network on one Ethernet network. The crosshaul is realized by a common Ethernet network (i.e. LAN in this case), where the FH traffic from RRHs needs to be packetized using Ethernet frame structure. In this way, the FH and BH traffic are aggregated by Ethernet switches, as shown in Figure 104 as well. The key benefit is to be able to use the IT LAN infrastructure to support both cellular networks (i.e. 2G/3G/4G/5G) and non-cellular networks like WiFi and wired Ethernet etc.

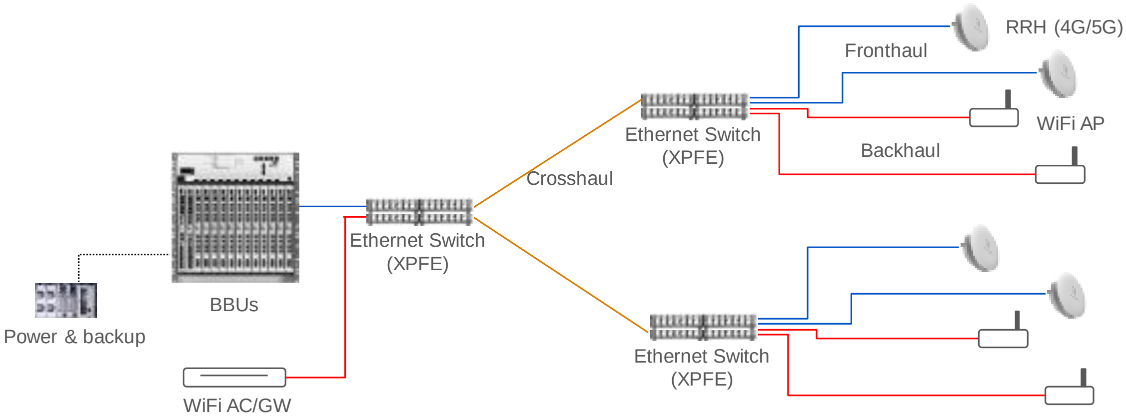

Figure 104: Example of an FH-based indoor small cell solution supporting crosshaul

In this work, we have focused on increasing the FH efficiency by FH compression [44] [45] which can significantly reduce the FH bit rates, and the system design with functions supporting advanced features of (1) **baseband resource pooling**, (2) **dynamic cell split** and (3) **energy saving** by switching off unused baseband resources and/or RRHs. In Section 4.5, we investigated the FH compression techniques improving FH efficiency by 3-5 times (also see in [44] [45]). In this section, we focus on the system level design.

To support the advanced features stated above, we introduce a new FH aggregation node into the system, as shown in Figure 105. Basically, the FH aggregation node is to reduce the aggregated FH traffic to/from the BBU to form one cell with multiple RRHs. This also increases the cell coverage, reduces the overall interferences between cells, and reduces the number of handovers needed. In downlink, the FH aggregation node multicasts one FH flow for one cell to multiple RRHs using Ethernet multicast function. In uplink, the aggregation node combines multiple FH flows from different RRHs to one FH flow for one cell and send to the BBU. Basically, it extracts the FH samples in the payloads of the Ethernet frames from different RHs, combines the FH samples and then puts it back into the payload. For compressed FH, the samples need to be decompressed first and then combined. The combined samples are compressed before sending to the BBU over the Ethernet network. In the example of Figure 105, the FH traffic through the LAN network is reduced by 4 times after FH aggregation, where 4 RRHs cover a big area as one cell.

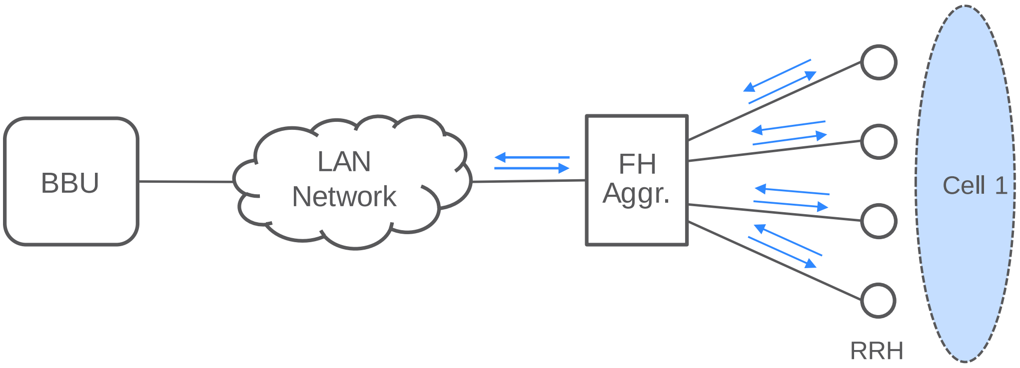

Figure 105: Example of FH aggregation for one cell

As shown in Figure 106, the FH aggregation node can also facilitate the feature of dynamic cell split. In Figure 106, the signals are combined and multicast in a smaller group of two RRHs each, which is different than that illustrated in Figure 105. This results in two cells instead one cell, which will increase the spatial reuse by a factor of two in this example and therefore system capacity is increased by allowing simultaneous transmissions in two cells. This is controlled by the BBU through the FH aggregation node by changing the RRH groups for combining and multicasting. This also enables the pooling of the baseband resources at the centralized BBUs. It can be used to dynamically distribute the system capacity on demand by creating more cells in high traffic demand area (i.e. many demanding users) and fewer cells in low traffic demand area. Comparing to DAS with many antennas as one cell, this approach can easily scale up the spatial reuse to one cell per antenna site level. Therefore, larger than 10 times more spatial reuse is achievable than DAS for large premises. It can also be used for energy saving by, for example, minimizing the number of cells and the number of active antennas when traffic is low, e.g. during nights. Then the unused baseband resources and the transceiver chains can be put into idle or sleep.

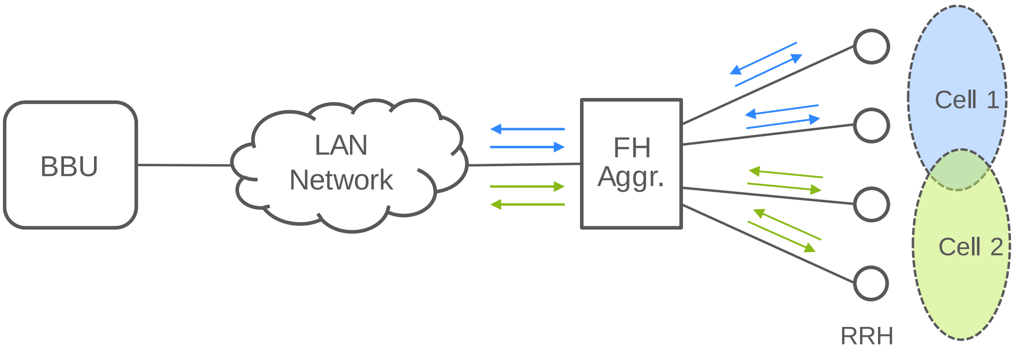

Figure 106: Illustration of cell split by FH aggregation

Furthermore, for a multi-building premise, the system can be easily extended to get connected with more buildings, as illustrated in Figure 107 for a 2-building case. The buildings can be inter-connected by fiber connections. This is the same as building up an enterprise network. This is the advantage of the system design being based on existing Ethernet networking technologies and deployment practices.

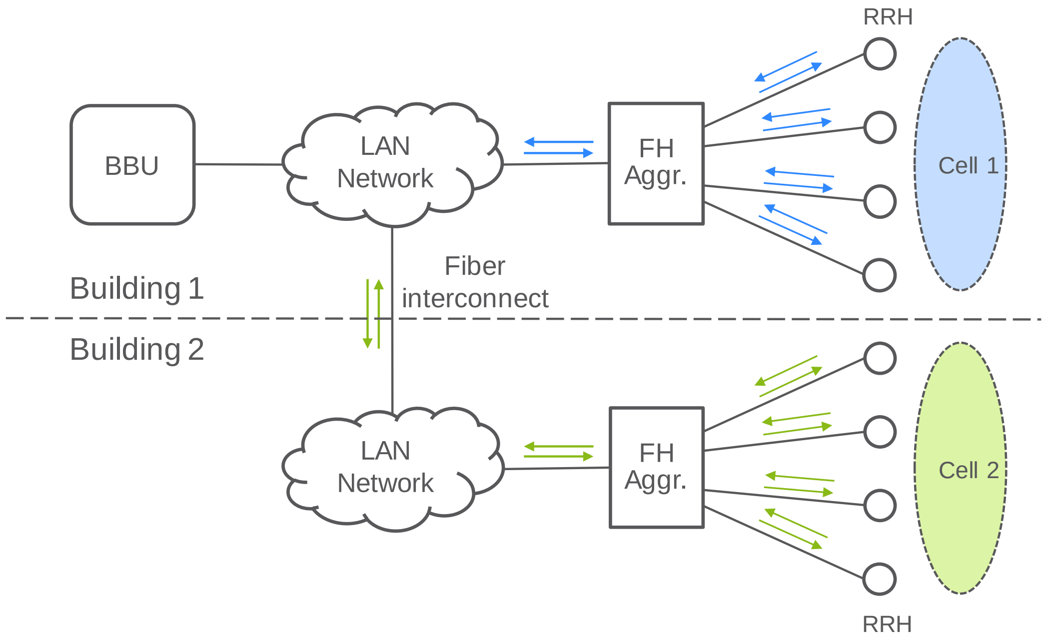

Figure 107: Illustration of baseband resource pooling over multi-buildings

System performance analysis

In this section, we analyze the number of FH flows in the number of 20 MHz antenna-carriers and then interpret the peak rates supported by the system. Assuming an LTE system of a 20 MHz antenna carrier, the service peak rate is 100 Mbit/s with 256 QAM. So we evaluate the service peak rate using different Ethernet bit rates (i.e. 1/2.5/5/10 Gbit/s) for FH with different copper-based Ethernet standards (i.e. 1000Base-T, 2.5GBase-T, 5GBase-T, 10GBase-T), as the copper-based Ethernet cabling are dominant in the in-building IT systems due to its low costs and ease to deploy.

The following lists the analysis assumptions.

- FH Compression: Assuming DL 4 times compression, UL 3.5 times compression based on the results presented in Section 4.5. UL compression is lower than DL due to the higher requirements in UL to cover a large dynamic range. The reference is based on 15 bits IQ data at CPRI sampling rate, i.e. sampling rate = 30.72 Msps for 20 MHz LTE signal.
    - Thereby, it is derived that the bit rates of one compressed 20 MHz LTE antenna-carrier FH flow are DL = 230 Mbit/s and UL = 264 Mbit/s
- Ethernet FH efficiency
    - Ethernet payload <= 1500 bytes.
    - FH C&M overhead in payload = 1/16 (in line with CPRI).
    - Ethernet frame overhead = 42 bytes (Preamble + header + FCS + IPG).
    - It can be derived that the Ethernet efficiency for FH <= 91%. In this study, we assume 91% efficiency.

Based on the assumptions above, the number of FH flows of 20 MHz antenna-carriers can be expressed as

$$N_{FH} = \left\lfloor \frac{R_E F_{FH}}{R_{FH}(1 + O_{CM})} \right\rfloor$$

where R_E is the Ethernet bit rate, $F_{FH} = 91\%$ is the Ethernet efficiency for FH, R_{FH} is the compressed FH bit rate, $O_{CM} = 1/16$ is the FH C&M overhead and $\lfloor x \rfloor$ represents the floor function taking the nearest integer smaller than x. Then the total peak rate supported by the corresponding Ethernet bit rate can be calculated as

$$r_{tot} = r_c N_{FH}$$

where $r_c = 100$ Mbit/s is the peak rate for a 20 MHz LTE carrier.

In this study, we focus on the copper-based Ethernet technologies, i.e. 1000Base-T, 2.5GBase-T, 5GBase-T and 10GBase-T, which are widely deployed dominating the indoor network solutions due to lower cabling and installation costs. Figure 108 shows the analysis results. Basically, 2.5 Gbit/s (2.5GBase-T) can support close to 1 Gbit/s air-interface peak rate, 5 Gbit/s (5GBase-T) can support close to 2 Gbit/s air-interface peak rate and 10 Gbit/s (10GBase-T) can support close to 4 Gbit/s air-interface peak rate. And UL peak rate is a bit less than DL, since the FH compression is assumed lower than DL. Given the results, the dense urban society use case, i.e. use case 3, for required peak rate of 2 Gbit/s can be approximately supported by 5GBase-T Ethernet and fully supported by 10GBase-T Ethernet. For the on-board small cells in the high-speed train use case, i.e. use case 1.a, all 1000/2.5G/5G/10GBase-T can support the requirements. Other use cases requiring 10Gbit/s peak rates cannot be supported by the considered long reach Ethernet technologies for standard reach of 100 meters per hop. Regarding the cabling, 1000Base-T and 2.5GBase-T need Cat 5e or better cable, while 5GBase-T needs Cat 6 or better cable and 10GBase-T Cat 6a or better cable. All these cables and the cabling installation are much cheaper than that for coax cabling used in DAS, using common IT installation practices.

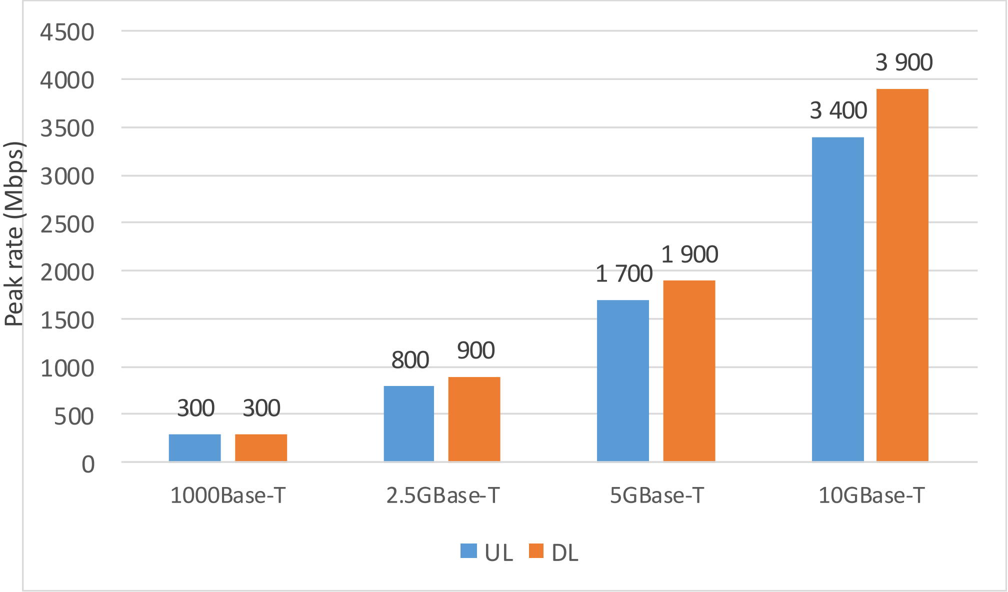

Figure 108: Peak rate analysis for different copper-based Ethernet technologies

Regarding the network latency, it includes transmission delay, queuing delay, processing delay and propagation delay. The propagation delay per 100-meter hop is about 50 ns. Processing delay of a switch is normally quite small (about 1 us or less). The processing for FH compression is also quite small as the complexity is low. e.g. for Huffman coding implementation. The transmission delays are listed in Table 20. for different Ethernet technologies assuming the longest Ethernet frame of 1500 bytes. It shows that even the slowest 1000Base-T technology only has about 12 us transmission delay. Comparing to the requirements of 100 us for FH, there is a large margin (at least more than 80 us with conservative considerations of all delay sources above) for the queueing delays in the switches and the de-jitter buffers at the receiver side. It should be sufficient to support a few switching hops, e.g. more than 3 hops.

Table 20: Transmission delay for different copper-based Ethernet technologies

	1000Base-T	**2.5GBase-T**	**5GBase-T**	**10GBase-T**
Transmission delay	12.34 us	4.93 us	2.47 us	1.23 us

5.1.2 Outdoor small cell network design

As mentioned in D2.1 [5], network densification by adding small cells plays a starring role to increase network capacity. In order to deploy a truly scalable and flexible outdoor small cells network able to serve the forecasted traffic demands, cost-effective wireless BH and FH (i.e. crosshaul) solutions are necessary. In this way, the efforts of deployment and re-configuration of the transport network required to support outdoor traffic profiles can be significantly reduced. With a plurality of choices for wireless transport technologies, this section focuses on mmWave technology due to its interesting characteristics. The vast amount of bandwidth available in mmWave frequency range may offer an opportunity to achieve the required data throughput and sustain the crosshaul traffic. Additionally, as mmWave signals are typically conveyed by narrow directional beams, effective spatial multiplexing can be achieved with minimum interference in multi-hop mesh deployments. For instance, as pointed out in D2.1 [5], a current EdgeLink Node (formerly known as EdgeHaul in [2]) is capable of delivering a peak throughput of up to 4 Gbit/s using 60 GHz band (V-Band), which is sufficient to support higher-layer functional splits. Note that potentially higher capacity can be unlocked when other mmWave bands (such as E, D, and W Bands) are employed. The ETSI millimeter wave transmission (mWT) industry specification group [39] is considering usage of these bands in the transport domain. Apart from the achievable capacity, several other issues should be addressed to make mmWave a feasible solution for 5G-Crosshaul transport network. For example, reducing the network latency, the development of a control plane scheme compatible with the required flexibility and adaptability capacities as stated in [35], and the required energy considerations for such deployments.

MmWave based links could be further enhanced when combined with OWC for long-range outdoor point-to-point communication. Infrared LEDs with highly directive optics together with spectrally efficient modulation allow high data rates. This, combined with rate adaptation mechanisms, could offer high availabilities figures also under severe weather conditions. Such hybrid links will be able to offer transmission at the required distances (up to 200 m) while providing a reliable low-cost solution for small cell back- and fronthaul in 5G.

Based on this context, the next sections cover different aspects of developed work within the 5G-Crosshaul project towards the deployment of the mmWave and OWC technology in an outdoor small cell scenario aiming to address the following questions:

- How can data-plane latency be reduced to support different fronthaul functional split profiles?
- How OWC compares to mmWave radio links in the same scenario and is it possible to aggregate effectively the capacity of both technologies?
- How can we develop the control-plane of an mmWave-based mesh network deployment to achieve the requirements imposed by 5G-Crosshaul network design?
- Can the outdoor small cell network operation be sustained with energy harvesting capabilities?

State of the art on the Data Plane

As mentioned previously, the trend of dense small cells deployment in 5G cellular networks is the use of wireless interfaces for backhaul/fronthaul solutions in premises where optical fibre is not available or too expensive to install in order to respond to the expected data-plane capacity demands. It is commonly accepted that wireless backhaul/fronthaul interfaces can be much more flexible and agile in terms of dynamic re-configurations, as compared to fixed optical networks. They can potentially support moving networks (such as in-vehicle-cells or drone-cells [36]), as well. With a plurality of choices for wireless transport technologies, mmWave has attracted a lot of attention on wireless transmission technologies for both 5G access and transport networks [37]. Thanks to the availability of its considerable bandwidth, mmWave based wireless hauling interfaces are quite promising to complement fixed optical solutions, for sake of delivering a seamless transport network.

Since mmWave can operate properly only when the radiated energy is concentrated on narrow and directional beams, a control framework for multi-hop mesh network will be employed to guarantee the presence of line-of sight (LoS) path in each mmWave transport link. Although SDN-controlled intelligent re-routing and multi-hops of an mmWave mesh network topology enable very flexible traffic path steering for wireless backhaul/fronthaul, latency may occur in each of the hops, mainly due to processing delay at each of the forwarding elements involved throughout the overall path. As the number of hops increases, the accumulated latency can become unsuitable for certain crosshaul traffic profiles. Figure 109 illustrates a schematic of a SDN-controlled mmWave-based crosshaul mesh network experiment conducted in the project. The measurement results suggest that the latency of mmWave mesh multi-hop transport network may be acceptable for backhaul traffic profile and fronthaul traffic profile covering higher layer functional split (between PDCP and RLC protocol stacks). However, latency-reduction mechanisms must be proposed in order to include mmWave technology in network deployments to support the diverse cases envisioned in 5G, as included in Chapter 2. An example of such deployment is a pure fronthaul deployment consisting of a single point-to-point connection between RRU and a BBU or between a RRU and a RRUs Gateway entity as defined in [38].

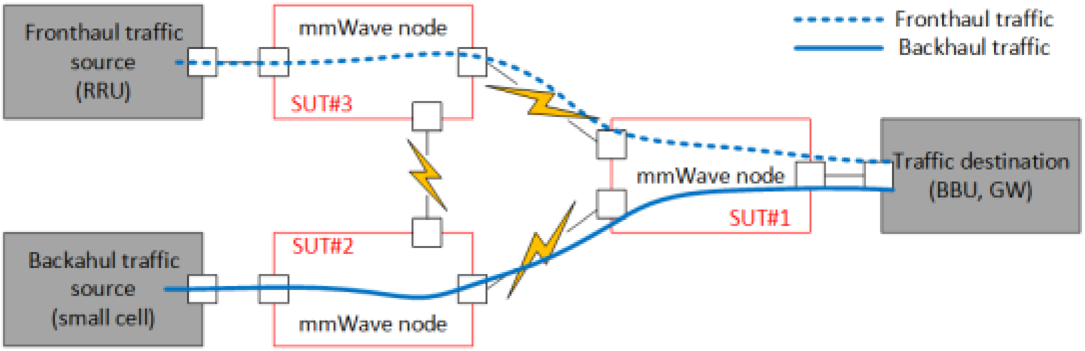

Figure 109: An illustration of a mmWave mesh transport network

Finally, the idea of using a RF backup for optical wireless is well known [38]. Previous results of laser based free space optical (FSO) systems with mmWave (V-Band) backup indicate high availabilities in various weather conditions, where the performance has been indirectly derived from recorded weather data.

Control and management plane

From the control-plane perspective, the 5G-Crosshaul network architecture aims to provide an adaptive and flexible design to manage and control the envisioned 5G transport networks, as detailed in D1.1 [1]. This architecture is based on two main concepts: Software Defined Networking (SDN) to provide a unified control, management and configuration of the 5G multi-technology transport network, and Network Function Virtualisation (NFV) to enable flexible function placement and cost-effective usage of the 5G-Crosshaul network resources.

Currently, the control, management and configuration of most of the outdoor wireless transport equipment is mostly based on proprietary web based Graphical User Interface (GUI) using different versions of Simple Network Management Protocol (SNMP) protocol or cumbersome command line interface (CLI) [5]. These tools can hinder the pursued objective in the 5G-Crosshaul project of an adaptive, unified and flexible control of a transport network composed by elements of different technologies and vendors. The need for specialised/trained personnel demanded by these tools make the appearance of network management problems caused by human errors relatively easy. This is mainly a consequence of the non-homogeneous methods to perform network control, management and configuration operations among equipment from different vendors.

As stated in D1.1 [1], the adoption of the SDN concept in transport networks allows the separation of the data and control planes, fostering network and device programmability. According to this concept, the XCI (5G-Crosshaul Control Interface) can communicate with the underlying XFEs (5G-Crosshaul Forwarding Element), via the SouthBound Interface (SBI). Hence, XCI collects and demands information about network topology, node and link capabilities. This information is then exposed to 5G-Crossshaul network applications via the NorthBound Interface (NBI) in order to achieve the required services and functionalities of the 5G-Crosshaul network.

Next, we review current developments of different SBI concepts/agents to integrate wireless outdoor network transport equipment into a SDN architecture.

When developing the SBI communication, we differentiate between two types of operations depending on their purpose. Control operations primarily deal with the forwarding/routing functionalities of network elements in the network. Management operations convey information regarding the configuration and administration of the elements. On the complex, flexible and programmable 5G-Crosshaul network, both control and management operations are present.

For the case of control operations, that is forwarding/routing operations, OpenFlow Protocol [7], defined by the Open Networking Foundation (ONF) is the de-facto protocol in the SDN environment, and thus, this protocol is considered within the 5G-Crosshaul network. However, for performing management operations via the SBI interface, there are several alternatives [5]. It is worth mentioning that current SDN controllers, such as OpenDayLight (ODL) or ONOS, support plug-ins for SNMP protocol, making possible the management of legacy equipment under a SDN network architecture. However, this approach may present scalability issues since different plugins have to be developed at the SDN controller side to deal with the characteristics of different equipment from different vendors.

For the case of management operations, in contemporary 5G-XHaul project [8], they propose extensions to the OpenFlow protocol to increase the number of statistics gathered at the wireless transport nodes to include radio conditions parameters so this information can trigger corrective actions (management operations) when the controller detects a precarious network state (e.g. link failure). Those adjustments may include any of the following actions: modification of the transmitted power, frequency channel management to reduce interferences, adjustment of carrier sense thresholds, etc. However, the way/protocols these actions are communicated to the different wireless transport nodes is not clearly specified in [8].

The Wireless Transport SDN group of the ONF presented in the last year several white papers ([9][10]) reporting the architecture and results from its still undergoing activities and proof of concepts (PoCs) with respect to the management of wireless transport networks. The aim of this work is to demonstrate the capabilities and benefits of utilizing a common Information Model (ONF TR-532) [11] for multi-vendor management of wireless network elements.

Initially, the first PoC of the ONF Wireless transport group [12] used an extension of the OpenFlow protocol to provide the management of wireless network elements, but from the second PoC, ONF selected NETCONF over OpenFlow as a protocol for configuration and management of the microwave devices for several reasons. NETCONF is a general-purpose management protocol, while OpenFlow is mainly intended for traffic forwarding. Also, YANG language can be used to implement the data model for NETCONF, hence, increasing the readability of the information model. Finally, some adapters, what ONF calls *mediators*, are used for translating the NETCONF/YANG information model to/from the existing proprietary management methods of each vendor’s device, allowing this approach (unified YANG information model + NETCONF) to be more flexible than an OpenFlow extension, thus, saving time in the development, the debugging and the model adoption phase.

Energy saving

Nowadays, the greenhouse gases emissions of ICT ecosystems already consume about 1500 TWh of energy annually, approaching 10% of the world's electricity generation and accounting for 2-4% of the carbon footprint due to human activities. In 5G, the trend is even worse, since mobile network operators will have to handle a much higher capacity demand [16], especially within urban areas for outdoor small cells deployments, where it will need to support up to 1000 times more capacity with respect to 4G due to network densification. This will dramatically increase the energy consumption while the hardware power efficiency will be improved at the same time. Nevertheless, according to the forecast from [17], the energy consumption of ICT might take a big share (up to 51%) of global electricity production by 2030, which would also translate in contributing to a significant amount (up to 23%) of greenhouse gas (GHG) emissions.

This led 3GPP, mobile vendors and operators to put the energy sustainability on their roadmaps to 5G. Analogously, the research community put a lot of effort into reducing the energy consumption of the radio communication networks, as testified by the vivid literature on the topic of energy efficiency (EE) [17]. One of the most promising solutions is represented by the dynamic *sleep mod*e (also called *switch ON-OFF*). However, this technique can guarantee only reduced energy savings [18]. According to this and considering the high-energy demand, the introduction of energy harvesting (EH) capabilities can represent a viable paradigm for enabling higher energy savings [20]. These works integrate the problem of EE by considering the erratic and intermittent nature of the renewable energy sources (RES) and the constrained amount of energy that can be stored. Up to now, the efforts concentrate in providing guidelines for dimensioning the network and the energy harvesting systems, while on-line approaches to control network elements have appeared only recently. In [21], the ski rental problem has been adapted to the ultra-dense small cell scenario for determining when to switch OFF. The analysis is carried out considering Poisson arrivals for energy and traffic, which may provide a non-realistic approximation to these processes. A solution based on Reinforcement Learning (RL) is presented in [22], where the performance of a single small cell (SC) has been optimized as a function of the local RES and storage conditions. However, the impact of the backhaul technology adopted is not being assessed. Moreover, the effect of multiple SCs simultaneously switching OFFs within the same area is not considered.

5.1.3 5G-Crosshaul extensions and features for outdoor small cell network reference scenario

This section addresses the three aspects described previously, i.e. data plane, control and management plane and energy saving. In the following, the key features and extensions investigated in 5G-Crosshaul are presented to improve mmWave-based crosshaul solutions, which could also be combined with OWC systems.

Latency-Reduction for mmWave-based wireless BH/FH

With a mesh network topology, multi-hop transmission can be applied to avoid radio blockage (which is particularly sensitive to mmWave) while extending the range of mmWave-based wireless backhaul/fronthaul. However, inevitable delay introduced by multi-hops transmission hinders the application of mmWave to some fronthaul use cases with stricter latency requirements (as shown in Table). The latency due to multi-hops is mainly caused by wireless packet decoding and re-encoding procedures at each of the 5G-Crosshaul Forwarding elements (XFEs). As the XFE would need to perform integrity checking of the whole data field of each of the received packets (based on CRC and interleaving mechanisms) before forwarding it, the delay incurred at a XFE is expected to increase with larger packet sizes. Basically, latency occurs because forwarding can only begin after the whole packet is decoded.

Hence, in a more centralized deployment using **Point-to-Point (PtP) transmission without a mesh topology**, reduced latency figures are achieved since there is not packet forwarding throughout multi-hop routes. However, there is a trade-off between the resultant latency and the risk of signal blockage. Nevertheless, if the BBU and RRU locations are properly planned, the probability of signal blockage can be reduced. However, further reduction on the latency figures in such mmWave wireless transport deployments can be tackled with a **fast-forwarding scheme** devised in 5G-Crosshaul project, as described below.

In the proposed fast-forwarding scheme, the wireless packet is divided into multiple segments called *codewords* that can be encoded and decoded independently. This is presumed in 5G-Crosshaul project that each codeword is encoded with LDPC. Furthermore, since no interleaving is applied across codewords, they are independently decodable. Thus, each codeword can be decoded even before the whole packet is completely received. A general mmWave packet structure at PHY level for fast-forwarding is shown in Figure 110.

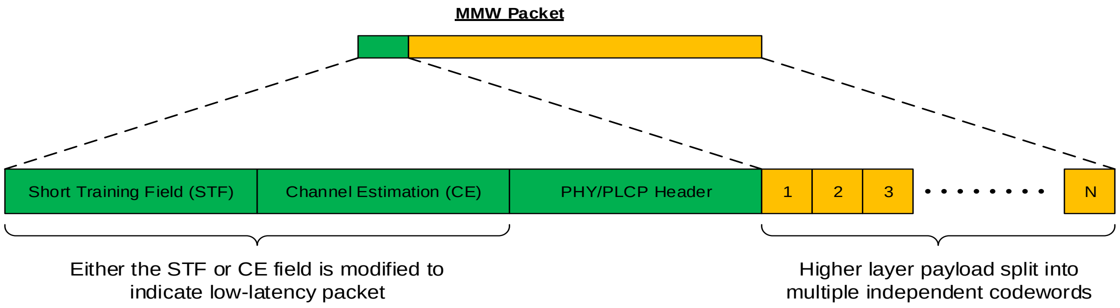

Figure 110: General mmWave packet structure for fast-forwarding.

Since the wireless packet maybe associated to different latency requirements (e.g. corresponding to different fronthaul functional split profiles), STF or CE field of the packet can be modified to indicate the latency profile of a packet. For instance, the order of Golay sequences in the PHY CE preamble can be reversed to indicate low-latency traffic, and the payload will be accordingly processed as multiple independent codewords. Such implicit indication of traffic type is shown in Figure 111.

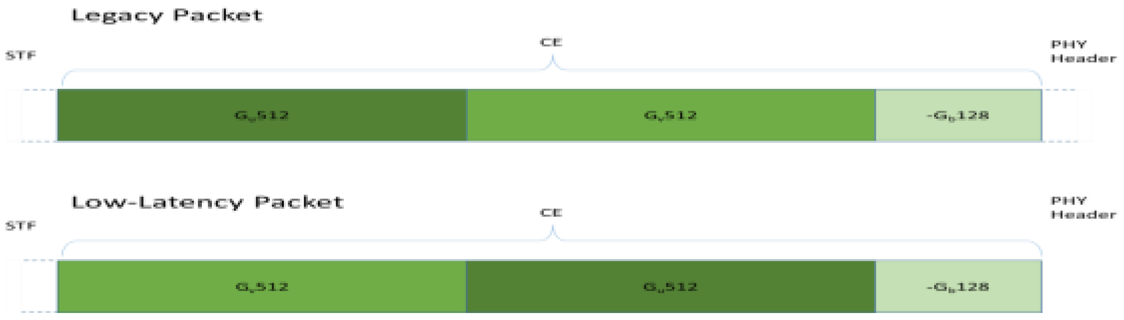

Figure 111: Golay sequence order-based traffic type indication

As a wireless packet is received in one radio port of the XFE, the received codewords can begin to be processed in the FEC decoder with a first-in first-out fashion prior to the reception of the remaining codewords. Once the codeword is validated, it is passed to the outgoing radio port of the XFE for purposes of forwarding even before the whole wireless packet is received. An illustrative comparison between the conventional forwarding (hop-by-hop packet transmission) and fast-forwarding is shown in Figure 112. This is clear that fast-forwarding is able to relay the packet in a more hastened manner as compared to hop-by-hop packet transmission.

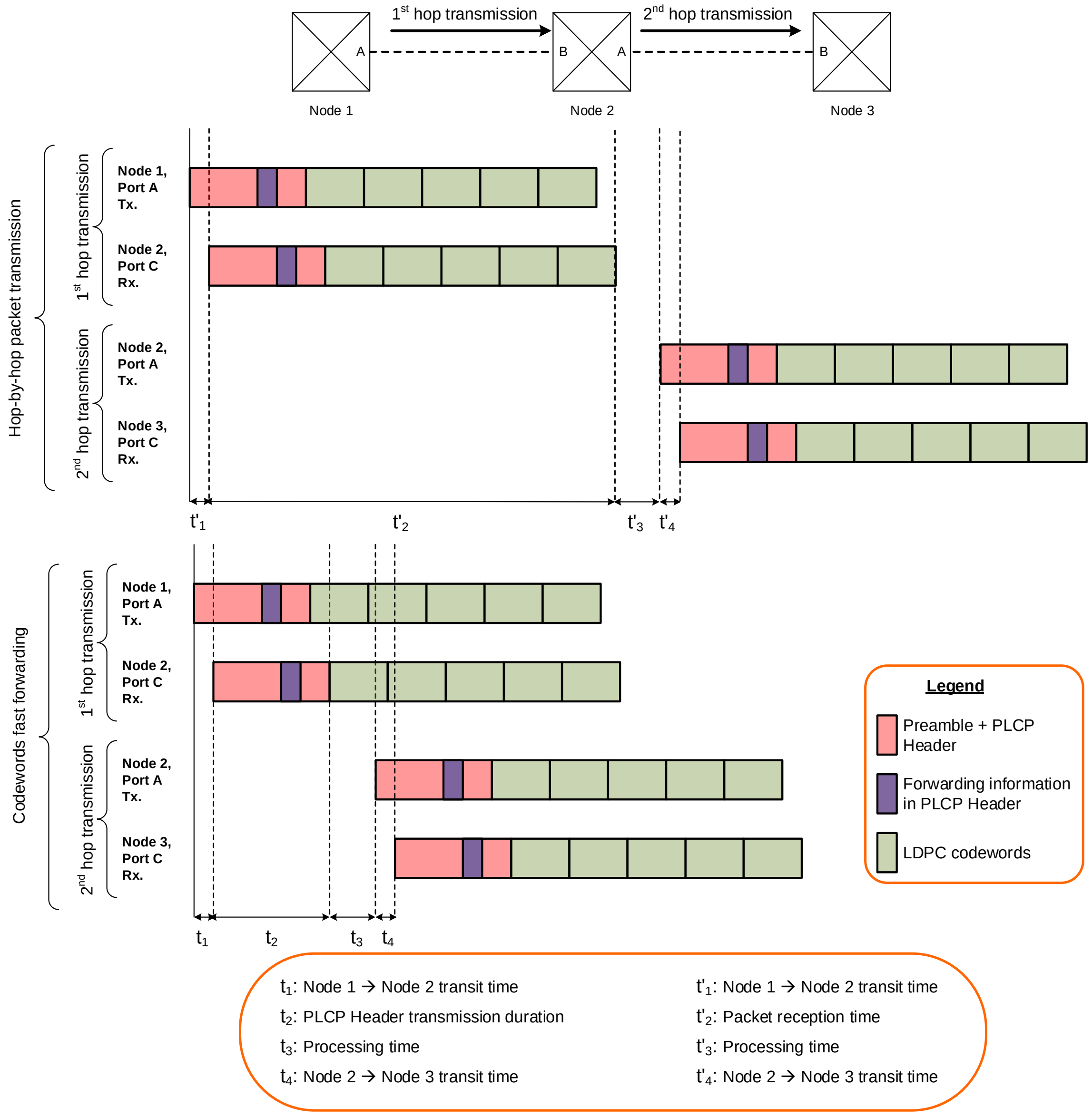

Figure 112: Illustrative comparison between conventional forwarding and fast-forwarding

In contrast to the conventional approach, where cyclic redundancy is applied to the whole data field of a wireless packet, per codeword CRC can be employed in the proposed fast-forwarding scheme. That is, in order to ensure that the reception of codeword is correct, a CRC is attached for each codeword and used to check the error whether the corresponding codeword is successfully received or not. If a codeword is detected as erroneous, the XFE will log the index of the incorrect codeword, and which will be sent in the NACK transmission to the previous hop source node. In addition, as a packet contains multiple codewords, a few bits or bit stream may be inserted for each codeword to for identification and out of order purposes. Alternatively, the identification of each codeword can be implicitly indicated using per-codeword CRC mask. When a packet is correctly received, the receiving node sends an ACK response. However, if there are one or more missing codewords in the received packet, the receiving node responds with a NACK containing the fields that identify erroneous codewords in the packet, so re-transmission can be undertaken by the source node accordingly. In yet another alternative, codeword level errors may be detected by observing the LDPC decoder syndrome output. If the syndrome indicates that the codeword is in error, which may be logged by the XFE, to be later reported to the transmitting node. This approach eliminates the overhead associated with codeword level CRC.

5G-Crosshaul Hybrid OWC/mmWave system for capacity aggregation

Figure 113 presents the hybrid OWC/mmWave node developed for the first study measuring real-time throughput results in a real outdoor deployment of an aggregated OWC/mmWave link and focused on the dependence on various weather parameters.

Figure 113: OWC and mmWave (V-Band) link in waterproof housings.

The developed OWC system [93] achieves a peak gross data rate of 1 Gbps. A commercially available real-time digital signal processing (DSP) unit with 100 MHz bandwidth using OFDM and a fine-granular rate adaptation with modulation formats up to 4096 QAM is used. The DSP includes all PHY and MAC functions as well as analog-to-digital and digital-to-analog converters. In combination with proprietary LED driver and photo-receiver electronics, high data rates are achievable.

At the transmitter, the low-cost infrared LED SFH 4451 with an active semiconductor area of 0.3 x 0.3 mm² was used with a central wavelength of 850 nm. The directly on the LED chip mounted parabolic reflector realizes a divergence of 17° at full width half maximum (FWHM) and enlarges the effective area of the LED to 1.65 mm². A convex lens with 166 mm focal length and 100 mm diameter reduces the divergence of the beam to 0.285° FWHM. The resulting spot at 100 m has a radius of only 0.5 m. The spot is practically homogenously illuminated, in contrast to the Gaussian beam profile of laser based free space optical systems. In this way, the initial alignment of the link is simplified and the system robustness against small misalignments is improved. Transceivers could, thus, be mounted on a streetlight, for instance.

The same convex lens focuses the received power onto the photodiode (Hamamatsu PD - S6968) having a relatively large effective area of 1.5 cm². Likewise the lens reduces the field of view (FOV) of the receiver to 2.4° to decrease background radiation, e.g. due to sunlight scattered at a cloud.

Optics and electronics were setup in a waterproof housing to withstand the outdoor conditions. A sunshade was installed to further reduce the influence of scattered sunlight.

Next to the OWC link, a commercially available 60 GHz link Siklu EtherHaul 600 device was installed. It offered a data rate up to 1 Gbps and operated in the V-Band (from 57 GHz to 64 GHz). The single-carrier waveform covers a bandwidth of 500 MHz. Coarse rate adaptation with modulation formats up to 64 QAM is used.

Progress towards 10 Gbps at 1 km with an optical wireless link

Most of the laser diode based optical systems that are commercially available today are able to bridge high distances up to 1 km. While high data rates are achievable, due to the very small optical spots, active tracking of the laser beam is necessary. In order to bridge high distances, a high link margin is mandatory to achieve high availabilities. Thus, costly avalanche photodiodes are used to increase the robustness of the links in bad weather conditions. A fixed data rate based on on-off-keying (OOK) is possible as long as the available link margin is not depleted. Heavy fog events though, representing the most challenging weather situations for optical links, can deplete this margin and the link will then be interrupted, which leads to a reduced link availability [94].

However, for mobile wireless front- and backhauling of small cells in modern 5G networks cost efficient solutions have to be developed. In the 5G Crosshaul project the possibility of implementing the concept of economic, short-range systems with rate adaptation to higher data rates and longer distances was evaluated. In particular, the possible use of infrared laser diodes, Si-PIN photodiodes, as well as an optical spot expansion was studied on a laboratory test level.

The combination of high optical output power and a high modulation frequency is mandatory and is the basis for the here proposed 10G link concepts. The following parameters arise out of the requirements for the optical link:

- Bandwidth ≥ 1 GHz (at high output power)
- Optical output power ≥ 100 mW
- Wavelength > 700 nm
- Directly-modulated light source
- No active beam tracking – optical spot at target c. Ø50 cm

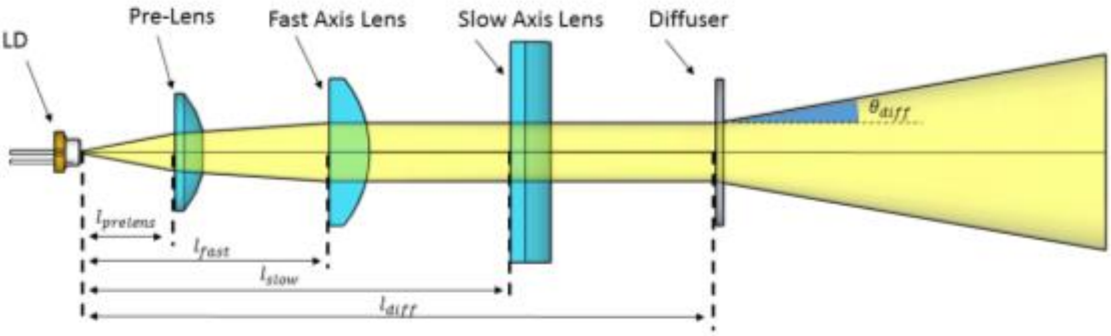

Figure 114: Illustration of the optical concept for the laser beam configuration. The Pre-Lens decreases the laser beam divergence. Two cylindrical lenses collimate the beam in fast and slow axis respectively. A subsequent optical diffuser spreads the beam at a defined divergence (θ_{diff}) and gives it a uniform power distribution.

A first objective of our work concentrated in the laser beam configuration. In order to achieve a relatively large and homogeneous optical target spot, a dedicated lens set, as well as special diffusors are necessary (see Figure 114). Etched fused silica diffusers allow for low optical losses with transmission efficiencies up to 90% as well as freely definable beam divergences. Experimental results with a corresponding lens and diffusor combination demonstrated a homogeneous Ø30 mm laser beam at an 8.5 cm distance (see Figure 115). Through a different diffuser with a significantly lower divergence angle the targeted optical spot at 1 km can easily be achieved.

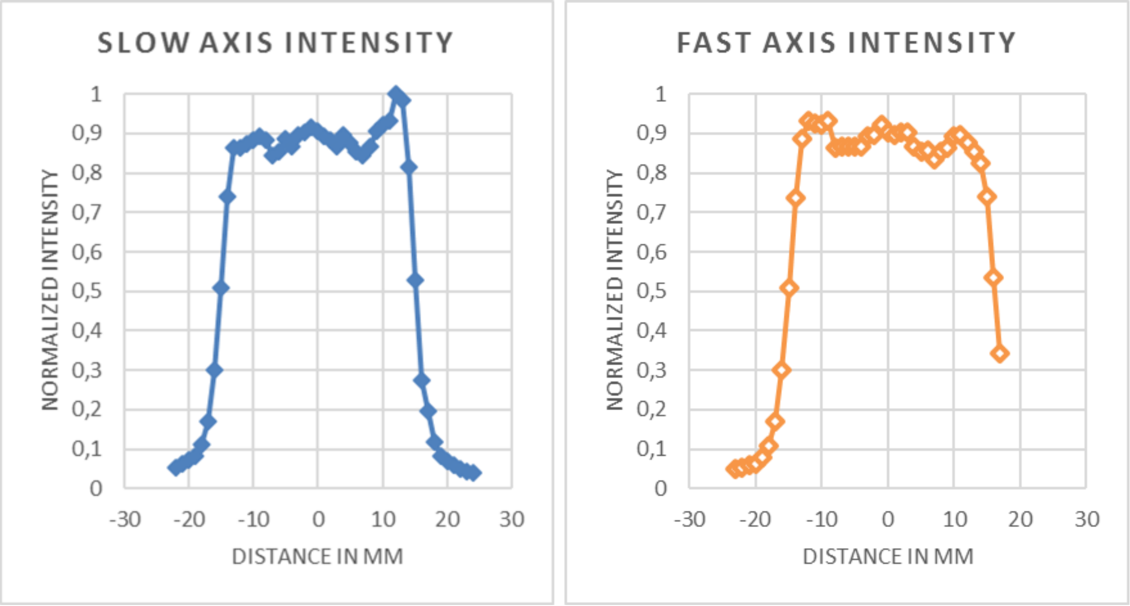

Figure 115: The intensity profile of the laser beam after its propagation through the optical beam configuration set (propagation length = 8.5cm, divergence angle = 20°). Both plots are normalized to the highest overall value.

A second aspect to achieve the previously mentioned goal is the expected bandwidth from near infrared high-power laser diodes at large signal modulation. Corresponding experiments have shown overall 3 dB frequency bandwidths well beyond 1 GHz (see Figure 116) at various bias currents.

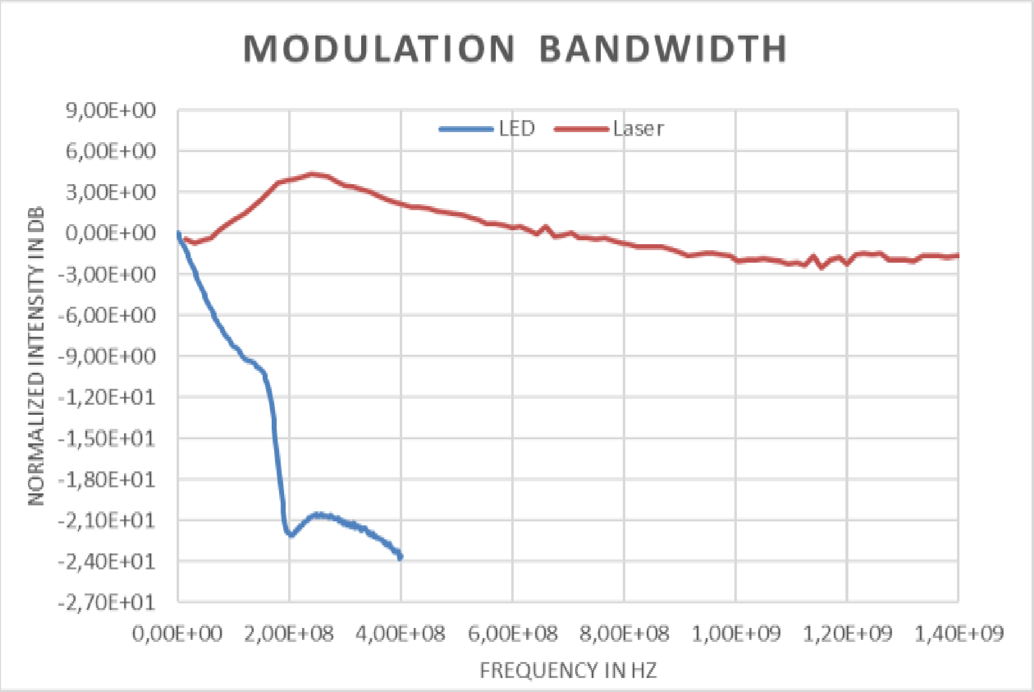

Figure 116: Measured results of the modulation bandwidth for a high-power near-infrared laser diode (Panasonic LNCT28PS01, red curve) showing a 3 dB bandwidth well beyond 1 GHz. A reference modulation bandwidth measurement of a near infrared LED (OSRAM SFH4451 – blue curve) shows the important advantage of implementing a laser diode as a light source for a 10 Gbps OWC link.

In conclusion, optical wireless technology can also be expanded for 10Gbit/s over 1 km links. Preliminary results in the lab have shown that relatively large optical spots (c. Ø50 cm at the target distance) are feasible without significant optical losses through a lens and diffuser combination. High-frequency measurements confirmed the larger modulation bandwidth (> 1 GHz) of high-power near-infrared laser diodes as a light source for a 10 Gbps OWC link.

5G-Crosshaul SBI agent for outdoor wireless small cell transport nodes

The SBI SDN agent developed within 5G-Crosshaul at the outdoor small cells wireless transport nodes has two components, which decouple the control operations from the management operations [14]. On one hand, we have the Forwarding Agent (FA) which is based on the OpenFlow protocol, provided by the implementation of the open source software switch running in the transport node. This agent oversees forwarding actions and it is technology-agnostic of the underlying wireless transport technology (e.g. mmWave, WiFi) since the matching headers taken into account to establish flow rules present an equivalent frame format.

On the other hand, each wireless transport node counts with its own Wireless Interface Agent (WIA), which exposes to the SDN controller and upper layers in the 5G-Crosshaul network an Application Programming Interface (API) in charge of configuring the underlying wireless network resources. A technology neutral information model using YANG modeling language is transformed into a JSON object which is exchanged between the SDN controller and the outdoor small cell wireless transport nodes via RestConf interface over HTTP requests, following the idea of the Common Orchestration Protocol (COP) used for the NBI and further developed within the 5G-Crosshaul project [13]. A Uniform Resource Identifier (URI) uniformly identifies every exchanged resource. This approach was followed because of its flexibility, scalability and commodity for practical implementation. The addition of new features is handled easily by extending the information model and defining its associated URIs. However, the extension of OpenFlow protocol requires, besides the definition of new structures and parameters, the inclusion of code into the internals of the used open source software switch and the SDN controller, limiting the scope and scalability of the solution.

The part of the WIA which resides in the SDN controller is the element called *"SBI_client"*. This element communicates with the *"SBI_server"* running at each outdoor small cell wireless transport node. When a transport node attaches the network (and during network steady state), the *SBI_client* can request (and modify) all the transport node configuration defined in the YANG information model accessing the URI */sbi/config/interface/<interface_name>/*. The *SBI_server* implements HTTP operations POST, PUT, DEL, GET for this kind of URI. As its turn, the *SBI_client* can perform GET and PUT operations on the specific parameters defined in the YANG model through the URI */sbi/config/interface/<interface_name>/ <parameter_name>/*. In addition, asynchronous notifications of network events are also modeled in the *SBI_server* following a publish/subscribe pattern using also the Restconf URI API. The SDN controller can subscribe to notification events and propagate this information to upper layers. The workflow for this functionality starts with an NFV deployed within the node to, for instance, monitor interferences in the wireless channels. This NFV generates and event, which is received by the *SBI_server*. The server redirects this event to its subscriber. The SDN controller, subscribed to this event, can inform a network app, which can trigger a frequency change in this interface.

Table 21 summarizes the set of parameters supported currently by the RestConf Agent to support the management of wireless network resources, which are derived from the requirements defined in [5] and based on current capabilities of available hardware, whose performance characterization has been reported in [5].

Table 21: Set of parameters defined in the wireless outdoor small cell scenario RestConf agent

Parameter	Config	Monitor	Inventory
Supported channels			X
Channel central frequency	X	X	
Supported channel bandwidth			X
Channel bandwidth	X	X	
Supported MCS			X
Current MCS	X	X	
Max. tx power per channel			X
Transmission Power	X	X	
Link Status	X	X	

As mentioned before, the feasibility of the configuration of some of these parameters depends on the hardware drivers capabilities of the interfaces (mmWave, WiFi) present in the transport node, which are still under development. In order to handle these particularities, the *SBI_server* follows the idea of *mediator* as in [9], supporting a specialization of the implementation of some operations defined in the YANG model depending of the type of technology/equipment at the interface of the transport node.

The *SBI_server* has been built following a three-tier architecture [15]. Based on this architecture, the *SBI_server* presents a user interface layer, a domain layer and the data layer. The aim of this architecture is to allow any of the three tiers to be upgraded or replaced independently in response to changes in requirements or technology and at the same time provide scalability and maintainability to the system. The user interface layer is in charge of interacting and offering the mentioned URIs to the *SBI_client.* The intelligence resides in the domain layer where a plug-in system allows defining the implementation of the YANG model based on the type of interface using the *mediator* element [9]. Finally, the data layer contains the data persistence mechanisms (e.g. database servers, file shares) and the data access APIs to expose the data to upper layers. In case of an incidence in the service supporting the *SBI_server* interface, the data layer saves the current information and retrieves it after the incidence is solved.

The development of this SBI agent follows the same philosophy presented by the ONF, decoupling control from management operations. It is worth mentioning this alignment even though our development started at the beginning of the 5G-Crosshaul project, back in 2015, before the ONF wireless transport group released results [9] and code following this approach in June 2016 and August 2016, respectively. However, they differ in the underlying protocol communicating with network elements. While the approach of ONF is based in NETCONF, the solution herein presented in based in RestConf, which provides more flexibility to add new features and does not impose a fixed data management system.

5G-Crosshaul local agent for outdoor small cell with energy harvesting capabilities

The local agent in each SC runs a machine learning solution based on the Q-learning (QL) algorithm to dynamically switch ON and OFF both the backhaul and the access according to the available harvested energy budget, the user traffic demand and the energy consumption of the node. QL is designed to learn a policy for optimizing the system performance in terms of throughput and energy efficiency by directly interacting with the observed environment. The decision-making process of each agent is defined by a Markov Decision Process with state vector $\vec{x_t} = \{x_t^1, x_t^2, \dots, x_t^N\}$$, where x_t^i is the state associated with SC$_i$ (will be described in the following), at time t. Based on x_t^i, each local agent *i* independently chooses an action $a_t^i$$ from an action set A. As a result of the execution of this action, the environment returns an agent dependent reward r_t^i, which allows the local update of a Q-value, $Q(x_t^i, a_t^i)$, indicating the appropriateness of selecting action a_t^i in state x_t^i. The Q-value is computed according to the rule:

$$Q(x_t^i, a_t^i) \leftarrow Q(x_t^i, a_t^i) + \alpha \left[r_t^i + \gamma \max_a Q(x_{t+1}^i, a') - Q(x_t^i, a_t^i) \right]$$

where α is the learning rate, γ is the discount factor, x_{t+1}^i is the next state for agent i and a' is the associated optimal action. For more details on RL and Q-learning the reader is referred to [23].

Considering outdoor SCs with energy harvesting capabilities, we defined the QL algorithm as follows:

- *State:* $x_t^i = \{S_t^i, B_t^i, Lx_t^i\}$

- *Action set*
    - *ON*: the SC is maintained at its full operational mode
    - *OFF*: the SC is switched OFF, users will be moved to macro when possible, otherwise dropped.
- *Reward function:*

$$r_t^i = \begin{cases} 0 & B_t^i < B_{th}\ or\ D_t > D_{th} \\ k\text{x}T_t^i & B_t^i \geq B_{th}\ and\ D_t \leq D_{th}\ and\ SC\ is\ ON \\ \dfrac{1}{B_t^i} & B_t^i \geq B_{th}\ and\ D_t \leq D_{th}\ and\ SC\ is\ OFF \end{cases}$$

where S_t^i represents the amount of harvested energy, B_t^i is the battery level and L_t^i is the load requested in the SC. D_t is the traffic dropped by the entire network (i.e., non-served users), T_t^i is the throughput of the SC. D_{th} is the threshold on system drop-rate (i.e., macro and SC), while B_{th} is the security threshold of the battery state of charge (SOC). This threshold is used to maintain the batteries in the correct SOC operative range $\Delta_{SOC} = [20\%, 90\%]$, in order to avoid to rapidly jeopardize the battery performance [24]. Each action is taken every hour. For a more comprehensive description of the algorithm, the reader can refer to [25].

The output of the agent is part of the Energy Management and Monitoring Applications (EMMA) framework designed in WP4. The main goals of EMMA are to monitor the energy parameters of the fronthaul and backhaul network elements, to estimate their energy consumption and trigger reactions. EMMA operates over different kinds of network technology domains. In particular, a monitoring layer, developed on top of an SDN controller, collects, aggregates and elaborates energy-related measurements for network domains (e.g., the battery level of the small cell B_t^i and the other main features of the Q-learning algorithm). Energy management is then implemented above the monitoring application. Hence, in this case, we consider a two-tier controller: one local based on Q-learning and a network-wide one collecting statistics from all the network elements. Thanks to energy monitoring functionalities of EMMA, we can design a dedicated EMMA application for multi-tier networks with energy harvesting capabilities (EMMA-EH) that considers network wide statistics for designing more energy efficient (EE) Radio Resource Management (RRM) policies interacting with the local ones. The goal of EMMA-EH is to improve the system EE and reduce its drop rate by assisting the SC local agents in their learning process.

5.1.4 Performance evaluation of 5G-Crosshaul extensions in the outdoor small cell network reference scenario

This section includes the evaluation of proposed 5G-Crosshaul work in two of the three aspects described previously, namely data plane and energy saving. Quantitative results for the control-plane solution are not provided in this internal report since control-plane issues are beyond the scope of WP2, belonging to the global 5G-Crosshaul network solution which is developed in the other work packages.

Laboratory measurements for fast-forwarding technique in mmWave-based wireless crosshaul

As discussed previously, mmWave point-to-point (PtP) transmission without mesh topology and fast-forwarding techniques could be applied to reduce the latency. In order to test if these latency reduction schemes have the potential to address some more strict requirements of certain functional splits in fronthaul interfaces, some laboratory measurements have been conducted.

In the experiment setup, point-to-point packet transmission from a server to a client laptop is assumed, in which 1512 bytes UDP packets are generated using *iperf*. Also, the channel condition has been configured to be sufficiently good to support a packet error rate (PER) lower than 2%. Only one sector of the EdgeLink is used. Moreover, some additional delay that is not measurable, such as latency that occurs in the Ethernet core and buffering, are taken into account in the simulations. Both of the cases with and without fast-forwarding have been examined, with adoption of MCS2 (BPSK with ½ coding rate) and MCS9 (QPSK modulation with 13/16 coding rate) as the modulation and coding schemes. Note that when fast-forwarding is enabled, each packet is divided into multiple segment codewords and encoded separately at the source transmitter, and some of these segments are transmitted even before the whole packet is received from the server to expedite the process. The measurement results of average throughput and latency are summarized in Table 22:

Table 22: Preliminary laboratory evaluation results of PtP mmWave-based crosshaul transmission with and without applying fast-forward techniques

	Without Fast-Forwarding		With Fast-Forwarding	
	Throughput (Mbit/s)	Latency (µs)	Throughput (Mbit/s)	Latency (µs)
MCS2	163	154	162	110
MCS9	360	111	357	89

Based on these preliminary laboratory results acquired from both measurements and simulations, it is clear that PtP configurations without mesh topology allows the latency to approach the requirement of low-layer functional split (~100 µs) as listed in Section 2. By incorporating fast-forwarding techniques into the mmWave transport, the latency can be further reduced to below 100 µs. Furthermore, it is worth noting that the throughput can be further increased to satisfy the throughput requirements defined for some uses cases included in Section 2 by using mmWave bands above 100 GHz (such as W-Band and D-Band) where much broader bandwidth is available. The trend of shifting to higher mmWave bands is well aligned with the work undertaken by the ETSI millimeter wave transmission (mWT) industry specification group [39]**.**

Performance evaluation of 5G-Crosshaul Hybrid OWC/mmWave system for capacity aggregation

This section presents the results of the first time study measuring real-time throughput results in a real outdoor deployment focused on the dependence on various weather parameters of an aggregated OWC/mmWave link developed within 5GCrosshaul project.

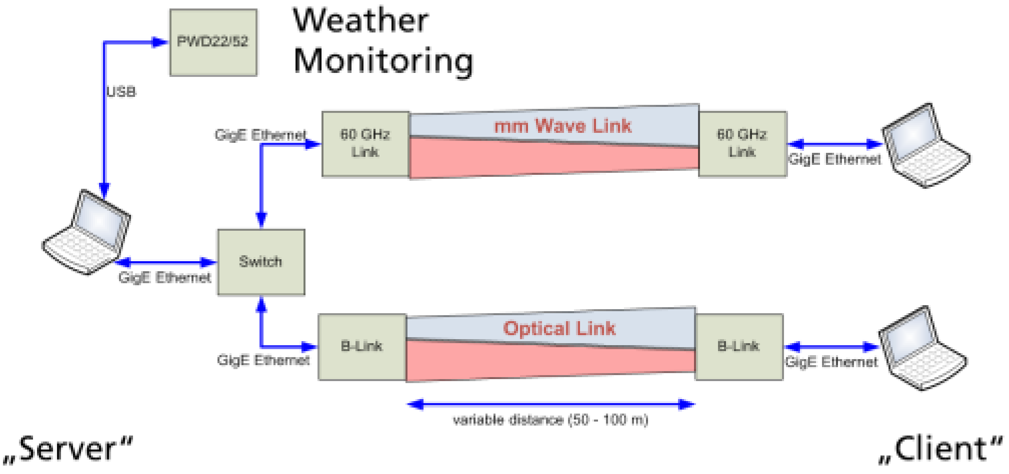

Figure 117: Measurement setup for a long-term monitoring of a hybrid optical/mmWave link in an outdoor deployment in Berlin

The long-term measurement took place in Berlin, Germany, based on a measurement setup schematically shown in Figure 117. The results presented here are from the period beginning December 2016 until mid-April 2017. The OWC and 60 GHz links were deployed outdoors at a distance of 100 m, between rooftops of the Fraunhofer Heinrich Hertz Institute (HHI) and the Technical University Berlin (TUB), with a height difference of 25 m to emulate a macro-cell-to-small-cell backhaul scenario (Figure 118). Next to both frontends at HHI, a weather station Vaisala PWD22 was deployed to study the impact of weather. Visibility (with a maximum value of 20 km) and precipitation (rain, snow, fog) were monitored every two minutes. The throughput of both links have been also recorded simultaneously so that weather effects on the performance could be studied in detail. Moreover, statistical results were obtained regarding the suitability for reliable backhauling of small cells.

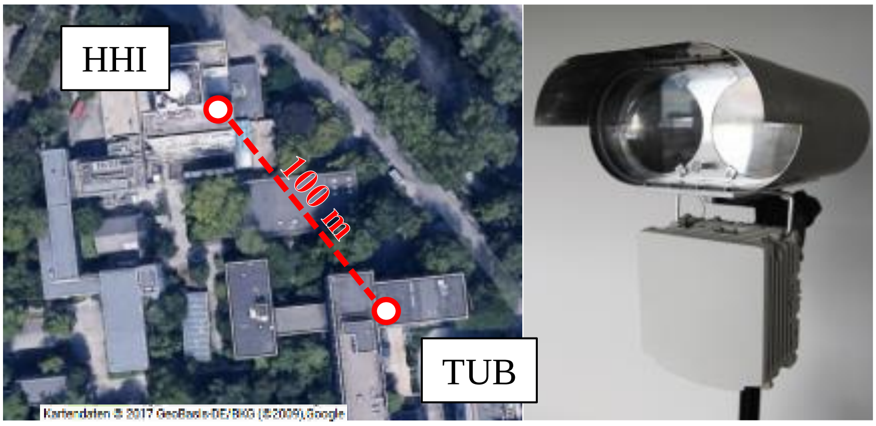

Figure 118: Left: Measurement site between the HHI and a TUB building with a transmission distance of 100 m and a height difference of 25 m. Right: OWC and 60 GHz link in waterproof housings.

Some remarks on the instantaneous weather effects on the performance of the hybrid OWC/mmWave system are shown next._In an outdoor scenario, visibility-reducing atmospheric effects, like snow, rain or fog are the main impairments for wireless backhaul links. Particles in the air scatter or attenuate the transmission signal and lead to a reduction of received power at the OWC, as well as the 60 GHz link. This leads to a reduced signal-to-noise-ratio (SNR). Nevertheless, as rate adaptation in implemented in both links, the connection remains stable, even if atmospheric losses of more than 170 dB/km (lowest measured visibility of 94 m) occur. In comparison to fixed data rates used in conventional free-space optical (FSO) links, no link margin is necessary and the link operates spectrally efficient. As an example for the instantaneous influence of bad atmospheric conditions, the worst hybrid link performance in the whole measurement period, on January 11, 2017, is described in Figure 119.

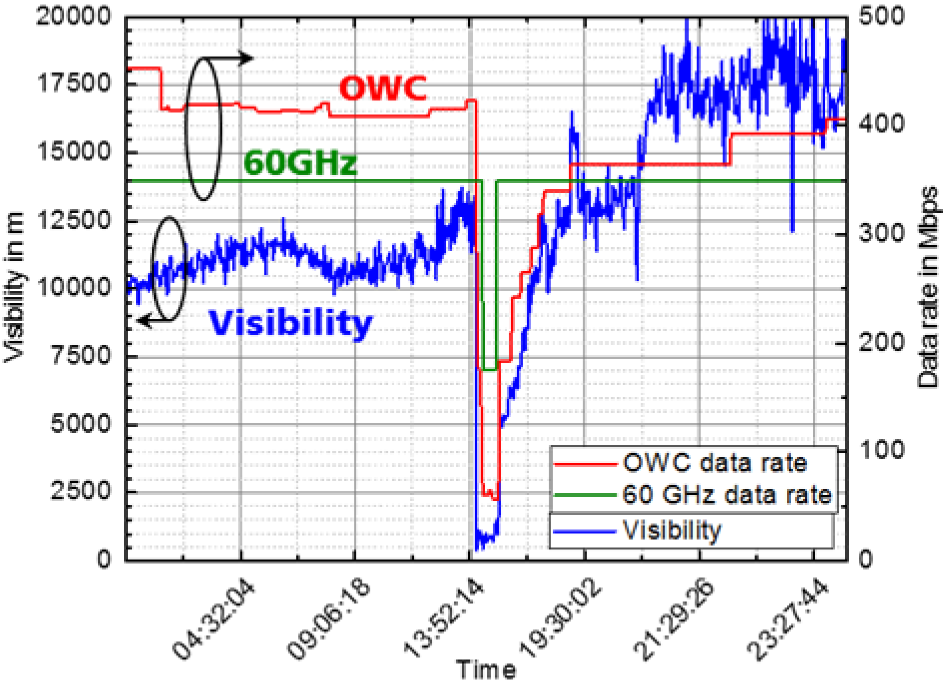

Figure 119: Visibility (blue curve), OWC data rate (red curve) and 60 GHz data rate (green curve) variation as a function of time. The displayed weather event occurred on January 11, 2017 with reduced visibility and heavy snowfall.

In Figure 119 the visibility (blue curve), OWC data rate (red curve) and 60 GHz data rate (green curve) are shown as a function of time. At around 14:00h, due to heavy snowfall the visibility drops suddenly from 12500 m to only several hundred meters. With the beginning of snowfall and the reduced visibility, data rates of both, OWC and mmWave, links drop at the same time. The data rate of the OWC link rate dropped to around 55 Mbps, while the mmWave link rate was reduced to 175 Mbps. The expected diversity of both links, which would require uncorrelated impacts of the weather, could not be observed in this case. Nevertheless, the minimum aggregated data rate of the hybrid link was 230 Mbps, which corresponds to the minimum aggregated data rate during the whole 4.5 months' period.

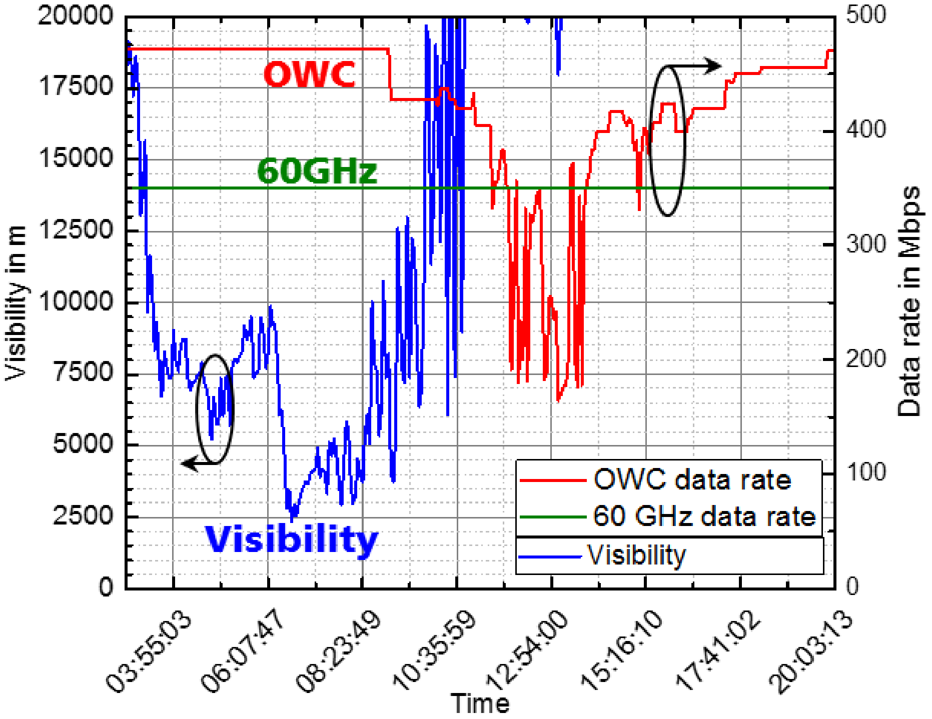

Figure 120: Visibility (blue curve), OWC data rate (red curve) and 60 GHz data rate (green curve) variation as a function of time. The displayed weather events occurred on March 18, 2017 with a particular angle of sunlight incidence.

As described in an earlier work [95], the influence of scattered and direct sunlight can also lead to reduced OWC link performance. Compared to these results, the FOV is now four times smaller. In addition, a sunshade was installed. However, during two weeks in the middle of March, a particular angle of incidence of the sunlight was observed, leading to a reduced data rate. As shown in Figure 120 for a partly cloudy day on March 18, 2017, the OWC data rate started to decrease around 9:00h. On the contrary, visibility increased to 20 km around 10:40h. Even though visibility was good, the OWC rate continued dropping and fluctuated between 350 and 190 Mbps. At 18:00, when the sun set, the rate returned to its initial value. Narrowband spectral filtering at the receiver and a further reduced FOV are necessary in order to minimize these sunlight effects.

Monitoring of the variation of the data rates for both links, optical and mmWave, led to quite interesting statistical results. To visualize statistical data, the cumulative distribution functions (CDF) for the visibility and the data rate of both links are shown in Figure 121 and Figure 122.

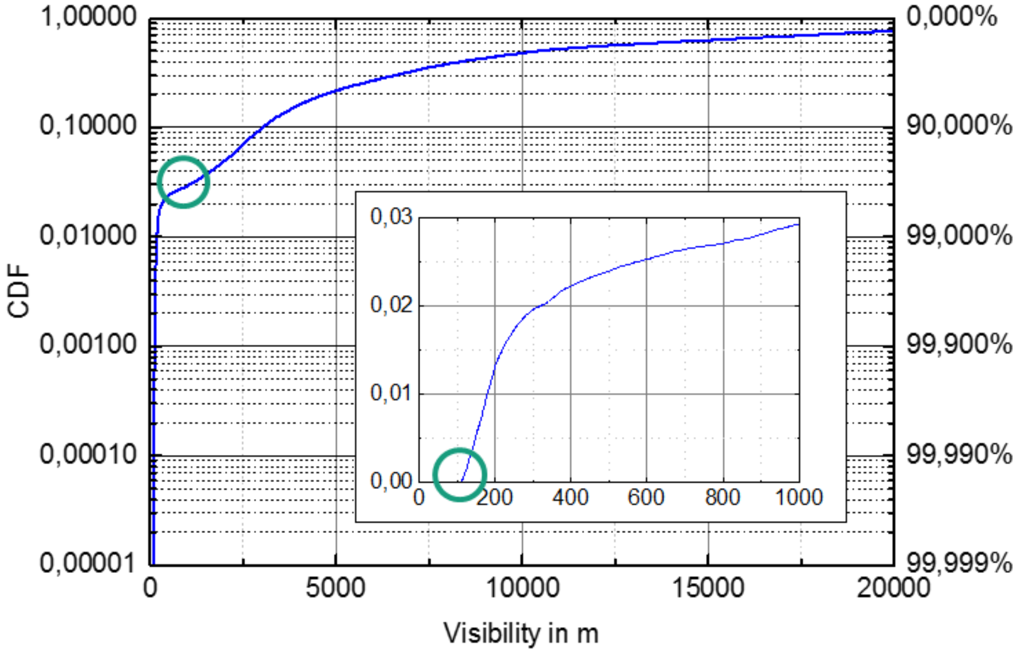

Figure 121: CDF for the measured visibility during the monitoring period. Visibilities higher than 1000 m for 97% of the time were measured, despite the wintertime monitoring period. The inset shows a minimum visibility of 94 m.

The CDF of all measured visibility values is shown in Figure 121. The CDF indicates at what probability the measured value is lower or equal to the value indicated on the abscissa. As mentioned above, during the monitoring period bad weather strongly reduced visibility. However, in 97% of the monitored time visibility remained better than 1 km, which corresponds to an atmospheric loss of less than 1.37 dB over the 100 m measurement distance. A minimum visibility of 94 m was measured, resulting in an atmospheric loss of more than 176 dB/km (s. also Figure 119).

Because of the short distance and due to the rate adaptation, low visibility led to reduced data rates; however, the link was never interrupted. Figure 122 displays a 99.999% link availability; it was actually 100% in the measurement period. In 99% of all cases, the data rate of the hybrid link was at least 495 Mbps.

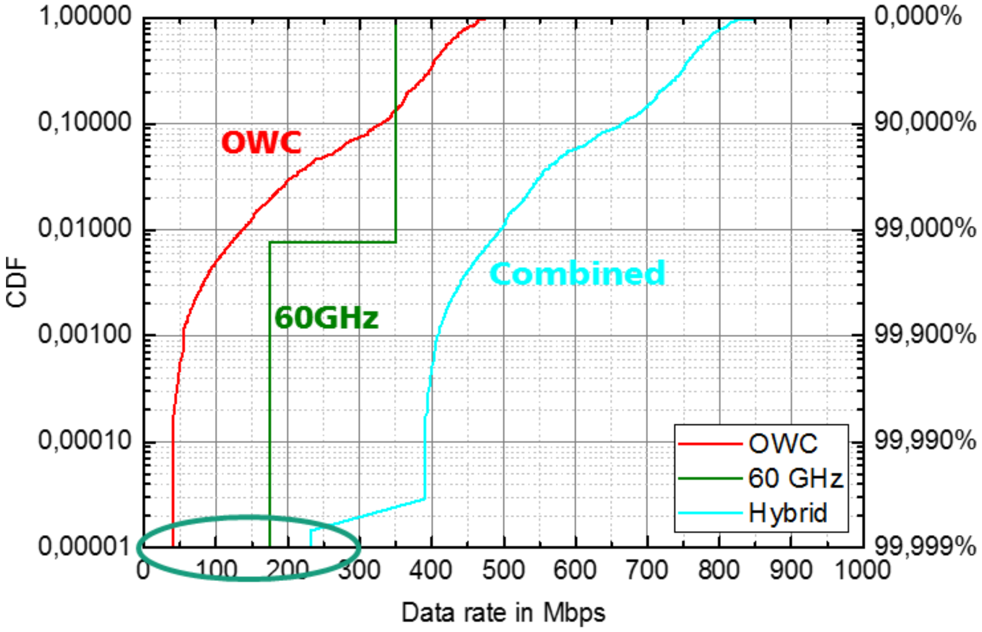

Figure 122: CDF of the data rate for OWC link (red curve), 60 GHz link (green curve) and the combined links (light blue curve). Data rates achieved with 99.999% probability for OWC, 60 GHz and combined are 40/178/329 Mbps, respectively.

The most interesting findings of the statistical results are situated in the few cases of really low visibility (CDF<1E-4) in the lower part of Figure 122. The combined data rate for these cases lies well beyond the addition of the statistical optical and mmWave data rates. This is related to the fact that, statistically seen, in bad weather cases, one of the two links is able to show relatively high data rates, and, thus, improves the overall statistics. The hybrid link, thus, offers higher robustness and increased throughput for the backhauling of small mobile radio cells as compared to a purely mmWave or optical link. In conclusion, over short distances visibility and achievable rates are sufficient to realize carrier-grade availability.

Performance evaluation of 5G-Crosshaul local agent for outdoor small cell with energy harvesting capabilities

The scenario studied in this analysis is composed of a SC with an mmWave backhaul link to the core network, which is providing capacity extension to a macro cell. Adopted traffic demand is of an urban business district and it is based on the model proposed in [26], with higher intensity during the day-time hours (11 AM to 6 PM). The power consumption depends on the traffic load and/or transmission power. The approximated linear model defined in [26] has been adopted. The electrical grid powers the macro base station. The SC is supplied by an array of 16x16 solar cells of Panasonic N235B solar modules (area 4.48 m^2), which have single cell efficiencies of about 21%, delivering about 186W/m^2 and a lithium-ion battery of 2KWh. The size of the energy supplier/storage has been dimensioned based on the typical power consumption of the LTE interface and of the IEEE 802.11ac/ad cards present in the wireless segment of the hierarchical multi-domain resource management of the 5G-Crosshaul proof of concept described in D5.1 [6].

We start by presenting the convergence performance. Since rigorous convergence results for multi-agent RL algorithms are still an open research question, here we refer to the convergence time as the first instant in which the Q-values remain stable within a certain tolerance. We say that the system has reached convergence when all the SC batteries are above B_{th} for a certain amount of time (e.g. within a window of consecutive days). The rationale behind this definition is to foster the energy sustainability of the SCs. An example of the convergence behaviour is shown in Figure 123, where the hourly battery level of a SC is plotted on a per hour basis for the month of January. An initial phase of instability can be noted until hour 500 (i.e., lasting about 20 days), where the SC adopts a greedy-like approach and drops frequently below the threshold since it is using the energy only according to instantaneous availability. After this amount of time, the local agent has gathered information from the environment for its Q functions to stabilize. After that point, the battery level drops below B_{th} less often and the density of points starts becoming more prominent above the battery threshold. In proximity of 1500 hours, we can appreciate a temporary instability due to the scarce amount of energy harvested during several consecutive days. However, we note that the algorithm promptly reacts and drives the system toward a good (zero-outage) region.

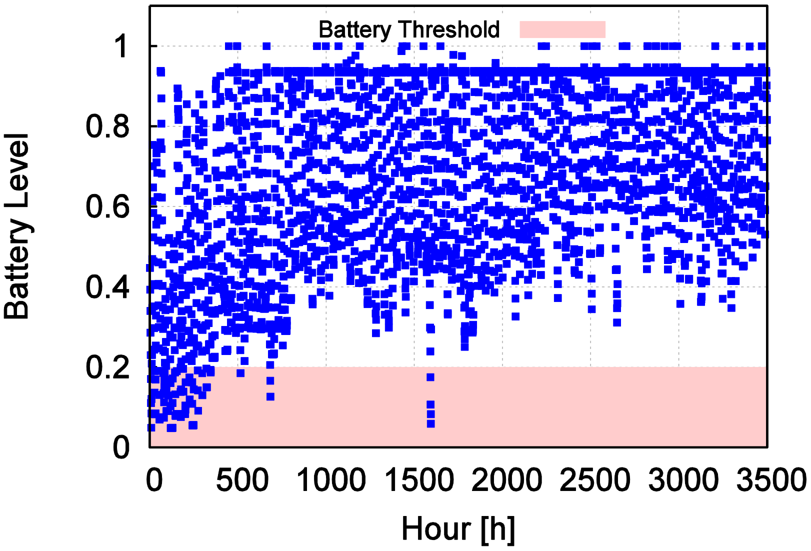

Figure 123: Battery level for the month of January of a single SC

Next, the performance of the QL is compared to a greedy (Gr) algorithm, which is switching off the SC when its battery is below the security threshold. Simulations are run during 180 simulated days of the same month (corresponding to different realizations), to train the algorithm. Three representative months are considered, January, April and July, to reflect different energy harvesting profiles synthetically generated with the SolarStat tool [27].

Figure 124 shows the daily ON/OFF behaviour of the SC in the three representative months of the year (January, April and July), by plotting the number of hours that the SC is in the off at a given hour of the day for the whole duration of the simulation (i.e., 180 days).

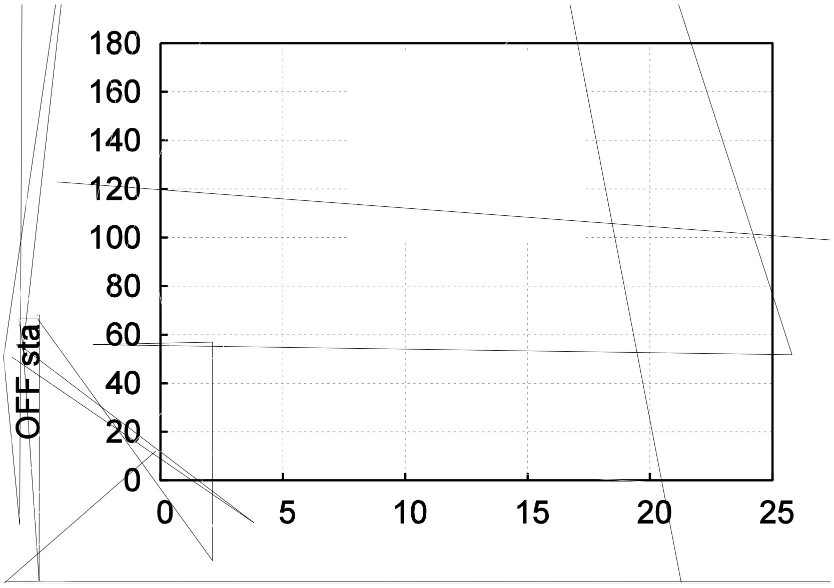

Figure 124: Number of hours spent in OFF state of the Q-learning and Greedy algorithms during the 24 hours of a day for the months of January, April and July.

Since the SC is deployed for the capacity extension of the macro cell, QL tends to have the SC ON during periods of high traffic volume (from 11 to 18) and OFF during periods of low traffic intensity. By doing so, SC can offload the macro cell, which cannot serve all the active users during peak hours, and satisfy the traffic demand. On the other hand, Gr is instantaneously using the harvested energy when available in the storage system. This is leading the SC to be off during high traffic periods and the macro to overflow. Therefore, QL achieves lower traffic drop rate (higher throughput) than Gr, as shown in Figure 125 below.

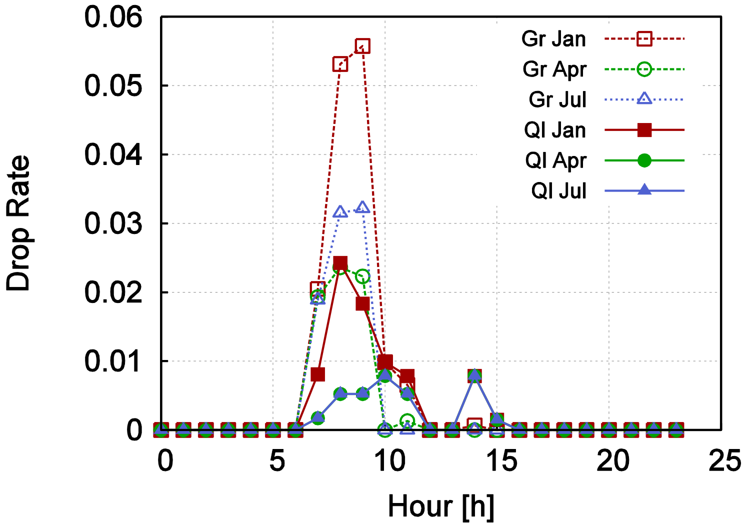

Figure 125: Traffic drop rate of the Q-learning and Greedy algorithms during the 24 hours of a day for the months of January, April and July

The use of harvesters in the SC allows a higher EE with respect to a scenario where the SC is attached to the grid, as shown in Figure 126 below. In particular, QL and Gr can achieve up to 9% of EE increase during a day. Finally, QL can get higher efficiency than Gr, since it can achieve higher throughput.

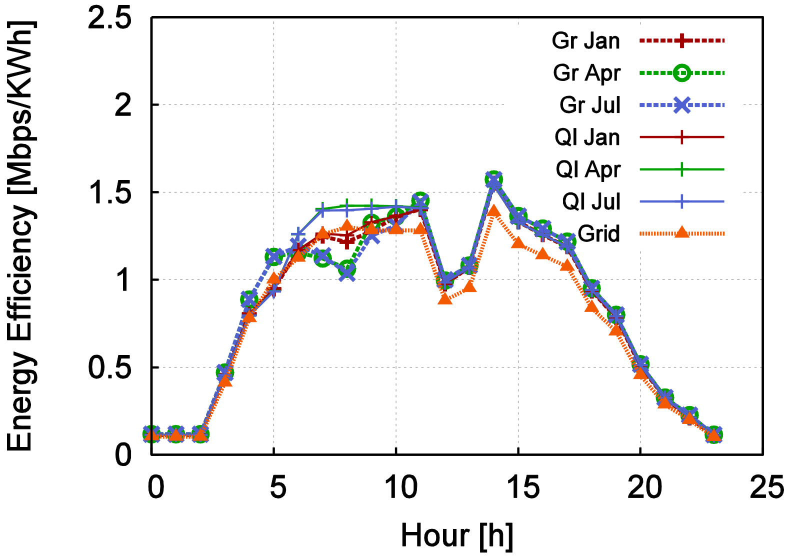

Figure 126: Energy efficiency of the Q-learning and Greedy algorithms during 24 hours in January, April and July. The scenario where the SC is attached to the grid is also shown

5.2 5G-Crosshaul over NG-PON2 and WDM-PON

5.2.1 Evaluation of a 5G-Crosshaul PtP WS WDM PON solution

Novel WS WDM PON solutions must guarantee 10G per DWDM channel and ultra-low latency performance for next-generation access PONs, which means that the total aggregated capacity of the proposed PON depends directly on the number of DWDM channels of the system. In this way, one critical point is to determine the maximum aggregated capacity that can be supported by any 10G-based DWDM system or, in other words, to evaluate the maximum number of channels that can be deployed for a PON. Assuming greenfield scenarios, this constraint (with the available commercial optics) is limited by the optical power budget of the PON system to face the required access reach which affects directly the channel count of the system. Current optics are limited in terms of optical features by different factors to be considered for networking design such as costs and the Side Mode Suppression Ratio (SMSR) which is related to the available launch power and sensitivity parameters in DWDM optical transceivers. SMSR describes the amplitude difference between the main signal mode and the largest neighboring side which is dependent on the transmission optical power and the sensitivity, i.e., the reachable optical budget. Hence, this parameter can be expressed as a function of channel count due to the corresponding path losses of a certain ratio split (power splitter based PONs). The available commercial lasers work in the SMSR range of 30-50 dB. Hence, optical amplification is needed to solve this important physical limitation (low optical power budget).

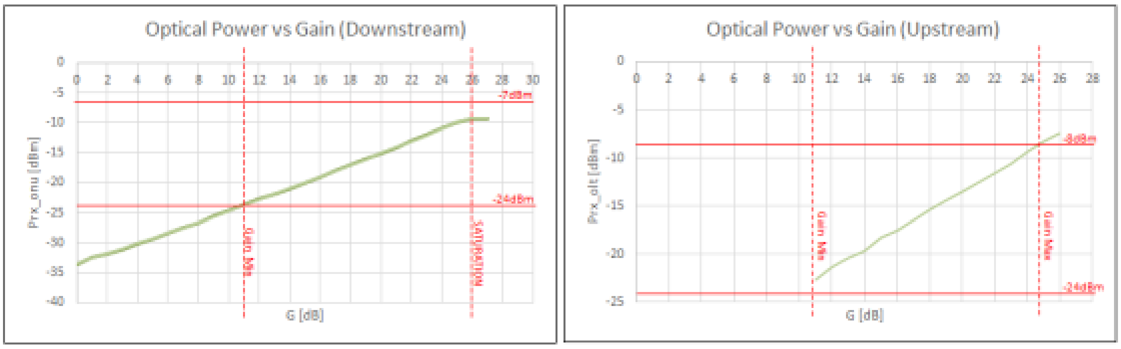

Figure 127: Available optical power budget of WS-WDM-PON

Figure 127 shows the level of optical amplification that can be adapted for our scenario in order to achieve the sensitivity in both OLT and ONU transceivers for a split ratio of 1:32 that is fixed theoretically as the max split ratio that can be supported by the WS-WDM-PON (actually the proposed solution presents an optical power budget of about 33-34 dB with the maximum amplification, however, higher gains worsens SNR levels in reception); in other words, 32 optical terminations (32 PtP DWDM links) or a total of 32 x 10 Gbit/s as maximum aggregated capacity. After experiments in the Berlin testbed, we have concluded the possibility of higher split ratio, which would involve a higher aggregated PON capacity.

It is important to highlight that NG-PON2 standard contemplates coexistence between different PON technologies, which means that a balance between techs must be considered (wavelength plan, fiber infrastructure, filtering, etc) and must be required. For example, GPON overlay with PtP WS-WDM-PON implies that some of the optical fiber terminations have to be assigned for GPON clients what decreases the final aggregated capacity of the WDM network. In addition, it reduces the Signal-to-Noise ratio of the PtP clients as shown in Figure 128.

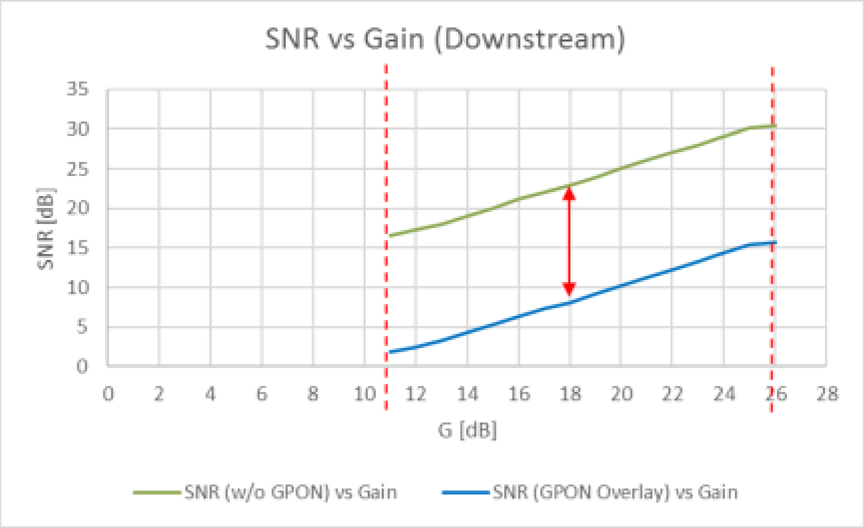

Figure 128: Signal-to-Noise ratio in a example of PON coexistence scenario

Currently, SDN WS WDM PON system has a total of three PtP DWDM links (two of them for two WS WDM ONUs and the remaining one for demonstrating wavelength tunability) deployed in the Berlin testbed, assuming 1:32 as the ratio split for the power splitter based PON. There are 29x free optical terminations which are susceptible of being occupied by other PON techs

(GPON, XGSPON, TWDM-PON. Other WS WDM system configurations as the previous WS WDM PON (SDN non-compatible) can support up to a maximum aggregated capacity of 240 Gbit/s (24 PtP DWDM links) which would allow fiber operators to add 8x legacy GPON lines or 8x future TWDM subscribers.

Focusing only on the PtP DWDM links, the following scenarios can be handled according to the corresponding network requirements in terms of bandwidth: On the one hand UC1a High-Speed Train and UC3 Dense Urban Society. Both of them require less than 10 Gbit/s per MBS (three sectors per site) for fronthaul mobile services, then, this is achievable with a single DWDM link. On the other hand, UC2 Media Distribution and UC5 Mobile Edge Computing demand (3x10) Gbit/s, which involves deploying three DWDM links for each MBS (one PtP DWDM link per sector). However, the WS WDM PON system is an Ethernet packet-based solution, CPRI-like traffic cannot be handled, in this way, UC1b Vehicle Safety is not currently supported.

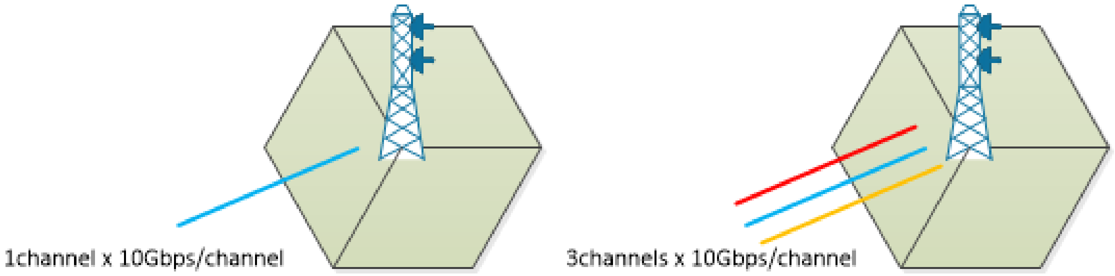

Figure 129: Access resources distribution to face Use-Cases network requirements

Regarding latency performance, this is very dependent on the switch OLT. Figure 130 shows the one-way latency results between OLT and ONU for standard Ethernet packet-based traffic, BBU latency and the fiber propagation of the access reach must be added. The results conclude that compliance with the minimum latency requirements for each of the UCs will not be limited by the network elements of the proposed access solution.

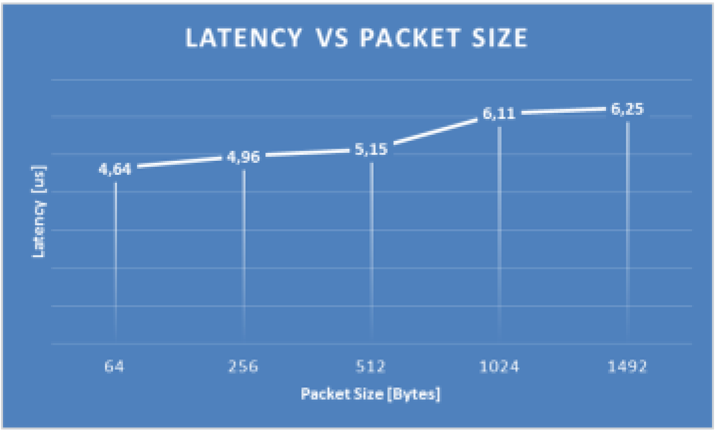

Figure 130: WS WDM PON latency performance

5.2.2 Evaluation of a 5G-Crosshaul DD-OFDM S-BVTs solution

Figure 131 shows the experimental setup for N=2 signal flows corresponding to the approach taken in task T2.4. The DSP and electrical up/down conversion at the transmitter/receiver are performed off-line, following the steps detailed in Figure 131. At the transmitter side, per each flow, randomly generated data are mapped into the corresponding constellation (ranging from BPSK up to 256 QAM). Adaptive bit/power loading is implemented using the rate adaptive version of the Levin-Campello algorithm [32]. Then, four training symbols are included every 100 OFDM frames. The resulting symbols feed an inverse fast Fourier transform (IFFT) of 512 subcarriers. Afterwards, a 2 % cyclic prefix (CP) is added and the obtained OFDM symbols are serialized. The digital OFDM signal, fixed to be running at 20 Gbaud, is clipped and upconverted to an intermediate frequency of 10 GHz by mixing with a digital oscillator. The resulting signal is converted to the analogue domain by a digital to analogue converter (DAC) at 64 GSa/s. This analogue signal is conditioned and injected to the corresponding Mach-Zehnder modulator (MZM) biased at the quadrature point and excited by a tunable laser source (TLS). The flows resulting after each MZM are, then, aggregated using an LCoS reconfigurable optical SSS, configured to have 25 GHz bandwidth per channel and slightly detuned in order to obtain an optical single sideband (SSB) signal. Two flows are generated in the C-band, centered at 1550.12 nm and 1550.92 nm, according to the wavelength plan detailed before. They are depicted in the inset of Figure 131.

The optical signal resulting from the transmitter is injected into the ADRENALINE testbed [6], whose simplified scheme is depicted in *Figure 131*. It is a 4-node photonic mesh network with amplified links of different lengths, ranging from 35 km to 150 km. The feeder section of the access trees, attached to selected ENs, is composed of different fiber spools (10 km, and 25 km). The power delivered to each tree is set to +5 dBm. Then, a variable optical attenuator is used to emulate the power splitters.

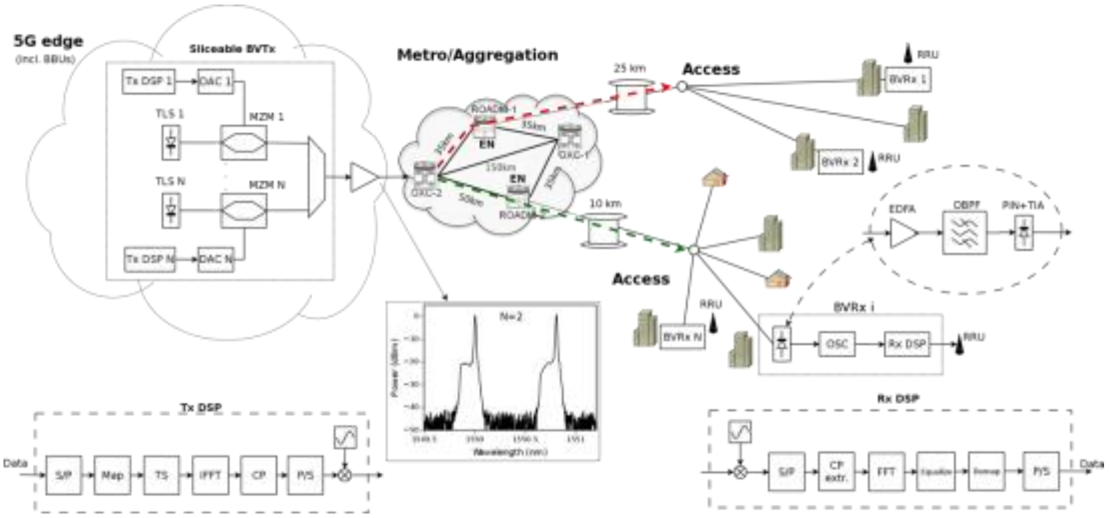

Figure 131: Experimental setup. DSP schemes of the transmitter (Tx DSP) and the receiver (Rx DSP).

At the receiver, the incoming signal is filtered out and photodetected. Finally, in order to emulate a high bandwidth avalanche photodiode in the set-up, a combination of gain-stabilized erbium doped fiber amplifier (EDFA), optical band pass filter (OBPF) and PIN diode is calibrated to obtain a -28 dBm sensitivity at 10^{-3} BER for OOK transmission at 10.7 Gbit/s. The detected current is then digitized by a real-time oscilloscope (OSC) running at 100 GSa/s. The baseband OFDM signal is recovered after downconversion, off-line demodulated, equalized and demapped.

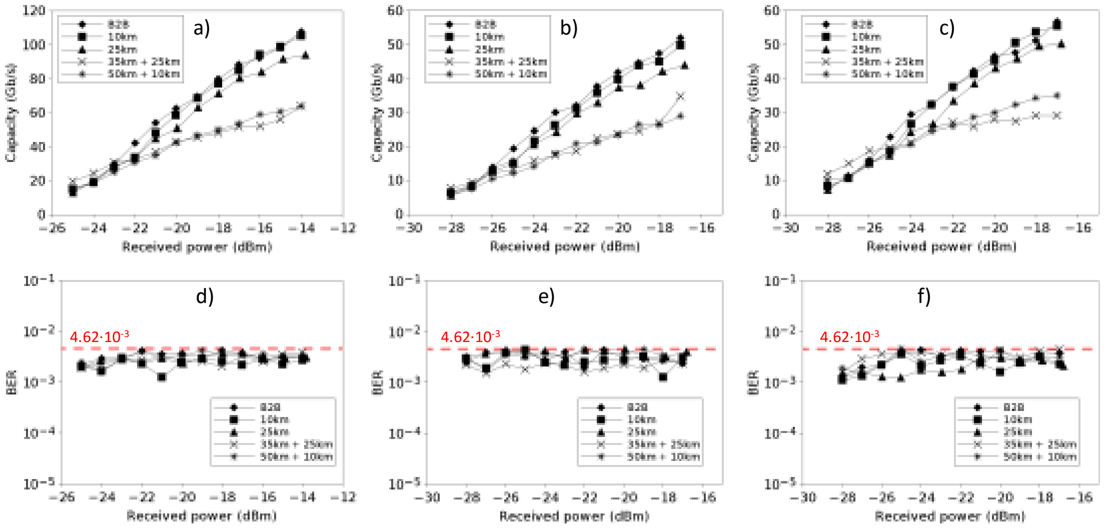

Figure 132: Experimental results for the cases of detecting both the two flows (a, d), and single slice individually,at 1550.12 nm (b, e) and1550.92 nm (c, f). (a, b,c) Maximum capacity versus received power. (d, e, f) BER versus received power.

Figure 132 shows the sensitivity measurements for the different cases analyzed, assuming a BER threshold of $4.62 \cdot 10^{-3}$ for a 7% forward error correction (FEC) overhead [34]. First, a back to back (B2B) configuration is tested, featuring a maximum aggregated gross capacity of 105.2 Gbit/s at -14 dBm of received power. At -17 dBm (which corresponds to a 20 dB power budget for the transmitted power, including a 3 dB margin), the maximum aggregated capacity is 88.4 Gbit/s. In this case, each slice when individually transmitted is featuring slightly above 50 Gbit/s. Next, the impact of the access trees is assessed after 10 km and 25 km of fiber. Figure 132 shows that these configurations are well aligned with the B2B case, with power penalties of less than 1 dB for all the analyzed cases.

For proving the proposed sliceable functionality, the different flows are transmitted over the optical meshed network of the ADRENALINE testbed, through two different links (35 km and 50 km). Next, signal paths continue through the different access segments to cope with a total distance of 60 km. In this case, we observe a capacity penalty of less than 42 % with respect to the B2B at -17 dBm, achieving beyond 50 Gbit/s when detecting both flows. When detecting the slices individually, the maximum capacity ranges between 28.9 Gbit/s and 34.8 Gbit/s at -17 dBm.

5.3 Virtualized RAN based on PDCP/RLC split

5.3.1 State of the Art

In CPRI-based C-RAN, the radio signals are digitized with a very high resolution so that the digitization has the least possible impact on the radio signals themselves. This implies that the fronthaul carries a very high bit rate, generally more than ten times higher than the one of the radio front, as seen in Chapter 2. Furthermore, latency constraints of the C-RAN fronthaul are very strict, allowing for transmission distances generally below 20 km. While the fronthaul throughput needed for the transmission of currently deployed mobile generations (2G, 3G and 4G) can still be provided by off-the-shelf, inexpensive optical transponders and the help of wavelength multiplexing (cf. Chapter 3), the current C-RAN architecture proves to be manifestly inadequate in view of the bit-rates envisaged for the 5G.

In Chapter 2, we have seen that other fronthaul interfaces are being considered to provide an appropriated optical transmission by allowing the needed bit-rate reduction in the optical front. Its main objective is to migrate, at a higher or lower layer, some signal processing blocks from the centralized equipment to the antenna site equipment in order to allow bit-rate reduction while ensuring a certain level of CoMP (Coordinated MultiPoint) and other radio coordination features. Besides the reduced bit-rate compared to C-RAN, another advantage of these new interfaces is that they could provide a variable bit-rate which would depend on the actual load of the wireless system instead of the theoretical peak rate. A basic illustrative concept of the RAN protocol layer splitting is shown in Figure 133a in which we also compared the bandwidth, latency and real-time processing constraints of different possible splits. Some considerations on the latency and bandwidth requirements of different splits are made in Chapter 2.

As far as latency is concerned, the new fronthaul can provide much relaxed constraints if a high layer split is implemented. This not only allows moving the centralization unit even farther away from the radio unit but also enables virtualization of certain functions from layers 3 and 2 of the radio protocol stack. Therefore, generic servers could be used to host these functions instead of specific hardware. Furthermore, the relaxed latency constraints also enable the use of point-to-multipoint architectures, contrary to the C-RAN where only point-to-point solutions were preconized for the fronthaul. This could ultimately allow for an intelligent infrastructure sharing with FTTx users in fixed-mobile convergent architectures.

Besides RAN virtualization, a centralized, software-based management and control and an Ethernet-based transmission are other trends expected to influence the choice of the new fronthaul interface. Another important technical driver refers to the possibility of implementing some sort of statistical multiplexing, such as it is the case with the backhaul segment.

5.3.2 vRAN scenario in 5G-Crosshaul

Figure 133b illustrates a possible new Ethernet-based RAN architecture created using a high layer split fronthaul. The Digital Units (DUs), currently located at the antenna site in the D-RAN architecture, can be virtualized and moved to the Master CO allowing further resource pooling and reusing of the existing backhaul, including both access and aggregation segments. A more intelligent Radio Unit (RU) compared to C-RAN is used at the antenna sites and a standard Ethernet switch can be used if a point-to-point transportation is chosen. Point-to-multipoint passive optical network (PON) can also be envisaged as previously mentioned, in which case standard GPON/XGSPON/NGPON2 optical network units (ONU) and Optical line terminations (OLT) are used (cf. Chapter 3).

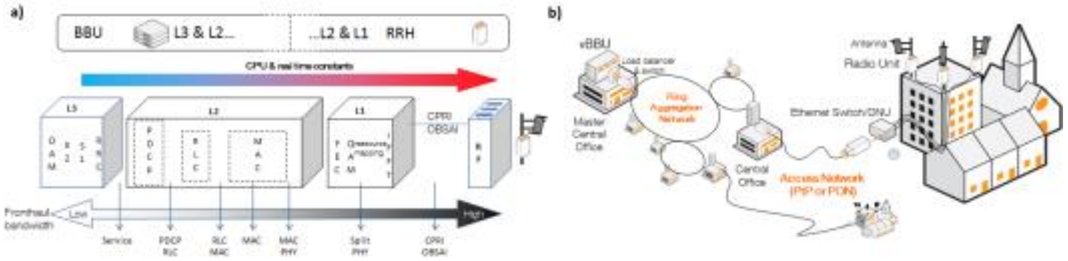

Figure 133: a) Possible functional splits in the RAN equipment. b) Illustrative architecture of the new Ethernet fronthaul based on a high layer split.

Here, we experimentally assess a proprietary virtual RAN (vRAN) solution based on a LTE layer 2 functional split of PDCP/RLC in Figure 133a. This proprietary solution encompasses network function virtualization, implemented within a server and uses standard Ethernet framing. It allows intersite CoMP and carrier aggregation, enhanced quality of service through mobile edge cloud (MEC) and live vBBU traffic migration.

Our objective here is three-fold. First, we investigate the bit-rate of such interface compared to the backhaul and to the current C-RAN fronthaul. Indeed, this is essential for matters of network dimensioning and ultimately to evaluate the capacity of the already deployed infrastructure to handle such traffic. Then, we assess its robustness to packet loss and latency in a point-to-point (PtP) optical architecture, which is very important to appropriately evaluate the impairments brought by conventional Ethernet network equipment. Finally, we demonstrate its transmission through a point-to-multipoint (PtMP) GPON architecture using a fixed bandwidth allocation scheme. This experiment targets a fixed-mobile convergent architecture. It is important to notice here that this functional split will be assessed using a 4G LTE signal. At the time of the experimentation, no actual prototype of a 5G new radio interface was available. This is why a standard G-PON system could be used despite its relatively low throughputs. A higher bit-rate PON system would probably be needed for actual 5G signals.

5.3.3 Experimental Results and Discussions

As shown in Figure 134, we will experimentally investigate two solutions for the transport of the new fronthaul interface: Ethernet PtP with switch and PtMP with a G-PON (Gigabit capable PON) system. We consider in the investigation only line rate for transmission about 1GEth but this investigation could be extrapolated for switches working at 10G Ethernet or 25G and 100G Ethernet and PON generation XGS-PON, the future 25G-PON and NG-PON2 or 100GE PON.

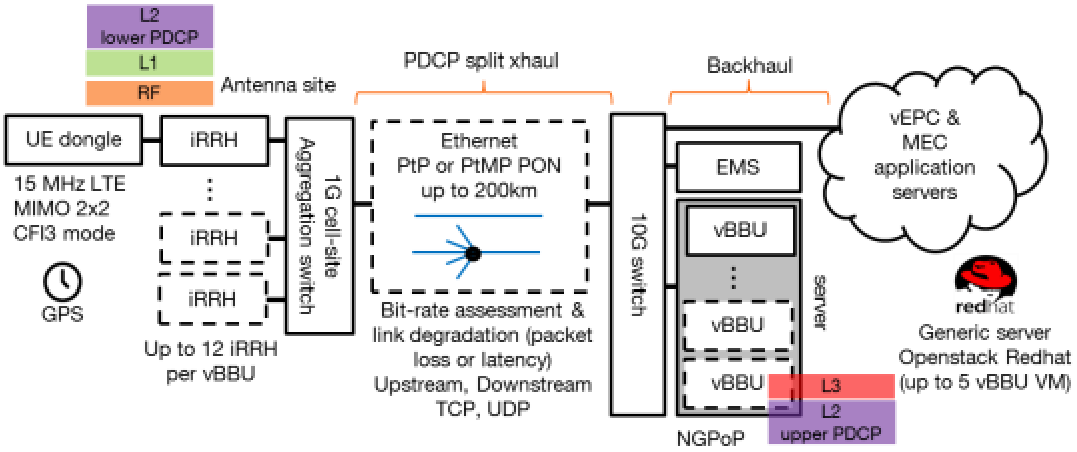

Figure 134: Experimental setup for Ethernet transport lab tests of new, high layer, functional split fronthaul

At the transmitter side, generic servers running on OpenStack host a virtual EMS (Element Management System), a virtual EPC (Evolved Packet Core) where the Mobile Edge Computing (MEC) is happening, and a virtual BBU (vBBU). Up to 5 vBBU virtual machines can be hosted per server. A 10G Top of Rack (ToR) Ethernet switch is used to connect these nodes. At the receiver side, an intelligent RRH (iRRH) is connected to a User Equipment (a computer, in this case) via a mobile dongle. We use a mobile signal based on LTE with 15 MHz bandwidth and 2x2 MIMO configuration and control format indicator (CFI) 3. The maximum raw and useful (excluding all control resource blocks) radio front downlink bit-rates considering 64QAM are 151.2 Mbit/s and 107.33 Mbit/s respectively.

For the PtP test, we will use common 1 GbE switches at both ends. Packet loss and latency will be then inserted with a dedicated test device in order to evaluate their impacts on the mobile throughput. Figure 135 shows the variation of the traffic on different segments of the PtP transmission for both uplink and downlink transmissions with user datagram protocol (UDP) packets. The actual radio traffic is limited to about 90 Mbit/s and 30 Mbit/s in the downlink and uplink respectively. We observe that the backhaul traffic is 6% higher than application layer (EPC) traffic. Also, a variable traffic is observed in the new fronthaul interface (xhaul in the figure) which is approximately 20% higher than the backhaul traffic.

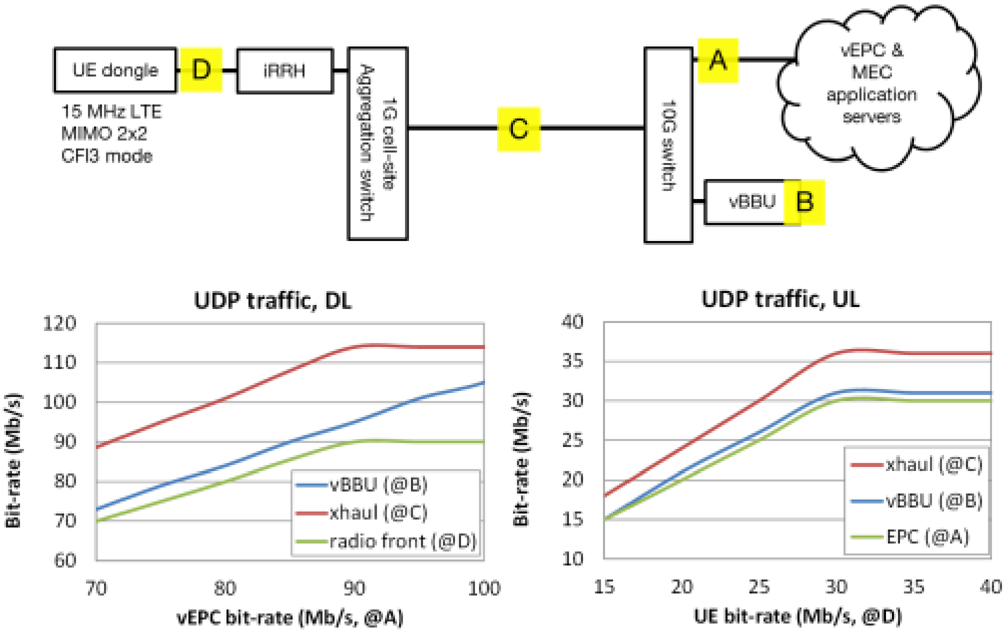

Figure 135: Evaluation of the new fronthaul bit-rate.

Figure 136 (bottom left) shows the impact of packet loss on the mobile LTE throughput in the downstream and upstream using TCP (Transmission Control Protocol) and UDP for the mobile signal between EPC and user equipment (UE). In few words, TCP continuously adapts the transmission bit-rate to the network capacity to avoid congestion while UDP transmits at a constant bit-rate. We can see that the LTE throughput is not impacted by packet loss down 1% for UDP transmission. For TCP, the impact on throughput is negligible for packet loss down 0.1% for the downstream and 0.4% for the upstream. Therefore, the transmission is robust since only 10^{-3} packet loss for non-priority data and 10^{-5} for priority data is recommended generally for Ethernet transmissions in the backhaul. Throughput degradation is noticed between TCP DL and UDP DL at 0% packet loss, which is due to the limited buffer capacity of the used LTE dongle. Similar TCP and UDP throughput at 0% packet loss has been shown in other tests with another dongle.

The one way latency impact is represented in Figure 136 (bottom right). No impact is observed for injected latencies down to 20 ms. Knowing that the latency in the current LTE network, between the master CO and the cell site gateway (Figure1.b), is between 5 and 10 ms, the re-use of the existing network for fronthaul should not affect the performances.

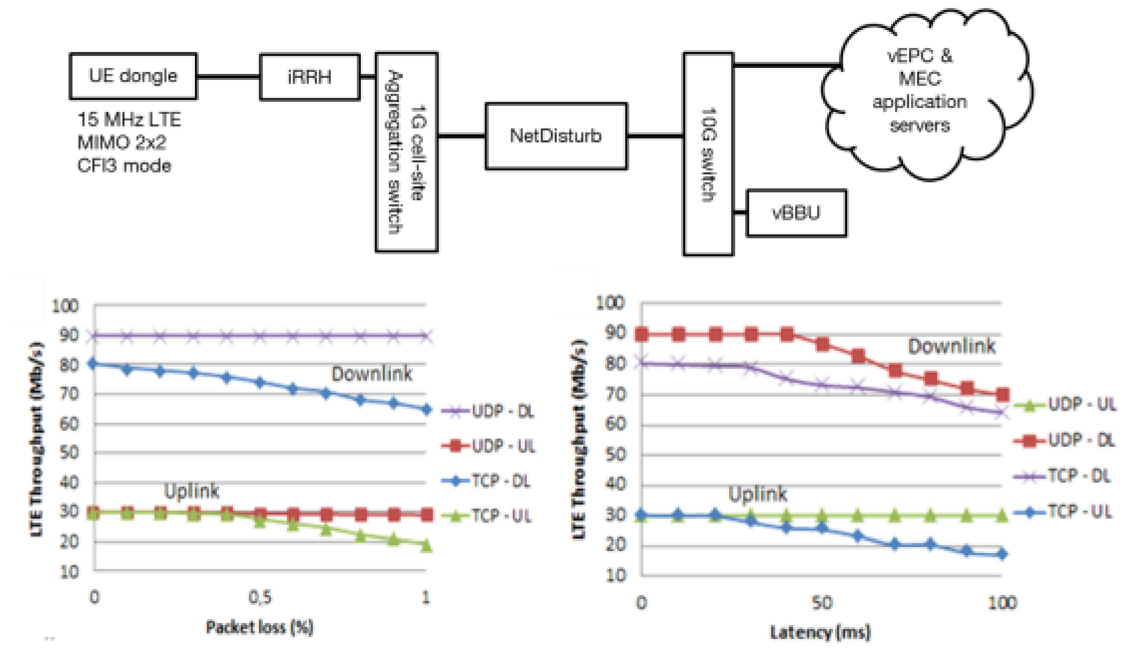

Figure 136: Impact of packet loss and latency on upstream and downstream TCP and UDP transmissions in PtP configuration.

For the PtMP fronthaul, an OLT is used after the ToR switch and an ONU is associated to the iRRH. A second ONU is added with standard Ethernet traffic to emulate additional traffic. Since G-PON operates under time division multiple access (TDMA), we allocate fixed upstream bandwidths for the upstream to the ONUs; 50 Mbit/s for ONU 1 connected to the iRRH and 750 Mbit/s for ONU 2 used for overloading the G-PON system. The overloading data consists of 1 Gbit/s and 600 Mbit/s Ethernet traffic for the downstream (OLT to ONU) and upstream (ONU to OLT) transmissions in the PON respectively. The overloading traffic and the mobile data are then encapsulated using standard GPON Encapsulation Method (GEM) frames. A virtual local area network (VLAN) is used to logically separate the mobile from the overloading traffic. With this configuration, we will evaluate the LTE throughput for different lengths of optical fibre. No dynamic bandwidth allocation algorithm is assessed in this experiment. Both overloading and mobile traffic were associated with a fixed bandwidth, with traffic container (T-CONT) type 1. Figure 137 shows the experimental setup, with green arrow indicating uplink traffic and red arrows indicating downlink traffic.

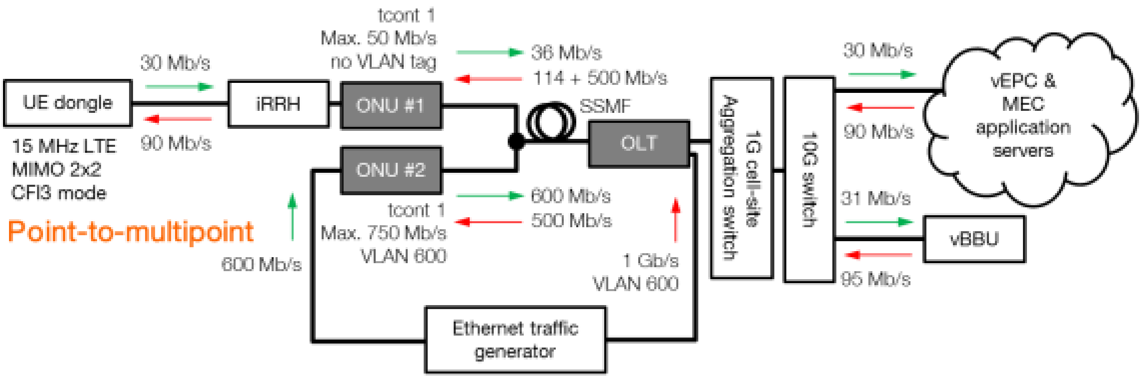

Figure 137: PtMP experimental setup for the evaluation of high layer split radio interface over G-PON.

Table 23 shows the TCP and UDP LTE throughputs for different transmission distances over G-PON. No impact is noticed when overloading the system with the second ONU. In fact, for the downstream, we obtained performances similar to PtP for 0 km and 10 km. A little impact is noticed in 25 km since it’s the maximal distance allowed with the used G-PON system.

For TCP transmission in the uplink, we notice some throughput degradation compared to PtP. This could be due to the packet latency unbalance (40 µs in the downstream and 140 µs in the upstream) and/or the packet jitter (0.9 µs in the upstream and 48 µs in the upstream) introduced by the G-PON system, which could affect the queuing policies used by the vRAN equipment. Some adjustments based on coordination between BBU and OLT should then be needed to transport this new functional split fronthaul with no impact on the LTE throughput and the quality of the delivered services.

Table 23: TCP and UDP LTE throughputs for different fibre lengths in G-PON.

LTE throughput (Mb/s)				
Fibre length (km)	UDP DL	UDP UL	TCP DL	TCP UL
0	90	30	82.9	20.8
10	90	30	82.9	20.3
25	88	30	81.6	19.7

6 Key contributions to the state of the art and verification of 5G-PPP KPIs

The following sections provide a summary of the contributions of this deliverable with respect to both current state of the art, and further relates such contributions with the 5G-Crosshaul use cases summarized in Chapter 2. Additionally, a summary table outlying the project’s objectives and Key Performance Indicators (KPIs) is provided along with the means for verification conducted within WP2.

6.1 Key contributions to the state of the art and their relationship with the project’s Use Cases

6.1.1 Multilayer optical nodes and fronthaul compression

In Chapter 4, both XPFEs and XCSEs have been investigated and evaluated for the transport of fronthaul and backhaul traffic, with respect to network dimensioning and planning. Essentially, both packet-switching and circuit-switching offer pros and cons separately, but complement themselves nicely since traffic forwarding at the packet granularity allows for statistical multiplexing and a more efficient use of wavelength resources, while circuit switching guarantees deterministic delays at the expense of wavelength consumption. Finding the optimal trade-off between both switching granularities depends on the amount of wavelength resources available in the network and the specific delay requirements of the functional split under use.

No matter which switching technology is used (i.e. circuit or packet), the simulation results show that the multi-layer scenario is able to support all use cases for most radio function split options, i.e. option 1-7a. Thanks to the use of high speed optical transmission it is possible to deliver large bandwidth amounts. Moreover, the use of DWDM allows logical all-optical point-to-point connectivity between the edge nodes without any intermediated processing, thus greatly reducing latency when necessary (i.e. single hop link). Clearly the critical points could be the cost and the availability of the fibers. Regarding the cost, novel technologies (i.e. silicon photonics described in chapter 3.3.3) is proposed to realize optical switches at low cost and size, while regarding the fiber availability it is necessary to consider alternative technology than the optical DWDM for covering scenarios with scarce fiber availability.

Regarding fronthaul compression, theoretical derivation of the compression bounds are described Chapter 4.5, showing the feasibility of FH compression rates of up to 5 times while keeping good performance levels at air interface. In particular, a new FH compression method is proposed and evaluated by simulations, showing about 4-5 times compression in downlink and 3-4 times compression in uplink. A prototype has been developed to showcase the implemented FH compression method and the compressed FH traffic is transported over Ethernet. The prototype will be demonstrated and integrated in WP5.

6.1.2 Indoor small cell scenario

Indoor small cell system design supporting the multiplex of FH and BH and advanced features of centralized baseband pooling, dynamical cell split (increase spatial reuse) and energy saving have been described in Chapter 5.1. Essentially, system dimensioning analysis results show that peak rate of approximately 4 Gbit/s over the air can be supported using 10GBase-T Ethernet technology and 5GBaseT Ethernet technology can support about 2 Gbit/s peak rate, showing that it fulfils the requirements for the dense urban society use case and the high-speed train use case defined in Chapter 2.

6.1.3 Outdoor small cell scenario

The considerable bandwidth provided by mmWave technology makes this technology a feasible alternative for transport network using wireless interfaces in the dense urban society use case considered in Chapter 2. Within 5G-Crosshaul, several other aspects besides bandwidth have been considered in order to enable the inclusion of mmWave technology as a driver for the development of 5G-Crosshaul networks under different deployment schemes, especially for the outdoor small cell scenario.

From the data-plane perspective, latency reduction techniques have been explored to reduce processing delays so mmWave can accommodate more demanding fronthaul traffic splits, such as option 7. Early results obtained in the data-plane field experiment of mmWave crosshaul network with a mesh topology (D5.1 [6]), wherein an average latency of 0.519 ms was observed, showed that the mesh multi-hop decentralized deployment could not satisfy latency requirements of demanding fronthaul traffic profiles. However, in a more centralized architecture, the proposed PtP topology can significantly curtail the latency down to around 100 ~150 μs, by eliminating the processing delay in each hop. Moreover, by applying fast-forwarding techniques, the latency can be further reduced. This way, mmWave interfaces can be applied to various functional split options envisaged in 5G. As reported in Chapter 5.1.4, the latency can be reduced to around 100μs when fast-forwarding technique is incorporated into mmWave-based transport interface.

In parallel, the usage of low-cost LED-based optical wireless links as a complementary solution to the mmWave technology may prove – as an aggregated hybrid optical/mmWave link - a substantial improvement in link robustness and speed. The results from the first time measured real-time throughput results in a real outdoor deployment of an aggregated OWC/mmWave link under various weather parameters obtained within the 5G Crosshaul project, show that the hybrid link offers higher robustness and increased throughput for the backhauling of small mobile radio cells as compared to a purely mmWave or optical link. Hence, this hybrid system offers the required performance to realize carrier-grade availability, providing sufficient achievable rates over short distance visibility. Furthermore, a feasibility work presented herein shows that optical wireless technology can also be expanded for 10Gbit/s over 1 km links.

With respect to the control plane, 5G-Crosshaul presents an approach for the SBI agent which decouples control operations from management operations. The aim of the proposed SBI agent is to provide a solution presenting scalability, maintainability and upgradability capacities (in line with other state of the art approaches [9]) to evolve with the requirements and the evolution of the 5G-Crosshaul network.

Finally, from the energy analysis presented herein, we can conclude that the extension of the Q-learning algorithm for SC deployments supplied with energy harvesters and storage systems is a valid solution to achieve higher network energy efficiency. In fact, considering the high number of SCs that will be inside the coverage area of a macro cell (> 10), it is expected that EE also increases by a similar order of magnitude. Furthermore, this analysis provides interesting inputs to the activities related to EMMA application in WP4, where hybrid solutions are presented. According to this concept, ON/OFF states in the small cells will be enabled and coordinated by a central agent to guide the learning process and avoid conflicts among local agents (running as an application of EMMA), as well as by distributed local controllers in the SCs, which are in charge of performing the learning process according to the local environment.

6.1.4 5G-Crosshaul over NG-PON2 and WDM-PON

Two novel optical-based solutions for 5G access-metro networking have been presented to address the new Use-Case proposals over the Crosshaul architecture. Firstly, a PtP DWDM solution represents an important improvement regarding efficient utilization of the network resources that allows the convergence between fixed and mobile services over the same fiber access infrastructure. The evaluation results based on lab tests shows the feasibility to support different functional split options to C-RAN and vRAN deployment. In particular, the fulfilment of the network requirements for certain RAN options are evaluated, determining the option 6 as the maximum level to be supported by the current system-prototype. In this way, the performance of the proposed solution satisfies the requirements of all Use Cases presented in Chapter 2.

Finally, a transparent delivery of mobile front-/back-haul for converged metro/access elastic networking has been experimentally demonstrated by DD-OFDM S-BVTs. Results show successful connections running at beyond 50 Gbit/s per flow from BBUs to the RRUs, when serving different paths and covering distances up to 60 km. Thus, it is a promising solution for serving the multiple endpoints employing S-BVT(s) at the 5G-edge nodes. This solution is aligned with use cases 2-3 (media distribution and dense urban society) of Chapter 2 in terms of throughput and post-FEC BER. Nevertheless, the distances covered (up to 60 km) need a relaxation on the transport latency, from 100 µs up to 1ms.

6.1.5 Virtualised RAN scenario

In this chapter, we experimentally assessed a real time the transport of a new fronthaul interface based on a high layer functional split, i.e. PDCP/RLC split, over an Ethernet network based on PtP switch and over a G-PON system. The results show 20% increase of traffic compared to regular backhaul. It also shows that it achieves quite high tolerance to latency and packet loss. The throughput measurements show that backhaul and FTTH infrastructures can be potentially used for the transport of such PDCP/RLC split over Ethernet with the necessity to do some joint adjustments in the RAN and transport equipment to achieve the optimal performance. Furthermore, the results indicate that the requirements in all use cases listed in Chapter 2 can be supported in the V-RAN scenario using higher speed PtP and PON systems.

6.2 Summary table of contributions and use cases

Table 24 summarizes the evaluation results for different scenarios. Basically, the optical solutions with high speed WDMPON and multi-layer packet-optical networks can manage to meet the requirements of all use cases, thanks to the high capacity transmission capability by optical technologies. More particularly, WDMPON only supports NR option 1-4 functional split (possibly up to option 6) while multi-layer packet-optical networks can support option 7 and up (a complete description of the option is provided in Section 4.3). For the indoor and outdoor small cell scenario, the cost-effective solutions based on copper Ethernet (up to 10Gbit/s) and mmWave technologies can fit with dense urban society use case. The indoor solution can also be used for high speed train use case. In the vRAN scenario, option 2 of PDCP/RLC functional split is evaluated experimentally. It shows how bandwidth and latency requirements can be relaxed down to the backhaul level and even good tolerance to packet losses.

Table 24: Summary of the evaluation results for different scenarios

Scenario	Functional split and technologies evaluated/analyzed	Use Case supported/fulfilled	Comments
Packet optical - layer optical network	NR option 7A with packet-optical networks.	UC 1.a: high-speed train UC 1.b: vehicle safety UC 2: Media distribution UC 3: Dense urban society UC4: Mobile edge computing	
Indoor Small Cell	FH compression of option 8 with copper based Ethernet technologies.	UC 1.a: high-speed train UC 3: dense urban society	Up to 10G Ethernet (i.e. 10GBase-T) is assumed for cost-effectiveness.
Outdoor Small Cell (mmWave and OWC)	NR option 1-4 and option 6, possibly also option 7 with mmWave-based solution.	UC 3: dense urban society	1 Gbit/s per sector transmission at 200 meters is going to be presented in D5.2 for option 2. Latency improvement techniques for supporting option 6 are included in this document in Section 5.1.3 and will be further investigated in D5.2. Option 7 may be possible
WDM-PON based	NR option 1-4 with PtP WS WDM-PON and DD-OFDM S-BVT.	UC 1.a: High-speed train UC 1.b: Vehicle safety UC 2: Media distribution UC 3: Dense urban society UC 4: Mobile edge computing	Telnet SDN WS-WDM-PON achieves 10Gbit/s per DL and per UL. Option 5 and 6 may be possible.

Virtualized RAN	NR option 2 with P2P switch and PON systems	UC 1.a: high-speed train UC 1.b: vehicle safety UC 2: Media distribution UC 3: Dense urban society UC4: Mobile edge computing	The experimental results are based on Gigabit P2P switch and G-PON system. However, it indicates the feasibility to support all use cases with higher speed optical networks using NR option 2 interface.

It is further worth noticing that if a lower layer split is evaluated such that a use case can be supported, it also indicates that the based transport technologies/solutions can also be used to support any higher layer split than the functional split evaluated. This is because that the higher layer split has less stringent requirements in bandwidth, latency and jitter.

6.3 Contributions with respect to objectives and project KPIs

Next tables overview the different objectives, R&D topics and KPIs defined in the proposal related with WP2, along with a summary of the contributions provided in this document D2.2 and D2.1 that demonstrate their fulfilment (in italics and blue style).

Table 25: Objective 2 and KPIs and verification within WP2

Objective 2	**Specify the XCI's northbound (NBI) and southbound (SBI) interfaces**
Description	Define interfaces to accelerate the integration of new physical technologies (SBI) and the introduction of new services (NBI) via novel or extended interfaces.
R&D Topics	• Specify an abstract network information model for Xhaul technologies, including abstracted control parameters and system status metrics. o *Already covered in D2.1 Chapter 4.* • Specify the set of southbound XCI actions (e.g., control the forwarding behaviour, configure radio parameters, deploy/migrate Xhaul functions). o *Based upon the initial specification provided in D2.1 [5], this document present the work developed within the framework of WP2 for the implementation of the SBI agent to control, manage and configure a transport node including mmwave technology in Section 5.1.3.* • Specify the set of northbound XCI actions (e.g., provisioning of new VPNs) to enable Service Level Agreement (SLA)-level reports, create new virtual Xhaul slices for multi-tenancy support. o *This topic has been covered in D3.2 [97], Sections 2 and 10.*
5GPPP KPI impact	• Enable the introduction/provisioning of new Xhaul services in the order of magnitude of hours (e.g., VPNs, network slices). o *The consecution of this KPI is a global project effort involving work of WP2, WP3 and WP4 and will be shown in WP5 Demo 3. In particular, WP2 contributes with the developed SBI agent to control, manage and configure a transport node including mmwave technology of Section 5.1.3.*
Verification	• Prototype of the XCI SBI including multiple technologies (CPRI over WDM, packet over mmWave) and the XCI NBI (capacity reconfiguration). o *The implementation here in described in Section 5.1.3 of the SBI*

	agent for packetized mmWave transport nodes constitutes one point of interaction with WP3 and it is included in Demo3 of WP5 about hierarchical orchestration of multi-domain multi-technology resources in a transport network.
WP/Tasks	WP2/T2.3, WP3/T3.2, WP4/T4.1, WP4/T4.2, WP6/T6.2

Table 26: Objective 3 and KPIs and verification within WP2

Objective 3	**Unify the Xhaul data plane**
Description	Develop a flexible frame format to allow the usage of fronthaul and backhaul on the same physical link to replace different technologies by a uniform transport technology for both fronthaul and backhaul.
R&D Topics	• Unified but versatile cross-technology frame format supporting all types of fronthaul (e.g., CPRI) and backhaul and their different demands on the type of payload, but also bandwidth, latency and synchronization. o *This objective has been addressed in D2.1 Chapter 8 through the introduction of a common MAC-in-MAC Ethernet based frame*. • Support for multi-tenancy in the unified data plane. o *This topic has been covered in D3.2 [97], Section 5.2.2. The common MAC-in-MAC Ethernet based frame allows to separate and isolate the traffic of different tenants.* • Design the Xhaul Packet Forwarding Element (XFE). o *A preliminary version of the XPFE was introduced in D2.1 Chapter 7 and further evaluated in D2.2 Chapter 4. The use of Strict Priority queueing favoring FH Ethernet packet shows reduced latency and almost negligible jitter at speeds above 40 Gb/s, even after traversing five consecutive nodes.*
5GPPP KPI impact	• CAPEX and OPEX savings due to the unified data plane (25%) and multi-tenancy (>80%, depending on the number of tenants). o *Reported in WP1's D1.2* • 80% increased energy efficiency due to consolidation of equipment.
Verification	• Prototype including XFE supporting a unified frame format. o *An XPFE with MAC-in-MAC support is evaluated in several experiments of demo 4, see D5.2 [98].*
WP/Tasks	WP2/T2.2, WP2/T2.3, WP3/T3.1

Table 27: Objective 4 and KPIs and verification within WP2

Objective 4	**Develop physical and link-layer technologies to support 5G requirements**
Description	Exploit advanced physical layer technologies, not currently used in the Xhaul network segment, as well as novel technologies, such as wireless optics, flexi-PON, etc. to increase coverage and aggregated capacity of integrated backhaul and fronthaul networks. Develop novel data plane solutions, capable of meeting the stringent latency, synchronization, and jitter requirements in all heterogeneous Xhaul scenarios.
R&D Topics	• Advanced high capacity mmWave, and disruptive wireless optical transmission. o *Section 3.1.3 presents the evaluation of two mmWave devices which have been further developed to fit as a technological alternative to be used in 5G-Crosshaul network as demonstrated in Section 5.1.4.* • Programmable optical transceivers for flexible bandwidth allocation. o *Section 3.2.6 presents transparent the delivery of mobile front-*

	o /back-haul for converged metro/access elastic networking (FlexiPON) which has been experimentally demonstrated with the use of DD-OFDM S-BVTs in Section 5.2.2. • Multi-building baseband pooling, dynamic cell splitting and combining, copper-based reconfigurable indoor fronthaul. o *Indoor small cell system design supporting the multiplex of FH and BH and advanced features of centralized baseband pooling, dynamical cell split (increase spatial reuse) and energy saving have been described in Chapter 5.1.* • Common framing structure for radio over packet. o *This objective has been addressed in D2.1 Chapter 8 through the introduction of a common MAC-in-MAC Ethernet based frame*. • L1 switching techniques cooperating with L2 switching to guarantee upper bounds on latency. o *Both XPFE and XCSE have been firstly assessed in D2.1 Chapters 6 and 7 and further evaluated separately first in D2.2 Chapter 4.2 and 4.3. An algorithm for the coordination of the two switching granularities is proposed in Chapter 4.4. The analysis and simulation results provided in this document is further demonstrated in WP5 (demo 4).* • Clock recovery at edge site for packetized fronthaul. o *In D3.2, Section 5.5 describes the state of the art PTP and syncE solutions for packet-based synchronization distribution. The prototype-based experimental lab tests show that the IEEE 1588 PTP can fulfill the FH requirements for synchronization*.
5GPPP KPI impact	• 10 Gbit/s over 1000 meters distance with hybrid wireless optical / mmWave. o *Section 5.1.3 of this document presents laboratory experimentation results with respect to this challenging objective. According to this, the proposed strategies are suitable to reach such performance values with optical wireless technology.* • Latency of < 1ms between 5G Point of Attachment (PoA) and mobile core. o *As reported in Table 24, an analysis of technologies and related network scenarios has been performed to support the use cases defined in WP1.* • 10x higher frequency reuse for indoor coverage. o *In D2.2 Section 5.1.1, a dynamical cell split feature is presented for a FH-based indoor small cell design. Comparing to DAS with many antennas as one cell, this feature can easily scale up the spatial reuse to one cell per antenna site level. Therefore, larger than 10 times more spatial reuse is achievable than DAS for large premises*.
Verification	• Proof-of-concept prototype, testing and measurement of each individual technology. o *MmWave stand-alone experiments can be found in Section 3.1.3, while Section 5.1.4 presents the use of mmwave in the context of the outdoor small cell reference scenario defined in 5G-Crosshaul project.* o *Programmable optical transceiver with flexible bandwidth allocation using DD-OFDM S-BVTs is assessed in Section 5.2.2*.
WP/Tasks	WP1/T1.1, WP2/T2.2, WP2/T2.3, WP2/T2.4

Table 28: Objective 5 and KPIs and verification within WP2

Objective 5	**Increase cost-effectiveness of transport technologies for ultra-dense access**

	networks
Description	Develop techniques to enable massive and cost-effective deployment of outdoor and indoor Small Cells, facing challenges such as hostile Radio Frequency (RF) propagation environment. Develop physical layer technologies with reduced cost per bit, as well as new energy saving schemes, which further reduce operational costs.
R&D Topics	• Colourless transmitters. ○ *This is addressed in Section 5 of D2.1.* • Silicon photonics. ○ *Chapter 3.3.3 presents a silicon-photonic mini ROADM featuring low cost, small size and reduced power consumption, and showing its ability to add/drop up to 12 10-Gb/s wavelengths.* • Evolve high-capacity wireless technologies (including mmWave). ○ *Chapter 3.1 analysis the performance of a number of wireless technologies in different scenarios both separately and combined together in a 1+1 configuration. Real-field experiments are conducted in Chapter 5.1.* • Share technology with fixed access, e.g., Next Generation Passive Optical Network (PON). ○ *Chapter 3.2 overviews NGPON2 technologies, their suitability in carrying FH traffic on different wavelengths as those used for residential traffic, and its coexistence with legacy access technologies such as GPON or XG(S)-PON. Furthermore, low CPRI-options coexisting with BH traffic has also been analysed in the context of XG(S)-PONs.* • Common adaptation layer for control-plane integration of heterogeneous optical, copper and wireless fronthaul/backhaul. ○ *Chapter 7 of D2.1 overviews the functional architecture for the 5G-Crosshaul packet forwarding element including mappers for each physical interface (fibre optic, millimeter wave, copper, etc).* • Hybrid conventional/energy powered architectures and sleep mode control. ○ *Section 5.1.3 and Section 5.1.4 present, evaluate and validate the suitability of an algorithm based on Q-learning for selectively ON/OFF network deployments of small cells supplied with energy harvesters and storage systems as a valid solution to achieve higher network energy efficiency.* • Indoor fronthaul solutions utilizing copper cable infrastructures. ○ *In D2.2, FH compression schemes described in Section 4.5 reduces the FH bit rate significantly enabling transporting FH over copper-based Ethernet network (i.e. xBase-T series), and FH-based indoor system design in Section 5.1.1 presented supports advanced features of baseband pooling and dynamic cell split over copper-based Ethernet and the performance analysis show it can deliver up to ~4Gbit/s at air interface with 10GBase-T Ethernet network.*
5GPPP KPI impact	• Reduce Total Cost of Ownership (TCO) by 30% by improved optical transmission and sharing mobile and fixed access equipment. ○ *This TCO reduction is achieved thanks to the Silicon Photonics mini ROADM described in Section 3.3.3.The verification of this figure will be reported in D1.2 of WP1.* • Reduce energy cost per bit by a factor of 10. ○ *In order to achieve this impact, the evaluation of the proposed Q-learning algorithm has to be done in combination of the EMMA application defined in WP4 to reach a network wide level. However, from the analysis of the Q-learning algorithm presented in Section*

	5.1.4, it is expected that EE also increases by a similar order of magnitude according to network densification. ○ *Reduce TCO of indoor systems by 50% compared to Distributed Antenna Systems.*
Verification	• Techno-economic study. ○ *This is addressed in deliverable D1.2*. • Energy-consumption measurements on prototypes. ○ *This is addressed in deliverable D1.2*.
WP/Tasks	WP1/T1.2, WP1/T1.3, WP2/T2.1, WP2/T2.2, WP2/T2.3, WP2/T2.4, WP3/T3.2

7 Summary and conclusions

5G-Crosshaul refers to an innovative transport that evolves by traditional wire connectivity among the radio equipment towards a network able to support both fronthaul, backhaul and different client traffic. A wide range of wireless, optical and copper technologies have been extensively studied in this document to check their suitability in providing support for the transport of crosshaul traffic. A collection of the experiments and simulations performed to validate the choice of technologies made during the first reporting period of the 5G-Crosshaul project is documented, confirming that the identified key technologies are capable of covering a wide range of scenarios, from rural areas to densely populated cities, scaling costs with required performance.

Examples of remarkable achievements obtained and reported in this deliverable are listed in the following:

- Prototype of silicon photonic integrated reconfigurable optical add drop multiplexer, providing optical 5G-Crosshaul networks with enhanced flexibility, at dramatically reduced cost compared to current solutions;
- Advanced compression schemes for fronthaul, allowing the reuse of the copper access infrastructure, as enabler for massive deployment of indoor small cell;
- SDN enabled mesh mmWave networks, as an enabler for indoor small cells and frequency reuse with wireless transport technologies;
- Prototype of time-deterministic multi-layer switch based on a protocol agnostic framing protocol, capable to arbitrarily multiplex backhaul and fronthaul client signals on the same optical channel;
- Highly spectrally efficient fronthaul schemes, based on Hybrid Analogue-Digital Radio over Fibre over WDM optical networks.

Finally, simulation and testbed experiments at the network level have been performed including a mix of heterogeneous data-plane technologies (e.g. copper Ethernet, mmWave, WDMPON, multi-layer packet-optical) to address the crosshaul challenges in 5G reference network scenarios and use cases. Three key 5G reference network scenarios have been considered, namely i) very dense deployment of indoor and outdoor small cells, ii) WDMPON-based network, and iii) virtualized RAN based network. They are evaluated via analysis, simulations, and lab tests on how and whether the corresponding crosshaul solutions can fulfill the derived bandwidth and latency requirements with different radio functional splits for the most relevant use cases of WP1 described in D1.1 [1], namely i) high-speed train and vehicle safety, ii) media distribution, iii) dense urban society, and iv) mobile edge computing that require up to 10 Gbit/s peak rates.

Such extensive evaluation of technologies both at node level and at different network scenarios confirm the suitability of the technologies under study in achieving the goals, objectives and KPIs targeted by the 5G-Crosshaul project.

Annex: Overview of novel evolved CPRI specification (eCPRI)

5G radio access networks promise to fulfill several apparently contradictional requirements at the same time. They will provide connectivity with ultra-high capacities and with ultra-low latencies for the various use-cases assumed for enhanced Mobile Broadband (eMBB), ultra-reliable and low latency communications (URLLC) and massive machine type communications (mMTC).

To allow higher capacities in mobile networks, new high frequency bands above 6GHz need to be explored, which requires new technologies, like massive MIMO (mMIMO) and beamforming.

5G radio access network deployments are expected to have substantial parts centralized (manifested in form of the 5G “Central Unit” (CU)) to allow the usage of IT cloud datacenter technologies, like virtualization. At the same time, due to the strict timing and latency requirements of some of the traffic streams, distributed network elements close to the radio antenna site are unavoidable (e.g in form of the 5G “Distributed Unit” (DU)).

A more flexible allocation of the individual functions and processing steps of the radio access network are needed, as services have different capacity and latency requirements that do not need, and cannot be fulfilled all at the same time.

The functional splits may range from a typical backhaul interface, such as the LTE S1/X2 or 5G NG-C/U interfaces, to an interface where digital samples of the air interface are exchanged.

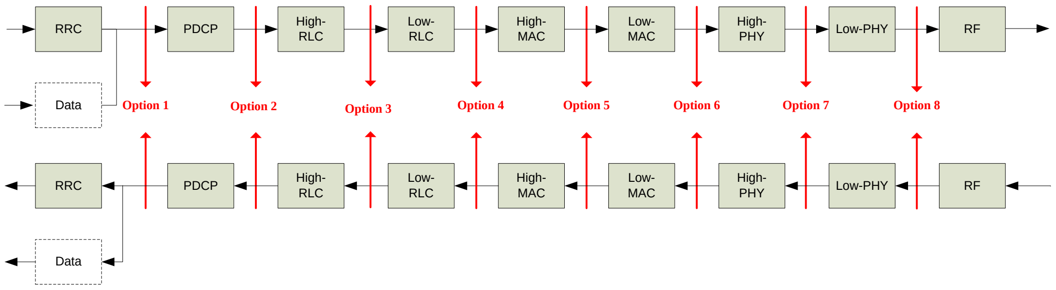

Figure 138: Functional Split between Central and Distributed Unit [2]

This annex will concentrate on the nature and the transport of traffic at the interfaces of split options 6 to 8, which demark the application area of the existing CPRI and the emerging eCPRI interface standards. These splits are used to distribute functional blocks between “radio equipment” (RE), comprising the RF block and the antenna, and another unit containing the “radio equipment control” (REC) and further baseband processing. The latter one may also be known as baseband unit (BBU), the first one as radio remote head (RRH) or radio unit (RU).

The eCPRI Specification V1.0 (2017-08-22) [99] details the possible functional split between the High-PHY and the Low-PHY further down by introducing two further splits in downlink and one more split in uplink (see Figure 139).

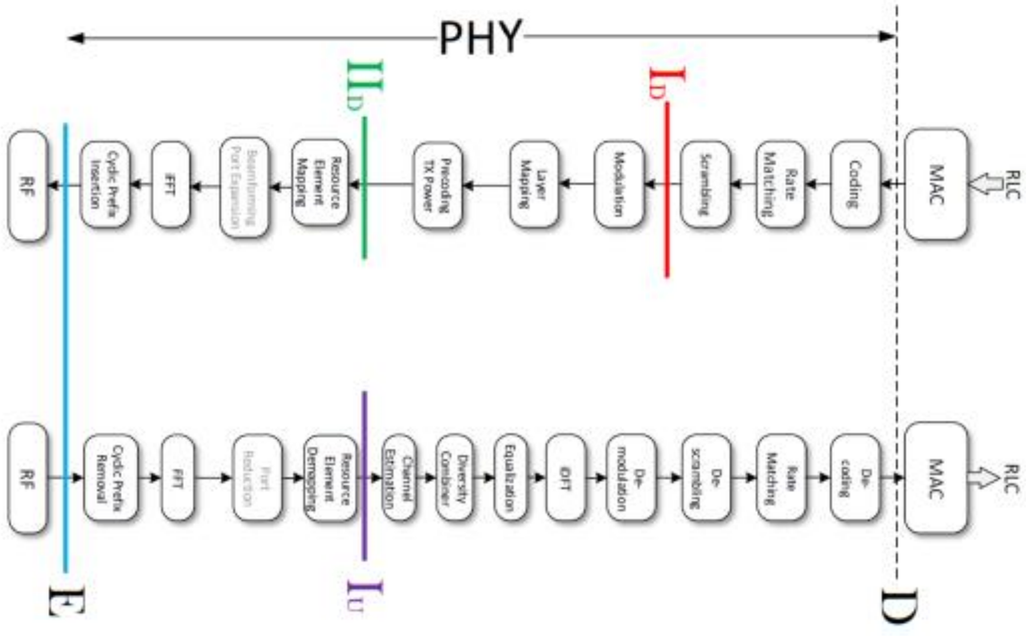

Figure 139: Detailed functional split between high PHY and low PHY (eCPRI V1.0)

In these splits, the split E demarks the classical CPRI interface for mainly the transport of time domain samples, while eCPRI supports on top the transport of frequency domain symbols (II_D/I_U) and even plain bitstreams (I_D or D).

<u>LTE air interface</u>

For the understanding of the transport requirements it is important to understand the air interfaces of LTE and 5G, as the structure of the transport streams and the required capacities are closely related to them. The LTE air interface is well defined (Figure 140).

- one radio frame has 10ms
- one subframe of lasts 1ms and has two slots
- each slot has thus 0.5 ms
- the TTI (scheduling) period is 1ms
- subcarrier spacing (SC) is 15kHz (fix)
- 6 or 7 symbols per carrier per slot
- 66.7 us symbol time (excluding cyclic prefix)
- 128 (i)FFT samples per symbol (for 1.25MHz carrier), up to 2048 (i)FFT samples per symbol (for 20 MHz carrier)
- one Resource Element (RE) equals 1SC x 1Symbol (carries e.g. 6 bits per each SC (e.g. in case of 64QAM))
- one Physical Resource Block (PRB) is defined to have 12SCs x (6 OR 7) Symbols

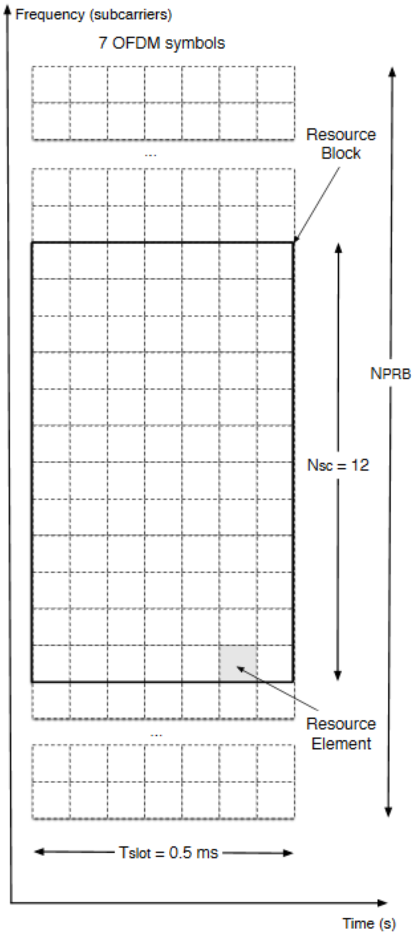

Figure 140: LTE DL RF resource grid

Based on above characteristics the needed tranport rate can be calculated for different carrier bandwidths. The following calculations are done for the downlink only and under the assumption that no MIMO is applied in the cell and just one carrier on one antenna is used. The required transport bandwidth multiplies with the amount of carriers and amount of layers used.

Each symbol time a certain number of I/Q samples are sent/received between REC and RE. Each of the I/Q samples represent the state of the whole carrier at a certain point in time. Thus, they are time domain samples. Knowing all the time samples of one symbol time, the modulation state of each of the subcarriers during that symbol time can be determined.

The required sampling rate depends on the bandwidth of the carrier and the number of subcarriers within, and is selected as a multiplicity of 3.8 MHz, which is the chip rate of the WCDMA radio networks. For OFDM the sampling rate can be expressed as $f_s = \Delta_{sc} * N_{FFT}$, with Δ_{sc} being the subcarrier spacing and N_{FFT} the amount of (i)FFT points per sample.

The accuracy of the I/Q representation (bits per I component and bits per Q component of one symbol) can be selected. As a good compromise between required bits and performance, M=15 or M=16 bits per component are often used.

Table 29: Required LTE raw I/Q time domain sample bitrate per carrier bandwidth

MHz/Cell	5	10	15	20
PRBs (with 12SCs, 15 kHz per SC)	25	50	75	100
MHz sampling rate	7,7	15,4	23,0	30,7
Sampling period [ns]	130,2	65,1	43,4	32,6
Symbol time, excl. CP [us]	66,7	66,7	66,7	66,7
FFT samples per symbol	512	1024	1536	2048
Bits per I or Q sample	15	15	15	15
IQ sample bitrate [Mbps]	230	461	691	922
Raw user data rate (for comparison) 64QAM, i.e. 6 bits per symbol per SC	25,2	50,4	75,6	100,8

Table 29 shows as well an estimate (control channels are excluded) of the achievable gross PHY user bitrate that can be transported over the air interface. Assuming for the example a 64QAM modulation of each subcarrier the bitrate for transporting the time domain samples is roughly ten times higher than the gross PHY bitrate.

In case a MIMO scheme is used, each of the RF chains/antennas is served by an individual RF resource grid, requiring multiple bit streams per cell. E.g. in case of a 4x2 MIMO (4 antennas on the eNB and 2 antennas on the UE side), 4 antenna streams are required between REC and RE and the bitrate needs to be fourfold.

CPRI interface for LTE

The traditional CPRI interface represents the split E in figure 2. It was first standardized almost 15 years ago by the CPRI initiative, which was founded in 2003, and has been updated several times since. CPRI is time division multiplexing (TDM) based. Each of the antenna streams (called AxC) is carried in CPRI words at dedicated positions (time slots) of the CPRI frame. The current version of the CPRI specification is CPRI Specification V7.0 [100].

CPRI has a basic time period of 260.416 ns, matching the sample rate of the air interface. The basic word length of CPRI is 8 bits. Per 15 data words, one control word is transported, which carries additional information and data channels, e.g. for synchronization, control and management purposes. A higher CPRI rate is achieved by transporting longer CPRI words within the same time period. CPRI line rates are expressed as “options”, with option 1 providing 614.4 Mbps and going up to (today) option 10 with 24.3 Gbps.

As the antenna stream is organized as continuous stream of e.g. 15 bit I and 15 bit Q samples and is mapped onto CPRI words having a length T of 8 to 128 bits, one sample may be carried in more than one CPRI word.

One Antenna for a 2.5 MHz cell requires 30 bits every 260.4 ns, thus requires 115.2 Mbps. A basic CPRI frame with option 1 can carry 460.8 Mbps of I/Q data (15*8*3.84MHz), sufficient for four AxCs for 2.5 MHz carriers. With four AxCs two 2.5 MHz cells with 2x2 MIMO can be supplied.

A basic CPRI frame can alternatively carry one AxC of a 10 MHz carrier.

The actual line rate of CPRI is higher than the I/Q sample rate. Beside the control word, adding 1/15 = 6.7% overhead, linecoding is used to secure the transmission. The selected line coding adds either 2 bit coding per 8 bit data or 2 bit coding per 64 bit data, depending on the selected option.

Table 30 shows the amount of useable AxCs per cell bandwidth and CPRI linerate.

Table 30: Amount of AxCs per carrier bandwidth and CPRI linerate

Amount of AxCs per linerate/cell bandwidth				5	10	15	20	MHz cell
Option	CPRI Rate [Mbps]	Coding	T	307,2	614,4	921,6	1228,8	Mbps/AxC
1	614,40	8B/10B	8	2	1			
2	1228,80	8B/10B	16	4	2	1	1	
3	2457,60	8B/10B	32	8	4	2	2	
4	3072,00	8B/10B	40	10	5	3	2	
5	4915,20	8B/10B	64	16	8	5	4	
6	6144,00	8B/10B	80	20	10	6	5	
7	9830,40	8B/10B	128	32	16	10	8	

Option	CPRI Rate [Mbps]	Coding	T	253,44	506,88	760,32	1013,76	Mbps/AxC
7a	8110,08	64B/66B	128	32	16	10	8	
8	10137,60	64B/66B	160	40	20	13	10	
9	12165,12	64B/66B	192	48	24	16	12	
10	24330,24	64B/66B	384	96	48	32	24	

M: 15, amount of bits per I or Q sample

T: CPRI wordlength in bits

Advantages of CPRI are the simple structure, which allows cost efficient implementations of the RE. This was one of the main targets when the interface was first specified as point-to-point fiber connection over a short distance, e.g. from the basement of a building to it’s rooftop.

However, operators discovered the advantages to have the REs locally separated from the RECs, which could be centralized e.g. in a so-called Baseband Hotel. This allows beside other advantages an easier physical access to the REC sites. Distances of several tens of kilometers between REC and RE are common today.

CPRI has many disadvantages as well, especially when intended to be used in a geographically distributed manner.

CPRI requires more than tenfold the bitrate of the transported end user bitrate, as it transmits modulated bitstreams. CPRI antenna flows carry as well redundant information, such as cyclic prefixes. It carries even “non”-information in form of unused PRBs. As the time samples represent the state of the whole cell, also the information of unused PRBs is included in the time sample flow. CPRI produces a constant bit rate traffic, independent on the real usage of the air interface.

CPRI has been designed for a specific purpose, the connection between REC and RE, without considering main stream Telco and IT networking technologies. Thus, although (derivates of) ethernet SFPs (interfaces) are used, due to the TDM nature of CPRI, no ethernet switches can be deployed. CPRI traffic aggregation and rearrangement, e.g. aggregating antenna traffic on RE sites or dynamically distributing antenna streams to several BBUs need to be done with dedicated CPRI TDM switches that represent costly niche products.

The upcoming technology discontinuities that are coming with 5G networks, namely massive MIMO and the anticipated overall high capacities demand for a new functionality split among RE and REC with a new interface that is designed to support main stream packet networking right away.

5G new radio (NR) air interface

The standardization of the new radio interface for 5G is currently in progress by the 3GPP. Not all aspects of the coming air interface are settled, but some main characteristics are known. Overall it is based on the LTE interface, but enriched with features that make it more suitable for the use cases envisioned with 5G.

One of the characteristics of 5G networks will be to support cells with wider bandwidths to allow higher end-user throughput without the need for carrier-aggregation or similar. Although the final selection has not been made new cell bandwidths of 100 MHz, 200 MHz or 400 MHz are very probable, especially for usage in higher bands above 6 GHz.

In order to keep the needed technology feasible, 3GPP agreed a maximum FFT size of 4096. As the subcarrier spacing is dependent on the FFT size, a flexible subcarrier spacing has been proposed. Depending on the cell bandwidth, several subcarrier spacings will be possible, spanning from 15 kHz like in LTE, and doubling from there in steps up to 240 kHz (or beyond).

Using a wider subcarrier spacing for a given cell bandwidth with less FFT samples means as well a shorter symbol time.

Table 31 summarizes these characteristics for the various combinations of cell bandwidth and subcarrier spacings. Regarding the amount of subcarries shown per subcarrier spacing, a simplified scheme has been taken, showing a maximum of up to 3300 subcarriers. The exact amount per each carrier bandwidth is right now under discussion by the 3GPP. It is however decided that a resource block (RB, corresponding to PRB in LTE) will contain 12 resource elements, also in case of 5G.

Table 31: Required 5G raw I/Q sample bitrate per carrier bandwidth

			Carrier Bandwidth [MHz]												
			5	10	15	20	30	40	50	60	80	100	150	200	400
PRBs (with 12SCs, 15 kHz per SC)	<6GHz		28	55	83	110	165	220	275						
Number of subcarriers			330	660	990	1320	1980	2640	3300						
Symbol time [us], excl. CP			66,7	66,7	66,7	66,7	66,7	66,7	66,7						
FFT samples per symbol			512	1024	1536	2048	3072	4096	4096						
PRBs (with 12SCs, 30 kHz per SC)			14	28	42	55	83	110	138	165	220	275			
Number of subcarriers			165	330	495	660	990	1320	1650	1980	2640	3300			
Symbol time [us], excl. CP			33,3	33,3	33,3	33,3	33,3	33,3	33,3	33,3	33,3	33,3			
FFT samples per symbol			256	512	768	1024	1536	2048	2048	3072	4096	4096			
PRBs (with 12SCs, 60 kHz per SC)		>6GHz		14	21	28	42	55	69	83	110	138	207	275	
Number of subcarriers				165	247	330	495	660	825	990	1320	1650	2475	3300	
Symbol time [us], excl. CP				16,7	16,7	16,7	16,7	16,7	16,7	16,7	16,7	16,7	16,7	16,7	
FFT samples per symbol				256	384	512	768	1024	1024	1536	2048	2048	3072	4096	
PRBs (with 12SCs, 120 kHz per SC)									35			69	104	138	275
Number of subcarriers									412			825	1237	1650	3300
Symbol time [us], excl. CP									8,3			8,3	8,3	8,3	8,3
FFT samples per symbol									512			1024	1536	2048	4096
PRBs (with 12SCs, 240 kHz per SC)									18			35	52	69	138
Number of subcarriers									206			412	618	825	1650
Symbol time [us], excl. CP									4,2			4,2	4,2	4,2	4,2
FFT samples per symbol									256			512	768	1024	2048
Bits per I or Q sample			15	15	15	15	15	15	15	15	15	15	15	15	15
Sampling rate [MHz]			7,7	15,4	23,0	30,7	46,1	61,4	61,4	92,2	122,9	122,9	230,4	307,2	614,4
Sampling period [ns]			130,2	65,1	43,4	32,6	21,7	16,3	16,3	10,9	8,1	8,1	4,3	3,3	1,6
Mbps IQ sample bitrate ("AxC" rate)			230	461	691	922	1382	1843	1843	2765	3686	3686	6912	9216	18432

To summarize the other known properties of the coming 5G air interface:

- all radio frames last T_f = 10 ms
- one radio frame has always 10 subframes with T_{subf} = 1 ms
- a slot carries 14 symbols
- one 1 ms subframe has a variable number of slots, depending on the subcarrier spacing
- 15kHz: 1 slots, 30kHz: 2 slots, 60kHz: 4 slots, 120kHz: 8 slots, 240kHz: 16 slots
- slots may comprise on top as well “minislots” containing down to 1 (for further study) or 2 symbols to support many UEs with low bitrate, as in case of IoT, or ultra-short latencies.

CPRI interface usage for 5G

I/Q samples for 5G can be transported via the standard CPRI interface. The bottom row of Table 31 shows the required raw bit rate for a given cell bandwidth. For 20 MHz cells, the same 922 Mbps can be seen (assuming same 15 bits are used per I- and Q-sample) as for LTE.

Table 32: Amount of AxCs per carrier bandwidth and CPRI linerate for 5G

Amount of AxCs per linerate/cell bandwidth				5	10	15	20	30	40	50	60	80	100	150	200	400	MHz cell
Option	CPRI Rate [Mbps]	Coding	T	307	614	922	1229	1843	2458	2458	3686	4915	4915	9216	12288	24576	Mbps/AxC
1	614,40	8B/10B	8	2	1												
2	1228,80	8B/10B	16	4	2	1	1										
3	2457,60	8B/10B	32	8	4	2	2	1	1	1							
4	3072,00	8B/10B	40	10	5	3	2	1	1	1							
5	4915,20	8B/10B	64	16	8	5	4	2	2	2	1	1	1				
6	6144,00	8B/10B	80	20	10	6	5	3	2	2	1	1	1				
7	9830,40	8B/10B	128	32	16	10	8	5	4	4	2	2	2	1			

Option	CPRI Rate [Mbps]	Coding	T	253	507	760	1014	1521	2028	2028	3041	4055	4055	7603	10138	20275	Mbps/AxC
7a	8110,08	64B/66B	128	32	16	10	8	5	4	4	2	2	2	1			
8	10137,60	64B/66B	160	40	20	13	10	6	5	5	3	2	2	1	1		
9	12165,12	64B/66B	192	48	24	16	12	8	6	6	4	3	3	1	1		
10	24330,24	64B/66B	384	96	48	32	24	16	12	12	8	6	6	3	2	1	

In case of a 400 MHz cell one AxC requires 18.4 Gbps. Assuming a 2x2 MIMO operation of the cells two SFPs with CPRI line rate option 10 (24.3 Gbps line rate) are needed per cell. Further assuming that a cell site will accommodate several cells and also MIMO will be applied, like 4x2 MIMO or higher, it quickly turns out that the traditional CPRI may be used in some cases (low bands, lower to medium cell bandwidths) but not for the full range of options that 3GPP will specify.

Especially with massive MIMO and beam forming, CPRI will quickly fall short.

Massive MIMO and beamforming are key technologies for 5G to tackle the challenges of the new high bands. They are used to e.g. increase the cell diameter (which is limited with mm-waves) or the end-user throughput, or the power consumption or all of it. At frequencies around 30 to 300 GHz the antenna component size is small enough to fit hundreds of them to a relatively small space. 64x64 cross-polarized antenna arrays have been demonstrated already and higher amounts of antenna elements are announced. Even if the amount of antenna elements is higher than the implemented RF RxTx chains feeding them, dozens of chains (64, 128, …) are needed to support more complex beamforming scenarios than e.g. simple beam-sweeping.

Trying to connect the REC and the RE for a 400 MHz cell to do massive MIMO using the traditional PHY split and the traditional CPRI would end up in a massive amount of CPRI SFPs with the highest CPRI linerates available today per cell.

New radio stack splits and eCPRI interface

To reduce the needed capacity, some of the baseband processing currently done within the baseband unit needs to be moved to the radio unit. Several options are proposed.

One option is to shift the FFT/iFFT to the radio unit. This will provide an interface where the individual resource elements are still visible, instead of transporting the time domain samples of the whole carrier. This allows to transport frequency domain symbols of those resource elements, that are really used by some UE in the cell. Also, massive MIMO and beamforming will happen in the RU and will not load the transport interface between REC and RE.

Another option is to go one step further and move the modulation as well to the radio unit. In this case the process of inflating end user data to I/Q frequency domain symbols would happen close to the antenna and not in the remote baseband unit. Assuming a 64QAM modulation, an I/Q symbol for a RE with 2 x 15 bits can carry 6 bits of end-user data. This means a ratio of 1 : 5. This looks attractive and may be at the end more effective as to compress the I/Q frequency domain symbols, where a better compression ratio than 1 : 3 may be difficult to achieve. However, as shown in the subsequent chapters, the amount of to be added control information will grow as well and other disadvantages will show up as well.

The new eCPRI [99] is defined to overcome some of the limitations that traditional CPRI has. Equipment capable to provide eCPRI interfaces is called eRE (the radio unit) or eREC (the baseband unit) respectively, compared to RE and REC in traditional CPRI nomenclature.

eCPRI defines message types suiting for the transport of information for all possible splits of the PHY.

- transport of time domain I/Q samples (split E in figure 2, same split as in case of CPRI)
- transport of frequency domain I/Q symbols (split II_d/I_u in figure 2)
- transport of encoded user data or MAC data (split I_d or split D in figure 2)

eCPRI enables lower transmission rates and its services are designed to keep the complexity and costs of the radio unit low.

The eCPRI standard focusses on the eCPRI services, like user data mapping and real-time-control, and makes no assumptions for control/management-plane, synchronization-plane and other functionality, other than that standard protocols from well-known packet based protocol suites are used.

Two possible southbound layers for the eCPRI protocol layer are possible

- eCPRI over Ethernet (in this case no IP layer for the user data is foreseen)
- eCPRI over IP (in this case ethernet may still be used underneath the IP layer, but as well any other suitable TRS L2 technology)

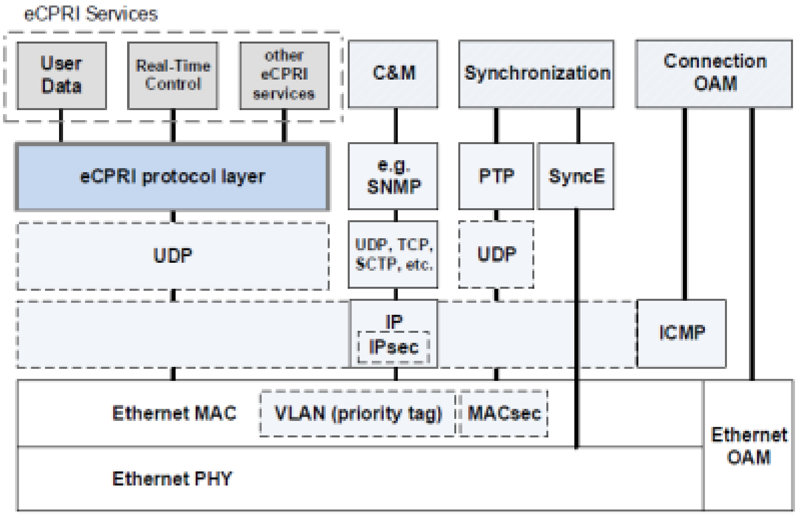

Figure 141: eCPRI protocol layer and eCPRI services [99]

The eCPRI data transfer is based on messages that are packed into the payload of the underlying transport technology like UDP/IP or ethernet. All messages carry the 4 byte eCPRI common header, which holds the type of the message and the payload size of the subsequent eCPRI message body. eCPRI messages can be concatenated to form a larger eCPRI "PDU". Concatenation is indicated by setting the concatenation indicator "C".

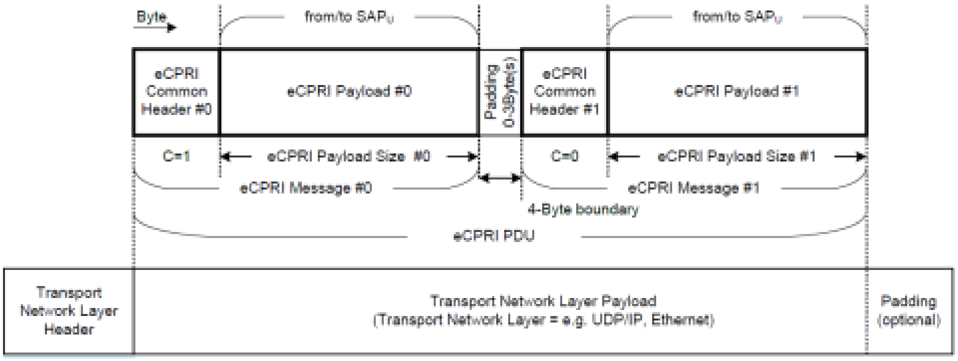

Figure 142: Example of two concatenated eCPRI messages [99]

The eCPRI specification defines 7 message types. For the transport of user plane data:

- type 0 for I/Q data (can be used for time and frequency domain I/Q data)
- type 1 for bit sequences (can be used for transporting unmodulated use data)
- type 2 for real time control data (containing meta data associated with the user plane data)

The actual content of the transmitted real-time control data will be highly dependent on the actual split used (and will differ according to the selected implementation), but comprises information on how the data subsequently received in the type 0 or type 1 user plane messages needs to be interpreted. Control data may comprise user data type identifyers, i.e. whether user data represents samples, symbols or a user data flow, or more fine-granular addressing, e.g., if the 16 bits of PC_ID in the common header are not enough to identify the target (antenna, user, beam, …), or to be used modulation scheme in case of user data bit stream.

The other message types that eCPRI defines are for generic data transfer (type 3), remote memory access (type 4), one-way delay measurement (type 5), remote reset (type 6) and for event indication (type 7).

eCPRI specification V1.0 defines a basic messaging framework, but the actual content is left to vendor specific implementation. The following calculations are therefore hypothetical and rather show an indication, which performance can be achieved.

Transport of time domain IQ samples (Split E)

According to the example given in the eCPRI interface specification the first transmitted information will be the control information associated to the subsequent flow of samples/symbols.

Following estimations and assumptions are made:

- the data stream is targeted towards one entity consuming one resource grid, e.g. one MIMO layer of one cell
- each message contains all samples of one symbol time in basic case

- however, if eCPRI message would be longer than e.g. 960 byte user payload data, two or more Ethernet frames/IP packets would be generated, each carrying up to 960 byte user data to minimize ahead of line blocking (corresponds to 256 time samples per message)
- each sample shall be composed of 15 bit I and 15 bits Q data (for consistency with the analysis of the traditional CPRI)
- one control data message is sent per TTI (possible intervals are: 1 ms, 0.5 ms, 0.25 ms, 0.125 ms, 0.063 ms, as TTI will depend on the subcarrier spacing)
- control frame carries some information for the carrier generating a small amount of overhead
  (e.g. 4 byte common header + 4 byte RTC header + 32 byte control information, per TTI)
- Ethernet and/or IP headers on top for each eCPRI message according to the selected transport stack option, see Table 34.

Table 33: Overhead sizes

Eth/Ip Header Items	IPv4	IPv6	
UDP	8		Bytes
IP Header	20	40	Bytes
IPSec ESP Header	10		Bytes
ESP AES Init Vector	16		Bytes
ESP Trailer	12		Bytes
IPSec Authentication	12		Bytes
IPSec Tunnel IP header	20	40	Bytes
Ethernet higher layer	22		Bytes
Other Ethernet	20		Bytes

Table 34: Eth, IP, Ipsec and eCPRI overheads

Eth/Ip Overhead		
eCPRI over Eth	42	OH Bytes per frame
eCPRI over IPv4	70	OH Bytes per packet
eCPRI over IPv6	90	OH Bytes per packet
eCPRI over IPv4/IPsec	140	OH Bytes per packet
eCPRI over IPv6/IPsec	180	OH Bytes per packet

eCPRI Overhead			
Common Header		4	OH Bytes per msg
Dedicated Header		4	OH Bytes per msg

OH Bytes per IQ-, Bit-, RTC-, Generic- Data Message
(decicated OH of other eCPRI message types vary)

The main contribution in terms of traffic volume is coming from the time domain IQ samples. Table 35 shows the rates for different carrier bandwidths and depending on the selected eCPRI transport option.

Table 35: eCPRI capacities in case of time-domain user data transport

I/Q Data Flow		Carrier Bandwidth [MHz]												
(Time Samples)		5	10	15	20	30	40	50	60	80	100	150	200	400
Bits/Sample	[b]	30	30	30	30	30	30	30	30	30	30	30	30	30
"AxC" Rate	[Mbps]	230	461	691	922	1382	1843	1843	2765	3686	3686	6912	9216	18432
Samples/IQmsg		256	256	256	256	256	256	256	256	256	256	256	256	256
Bytes/IQmsg	[B]	960	960	960	960	960	960	960	960	960	960	960	960	960
IQmsg rate	[kpps]	30	60	90	120	180	240	240	360	480	480	900	1200	2400
eCPRI OH Rate	[Mbps]	2	4	6	8	12	15	15	23	31	31	58	77	154
eCPRI IQ Datarate	[Mbps]	232	465	697	929	1394	1859	1859	2788	3717	3717	6970	9293	18586
eCPRI IQ Rate over Eth	[Mbps]	242	485	727	970	1454	1939	1939	2909	3878	3878	7272	9696	19392
eCPRI IQ Rate over IPv4	[Mbps]	249	498	747	996	1495	1993	1993	2989	3986	3986	7474	9965	19930
eCPRI IQ Rate over IPv6	[Mbps]	254	508	762	1016	1524	2031	2031	3047	4063	4063	7618	10157	20314
eCPRI IQ Rate over IPv4/IPsec	[Mbps]	266	532	798	1064	1596	2127	2127	3191	4255	4255	7978	10637	21274
eCPRI IQ Rate over IPv6/IPsec	[Mbps]	276	551	827	1102	1653	2204	2204	3306	4408	4408	8266	11021	22042

With above assumption on the payload size of the eCPRI real time control message of 32 Bytes and its frequency the estimated overhead for the control traffic on top of the user traffic is well below 5%. In terms of packets per second the overhead is a bit bigger, but still well below 10%.

Table 36 shows the amount of "AxCs" that can be fit to one Ethernet SFP. On top of the reservation for the real-time control traffic some more reservation is added for other traffic, like management traffic. Overall an additional reservation/spare capacity of 10% is applied.

Compared to plain CPRI, eCPRI for time domain samples allows to fit either same amount of "AxCs", or slightly less, depending on the selected transport option. This may be overcome by CPRI compression or other methods to avoid using 30 bits per IQ time sample.

Table 36: Number of AxC per carrier bandwidth per SFP for time domain sample transport

Amount of AxC per SFP			Carrier Bandwidth [MHz]												
(time samples, 90% line rate usage)			5	10	15	20	30	40	50	60	80	100	150	200	400
"AxC" line rate eCPRI over Eth		[Mbps]	244	487	730	972	1457	1942	1950	2911	3881	3889	7282	9706	19402
"AxC" line rate with IPv6/Ipsec		[Mbps]	279	558	834	1109	1660	2211	2232	3313	4415	4436	8294	11049	22070
10G SFP	eCPRI over Eth		36	18	12	9	6	4	4	3	2	2	1	0	0
	eCPRI over IPv6/Ipsec		32	16	10	8	5	4	4	2	2	2	1	0	0
25G SFP	eCPRI over Eth		92	46	30	23	15	11	11	7	5	5	3	2	1
	eCPRI over IPv6/Ipsec		80	40	26	20	13	10	10	6	5	5	2	2	1
40G SFP	eCPRI over Eth		147	73	49	37	24	18	18	12	9	9	4	3	1
	eCPRI over IPv6/Ipsec		129	64	43	32	21	16	16	10	8	8	4	3	1
100G SFP	eCPRI over Eth		369	184	123	92	61	46	46	30	23	23	12	9	4
	eCPRI over IPv6/Ipsec		322	161	107	81	54	40	40	27	20	20	10	8	4

Transport of frequency domain symbols (Split I_U/II_D)

With this PHY split the IQ symbols per subcarrier are transported. The final IQ time samples are calculated by the radio unit once all frequency domain symbols of one symbol time have been received. This allows to omit unused resource blocks or to transmit redundant data only once, like cyclic prefixes. Thus, the needed data rate is smaller compared to the transmission of time samples, even, if the resource grid is fully used.

However, this comes at the expense of a wider control flow, as now some of the information that earlier has been coded into the samples need to be transmitted via the separate control stream. Still, the gain outweighs the costs. Another advantage is that transport multiplexing gains in case of not fully used cells can be realized more easily.

Table 37: eCPRI capacities in case of frequency domain user data transport

I/Q Data Flow (Frequency Domain Symbols)		Carrier Bandwidth [MHz]												
		5	10	15	20	30	40	50	60	80	100	150	200	400
Bits/Symbol	[b]	30	30	30	30	30	30	30	30	30	30	30	30	30
N Subcarrier, max		330	660	990	1320	1980	2640	3300	1980	2640	3300	2475	3300	3300
Symbol Time, excl. CP, max	[us]	66,7	66,7	66,7	66,7	66,7	66,7	66,7	33,3	33,3	33,3	16,7	16,7	8,3
Slot duration (14 symb), max	[us]	1000	1000	1000	1000	1000	1000	1000	500	500	500	250	250	125
Avg Symb Time, incl CP, max	[us]	71,4	71,4	71,4	71,4	71,4	71,4	71,4	35,7	35,7	35,7	17,9	17,9	8,9
Symbol Rate	[MSymb/s]	5	9	14	18	28	37	46	55	74	92	139	185	370
"AxC" rate	[Mbps]	139	277	416	554	832	1109	1386	1663	2218	2772	4158	5544	11088
IQmsg rate*	[kpps]	18	36	54	72	108	144	180	217	289	361	541	722	1444
eCPRI OH Rate	[Mbps]	1	2	3	5	7	9	12	14	18	23	35	46	92
eCPRI IQ Datarate	[Mbps]	140	280	419	559	839	1118	1398	1677	2236	2795	4193	5590	11180
eCPRI IQ Rate over Eth	[Mbps]	146	292	437	583	875	1167	1458	1750	2333	2916	4375	5833	11666
eCPRI IQ Rate over IPv4	[Mbps]	150	300	450	599	899	1199	1499	1798	2398	2997	4496	5994	11989
eCPRI IQ Rate over IPv6	[Mbps]	153	305	458	611	916	1222	1527	1833	2444	3055	4582	6110	12220
eCPRI IQ Rate over IPv4/IPsec	[Mbps]	160	320	480	640	960	1280	1600	1920	2559	3199	4799	6399	12797
eCPRI IQ Rate over IPv6/IPsec	[Mbps]	166	331	497	663	994	1326	1657	1989	2652	3315	4972	6630	13259

*Payload [Byte] 960

Table 37 shows the calculation of the “AxC” rate based on number of subcarriers and symbol-time.

Please note that the ratio of number of subcarriers to symbol-time is constant per carrier bandwidth and is independent of the selected subcarrier spacing for the cell. In the table, the maximum amount of possible subcarriers for a particular carrier bandwidth has been selected, thus the smallest subcarrier spacing, which gives the longest symbol times.

To avoid ahead of line blocking, the payload size of the data packets has been set to 960 bytes.

Compared to the required user data rates in Table 35 only about 2/3 of the time domain rate is needed for a fully used resource grid.

The control flow will depend almost proportionally on the number of bits spent for the information per subcarrier, the amount of subcarriers and the TTI rate. As for a given carrier bandwidth the quotient of amount of subcarriers and the TTI is constant the control flow rate will be only proportional to the carrier bandwidth and the amount of bits spent per subcarrier. Overall the amount of control traffic can be estimated to be still low compared to the user date traffic (below 10% overhead on top for the message rate and below 10% overhead for the user traffic rate).

Table 38 shows the amount of frequency domain “AxCs” that can be fit to one Ethernet SFP. Again, on top of the reservation for the real-time control traffic some more reservation is added for other traffic, like management traffic. Overall a reservation/spare capacity of 10% on top is applied.

Table 38: Number of AxC per carrier bandwidth per SFP for frequency domain symbol transport

Amount of AxC per SFP		Carrier Bandwidth [MHz]												
		5	10	15	20	30	40	50	60	80	100	150	200	400
"AxC" line rate eCPRI over Eth	[Mbps]	148	296	443	590	885	1179	1478	1767	2356	2950	4421	5892	11778
"AxC" line rate with IPv6/Ipsec	[Mbps]	170	340	507	674	1009	1343	1695	2011	2679	3366	5036	6707	13389
10G SFP	eCPRI over Eth	60	30	20	15	10	7	6	5	3	3	2	1	0
	eCPRI over IPv6/Ipsec	52	26	17	13	8	6	5	4	3	2	1	1	0
25G SFP	eCPRI over Eth	152	76	50	38	25	19	15	12	9	7	5	3	1
	eCPRI over IPv6/Ipsec	132	66	44	33	22	16	13	11	8	6	4	3	1
40G SFP	eCPRI over Eth	243	121	81	60	40	30	24	20	15	12	8	6	3
	eCPRI over IPv6/Ipsec	211	105	70	53	35	26	21	17	13	10	7	5	2
100G SFP	eCPRI over Eth	608	304	203	152	101	76	60	50	38	30	20	15	7
	eCPRI over IPv6/Ipsec	529	264	177	133	89	67	53	44	33	26	17	13	6

Transport of unmodulated user data (Split I_D or D)

Finally, the remaining option is discussed. In this case the modulation takes place at the radio unit as well. This will on on one hand result in the lowest user data transmission bitrates between eREC and eRE, but means as well in the most complex RU design and a high control flow bitrate.

Table 39 below shows as one peak case the bitrates, if all UEs would have ideal conditions and all would use e.g. a 256QAM. In this case 8 bits of end user data could be transported per one resource element of the resource grid. Neglecting all resource blocks that are used e.g. for the control channels, i.e. for the radio system itself, the theoretical amount of data that can be transported by a carrier of a given bandwidth can be roughly estimated per Table 39.

Table 39: eCPRI capacities in case of unmodulated user data transport

Data Flow (Bitstream)		Carrier Bandwidth [MHz]												
		5	10	15	20	30	40	50	60	80	100	150	200	400
Bits/RE (256QAM)	[b]	8	8	8	8	8	8	8	8	8	8	8	8	8
N Subcarrier, max		330	660	990	1320	1980	2640	3300	1980	2640	3300	2475	3300	3300
Symbol Time, excl. CP, max	[us]	66,7	66,7	66,7	66,7	66,7	66,7	66,7	33,3	33,3	33,3	16,7	16,7	8,3
Slot duration (14 symb), max	[us]	1000	1000	1000	1000	1000	1000	1000	500	500	500	250	250	125
Avg Symb Time, incl CP, max	[us]	71,4	71,4	71,4	71,4	71,4	71,4	71,4	35,7	35,7	35,7	17,9	17,9	8,9
RE rate	[MRE/s]	5	9	14	18	28	37	46	55	74	92	139	185	370
"AxC" rate	[Mbps]	37	74	111	148	222	296	370	444	591	739	1109	1478	2957
Bitstream msg rate*	[kpps]	5	10	14	19	29	39	48	58	77	96	144	193	385
eCPRI OH Rate	[Mbps]	0,3	0,6	0,9	1,2	1,8	2,5	3,1	3,7	4,9	6,2	9,2	12,3	24,6
eCPRI Bitstream Datarate	[Mbps]	37	75	112	149	224	298	373	447	596	745	1118	1491	2981
eCPRI IQ Rate over Eth	[Mbps]	39	78	117	156	233	311	389	467	622	778	1167	1555	3111
eCPRI IQ Rate over IPv4	[Mbps]	40	80	120	160	240	320	400	480	639	799	1199	1599	3197
eCPRI IQ Rate over IPv6	[Mbps]	41	81	122	163	244	326	407	489	652	815	1222	1629	3259
eCPRI IQ Rate over IPv4/IPsec	[Mbps]	43	85	128	171	256	341	427	512	683	853	1280	1706	3413
eCPRI IQ Rate over IPv6/IPsec	[Mbps]	44	88	133	177	265	354	442	530	707	884	1326	1768	3536

*Payload [Byte] 960

Regarding the control flow one can assume, that now on top of the control data for the frequency domain symbols of the previously discussed split, which still needs to be transported to the eREC, further information, e.g. on the to be used modulation needs to be sent to the eRE. The amount of control flow may now become significant compared to the user data flow, lowering the overall achievable gain.

With some additional reservation done for other traffic types the following numbers of supported "AxCs" for the transport of unmodulated data can be estimated.

Table 40: Number of AxC per carrier bandwidth per SFP unmodulated user data transport

Amount of AxC per SFP		Carrier Bandwidth [MHz]												
		5	10	15	20	30	40	50	60	80	100	150	200	400
"AxC" line rate eCPRI o Eth	[Mbps]	42	85	126	168	251	334	423	500	666	838	1253	1668	3329
"AxC" line rate with IPv6/Ipsec	[Mbps]	50	100	147	194	287	381	494	568	755	962	1430	1898	3772
10G SFP	eCPRI over Eth	212	106	71	53	35	26	21	17	13	10	7	5	2
	eCPRI over IPv6/Ipsec	180	90	61	46	31	23	18	15	11	9	6	4	2
25G SFP	eCPRI over Eth	530	265	178	134	89	67	53	44	33	26	17	13	6
	eCPRI over IPv6/Ipsec	450	225	153	116	78	59	45	39	29	23	15	11	5
40G SFP	eCPRI over Eth	849	424	284	214	143	107	85	71	54	42	28	21	10
	eCPRI over IPv6/Ipsec	721	360	245	185	125	94	72	63	47	37	25	18	9
100G SFP	eCPRI over Eth	2123	1061	712	536	358	269	212	179	135	107	71	53	27
	eCPRI over IPv6/Ipsec	1803	901	613	464	313	236	182	158	119	93	62	47	23

Also for this split multiplexing gains can be easily realized in case that the aggregated actual end user data flows are lower in bitrate than the possible peak rate supported by the carrier.

In terms of data volume this split is by far the most efficient one. Though some drawbacks are associated with this solution as well.

RUs are placed usually on rooftops, poles and masts and a lot of the incorporated functionality is implemented in dedicated HW to reduce the costs down for the required performance. They are kept intentionally as simple as possible to serve future radio features without the need for SW updates. Complex radio features are rather implemented in the BBU, where SW updates can be accomplished more easily. Keeping complex features out of the RU will also extend the projected lifetime in the field, avoiding the need to replace the RUs due to the introduction of new radio features.

Functionality kept outside of the RU can furthermore be more easily implemented in a centralized or virtualized way. Therefore, increasing the functionality of RUs to save bandwidth reduces potential gains in operability due to centralization of BBU functionality.

Bibliography

[1] 5G-Crosshaul D1.1: Initial specification of the system architecture accounting for the feedback received from WP2/3/4, June 2016.

[2] 3GPP Technical Report 38.801: Study on new radio access technology: Radio access architecture and interfaces, March 2016

[3] IEEE 802.1CM: Time-Sensitive Networking for Fronthaul, July 2016

[4] 3GPP Technical Report 36.213: Evolved Universal Terrestrial Radio Access (E-UTRA); Physical layer procedures, September 2016

[5] 5G-Crosshaul D2.1: Detailed analysis of the technologies to be integrated in the XFE based on previous reports from WP2/3, June 2016

[6] 5G-Crosshaul D5.1: Report on validation and demonstration plans, October 2016.

[7] ONF, OpenFlow Switch Specification Version 1.3.0, June 2012.

[8] 5G-XHaul, D4.11: Wireless backhauling using Sub-6 GHz systems, December 2016.

[9] ONF, Wireless Transport SDN Proof of Concept 2 Detailed Report, June 2016

[10] ONF, Third Wireless Transport SDN Proof of Concept White Paper, December 2016

[11] ONF, TR-532, Microwave Information Model, December 2016

[12] ONF, Wireless Transport SDN Proof of Concept white paper, October 2015

[13] 5G-Crosshaul D3.1: XFE/XCI design at year 1, specification of southbound and northbound interface, October 2016

[14] J.Núñez, J. Baranda, I. Pascual, J. Mangues, WiseHAUL: An SDN-empowered Wireless Small Cell Backhaul testbed , in Proceedings of the 17 IEEE International Symposium on a World of Wireless, Mobile and Multimedia Networks (WoWMoM), 21-24 June 2016, Coimbra, Portugal.

[15] Eckerson, Wayne W. "Three Tier Client/Server Architecture: Achieving Scalability, Performance, and Efficiency in Client Server Applications." Open Information Systems 10, 1 (January 1995): 3(20)

[16] Cisco Systems Inc., “Cisco visual networking index global mobile data traffic forecast update 2013-2018,” White Paper, Feb. 2013.

[17] A. S. G. Andrae and T. Edler, “On global electricity usage of communication technology: Trends to 2030,” Challenges, vol. 6, no. 1, p. 117, 2015.

[18] Mohammed H. Alsharif, Rosdiadee Nordin, and Mahamod Ismail, “Survey of Green Radio Communications Networks: Techniques and Recent Advances,” Journal of Computer Networks and Communications, vol. 2013, Article ID 453893, 13 pages, 2013.

[19] P. Dini, M. Miozzo, N. Bui and N. Baldo, "A Model to Analyze the Energy Savings of Base Station Sleep Mode in LTE HetNets," 2013 IEEE International Conference on Green Computing and Communications and IEEE Internet of Things and IEEE Cyber, Physical and Social Computing, Beijing, 2013, pp. 1375-1380.

[20] H. Al Haj Hassan, L. Nuaymi, and A. Pelov, “Renewable energy in cellular networks: A survey,” in IEEE Online Conference on Green Communications (GreenCom), Oct. 2013.

[21] G. Lee, W. Saad, M. Bennis, A. Mehbodniya, and F. Adachi, “Online ski rental for scheduling self-powered, energy harvesting small base stations,” in 2016 IEEE International Conference on Communications (ICC), May 2016, pp. 1–6.

[22] M. Mendil, A. D. Domenico, V. Heiries, R. Caire, and N. Hadjsaid, “Fuzzy Q-Learning based Energy Management of Small Cells Powered by the Smart Grid,” in IEEE PIMRC, Valencia, Spain, 2016.

[23] R. S. Sutton and A. G. Barto, „Reinforcement Learning: An Introduction“, MA: MIT Press, 1998.

[24] Lithium Batteries Failures, available on-line at http://www.mpoweruk.com/lithium_failures.htm.

[25] M. Miozzo, L. Giupponi, M. Rossi, P. Dini, Distributed Q-Learning for Energy Harvesting Heterogeneous Networks , in Proceedings of 2015 IEEE International Conference on Communications (ICC2015), 8-12 June 2015, London (UK).

[26] EU EARTH: Energy Aware Radio and Network technologies, D2.3: Energy Efficiency analysis of the reference systems, areas of improvements and target breakdown, Deliverable D2.3, www.ict-earth.eu, 2010.

[27] M. Miozzo, D. Zordan, P. Dini, M. Rossi, SolarStat: Modeling Photovoltaic Sources through Stochastic Markov Processes , in Proceedings of IEEE Energy Conference, 13-16 May 2014, Dubrovnik (Croatia).

[28] J. M. Fàbrega et al. "Demonstration of Adaptive SDN Orchestration: A Real-Time Congestion-Aware Services Provisioning Over OFDM-Based 400G OPS and Flexi-WDM OCS," J. Lightwave Technol. 35, 506-512 (2017)

[29] NGMN, “Next Generation Mobile Networks 5G White Paper”, February 2015

[30] A. Napoli et al. “Next Generation Elastic Optical Networks: the Vision of the European Research Project IDEALIST,” Communications Magazine, IEEE, vol. 53, no. 2, pp. , Mar 2015

[31] N. Sambo et al., “Next Generation Sliceable Bandwidth Variable Transponders,” Communications Magazine, IEEE, vol. 53, no. 2, pp. 163–171, Mar 2015.

[32] M. Svaluto Moreolo et al. “SDN-enabled Sliceable BVT Based on Multicarrier Technology for Multi-Flow Rate/Distance and Grid Adaptation,” Journal of Lightwave Technology, vol. 34, no. 8, Apr. 2016

[33] T. Pfeiffer, "Next generation mobile fronthaul and midhaul architecture" Journal of Optical Communications and Networking, vol. 7, no. 11, Nov. 2015

[34] ITU-T recommendation G.975.1 (2004)

[35] IEEE Standards Association, Enhancements for Very High Throughput in the 60 GHz Band, IEEE Std 802.11ad™-2012

[36] I. Bor-Yaliniz and H. Yanikomeroglu, “The new frontier in RAN heterogeneity: Multi-tier drone-cells, IEEE Commun. Mag., vol. 54, no. 11, pp. 48–55, Nov. 2016.

[37] T. S. Rappaport, S. Sun, R. Mayzus, H. Zhao, Y. Azar, K. Wang, G. N. Wong, J. K. Schulz, M. Samimi, and F. G. Jr., “Millimeter wave mobile communications for 5G cellular: It will work!” IEEE Access, vol. 1, pp. 335–349, May 2013.

[38] Ping-Heng Kuo and Alain Mourad, “Millimeter Wave for 5G Mobile Fronthaul and Backhaul”, in Proceedings of the 26th EUCNC, June 12-15 2017, Oulu, Finland.

[39] ETSI mWT ISG, http://www.etsi.org/technologies-clusters/technologies/millimetre-wave-transmission

[40] J. E. Gabeiras et al: “Is multilayer networking feasible?” Optical Switching and Networking, vol. 6, pp. 129 – 140, 2009.

[41] F. Rambach et al: “A multilayer cost model for metro/core networks”. IEEE/OSA J. Optical Commun. Netw., vol. 5, pp. 210-225, 2013

[42] FCC Title 47 Part 15.247(b) and (c), FCC Title 47 Part 15.407(a)

[43] Chenguang Lu, Miguel Berg, Elmar Trojer, Per-Erik. Eriksson, Kim Laraqui, Olle V. Tidblad and Henrik Almeida, “Connecting the dots: small cells shape up for high-performance indoor radio,” Ericsson Review, vol. 91, December 2014.

[44] Chenguang Lu, Miguel Berg, Leonado Ramalho and Aldebaro Klautau, “Bit-Rate Bound Derivation for Compressed Time-domain Fronthaul”, EUCNC 2016 workshop Towards Converged X-Haul for 5G Networks, Athens, Greece, June 2016.

[45] Leonardo Ramalho, Maria Nilma Fonseca, Aldebaro Klautau, Chenguang Lu, Miguel Berg, Elmar Trojer, and Stefan Höst, “An LPC-Based Fronthaul Compression Scheme,” IEEE Communications Letters, November 2016.

[46] Klaus Grobe and Michael Eiselt: “Wavelength Division Multiplexing. A practical engineering guide”. WILEY SERIES IN PURE AND APPLIED OPTICS, John Wiley & Sons, Inc., 2014.

[47] Long Term Evolution Protocol Overview, NXP, Document number LTEPTCLOVWWP Rev 0, October 2008.

[48] Small cell virtualization functional splits and use cases, Small Cell Forum, version 159.07.02.

[49] U. Dötsch, M. Doll, H. P. Mayer, F. Schaich, J. Segel and P. Sehier, "Quantitative analysis of split base station processing and determination of advantageous architectures for LTE," in Bell Labs Technical Journal, vol. 18, no. 1, pp. 105-128, June 2013.

[50] M. Karimi und M. Uysal, „Novel adaptive transmission algorithms for free-space optical links,“ IEEE Trans. on Communications, pp. 50-58, December 2012.

[51] V. Vucic et al., „513 Mbit/s Visible Light Communications Link Based on DMT-Modulation of a White LED,“ Journal of Lightwave Technology, pp. 3512-3518, December 2010.

[52] I. I. Kim und E. Korevaar, „Availability of Free Space Optics (FSO) and hybrid FSO/RF systems,“ in Optical Wireless Communications IV, Denver, 2001.

[53] F. Nadeem et al., „Weather Effects on Hybrid FSO/RF Communication Link,“ IEEE Journal on Sel. Areas in Coms (JSAC), Dec.2009.

[54] Dash, Debashis, Hassan El Madi, and Guru Gopalakrishnan. "WiGig and IEEE 802.11 ad-For multi-gigabyte-per-second WPAN and WLAN." arXiv preprint arXiv:1211.7356 (2012).

[55] InterDigital, EgdeHaulTM Solution Datasheet, available at http://www.interdigital.com/data_sheets/edgehaul

[56] JDSU, White Paper - “A Performance Comparison of WSS Switch Engine Technologies”

[57] Enrico Forestieri and Giancarlo Prati: Novel Optical Line Codes Tolerant to Fiber Chromatic Dispersion, IEEE JLT Vol. 19, No. 11, November 2001

[58] Common Public Radio Interface, available at http://www.cpri.info

[59] ”5G radio access”, Ericsson White Paper, April 2016, available at: https://www.ericsson.com/res/docs/whitepapers/wp-5g.pdf

[60] Bin Guo, Wei Cao, An Tao, and Dragan Samardzija, ”LTE/LTE-A signal compression on the CPRI interface,” in Bell Labs Technical Journal, vol.18, no.2, pp.117-133, Sept. 2013.

[61] Shinobu Nanba and Akira Agata, ”A new IQ data compression scheme for fronthaul link in Centralized RAN,” in Personal, Indoor and Mobile Radio Communications (PIMRC Workshops), 2013 IEEE 24th International Symposium on , vol., no., pp.210-214, 8-9 Sept. 2013.

[62] Karl F. Nieman and Brian L. Evans, ”Time-domain compression of complex-baseband LTE signals for cloud radio access networks,” Global Conference on Signal and Information Processing (GlobalSIP), 2013 IEEE, Austin, TX, 2013, pp. 1198-1201.

[63] Michael Bernhard, David Rörich, Thomas Handte, and Joachim Speidel, ”Analytical and numerical studies of quantization effects in coherent optical OFDM transmission with 100 Gbit/s and beyond,” ITG-Fachtagung Photonische Netze, Leipzig, Germany, 7-8 May 2012, pp. 34-40.

[64] 3GPP; Technical Specification Group Radio Access Network; E-UTRA; User Equipment (UE) radio transmission and reception, Release 13.3; 3GPP TS 36.101 V13.3 (2016-03)

[65] 3GPP; Technical Specification Group Radio Access Network; E-UTRA; Base Station (BS) radio transmission and reception, Release 13.3; 3GPP TS 36.104 V13.3 (2016-03)

[66] NGMN, “Next Generation Mobile Networks 5G White Paper”, February 2015.

[67] C.-L. I, J. Huang, R. Duan, C. Cui, J. Jiang, and L. Li, “Recent progress on C-RAN centralization and cloudification,” Access, IEEE, vol. 2, pp. 1030–1039, 2014.

[68] D. Samardzija, J. Pastalan, M. MacDonald, S. Walker, and R. Valenzuela, “Compressed Transport of Baseband Signals in Radio Access Networks,” Wireless Communications, IEEE Transactions on, vol. 11, no. 9, pp. 3216–3225, September 2012.

[69] J. Lorca and L. Cucala, “Lossless compression technique for the fronthaul of LTE/LTE-advanced cloud-RAN architectures,” in World of Wireless, Mobile and Multimedia Networks (WoWMoM), 2013 IEEE 14th International Symposium and Workshops on a, June 2013, pp. 1–9.

[70] S.-H. Park, O. Simeone, O. Sahin, and S. Shamai Shitz, “Fronthaul Compression for Cloud Radio Access Networks: Signal processing advances inspired by network information theory,” Signal Processing Magazine, IEEE, vol. 31, no. 6, pp. 69–79, Nov 2014.

[71] A. Gersho and R. M. Gray, Vector Quantization and Signal Compression. Kluwer Academic Publishers, 1992.

[72] G. Higgie and A. Fong, “Efficient encoding and decoding algorithms for variable-length entropy codes,” Communications, IEEE Proceedings, vol. 150, no. 5, pp. 305–11–, Oct 2003.

[73] Z. Aspar, Z. Yusof, and I. Suleiman, “Parallel Huffman decoder with an optimized lookup table option on FPGA,” in TENCON 2000. Proceedings, vol. 1, 2000, pp. 73–76 vol.1.

[74] ITU-T Recommendation G.989.2, “40-gigabit-capable passive optical networks (NG-PON2): Physical media dependent (PMD)”

[75] 3GPP TS 36.141: E-UTRA BS conformance testing, Rel. 10, V10.1.0, 2011.

[76] "Jitter Analysis: The dual- Dirac Model, RJ/DJ, and Q-Scale", Agilent Technologies (2004).
[77] A. Gersho, IEEE Trans. Circuits Syst, cas-25, no.7, 1978.
[78] K. Nieman and B. Evans, IEEE GlobalSIP, pp. 1198-1201, 2013.
[79] Y. Linde et al., IEEE Trans. Commun., vol.28, no.1, pp.84-95, 1980.
[80] B. Guo et. al, Bell Labs Tech. Journal, vol.18, no.2, pp.117-133, 2013.
[81] Y. Koo Kwon et al. "Optical transceiver for CWDM networks with multi subchannel interface" OFC, 2014.
[82] Thomas Pfeiffer "Next Generation Mobile Fronthaul Architectures" OFC(2015).
[83] ORI Specification, v. 4.1.1, October 2014.
[84] K. Murphy, "Centralized RAN and Fronthaul", White Paper, Ericsson, 2015
[85] EBLINK patent US 9020070 B2 : High capacity wireless communications systems and methods
[86] EBDIRTECH16-MEM136-10 Eligibility and Application of EBLINK CPRI Solution to RoF Technology (contribution to 5G-Crosshaul /WP2 Barcelona 5-7/04/2016 Meeting)
[87] D. Bertsekas, R. Gallager: Data Networks (2nd ed.), Prentice Hall Inc., Jan 1992. ISBN: 0-13-200916-1
[88] J. A. Hernández, P. Serrano: Probabilistic models for computer networks: Tools and solved problems, Lulu.com, March 2015. ISBN-13: 978-1291546873
[89] R Sánchez, J. A. Hernández, J. Moltalvo-García, D. Larrabeiti: Provisioning 1 Gb/s symmetrical services with Next-Generation Passive Optical Networks, IEEE Communications Magazine, vol. 54, no. 2, pp. 72-77 (Feb, 2016).
[90] A. de la Oliva, J. A. Hernández, D. Larrabeiti, A. Azcorra: An overview of the CPRI specification and its application to C-RAN based LTE scenarios, IEEE Communications Magazine, vol. 54, no. 2, pp. 152-159 (Feb. 2016).
[91] J. García-Reinoso, J.A. Hernández, I. Seoane, I. Vidal, "On the effect of sudden data bursts in the upstream channel of Ethernet PONs employing IPACT under the gated-service discipline", *Optical Switching and Networking*, Volume 13, July 2014, Pages 94-102.
[92] Peraso W110 chipset, available online at: http://www.perasotech.com/gp_product/consumer-ic-products/.
[93] D. Schulz et al., „Robust Optical Wireless Link for the Backhaul and Fronthaul of Small Radio Cells," IEEE Journal of Lightwave Technology, March 2016.
[94] D. Schulz et al., „Long-Term Outdoor Measurements Using a Rate-Adaptive Hybrid Optical Wireless/60 GHz Link over 100 m," in ICTON, Girona, Spain, 2017
[95] D. Schulz et al., „Initial outdoor trials with optical wireless links for smallcell backhauling," in ITG Photonic Networks, Leipzig, 2015.
[96] H. Si et al., "A Novel and Efficient Vector Quantization Based CPRI Compression Algorithm," CoRR, 2015. [Online]. Available: http://arxiv.org/abs/1510.04940.
[97] 5G-Crosshaul, Deliverable 3.2, Final XFE/XCI design and specification of southbound and northbound interfaced, October 2017

[98] 5G-Crosshaul, Deliverable 5.2, Report on experimentation results and proof of concept (under preparation)

[99] Specification, eCPRI, "V1.0 Common Public Radio Interface: eCPRI Interface Specification," Ericsson AB, Huawei Technologies Co. Ltd, NEC Corporation and Nokia, August 2017

[100] Specification, CPRI, "V7.0 Common Public Radio Interface (CPRI); Interface Specification," Ericsson AB, Huawei Technologies Co. Ltd, NEC Corporation, Alcatel Lucent and Nokia Networks, October 2015